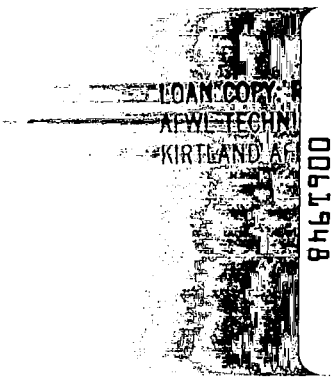

NASA Contractor Report 3336

Kinetic Energy Budgets in Areas of Intense Convection

Henry E. Fuelberg, Emil M. Berecek,
David M. Ebel, and Gary J. Jedlovec

CONTRACT NAS8-33370
NOVEMBER 1980

NASA

NASA Contractor Report 3336

Kinetic Energy Budgets in Areas of Intense Convection

Henry E. Fuelberg, Emil M. Berecek,
David M. Ebel, and Gary J. Jedlovec
Saint Louis University
Saint Louis, Missouri

Prepared for
Marshall Space Flight Center
under Contract NAS8-33370

NASA
National Aeronautics
and Space Administration

**Scientific and Technical
Information Branch**

1980

FOREWORD

This report is one of several to be published from research conducted under NASA Contract NAS8-33370 entitled "Kinetic Energy Budgets in Areas of Intense Convection." The results are only a portion of the total research effort being conducted to unravel the interactions that occur between storm areas and their surrounding environments.

One way of describing wind variability and those processes which produce it, whether storm related or not, is through a kinetic energy budget analysis which describes the various sources and sinks of wind speed. Results of such a study for the Red River Valley tornado outbreak (10 April 1979) are presented in Chapter I using 3 h data from the AVE-SESAME 1 Experiment. Also in Chapter I is a description of the kinetic energy balance during AVE 6, a period of low wind speeds which included a short wave passage.

Because rawinsonde data contain random errors that affect computations of any diagnostic study, it is important to have a quantitative measure of their effects in the derived results. Chapter II consists of an error analysis of several widely used kinematic parameters, including velocity divergence, vorticity advection, and kinematic vertical motion. Chapter III contains an error analysis of the kinetic energy balance during a period of strong jet stream activity.

Meteorologists constantly are seeking new computational procedures that will better describe the state of the atmosphere. Vertical motion is an especially difficult, yet vital, parameter to obtain. Chapter IV presents results of a possible new approach to this problem--downward integration of the continuity equation from 100 mb to obtain kinematic vertical motions.

ACKNOWLEDGMENTS

The authors gratefully acknowledge support provided under NASA Contract NAS8-33370, which is under the auspices of the Atmospheric Sciences Division, Space Sciences Laboratory, National Aeronautics and Space Administration, Marshall Space Flight Center, Alabama. Several individuals of that organization deserve special thanks for their encouragement and assistance toward completing the goals of the research; they are the contract monitor, Mr. Kelly Hill, and Drs. William W. Vaughan, Robert E. Turner, and Gregory S. Wilson.

At Saint Louis University, we express our appreciation to Pat Ryan and Cathy Nicksich for typing portions of the manuscript, Bill Abeling for preparing the figures in Chapters I and II, and Karen Koenig for preparing the figures in Chapter IV. Drs. Donald Martin and Ross Heinrich read portions of the manuscript and offered valuable suggestions for improvement. A scholarship from the Air Force Institute of Technology which allowed Captain Berecek to attend Saint Louis University is gratefully acknowledged.

TABLE OF CONTENTS

TABLE OF CONTENTS (Continued)

TABLE OF CONTENTS (Concluded)

LIST OF TABLES

LIST OF TABLES (Concluded)

LIST OF FIGURES

LIST OF FIGURES (Continued)

LIST OF FIGURES (Concluded)

CHAPTER I

THE SYNOPTIC-SCALE KINETIC ENERGY BUDGETS OF THE AVE-SESAME 1 AND AVE 6 PERIODS

by

Henry E. Fuelberg

and

Gary J. Jedlovec

Department of Earth and Atmospheric Sciences
Saint Louis University
Saint Louis, Missouri 63103

ABSTRACT

Kinetic energy budgets have been computed for the Red River Valley tornado outbreak using 3 h synoptic-scale data from the AVE-SESAME 1 Experiment, and also for the AVE 6 period which included a a short wave passage through the region.

The AVE-SESAME 1 period was characterized by strong jet intrusion which caused horizontal flux convergence to be the dominant energy source for the region. Cross-contour destruction of energy associated with supergradient flow ahead of the jet was the major sink. Transfer of energy from subgrid to grid scales was the second greatest source. Time-height cross sections and horizontal maps revealed the 3 h variability of the period. The development of a low-level jet within the area greatly influenced the energetics of the lower troposphere. In the upper levels, an advancing jet streak appeared to have subsynoptic-scale features which greatly influenced local conditions. The energy balance of storm areas was found to differ greatly from that of the entire region and areas of non-precipitation. In contrast to the other areas, the storm environment had cross-contour generation of kinetic energy and negative dissipation down to subgrid scales. Because jet influences dominated the energy budget, it was not possible to isolate possible feedback mechanisms

due to the storms. By adjusting the divergence component of the horizontal flux divergence term according to the O'Brien scheme, new values of the flux term were obtained. The adjusted values showed better continuity and had better internal consistency with values of vertical motion than did original fields.

Low kinetic energy content with small generation and transport processes were the dominant features of the AVE 6 period. Several major changes occurred in the budget as an upper-level trough passed through the region. Differences between storm area energetics and those of the entire region were similar to those seen in SESAME 1.

CHAPTER I

THE SYNOPTIC-SCALE KINETIC ENERGY BUDGETS OF THE AVE-SESAME I AND AVE 6 PERIODS

1. STATEMENT OF THE PROBLEM

a. Introduction

The quality of numerical forecasts has improved during recent years as fine-mesh models have become operational. These models were the product of years of forecast experience and research with synoptic-scale events. Insights were gained on how best to model the atmosphere on this finer scale by introducing mathematical treatments and engineering procedures which expedite production without violating the more rigid constraints imposed by the modelling equations. Progression to still higher plateaus of forecast excellence, however, awaits an increased knowledge of how best to handle the physics of the smaller scales. Specifically, how do occurrences on the subsynoptic scale influence (and how are they influenced by) processes occurring on the coexisting larger and smaller scales. Parameterization schemes are used in the numerical models to incorporate a few of the effects of the smaller scales, but much more work remains to be done in this regard.

Areas of intense convection are subsynoptic-scale phenomena whose formation is influenced by meteorological conditions on both larger and smaller atmospheric scales. After formation, large areas of storms are thought to modify their synoptic-scale environments through "feedback" mechanisms which, presently, are incompletely understood. This research focuses on the interactions that occur between severe storms and their synoptic-scale wind fields by considering the time and space variability of environmental kinematic parameters such as divergence, vorticity, and vertical motion, and the environmental kinetic energy balance which delineates the causes for changes in wind speed. Through such studies of storm-environment interactions, it is hoped that techniques can be developed to incorporate the effects of such interplay into the numerical models.

b. Previous studies

There is increasing evidence that large areas of intense convection produce effects on their surrounding atmospheric volumes that can be detected using synoptic-scale data. Aubert (1957) showed that latent heat release associated with thunderstorms produced increases in large-scale

horizontal convergence below the level of maximum condensation and enhanced horizontal divergence above that level. He found decreases in values of geopotential height in the lower troposphere and increases in the upper troposphere. Ninomiya (1971a and b), using satellite pictures, found that the pre-existing flow at the cirrus level over tornado-producing thunderstorms changed into outflow as the thunderstorms developed. The existence of a mid-tropospheric warm core and a significant field of convergence below 700 mb were observed using synoptic-scale rawinsonde data. The downward convective transport of horizontal momentum was shown to intensify the low-level jet stream. Each of these phenomena was attributed to latent heat release. Fankhauser (1971) indicated that mature thunderstorms may divert and distort mid-tropospheric air motion in a manner similar to that of solid objects.

Recently, Maddox (1980), using enhanced infrared satellite imagery, studied the synoptic-scale environments of large convective storm areas, which he termed "mesoscale convective complexes". He observed upper-tropospheric height rises, greatly enhanced upper-level divergence, and the formation of jet streaks near these complexes and hypothesized that they were produced by a deep layer of mid-tropospheric, convective warming (Maddox et al., 1980; Fritsch and Maddox, 1980; Maddox, 1980). Fuelberg and Scoggins (1978) computed the synoptic-scale kinetic energy balance of the mesoscale convective complex described by Maddox et al. (1980) and found the upper-tropospheric storm environment to be characterized by strong positive generation of kinetic energy due to cross-contour flow, horizontal flux divergence of energy, upward transport of energy, and transfer of kinetic energy from the resolvable to the subgrid scales of motion. The Fuelberg and Scoggins study of storm-environment interactions was aided by the availability of 3 h rawinsonde data from NASA's fourth Atmospheric Variability Experiment (AVE 4).

The literature contains relatively few studies describing the kinetic energy balance of the convective environment. Several of these studies are based on synoptic-scale data at 12 h intervals. Danard (1964,1966) used numerical methods with and without the inclusion of latent heat to compute the effects of a large precipitation area on certain energy budget terms. The production of kinetic energy due to rising air and cross-contour flow was enhanced considerably by latent heat release whose effect was of the same order of magnitude as that caused solely by dry adiabatic processes. The kinetic energy

budget of atmospheric volumes surrounding trade wind cloud clusters in the Pacific Ocean was investigated by Williams (1970), who found them to be vertical transporters of kinetic energy with little internal generation or dissipation. Kinetic energy was found to be imported in the lower half of the troposphere, transported upward within the convective clouds, and exported in the upper-tropospheric outflow. The kinetic energy budget for clear areas was considerably different from that of the clusters. Robertson and Smith (1980), also using synoptic-scale data at 12-h intervals, studied storm-environment energetics during the Jumbo (3-5 April 1974) and Palm Sunday (10-12 April 1965) tornado outbreaks. Negative generation of kinetic energy and horizontal flux convergence of energy were found to be the dominant processes during the two periods. Vincent and Schlatter (1979) proposed that transfer of potential energy on the cumulus scale to kinetic energy on the synoptic scale could explain mid-tropospheric regions of positive dissipation observed near tropical storm Candy (1968).

Compared to investigations of the synoptic-scale storm environment, even fewer studies have considered kinetic energy budgets of the subsynoptic-scale storm environment (a lack of mesoscale data is a serious obstacle to such research). Three such studies have used data from the mesoscale network of nine rawinsonde stations (∿80 km spacing) by the National Severe Storm Laboratory (NSSL) (McInnis and Kung, 1972; Kung and Tsui, 1975; Tsui and Kung, 1977). Areas of convection were found to be centers of major energy generation, transport and dissipation. Some of the processes were an order of magnitude larger than corresponding processes on the synoptic scale. Large generation of kinetic energy by cross-contour flow was nearly balanced by dissipation to subgrid scales of motion, while boundary terms and local changes were comparatively small. A relation between variations in energy variables and the growth and decay of storms was noted. Data from the AVE-SESAME 1979 Experiments will provide additional opportunities to study subsynoptic-scale interactions between storms and their environments.

The previously mentioned study by Fuelberg and Scoggins (1978) used AVE rawinsonde data with a synoptic-scale spacing but with a subsynoptic-scale time interval (3 h). Additional studies of this type were reported by Fuelberg (1979a). In contrast to the significant energy variability noted during the severe storm periods, the higher resolution AVE

data did not indicate major wind fluctuations during the winter-time AVE 3 period (Fuelberg and Scoggins, 1980).

c. Objectives

Operational forecast models such as the LFM do not allow for major feedback mechanisms from storm areas, but it is hypothesized that the inclusion of such effects would yield improved forecast results. Before such effects can be parameterized, however, much additional information needs to be gained. This research has been directed toward that goal. The specific items that have been investigated are:

1) The relation between spatial fields of kinetic energy budget terms and the locations and movements of convection and other discernible map features,

2) A description of the average kinetic energy budgets for each experimental region,

3) The relation between temporal variations in kinetic energy budget terms and the life cycles of convective activity and, as a result of the above,

4) The suitability of using satellite-derived data, especially VAS data, for diagnosing the variability of the wind field.

2. THEORETICAL CONSIDERATIONS

The kinetic energy budget equation for a fixed volume in the isobaric coordinate system is given by Smith (1969) as:

$$\frac{\partial K}{\partial t} = \iint -\vec{V}\cdot\vec{\nabla}\phi \; - \iint \vec{\nabla}\cdot k\vec{V} \; - \iint \frac{\partial \omega k}{\partial p} \; + \iint \vec{V}\cdot\vec{F} \; + \int k_o \frac{\partial p_o}{\partial t} \qquad (1.1)$$

(a) (b) (c) (d) (e) (f)

where

$$\iint = \frac{1}{gA} \iiint dx\, dy\, dp$$

$\vec{V}$ = the horizontal wind vector,

$\omega = \frac{dp}{dt}$ is the vertical motion in isobaric coordinates,

$k = (u^2 + v^2)/2$ is horizontal kinetic energy per unit mass,

$K = \iint k$,

$\phi = gz$ is geopotential height,

$\vec{F}$ = the frictional force,

A = the computational area, and

$_o$ = a subscript denoting surface values.

Local changes in kinetic energy for a fixed volume, term (a) above, are due to five processes. Term (b) represents kinetic energy generation (Kung, 1966) or conversion of potential to kinetic energy (Smith, 1970) due to cross-contour flow. Terms (c) and (d) are the horizontal and vertical components of flux divergence of kinetic energy. Term (f) represents changes in kinetic energy due to changes in the mass of the volume being studied. Since this term was found to be at least two orders of magnitude smaller than the other terms in (1.1), it will not be included in future discussions.

Term (e) conceptually represents thermodynamic frictional processes, but when computed as a residual to the kinetic energy equation, it also represents a transfer of energy between grid and subgrid scales of motion, due mostly to unresolvable eddy processes

(Smith and Adhikary, 1974; Kung and Smith, 1974). The term is often called the "dissipation" term. The residual dissipation term also contains errors accumulated from other terms in the kinetic energy equation, but error simulations have shown that these are not the dominant components of the dissipation term (Vincent and Chang, 1975; Kornegay and Vincent, 1976; Ward and Smith, 1976; Fuelberg and Scoggins, 1980; Robertson and Smith, 1980). Since the resolvable scales of motion in a given study are generally known, this residual term allows one to infer the importance of motions which are not readily detectable with the input data scale and computational procedures being used. For example, if synoptic-scale data are used, the net effect on kinetic energy of mesoscale and microscale processes that are not adequately described by the input data can be inferred.

Release of potential energy ($\omega\alpha$) is related to kinetic energy generation ($-\vec{V}\cdot\vec{\nabla}\phi$) by

$$\iint -\vec{V}\cdot\vec{\nabla}\phi = \iint \vec{\nabla}\cdot\phi\vec{V} - \iint \omega\alpha, \tag{1.2}$$

where the first term on the right represents boundary work (Smith, 1969). This equation emphasizes that the release of potential energy in a limited volume is not necessarily accompanied by a corresponding amount of local kinetic energy generation because of interactions between the limited volume and its surroundings.

3. DATA AND ANALYTICAL PROCEDURES

a. The AVE-SESAME 1 data

The first AVE-SESAME period ran from 1200 GMT 10 April through 1200 GMT 11 April 1979 and consisted of three hourly rawinsonde soundings at twenty-three National Weather Service (NWS) stations plus an additional sixteen special sites (see Fig. 1.1). Subsynoptic-scale time and space resolution were thereby obtained. Further details of the AVE-SESAME program are given by Alberty *et al.* (1979), Barnes (1979), and Hill *et al.* (1979). Data reduction procedures used to process the rawinsonde data are described by Fuelberg (1974) while the data at 25 mb intervals are given by Gerhard *et al.* (1979). Since the present study focused on synoptic-scale conditions, only the NWS data were used in the computations described in this report. Tasks in the upcoming year will study subsynoptic-scale interactions by using the combination of NWS and special site observations.

b. The AVE 6 data

The AVE 6 period consisted of observations at 0000, 1200, 1500, 1800, and 2100 GMT on 27 May 1977 and 0000, 0300, and 1200 GMT on 28 May. The twenty-two rawinsonde stations that participated are shown in Fig. 1.2. These data at 25 mb intervals are given by Dupuis and Hill (1977).

c. Analytical procedures

Because computational procedures for this study were similar to those used by Fuelberg and Scoggins (1978), they will be described only briefly in the present paper. Data were interpolated from the randomly spaced stations onto a grid system with a spacing of 158 km using the Barnes (1964) objective analysis scheme. Gridded analyses of the input data were produced at the surface and at 50 mb intervals from 900 to 100 mb (18 levels). Input wind data were averaged over 50 mb layers to reduce the effects of random errors. Centered finite differences were used where possible to compute all space and time derivatives. However, forward and backward time differences were used for the first and last observation times, respectively.

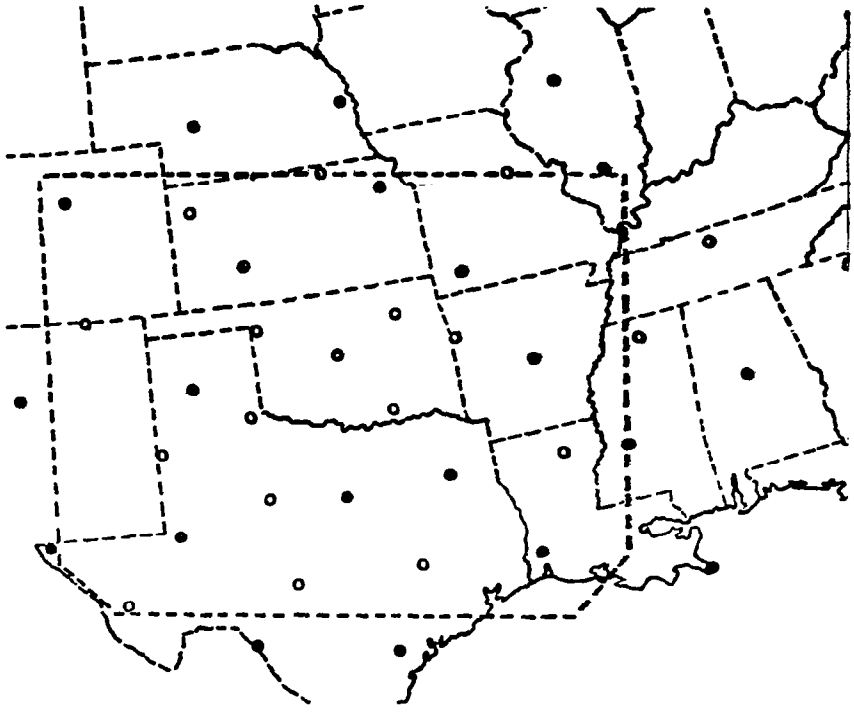

Fig. 1.1. NWS (·) and special site (o) rawinsonde stations participating in AVE-SESAME 1. The energy budget was averaged within the region indicated by the dashed line.

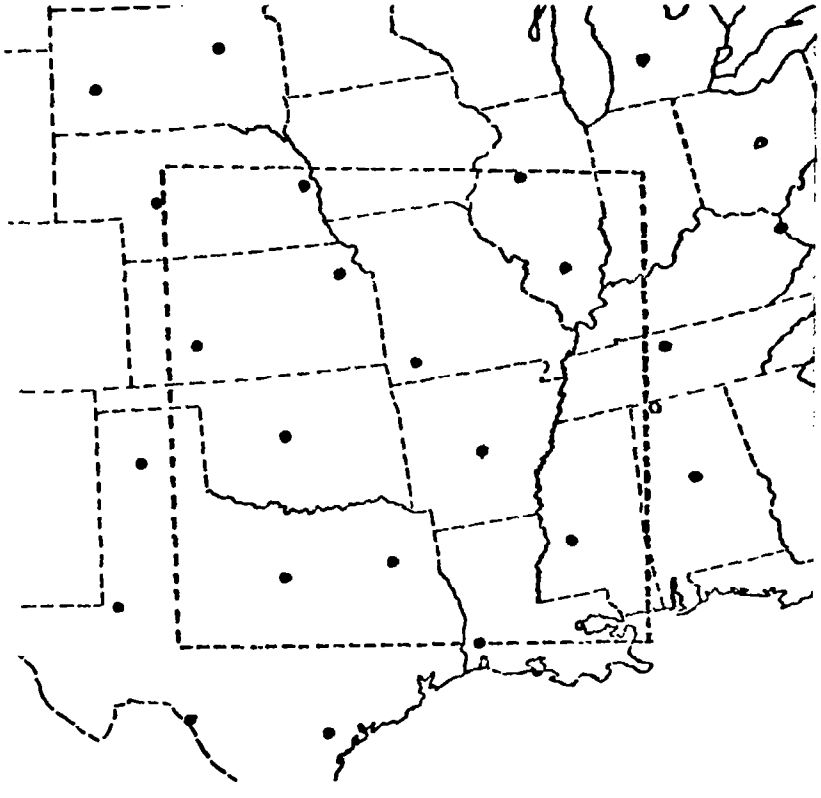

Fig. 1.2. Rawinsonde stations participating in AVE 6. See Fig. 1.1 for other details.

Grid-point values of terms in (1.2) and (1.1), except term (e), were computed at each of the 18 levels and integrated over 50 mb layers using the trapezoidal rule. The dissipation term, term (e), was computed as a residual to balance (1.1) at each grid point in each 50 mb layer. Kinematic values of vertical motion were used. Vertical motion at the surface was assumed to be zero, and an adjustment scheme by O'Brien (1970) was applied so that values at 100 mb also equalled zero. Values of horizontal divergence were adjusted according to O'Brien's procedure to make them consistent with the ω values. As described in a later section, these adjusted values of divergence then were used in an alternate method of computing horizontal flux divergence of kinetic energy.

4. SYNOPTIC CONDITIONS OF AVE-SESAME 1

The AVE-SESAME 1 period coincided with the Red River Valley tornado outbreak which included deadly tornadoes at Wichita Falls and Vernon, Texas, and Lawton, Oklahoma, plus many other less damaging storms. By the end of the day on 10 April, 56 people had been killed, 1,916 injured, and damage estimates totalled several hundred million dollars (NOAA, 1980).

Synoptic conditions at 1200 GMT 10 April are shown in Fig. 1.3. At the surface, an anticyclone centered over the Great Lakes bathed the eastern half of the country in cool, dry air. A deep cyclone (988 mb center), located over the Colorado-Wyoming border, was the anchor point for a cold front extending southward into New Mexico and a stationary front extending southeastward into Nebraska and Kansas. A stationary front also was positioned along the Gulf Coast. The circulation around the low carried warm, moist air over southern Texas as the stationary front over the Gulf moved northward as a warm front. A developing dry line in the Texas Big Bend separated dew points of 21°F at El Paso and 12°F at Marfa from values in the fifties and sixties in central Texas. A cool maritime anticyclone was located off the coast of California.

An amplifying baroclinic wave was the dominant feature at 500 and 300 mb (Fig. 1.3). The system exhibited a negative tilt, stretching from Washington into southwestern New Mexico. A weakening short wave extended in a northwest to southeast direction through the Midwest, while a ridge was located from the middle Mississippi River Valley into the Dakotas. Due to a 700 mb dry layer over most of Texas and warm moist air below, the Texas-Oklahoma region was quite unstable, even at 1200 GMT.

A low-level southerly wind maximum extending from the middle Texas coast into Kansas contained speeds as great as 20 m s^{-1}, while a middle-level jet extended from southern New Mexico into Oklahoma with speeds up to 30 m s^{-1}. The 300 mb jet was parallel to the mid-tropospheric flow over the AVE-SESAME 1 area. Maximum winds at 300 mb over the experiment region were 50 m s^{-1} along the Gulf Coast; however, the main jet maximum was located on the back side of the trough near California and southern Arizona.

The visible satellite image for 1331 GMT (Fig. 1.4) reveals the

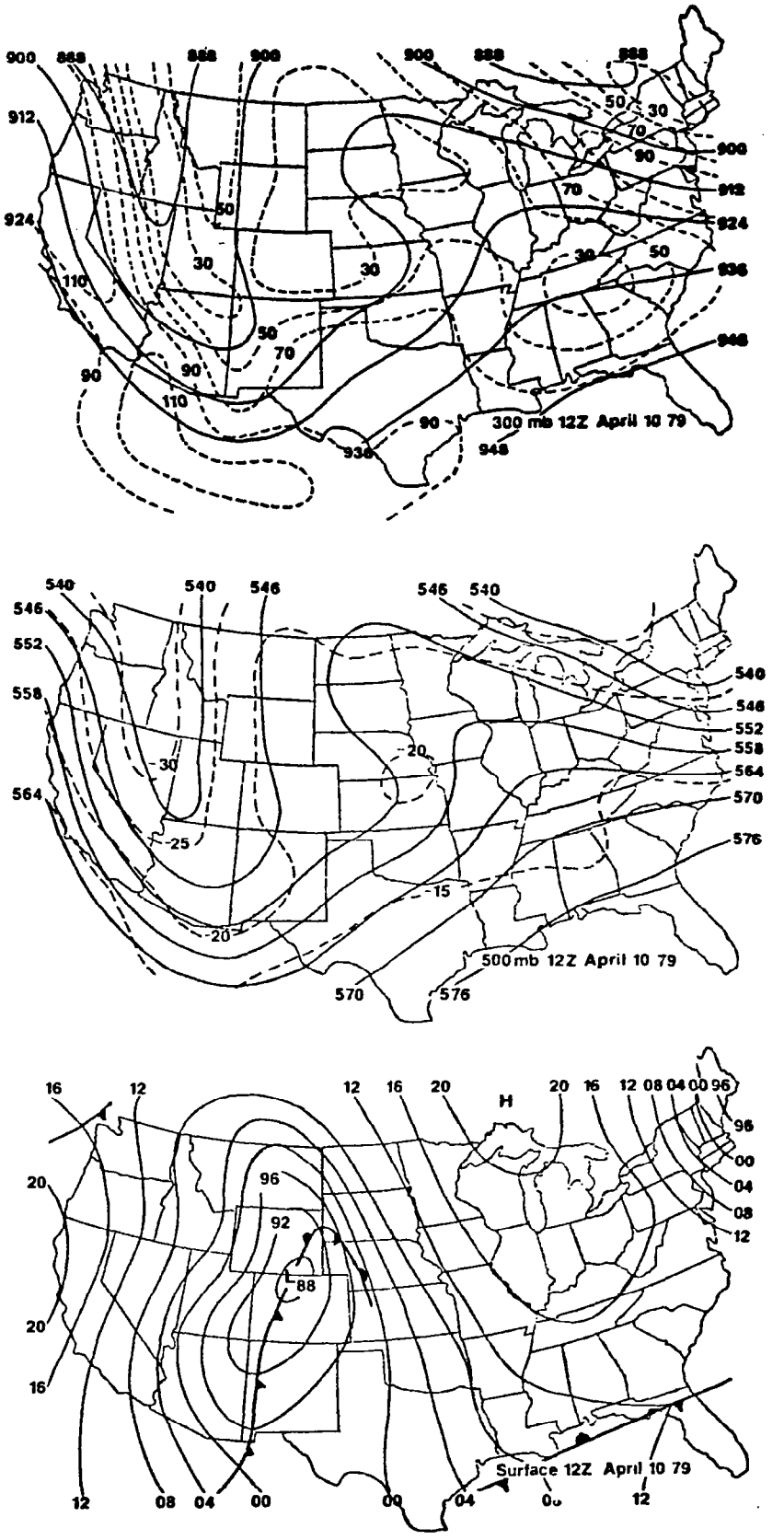

Fig. 1.3. Synoptic conditions at 1200 GMT 10 April 1979. Dashed lines at 500 mb are isotherms. Dashed lines at 300 mb are isotachs (kts).

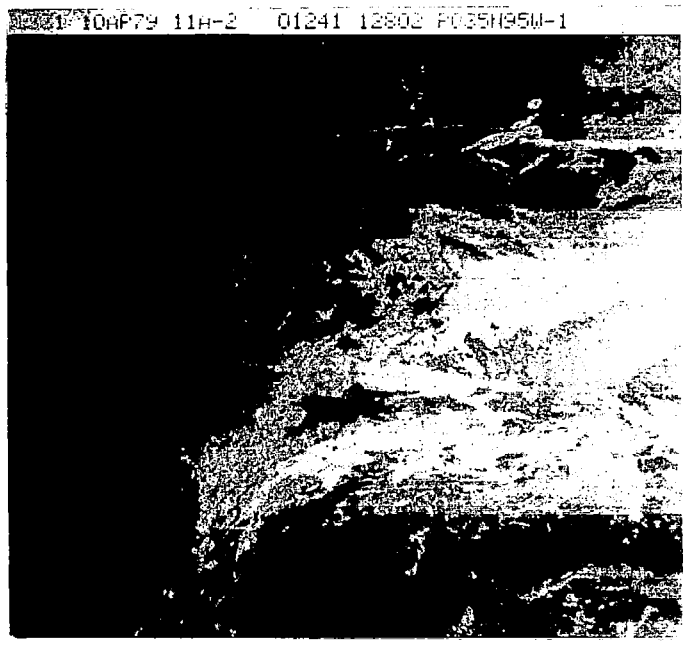

Fig. 1.4. Visible satellite image for 1331 GMT 10 April 1979

cloud cover near the beginning of the AVE-SESAME 1 period. Showers and thunderstorms were occurring from Arkansas, through southwestern Missouri, into Kansas, but no severe activity was reported at this time.

Major changes in synoptic conditions occurred during the day of 10 April which set the stage for the tornado outbreak that began near 1800 GMT. These changes are easily seen using the special 3 h midwestern AVE-SESAME 1 data. The movement of short waves through the major trough and into the Red River Valley was a major factor leading to storm development and can be observed in the patterns of adjusted horizontal divergence (Fig. 1.5) and relative vorticity (not shown). One should recall that only NWS sources have been used in this diagnosis. At 1500 GMT, low-level convergence over Arkansas corresponded well with the shower activity in that region. There was evidence of low-level convergence over the western portion of the computational region although high terrain restricted the view of that area at 850 mb. The dominant feature at 300 mb was a center of divergence (4.5×10^{-5} s^{-1}) located over northeastern New Mexico. By 1800 GMT, the areas of low-level convergence and upper-level divergence had moved eastward toward the Texas panhandle.

Compared to 3 h earlier, regional conditions at 2100 GMT were characterized by greatly enhanced convergence at 850 mb as well as

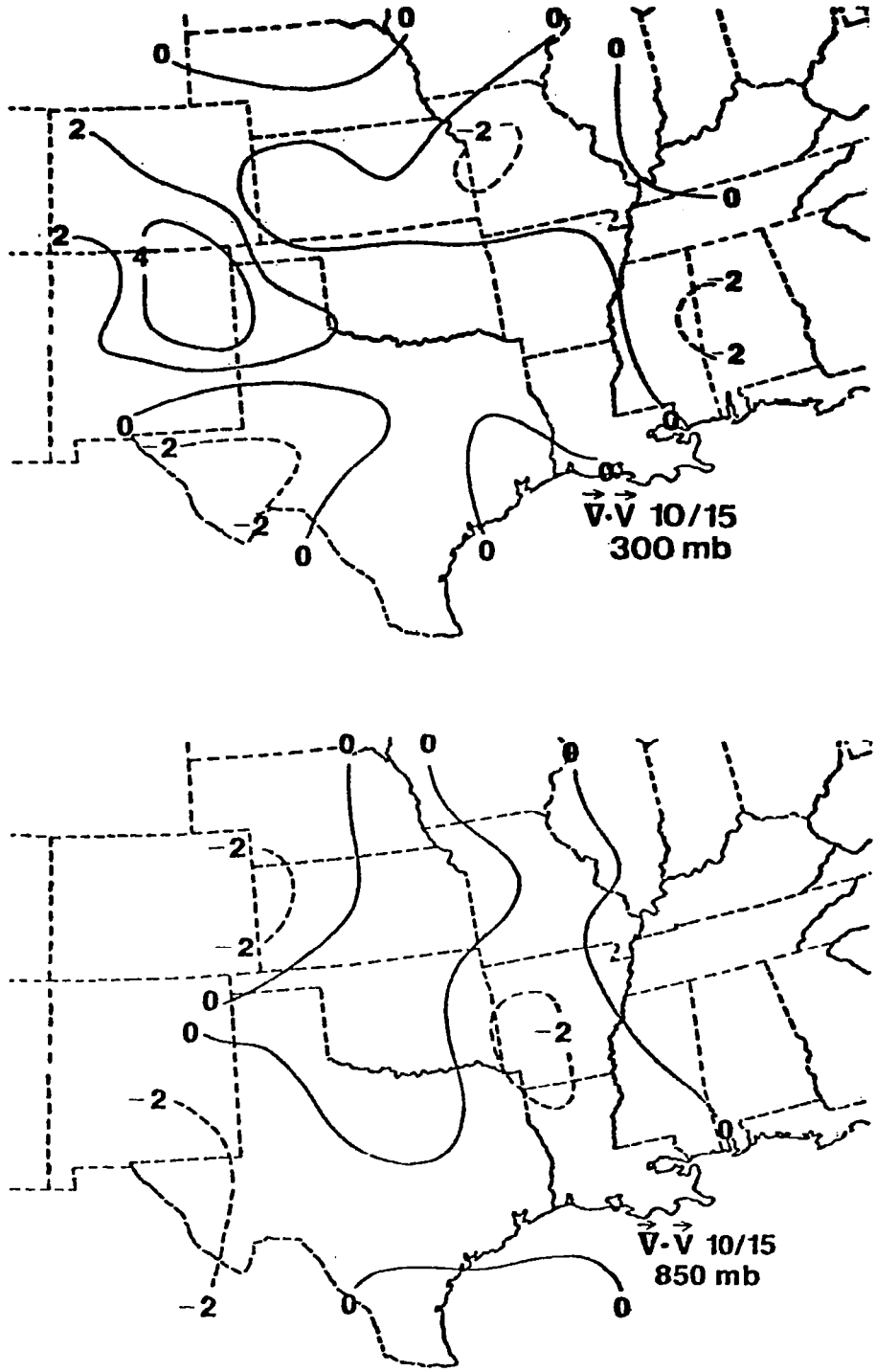

Fig. 1.5. Adjusted horizontal divergence at 850 and 300 mb (10^{-5} s^{-1}) from 1500 GMT 10 April through 0000 GMT 11 April.

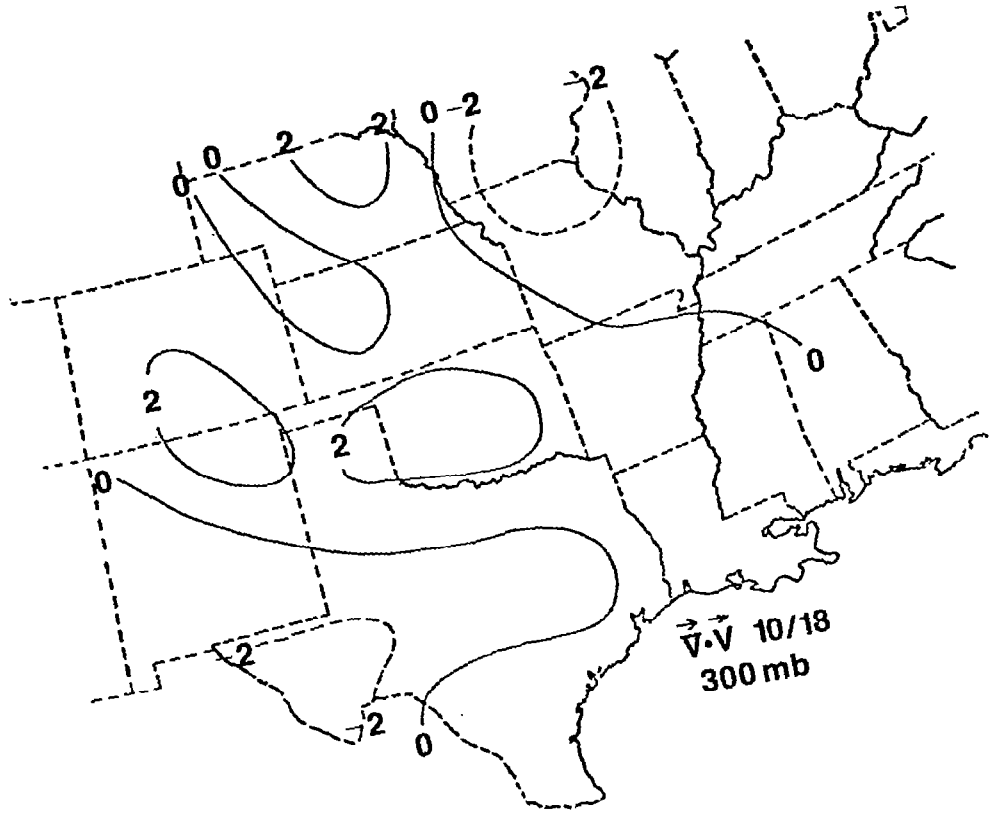

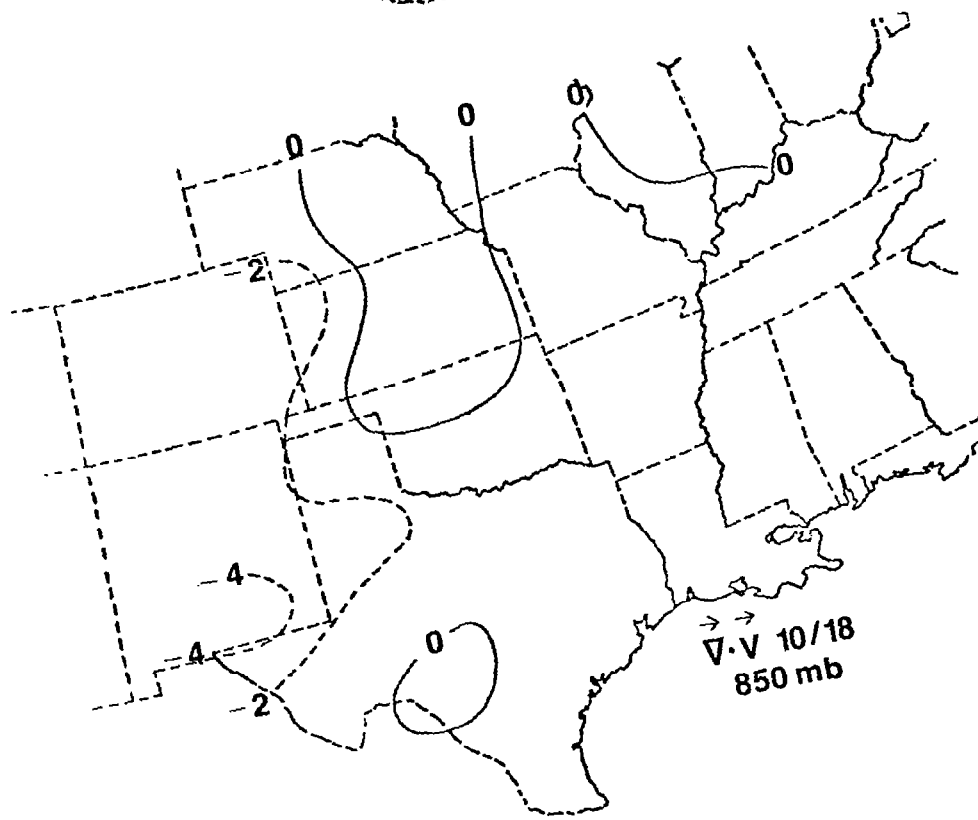

Fig. 1.5. (Continued)

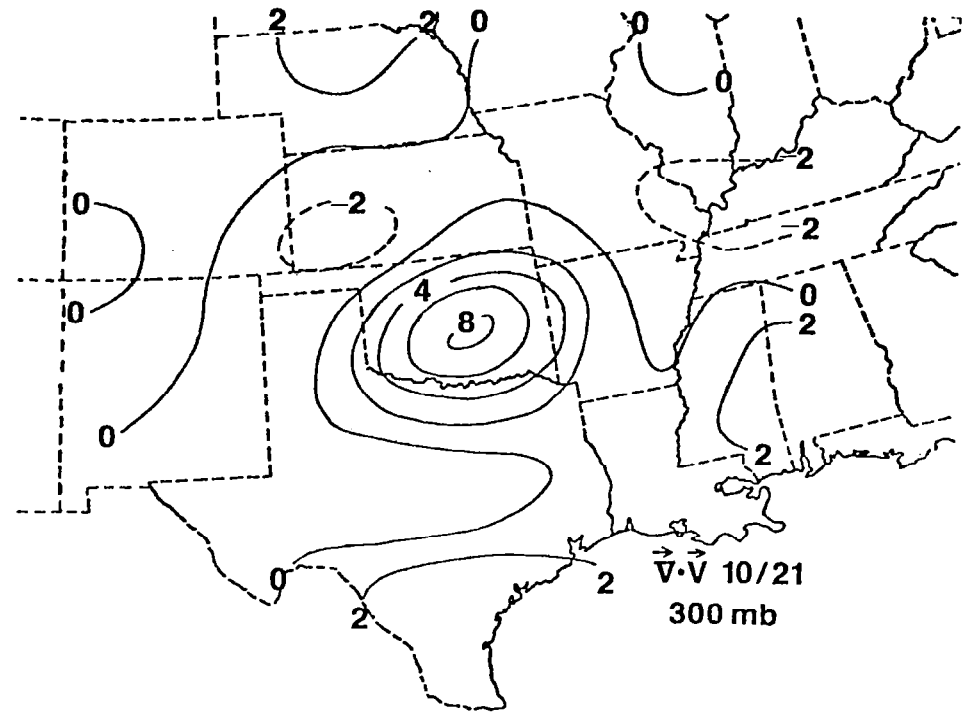

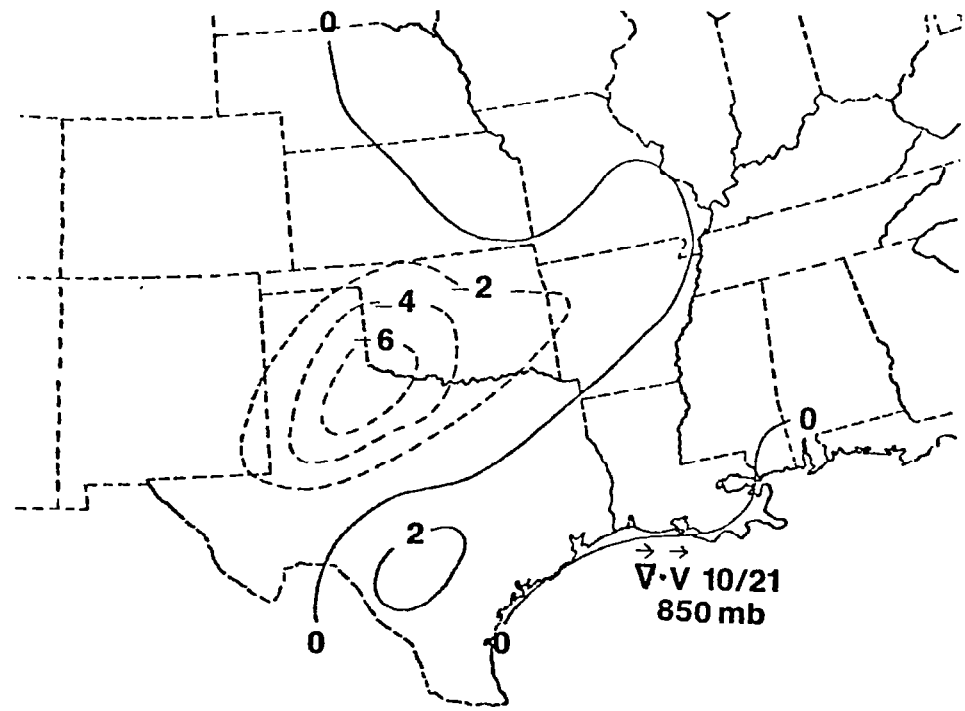

Fig. 1.5. (Continued)

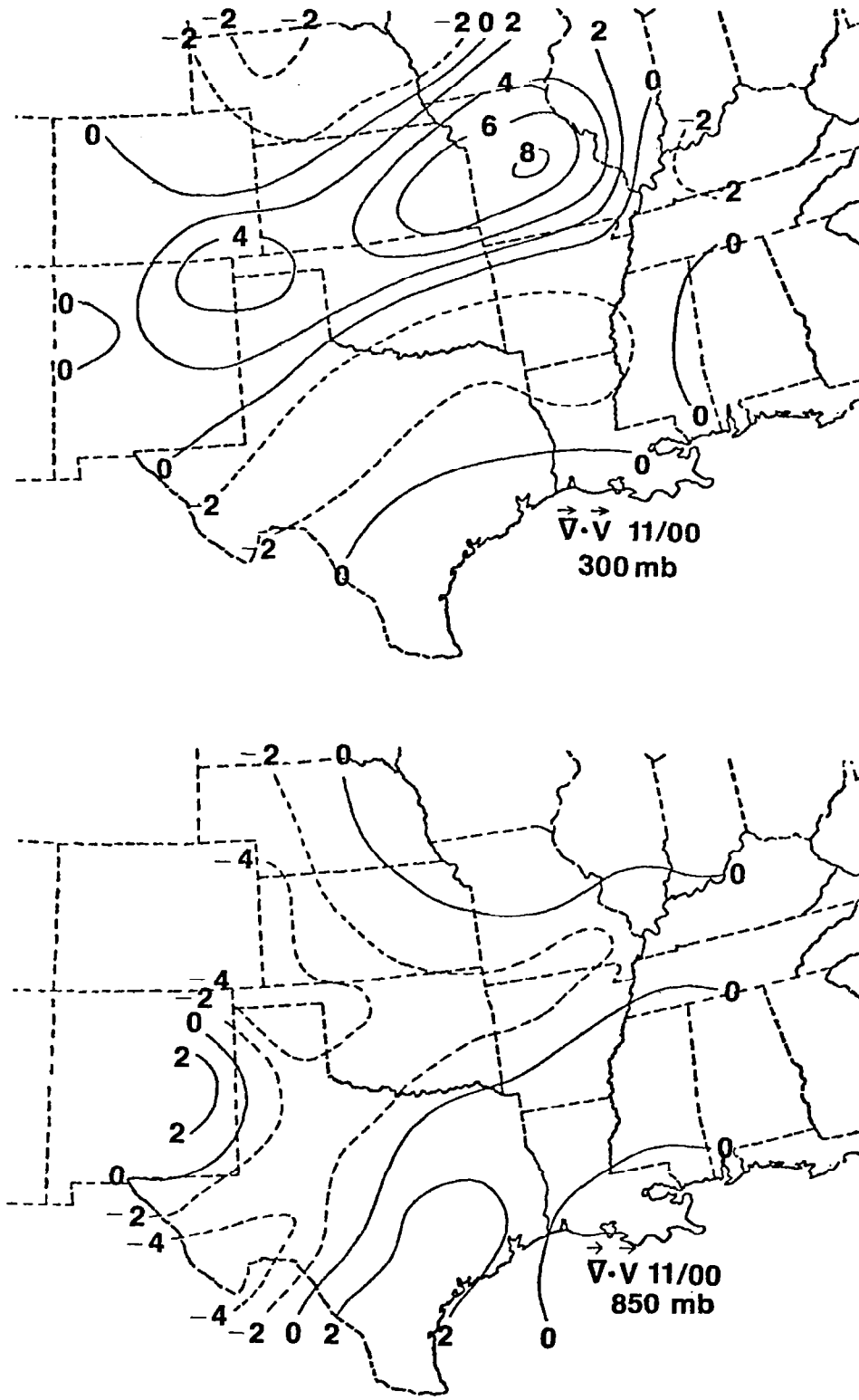

Fig. 1.5. (Concluded)

greatly enhanced divergence at 300 mb, with both centers located near the Red River Valley (Fig. 1.5). These divergence-convergence patterns produced a well-defined center of upward vertical motion centered over western Oklahoma with values at 500 mb as great as 15 $\mu b\ s^{-1}$ (Fig. 1.6). Figure 1.5 shows that the area of low-level convergence became weaker and less defined by 0000 GMT 11 April as the area of 300 mb divergence moved into Missouri and the Texas-Oklahoma panhandles. A broad region of upward vertical motion extended from Illinois westward through Oklahoma, Colorado, and New Mexico (Fig. 1.6).

Coincident with the movement of the short wave aloft were other factors that aided the formation of the storm outbreak. Moller (1980) observed the development of a surface mesolow near Midland, Texas, at 1700 GMT which moved northward to near Wichita Falls and dissipated by 0200 GMT. He hypothesized that this surface feature was associated with the short wave trough aloft. The surface dryline over West Texas in the early morning intensified and moved northeastward toward the Red River Valley during the afternoon in association with the surface mesolow and wave aloft.

A strong low-level jet (LLJ) developed over northeastern Texas during the day of 10 April. The LLJ occurred in the exit region of an advancing upper-level jet streak and may be dynamically linked through mass-momentum adjustments to the upper-level streak in a manner similar to that described by Uccellini and Johnson (1979). The LLJ developed rapidly near 1800 GMT and by 0000 GMT 11 April, its maximum winds at 850 mb were 30 $m\ s^{-1}$ over Oklahoma. The LLJ was not confined to the planetary boundary layer and did not possess an early morning maximum of wind speed. Uccellini (1979) noted that LLJ's associated with lee side cyclogenesis and upper-level propagating jet streaks often possess such characteristics. The effect of the LLJ was to rapidly transport heat and moisture into Texas and Oklahoma.

Because of the above mentioned processes, conditions were ripe for severe storm formation over northeastern Texas and central Oklahoma during the afternoon of 10 April. Thermal and moisture conditions at 2100 GMT yielded K Index (Total Totals) values of 38 (49) at Amarillo, 46 (48) at Oklahoma City, and 87 (55) at Stephenville. In

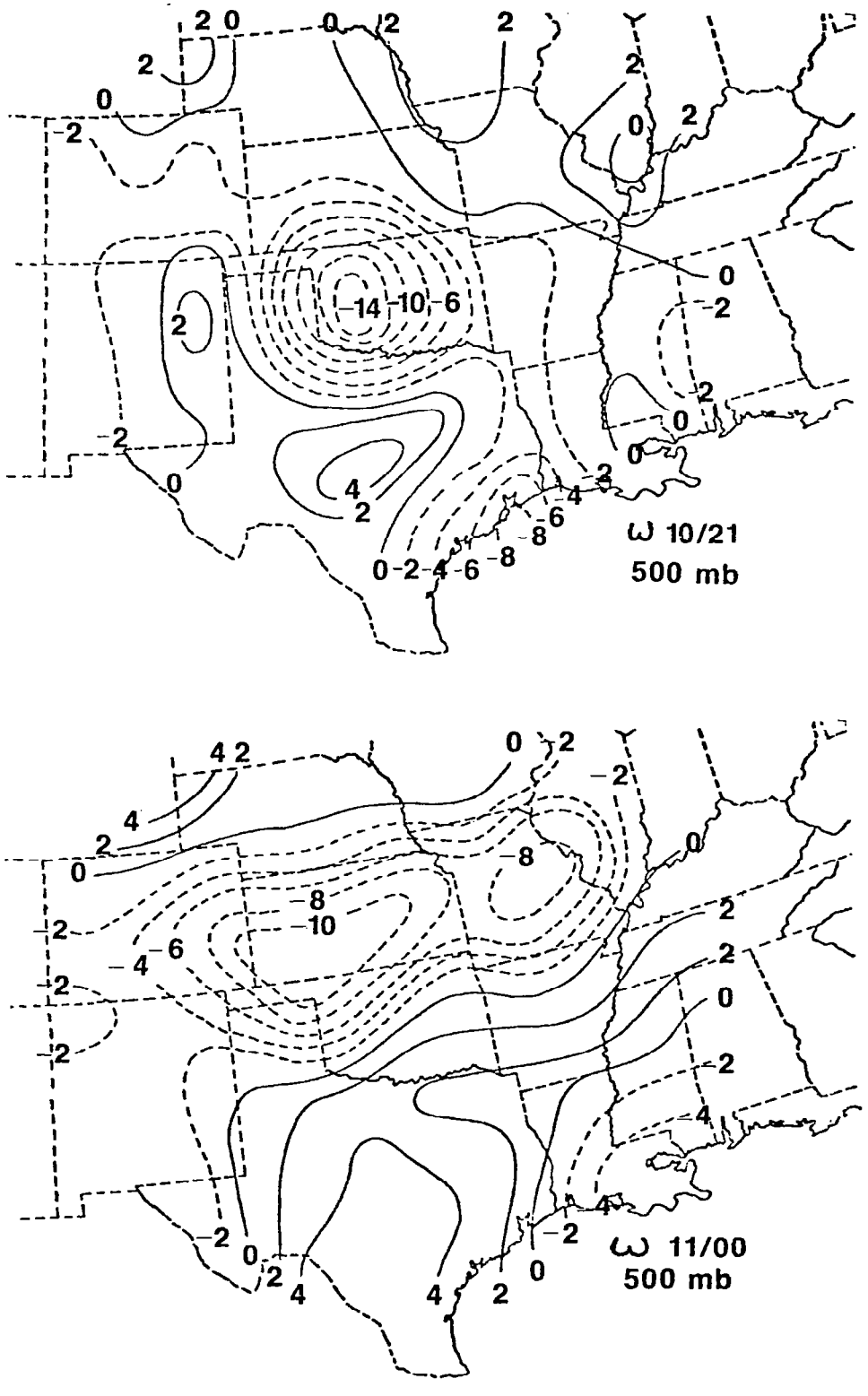

Fig. 1.6. Vertical motion (ω) at 500 mb (μb s^{-1}) for 2100 GMT 10 April and 0000 GMT 11 April.

addition, well-defined low-, middle-, and upper-level jets intersected each other near the Red River Valley. The surface dry line and triggering from the short wave aloft, mesolow, and warm front completed the scenario.

Radar summaries for the AVE-SESAME 1 period are given at 3 h intervals in Fig. 1.7. Severe thunderstorm activity first began at about 1735 GMT near Stephenville, Texas, where echo tops reached 15.2 km (50,000 ft). Near 1900 GMT, an area of storms which spawned several weak tornadoes formed near Lubbock, Texas. The area of thunderstorm activity expanded and moved northward, stretching from western Arkansas, through Oklahoma, and into the Texas panhandle by 2035 GMT (Fig. 1.7). The visible satellite picture for 2100 GMT shows the area of developing storms (Fig. 1.8). Several violent tornadoes occurred between Childress and Wichita Falls near 2100 GMT. The Vernon tornado which killed eleven people struck at 2145 GMT, while tornadoes struck Lawton at 2315 GMT and Harrold, Texas, at 2200 GMT. The Wichita Falls tornado, which killed forty-three persons and injured over 1700, struck shortly after 0000 GMT 11 April. Moller (1980) noted that the damaging tornadoes occurred in the northeast quadrant of the surface mesolow, on the western side of a strong moisture ridge, and in the tightest gradient of a surface temperature ridge. The radar summary at 2335 GMT (Fig. 1.7) and satellite photograph at 2300 GMT (Fig. 1.8) show the appendage of severe storms in the vicinity of Wichita Falls with radar tops up to 17.7 km (58,000 ft), as well as the general area of storms to the north.

Synoptic conditions for the entire United States at 0000 GMT 11 April (Fig. 1.9) reveal the large-scale changes that have occurred since 1200 GMT (Fig. 1.3), the time of the previous nationwide rawinsonde observations. The surface cyclone moved to southeastern Colorado, remaining near the same intensity, while the Pacific cold front moved eastward into the Texas panhandle and Big Bend regions. Movement of the warm front into Oklahoma carried warm, moist air over the eastern two-thirds of Texas. At 500 mb, the long-wave trough over the Rocky Mountains moved eastward and developed a cut-off center over the four corners region. The short wave seen over Kansas at 1200 GMT was not apparent in the height field 12 h later. The eastward progression of the major trough also was evident at 300 mb. Winds of 55 m s^{-1} (110 kts) associated

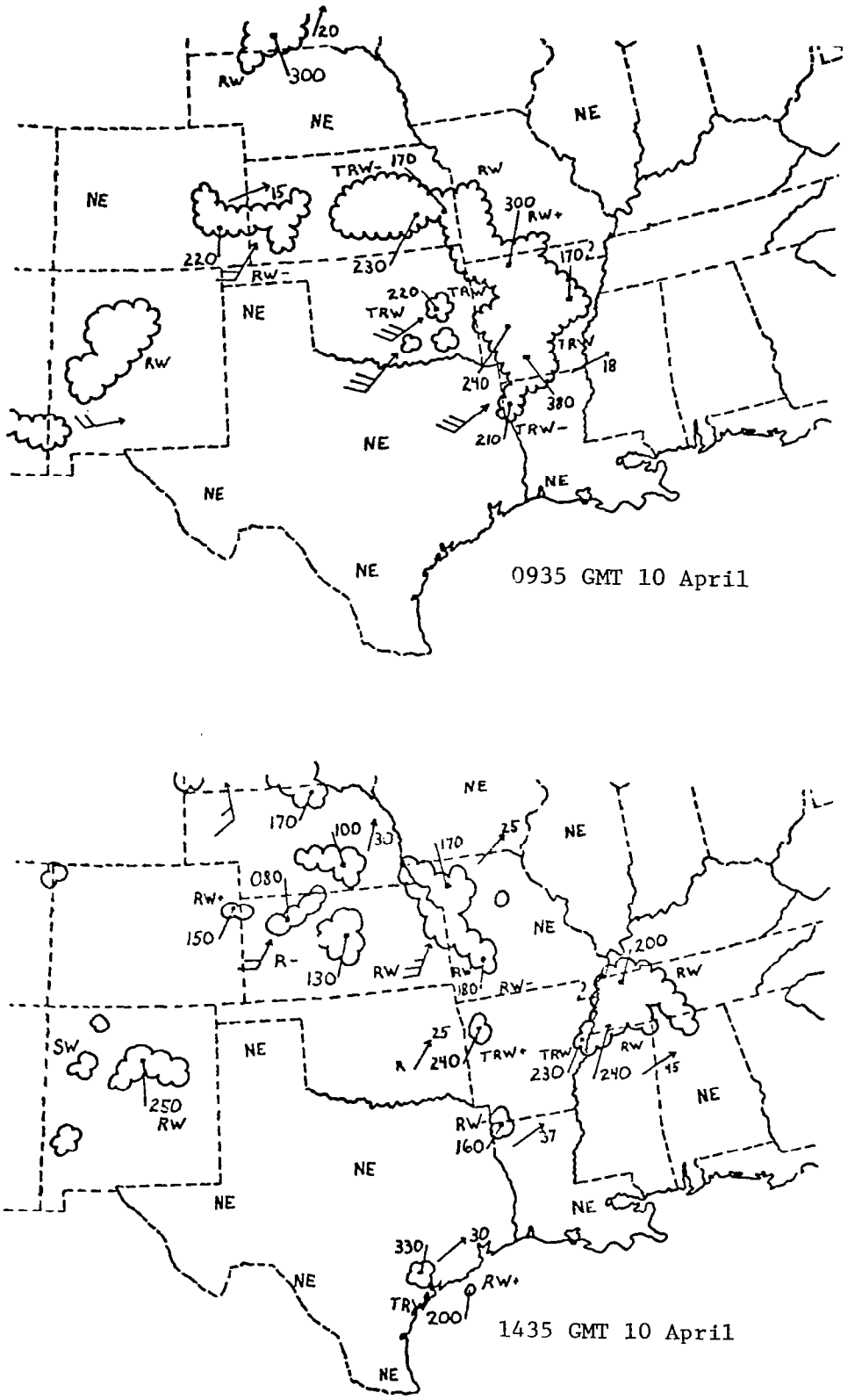

Fig. 1.7. Radar summaries between 0935 and 2335 GMT 10 April 1979.

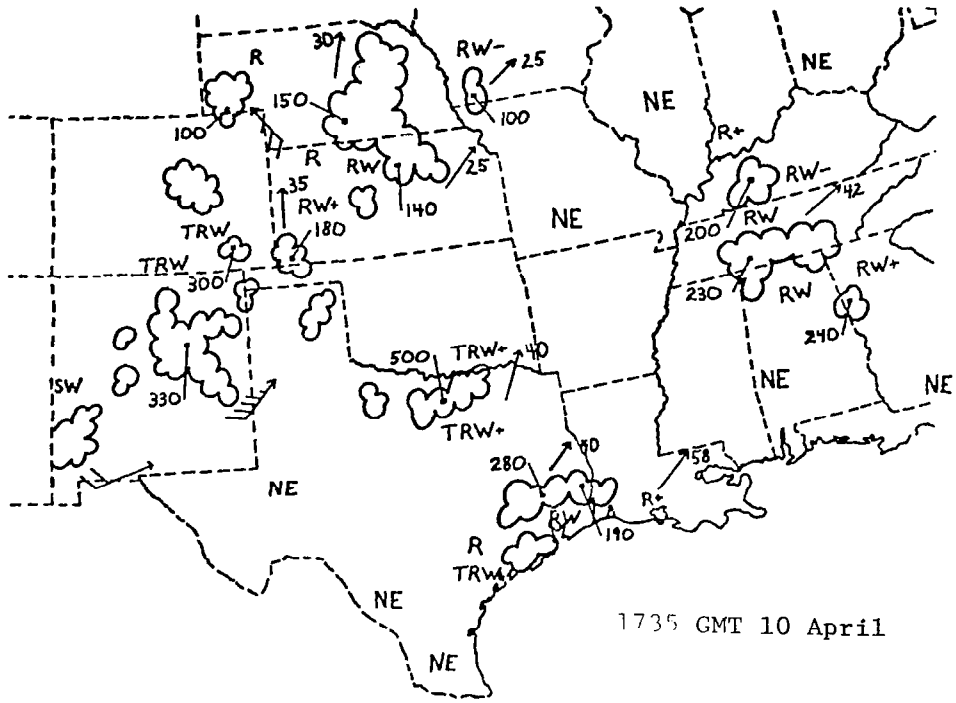

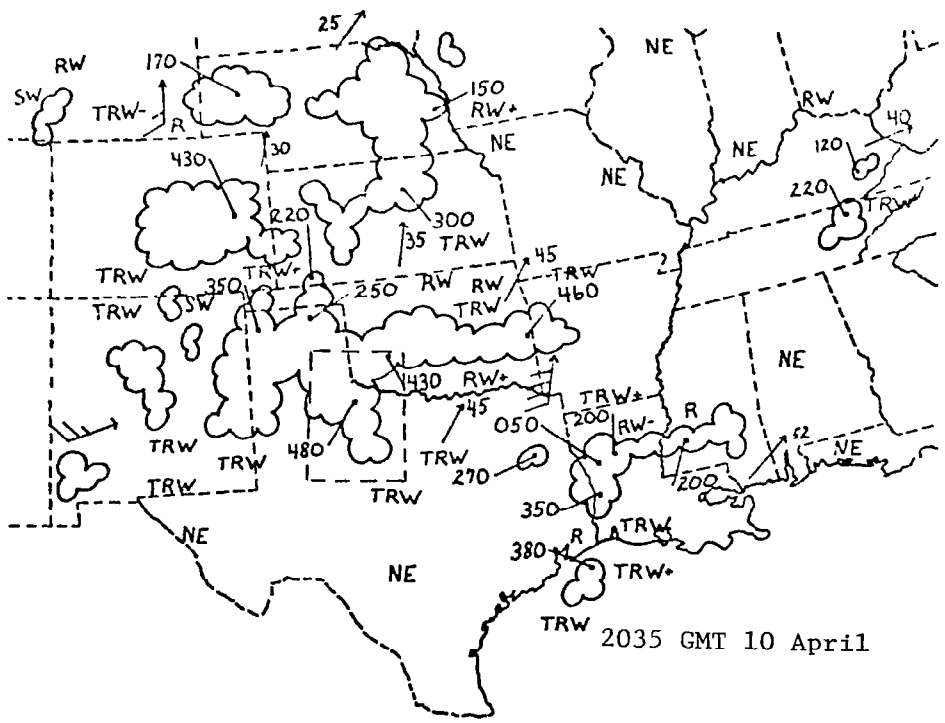

Fig. 1.7. (Continued)

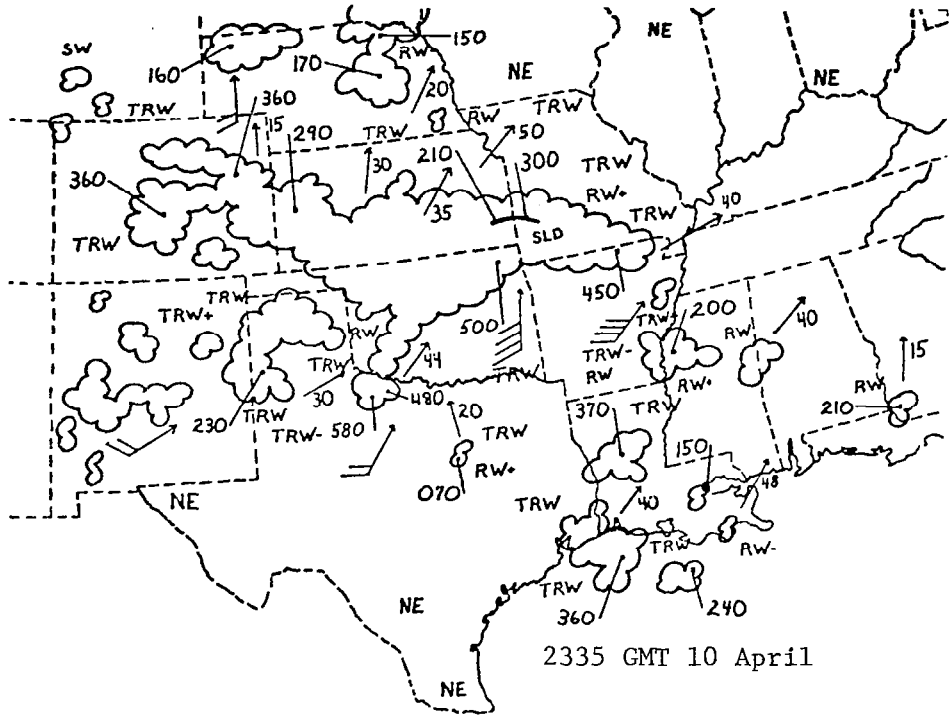

Fig. 1.7. (Concluded)

with the advancing jet streak penetrated into West Texas, but highest winds of 65 m s^{-1} (130 kts) still were located along the California-Nevada border. The short wave which was helping to produce the severe storms over the Red River Valley was not evident in the height fields at 500 or 300 mb but, as described earlier, was easily detectable in the divergence patterns (Fig. 1.5). At 0000 GMT, the LLJ containing southerly flow was centered over Oklahoma with speeds at 850 mb of 30 m s^{-1}.

There is evidence of a second short wave moving into Texas during the last half of the AVE-SESAME 1 period. Fields of kinematic parameters for 0900 GMT 11 April are given in Fig. 1.10. The area of low-level convergence over central Texas at 0900 GMT had moved steadily northeastward from out of the Big Bend region, being barely detectable near 0000 GMT 11 April (Fig. 1.5). Likewise, the area of upper-air divergence over Oklahoma at 0900 GMT first was apparent over New Mexico at earlier times. Upward vertical motion was occurring over a broad portion of the AVE-SESAME 1 region stretching from Illinois into Texas. At 0900 GMT, maximum upward motion was 9 $\mu b\ s^{-1}$ over southwestern Oklahoma. Moller

2100 GMT 10 April

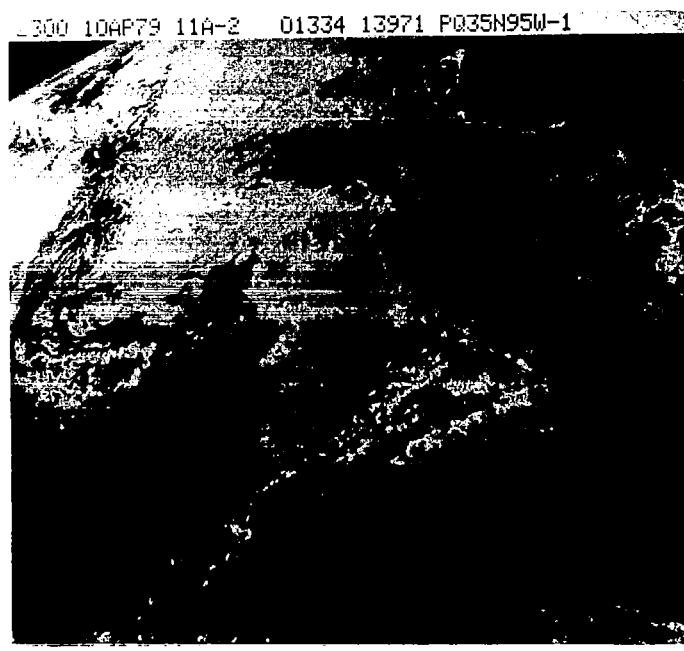

2300 GMT 10 April

Fig. 1.8. Visible satellite images for 2100 and 2300 GMT 10 April.

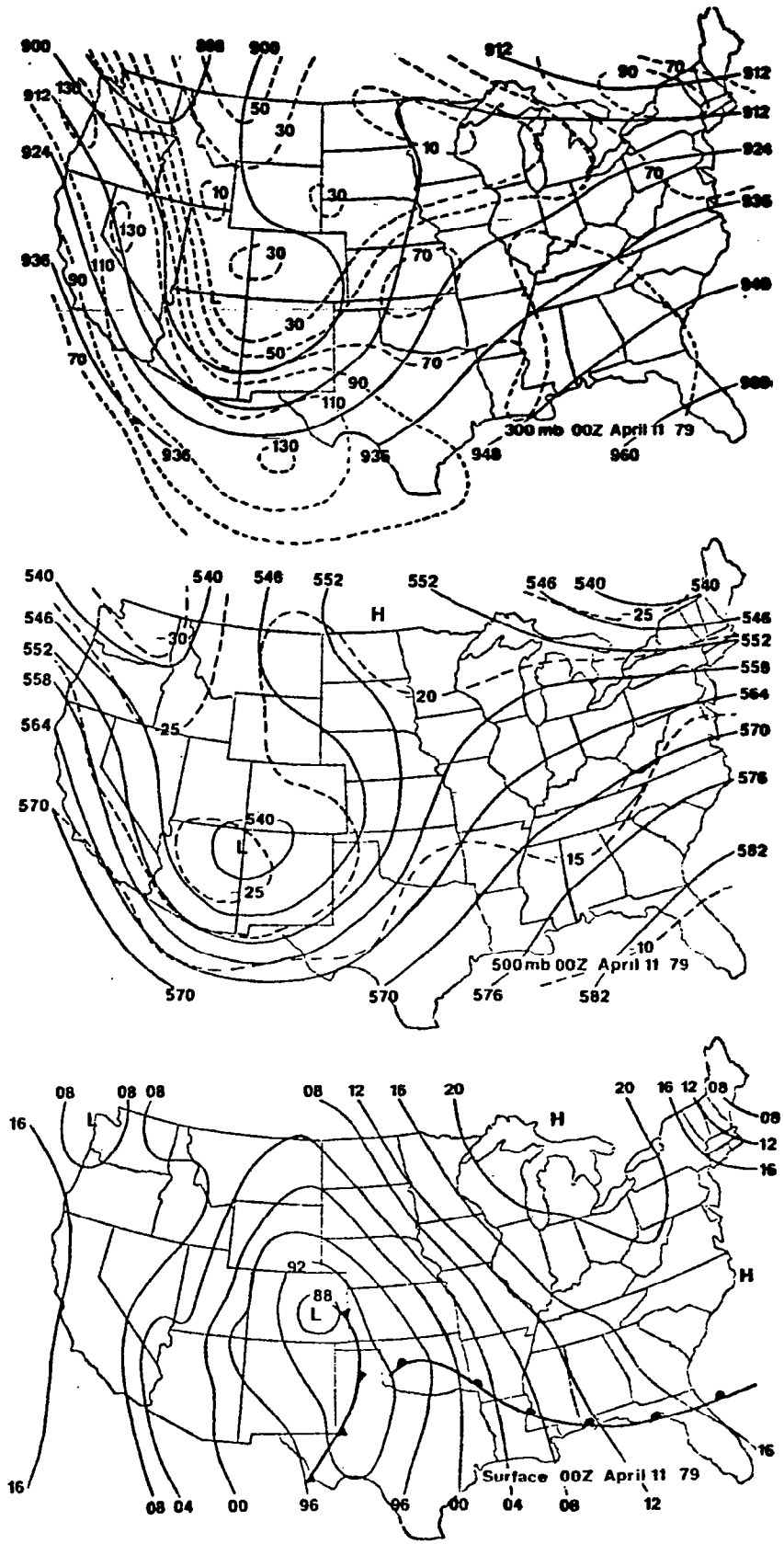

Fig. 1.9. Synoptic conditions at 0000 GMT 11 April 1979. See Fig. 1.3 for other details.

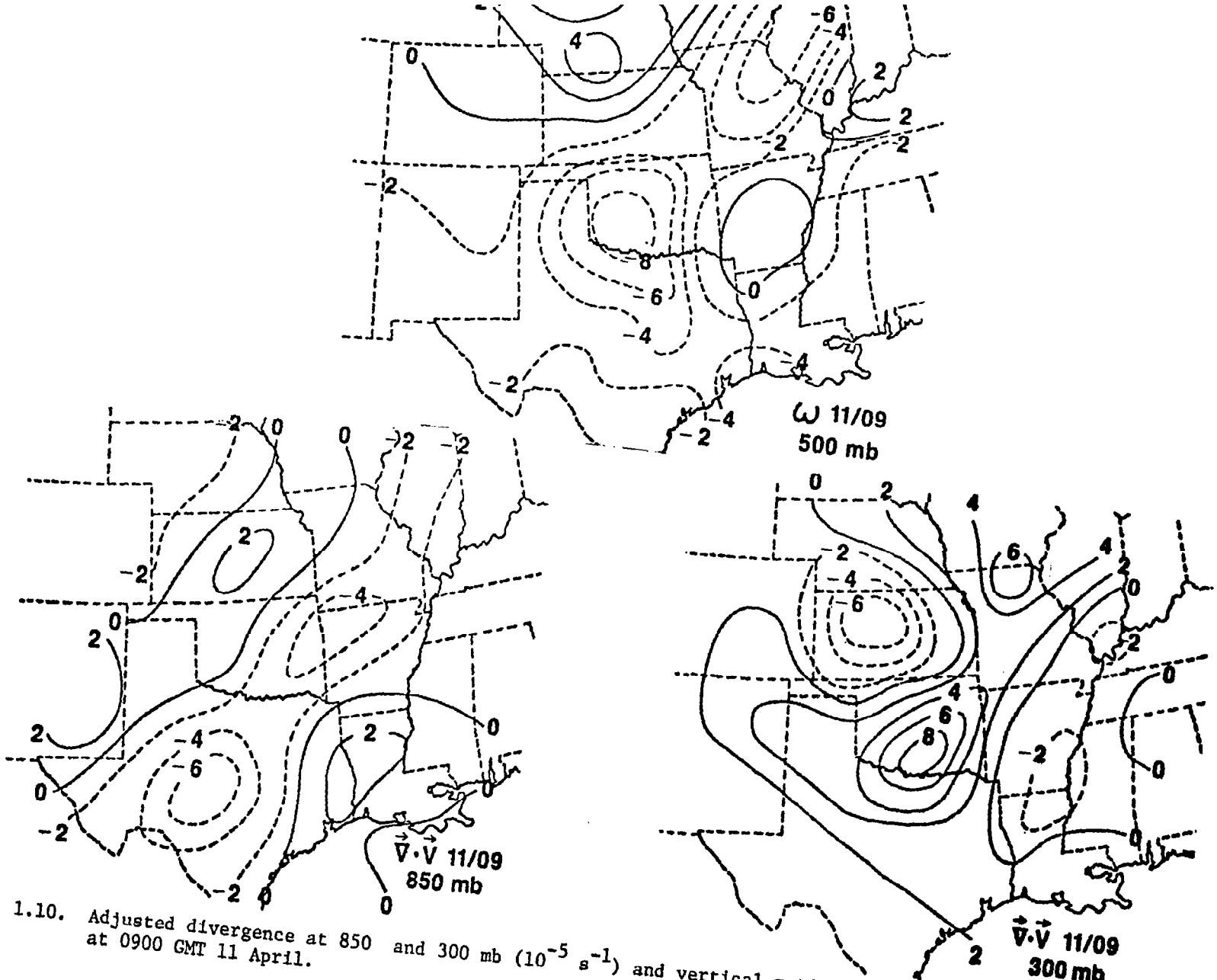

Fig. 1.10. Adjusted divergence at 850 and 300 mb (10^{-5} s^{-1}) and vertical motion (ω) at 500 mb (μb s^{-1}) at 0900 GMT 11 April.

(1980) observed the formation of a second surface mesolow near San Angelo, Texas, near 0200 GMT, but the feature could only be detected for one hour due to data sparsity and interference from nearby thunderstorms.

The LLJ centered over Oklahoma at 0000 GMT 11 April moved into northwestern Arkansas by 0300 GMT while increasing in strength to 35 m s^{-1}. During the next nine hours, it travelled into southeastern Arkansas and slightly decreased in intensity. The upper-level jet streak continued to advance into west central Texas between 0000 and 1200 GMT as the area of lowest stability gradually shifted eastward.

A new area of intense thunderstorms began to form in west Texas near 0100 GMT, apparently in response to the second minor wave. The developing area can be seen in the satellite photo for 2300 GMT 10 April (Fig. 1.8). Figure 1.11 shows that maximum echo tops reached 16.2 km (53,000 ft) at 0235 and 0535 GMT. The area of storms moved into central Texas during the evening and produced numerous tornadoes southwest of Stephenville between 0300 and 0600 GMT. The thunderstorms producing the Wichita Falls and other nearby tornadoes near 0000 GMT (Figs. 1.7-1.8) moved northeastward into Oklahoma during the next 6 h with maximum echo tops remaining at or above 15.2 km (50,000 ft) (Fig. 1.11). Several tornadoes were spawned from these storms until approximately 0600 GMT. Near 0700 GMT as the Oklahoma storms began to weaken, redevelopment occurred in extreme southeastern Oklahoma and northeastern Texas. These storms moved into central Arkansas by 1135 GMT, the end of the AVE-SESAME 1 period. Radar summaries (Fig. 1.11) and infrared satellite imagery (Fig. 1.12) for the last 12 h of the period reveal that, in addition to the severe storm areas already described, widespread convective activity occurred throughout the Midwest States and middle Mississippi River Valley.

Figure 1.13 shows synoptic conditions for the United States at the end of the AVE-SESAME 1 period, 1200 GMT 11 April. The surface low over southeastern Colorado remained nearly stationary as the central pressure lowered to 984 mb. The Pacific cold front continued eastward forming an occlusion which extended from the surface low southeastward into Oklahoma. The cold front stretched from near Oklahoma City

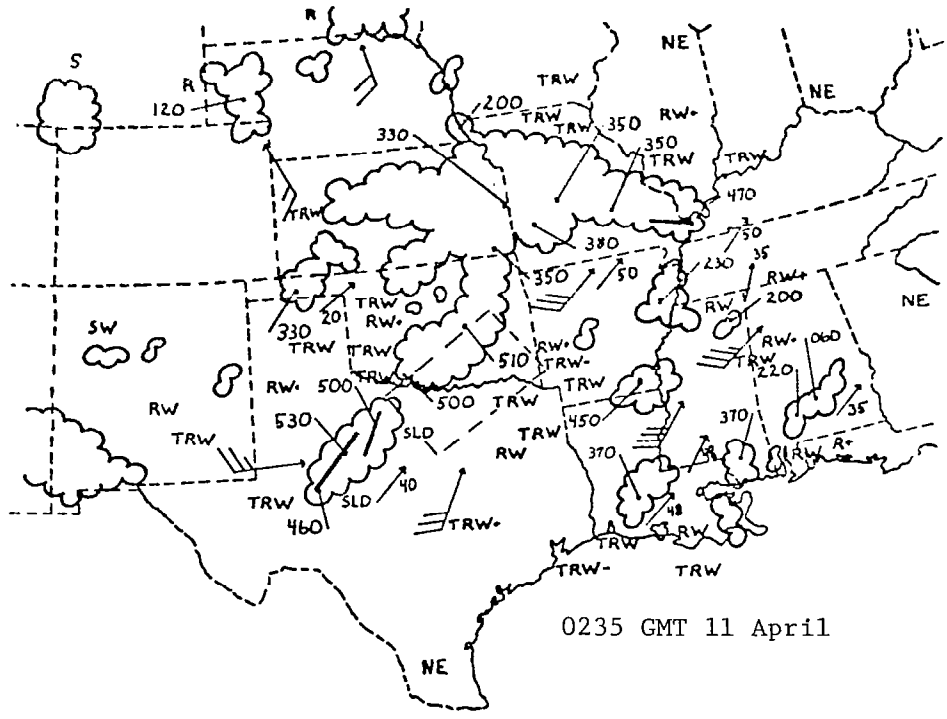

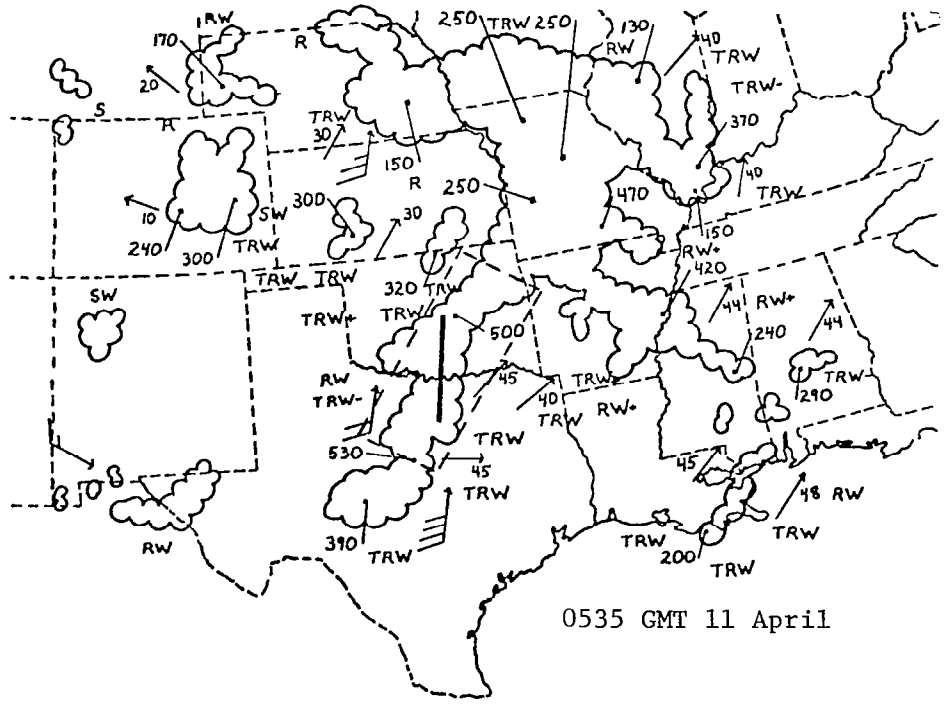

Fig. 1.11. Radar summaries between 0235 and 1135 GMT 11 April 1979.

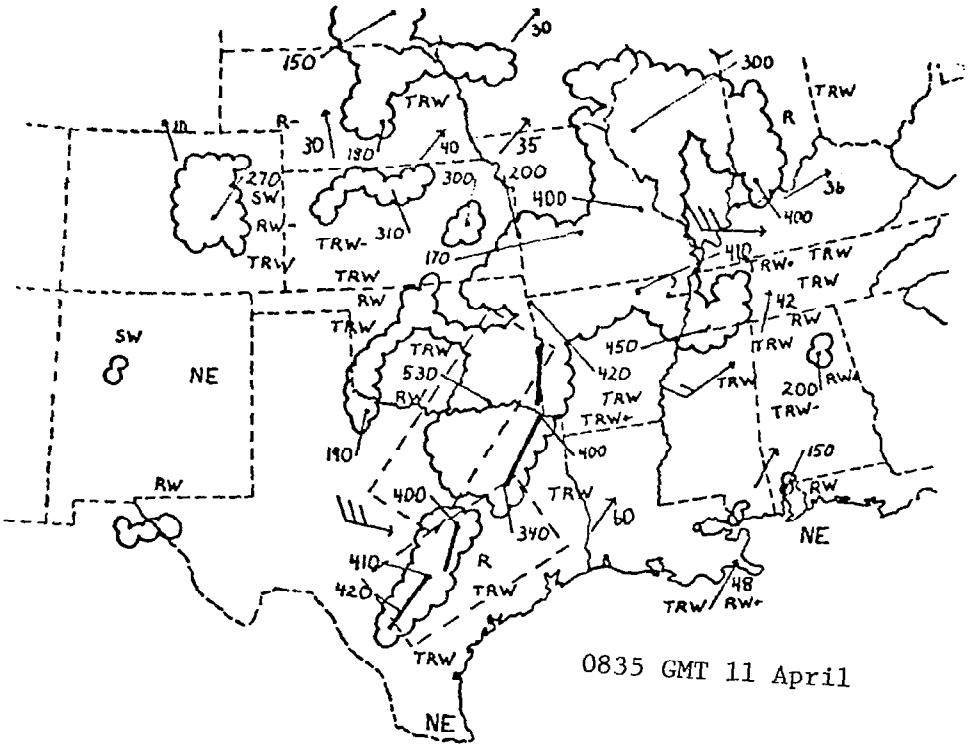

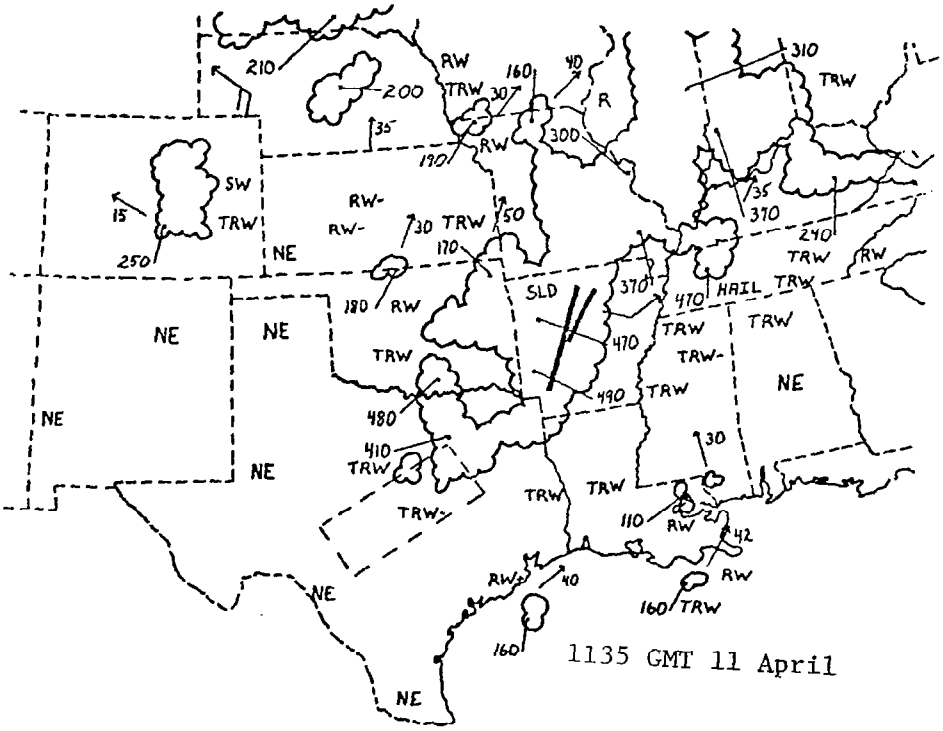

Fig. 1.11. (Concluded)

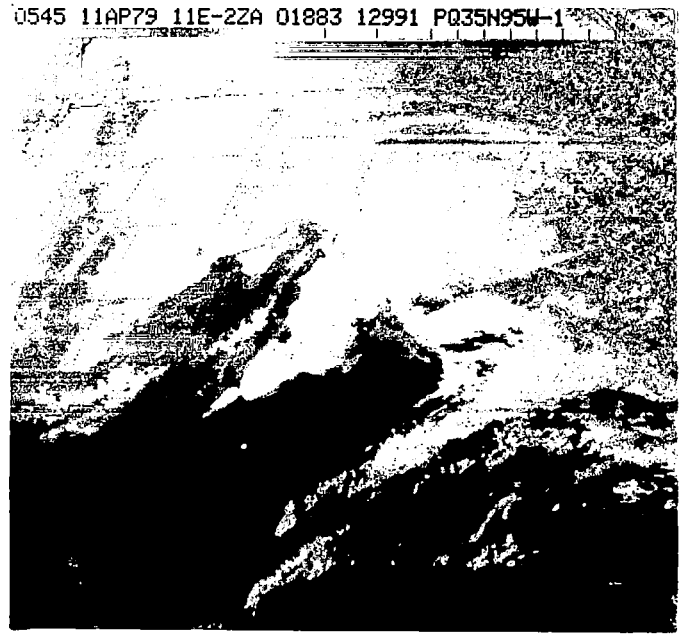

0545 GMT 11 April

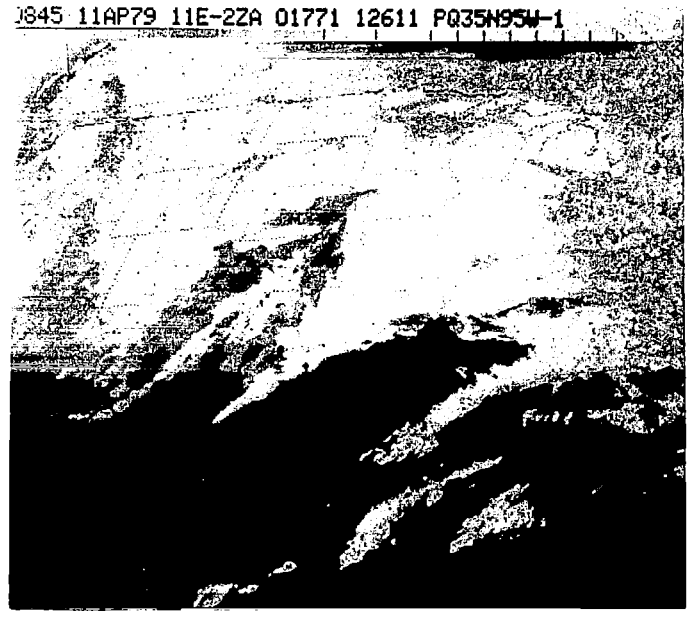

0845 GMT 11 April

Fig. 1.12. Infrared satellite images for 0545, 0845, and 1145 GMT 11 April 1979.

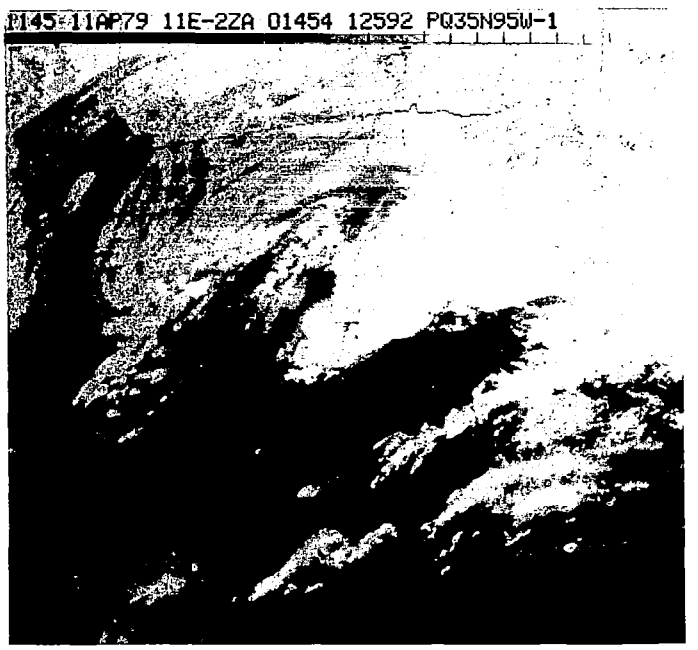

1145 GMT 11 April

Fig. 1.12. (Concluded)

to San Antonio, but the warm front moved little. At 500 and 300 mb the major trough over the Rockies deepened and continued its eastward movement. The jet streak located at the base of the trough 12 h earlier had rotated into the western portions of Texas with winds of 55 m s^{-1} (110 kts). Another region of strong winds remained over the Pacific Coast.

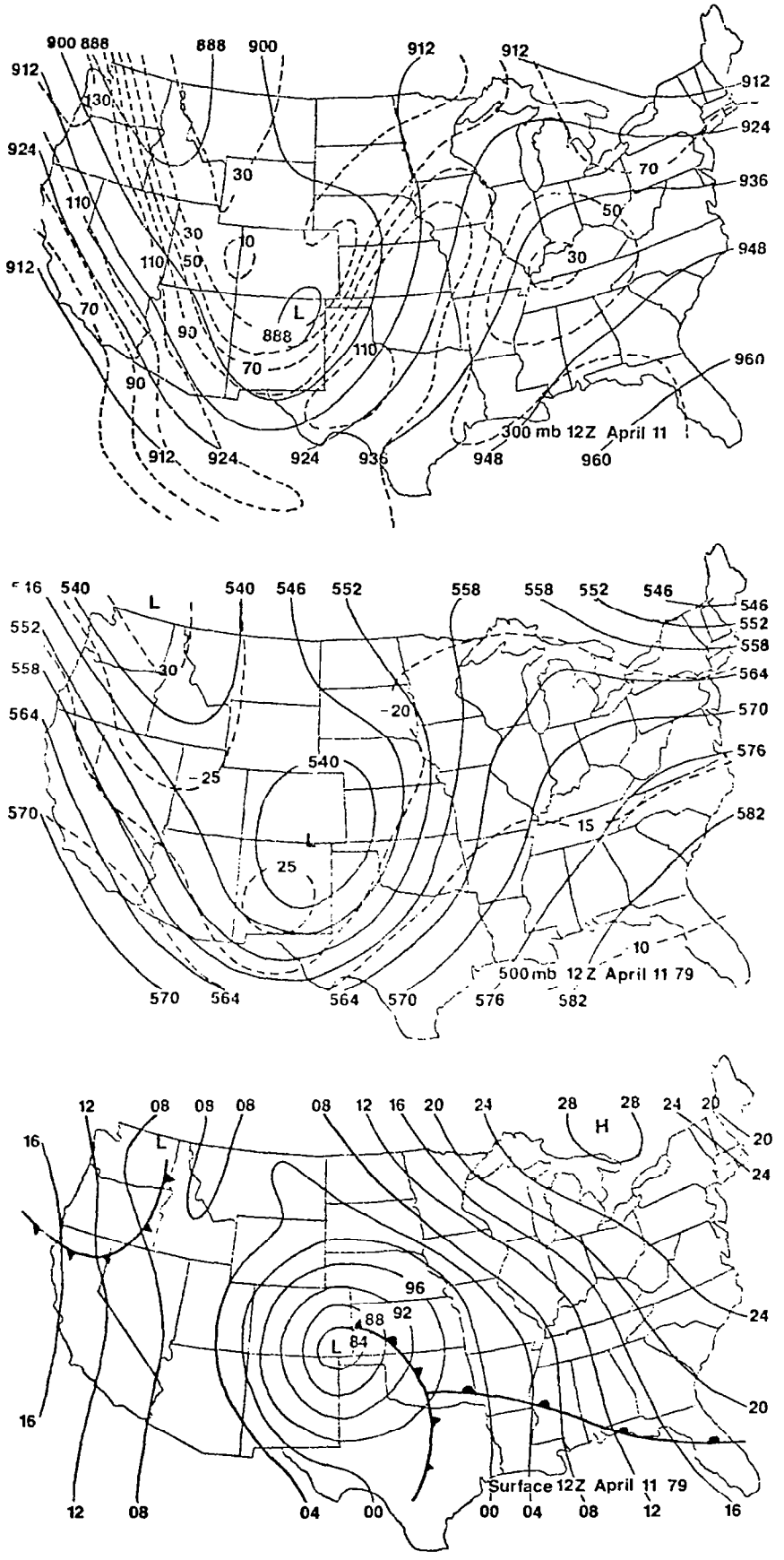

Fig. 1.13. Synoptic conditions at 1200 GMT 11 April 1979. See Fig. 1.3 for other details.

5. KINETIC ENERGY BALANCE DURING AVE-SESAME 1

a. Area-time averaged energetics

The kinetic energy budget equations (1.1-1.2) were evaluated at each of the nine observation times of AVE-SESAME 1. To avoid problems associated with data sparsity at the boundaries of the original 14 x 14 data grid, the average energy budget for the region was calculated over an interior 7 x 9 grid having an area of 1.6×10^6 km^2 (see Fig. 1.1). The average budget for the combined nine time periods is given in Table 1.1. With the exception of terms $(\vec{\nabla}\cdot k\vec{V})_a$ and D_a, which will be described in a later section of this report, meanings of the terms have been given in Section 2.

Kinetic energy content of the surface to 100 mb vertical column is 35.28×10^5 J m^{-2}, with greatest sublayer values occurring above 400 mb in association with the jet stream. The area experiences a local gain of kinetic energy during the period (13.25 W m^{-2}). Although largest increases are found in the upper troposphere in association with jet intrusion from the southwest, a secondary maximum occurs in the lower troposphere and is related to the formation of the LLJ.

Generation of kinetic energy is an important sink for the total column during the period as a whole ($-\vec{V}\cdot\vec{\nabla}\phi < 0$). Although cross-contour flow is a source of energy below 600 mb, the large values of destruction centered near 200 mb dominate and produce a vertical total of -30.9 W m^{-2}. Vertical flux divergence integrates to zero in the total surface to 100 mb layer because of boundary values prescribed for vertical motion, but within the column, flux divergence ($\partial\omega k/\partial p > 0$) predominates below 300 mb while convergence occurs above. Since widespread upward vertical motion occurs during the period, the flux values are consistent with an upward transport of energy.

As expected during cases of strong jet intrusion, horizontal flux convergence ($\vec{\nabla}\cdot k\vec{V} < 0$) is observed for the AVE-SESAME 1 case. However, it is significant that this external process is the largest source of local kinetic energy. Although flux convergence occurs at all levels, the process is a maximum in the upper troposphere where the jet is found.

The dissipation term has been interpreted to represent grid-

Table 1.1. Area-averaged kinetic energy budget for the combined nine observation times of the AVE-SESAME I period. All units are W m^{-2} except for K which is 10^5 J m^{-2}.

Pressure Layer (mb)	K	$\partial K/\partial t$	$\vec{\nabla}\cdot k\vec{V}$	$\{\vec{\nabla}\cdot k\vec{V}\}_a$	$\partial \omega k/\partial p$	$-\vec{V}\cdot\vec{\nabla}\phi$	D	D_a	$-\omega\alpha$
200-100	7.78	0.18	-2.22	-1.65	-5.24	-11.51	4.23	4.80	94.7
300-200	8.71	2.15	-7.30	-5.88	-4.67	-14.91	5.09	6.52	255.6
400-300	6.01	2.53	-13.88	-12.19	0.34	-10.39	-0.61	1.08	314.7
500-400	4.35	2.62	-7.12	-6.24	0.90	-5.11	1.51	2.40	309.3
600-500	3.11	1.75	-2.70	-2.44	2.26	-0.55	1.86	2.12	269.6
700-600	2.10	1.15	-1.69	-1.59	2.44	1.44	0.46	0.56	215.9
800-700	1.58	1.47	-1.64	-1.60	1.93	2.28	-0.53	-0.49	146.7
900-800	1.21	1.04	-1.56	-1.53	1.48	4.16	-3.20	-3.17	63.6
Sfc-900	0.43	0.36	-0.43	-0.46	0.55	3.69	-3.21	-3.24	8.9
Vertical Total	35.28	13.25	-38.55	-33.58	0.00	-30.90	5.60	10.58	1677.9
Vertical Total 12 h Data	34.82	13.84	-27.88	-27.94	0.00	-33.09	19.05	18.89	1481.0

(resolvable) to subgrid- (unresolvable) scale energy transfers (see Section 2). During AVE-SESAME 1, there is an "upwelling" of kinetic energy into the resolvable scales (D > 0) that is the second greatest energy source to the region. These positive values occur in the upper atmosphere while the more traditional negative dissipation is found near the surface where frictional effects dominate.

A large amount of potential energy is released by vertical overturning for conversion to kinetic energy. Smith (1980) recently defined the term "conversion efficiency" (COE) to compare energy released ($\omega\alpha$) to the kinetic energy actually generated ($-\vec{V}\cdot\vec{\nabla}\phi$). During AVE-SESAME 1 the value of COE is -2.8%, indicating that in spite of the tremendous energy release, destruction of kinetic energy still occurs. For a composite of cyclone cases, COE has been found to be near +3% (Smith, 1980).

Rawinsonde data possess errors which affect values of a derived energy budget. An error analysis currently is underway to assess their effects on the energy balance of the present study, and results of this analysis will be described in a future report. An error analysis has been performed on the AVE 3 case in which computational procedures were similar to those used here. Those conclusions are described in Chapters II and III of this report and in Fuelberg and Scoggins (1980). The AVE 3 analysis and those of others (e.g., Robertson and Smith, 1980; Vincent and Chang, 1975; Chen and Bosart, 1977) have shown that the generation and horizontal flux divergence terms and therefore the residual dissipation term are sensitive parts of the budget equation, but that input data errors generally do not affect conclusions that are made. To investigate alternative computational procedures that might produce more accurate results, the horizontal flux term of (1.1) was written as

$$(\vec{V}\cdot k\vec{V})_a = k(\vec{V}\cdot\vec{V})_a + \vec{V}\cdot\vec{\nabla}k \qquad (1.3)$$

and then recomputed. The advection term on the right was evaluated in the usual manner, but the error sensitive horizontal divergence term appearing on the right was adjusted using the O'Brien (1970) scheme so that values would be consistent with the assumption of ω = 0 at 100 mb (See Section 2). Examples of the divergence adjustment procedure can

be found in O'Brien (1970), Chien and Smith (1973), and Fankhauser (1969). The two terms then were added to give "adjusted horizontal flux divergence". Since the dissipation term is computed as a residual in (1.1), new values called "adjusted dissipation" were obtained as well.

Results of the procedure are given in Table 1.1. The total column value of -33.58 W m^{-2} for the adjusted flux $(\vec{\nabla}\cdot k\vec{\nabla})_a$ corresponds closely to the unadjusted value of -38.55 W m^{-2}. The effects of the adjustment are most pronounced above 500 mb. Figure 1.14 compares spatial fields of the two procedures at 2100 GMT. The original and adjusted patterns and values are almost identical in the surface to 700 mb layer. In the 400-100 mb layer, the orientations of the fields generally are similar, but values at the major centers are modified. For example, the unadjusted central value over Oklahoma is 272 W m^{-2} while the adjusted value is 181 W m^{-2}, a decrease of 33%. In the Oklahoma area the adjustment procedure reduces upper-level positive velocity divergence producing consistency with $\omega = 0$ at 100 mb, but in general, the adjustment may increase or decrease the values at a given level of a particular grid point. A careful study of results from each of the nine times suggests that the fields of adjusted flux divergence show better continuity than the original fields. The adjustment process clearly produces values that are more consistent with the assumed ω profiles. While adjustment often produces significant changes in individual grid-point values near centers of action, much smaller changes are observed outside of the centers. Table 1.1 shows that the adjusted residual dissipation D_a is changed in a manner similar to that of the flux term from which it is derived. Again, the adjusted fields (not shown) exhibit better continuity than the original D patterns. Unless otherwise stated, adjusted values will be used throughout the remaining discussion of the AVE-SESAME 1 case.

It is informative to compare the vertically integrated, area-averaged budget of AVE-SESAME 1 with budgets of similar synoptic situations (Table 1.2). The AVE 4 case included two large areas of convection, called mesoconvective complexes (Maddox et al., 1980), but basically zonal flow and lack of strong jet penetration are the probable causes for its having horizontal flux divergence (not convergence as in the current study) and weaker values of cross-contour destruction and positive dissipation than AVE-SESAME 1. Both the

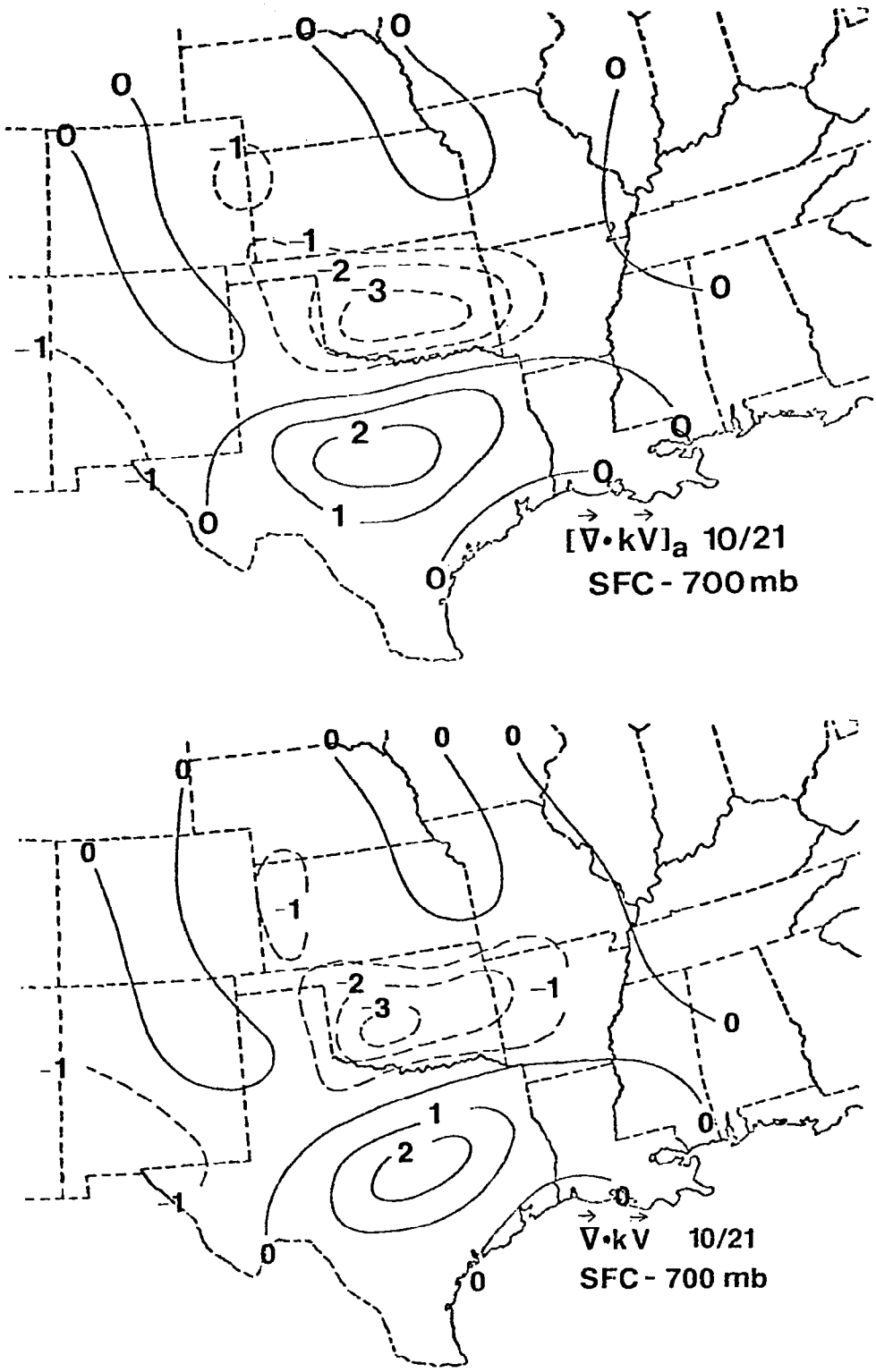

Fig. 1.14. Original $(\vec{\nabla}\cdot k\vec{V})$ and adjusted $(\vec{\nabla}\cdot k\vec{V})_a$ fields of horizontal flux divergence (10^1 W m^{-2}) for 2100 GMT 10 April 1979.

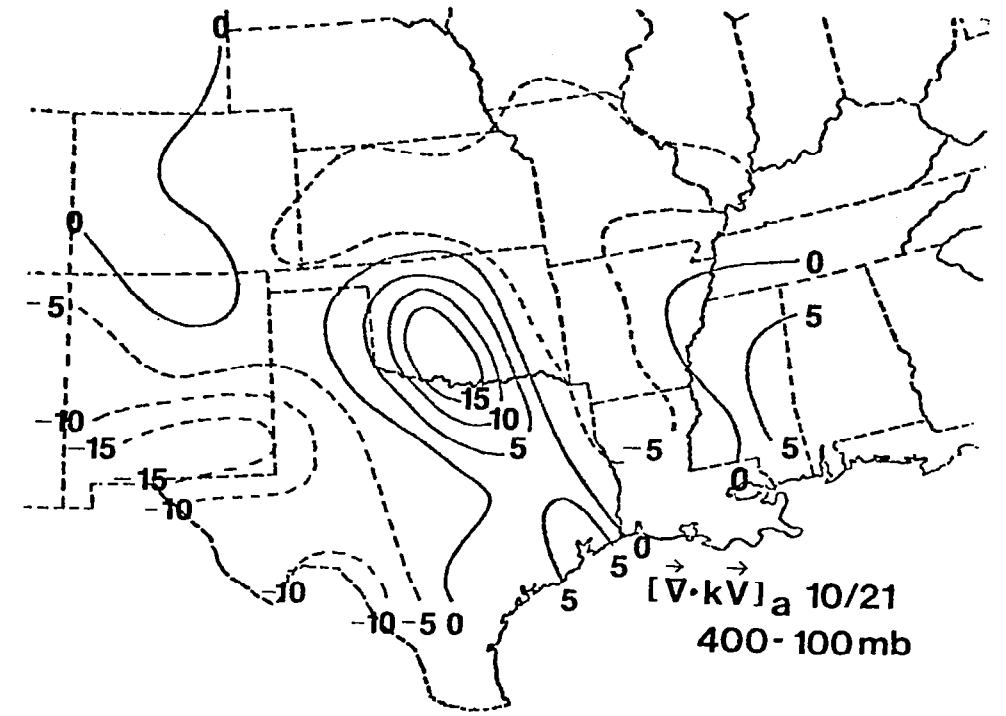

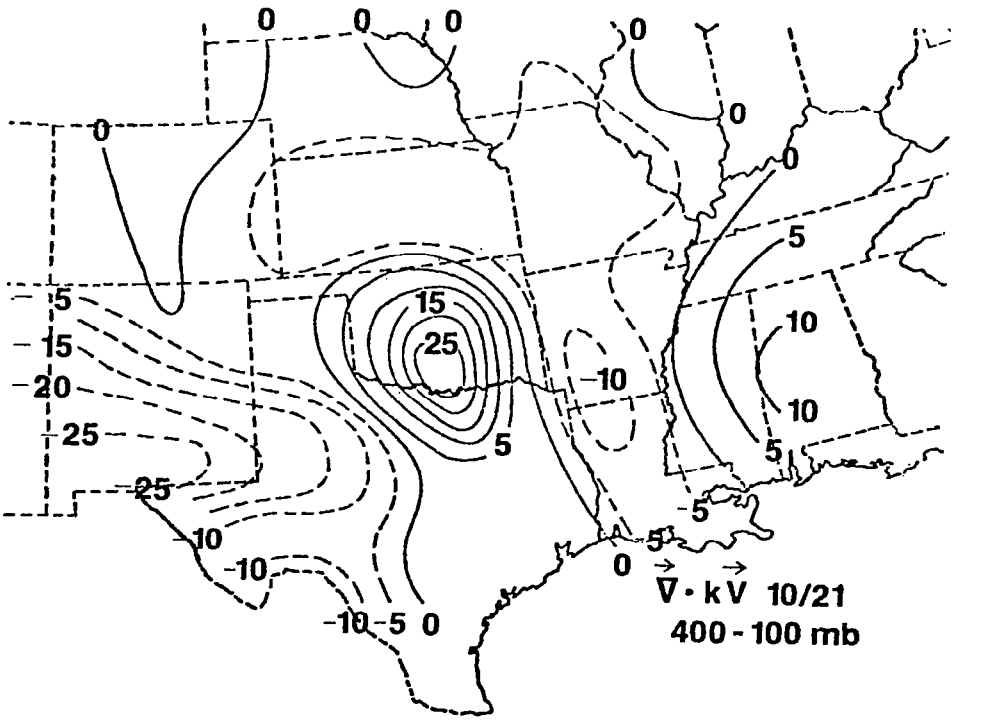

Fig. 1.14. (Concluded)

Table 1.2. Comparison of vertically integrated, area-averaged kinetic energy budgets. All units are W m^{-2} except for K which is 10^5 J m^{-2}.

Period and Source	K	$\partial K/\partial t$	$\vec{\nabla}\cdot k\vec{V}$	$-\vec{V}\cdot\vec{\nabla}\phi$	D
AVE-SESAME 1 10-11 April 1979 Current Study	35.3	13.3	-38.6	-30.9	5.6
AVE 4, entire area 24-25 April 1975 Fuelberg and Scoggins (1978)	19.9	-3.7	1.6	-4.0	1.6
AVSSE 1, entire area 27-28 April 1975 Fuelberg (1979a)	25.6	7.1	-3.8	-8.6	11.9
AVSSE 2, entire area 6-7 May 1975 Fuelberg (1979a)	25.5	3.7	-20.7	-41.3	24.3
Palm Sunday Outbreak Cyclone Vicinity 10-12 April 1965 Robertson and Smith (1980)	28.7	6.7	-25.6	-27.6	8.7
Jumbo Outbreak Cyclone Vicinity 3-5 April 1974 Robertson and Smith (1980)	31.7	4.5	-21.2	4.7	-21.4

AVSSE 1 and 2 cases were characterized by major troughs over the Rockies, just west of the computational regions, but jet stream penetration into Texas makes AVSSE 2 a closer synoptic match with the present study. While there is qualitative agreement between each budget term for AVSSE 1 and 2 and AVE-SESAME 1, the AVSSE 2 values show the best agreement in magnitude. It is somewhat difficult to compare conditions and budgets associated with the Palm Sunday and Jumbo outbreaks with AVE-SESAME 1 because both previous studies occupied two day periods, instead of one, and therefore consisted of a more varied situation. Generally, however, both were characterized by short wave and jet propagation through a long wave located over the Rocky Mountains, as is AVE-SESAME 1. Energy budgets of the Palm Sunday and AVE-SESAME 1 cases show very good agreement, but signs of both the generation and dissipation terms differ for the Jumbo and AVE-SESAME 1 cases. The differences probably are due to contrasts in the flow during the latter half of the Jumbo period.

b. Time variability of the energetics

Because 3 h rawinsonde data are quite rare, it is useful to examine the short term variability of the flow. Figure 1.15 gives time-height cross sections of area-averaged kinematic quantities. Values of relative vorticity show a rather steady increase at all levels during the period with largest values near the top of of the column. Greatest positive vorticity advection ($-\vec{\nabla}\cdot\vec{\nabla}\zeta > 0$) over the area occurs near 250 mb between 2100 GMT 10 April and 0000 GMT 11 April, near the beginning of the severe storm outbreak. Upward vertical motion ($\omega < 0$) occurs throughout most of the atmosphere, but largest values occur in the middle troposphere near 0300 GMT. This observed variability is due to the westward movement of the major trough over the Rockies and, to some extent, to flow variations within the computational region. The role of the thunderstorms in producing changes in these parameters also must be considered. Although horizontal maps of divergence (Figs. 1.5, 1.10) and the historical sequence of storm development described in the previous section suggested the movement of two short waves through the long wave and into the Texas-Oklahoma region, two waves are not evident in the area-averaged kinematics (Fig. 1.15). The limited dimensions of the waves and their close

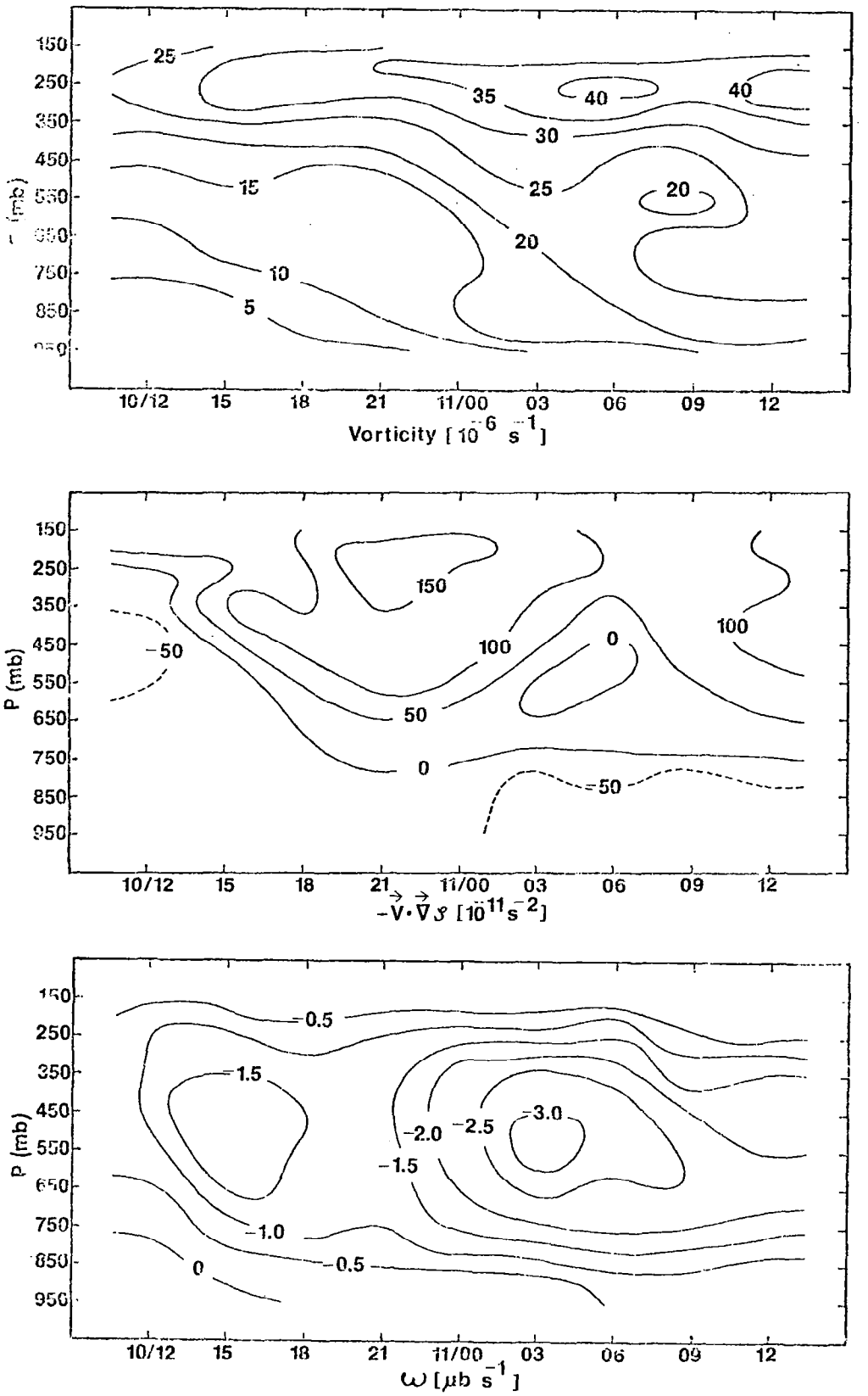

Fig. 1.15. Time-height cross sections of area-averaged kinematic quantities for AVE-SESAME 1.

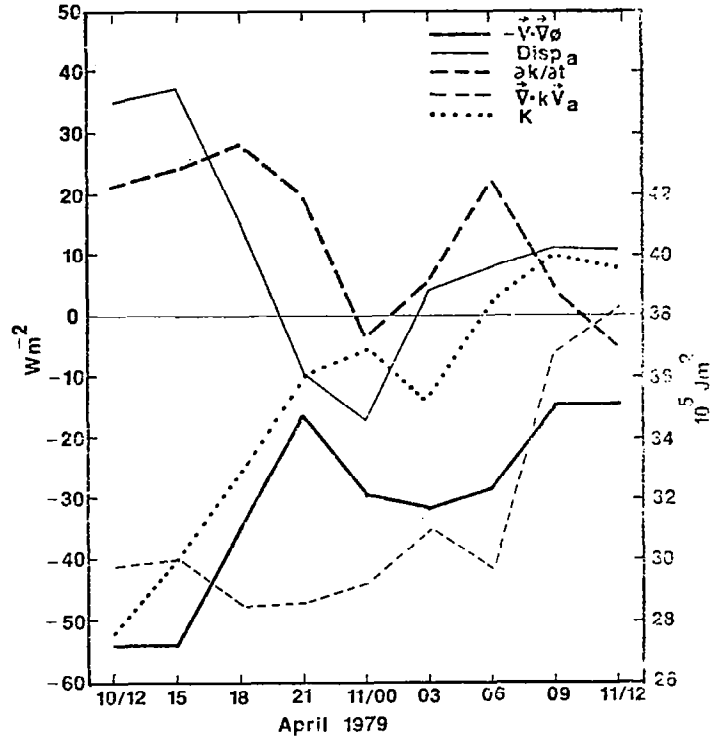

Fig. 1.16. Time series of energy budget terms integrated between the surface and 100 mb.

proximity to each other in both time and space apparently make them indistinguishable in the area averaging process. The figure clearly shows that there is adequate lift over the area to trigger convective activity.

Time series of vertically integrated energy parameters (Fig. 1.16) and time-height cross sections (Fig. 1.17) indicate the changing nature of the kinetic energy balance during the 24 h period. The major feature revealed by the K and $\partial K/\partial t$ profiles is the increase in energy content during the experiment. Largest content occurs near 0900 GMT, but there is a weaker secondary maximum near 0000 GMT. Horizontal flux convergence (adjusted) is the greatest source of the energy increases. Maximum values, found near 300 mb, remain nearly constant through 0600 GMT, reflecting the advection of energy into the area by the advancing jet streak. Because strongest winds are located within the area by

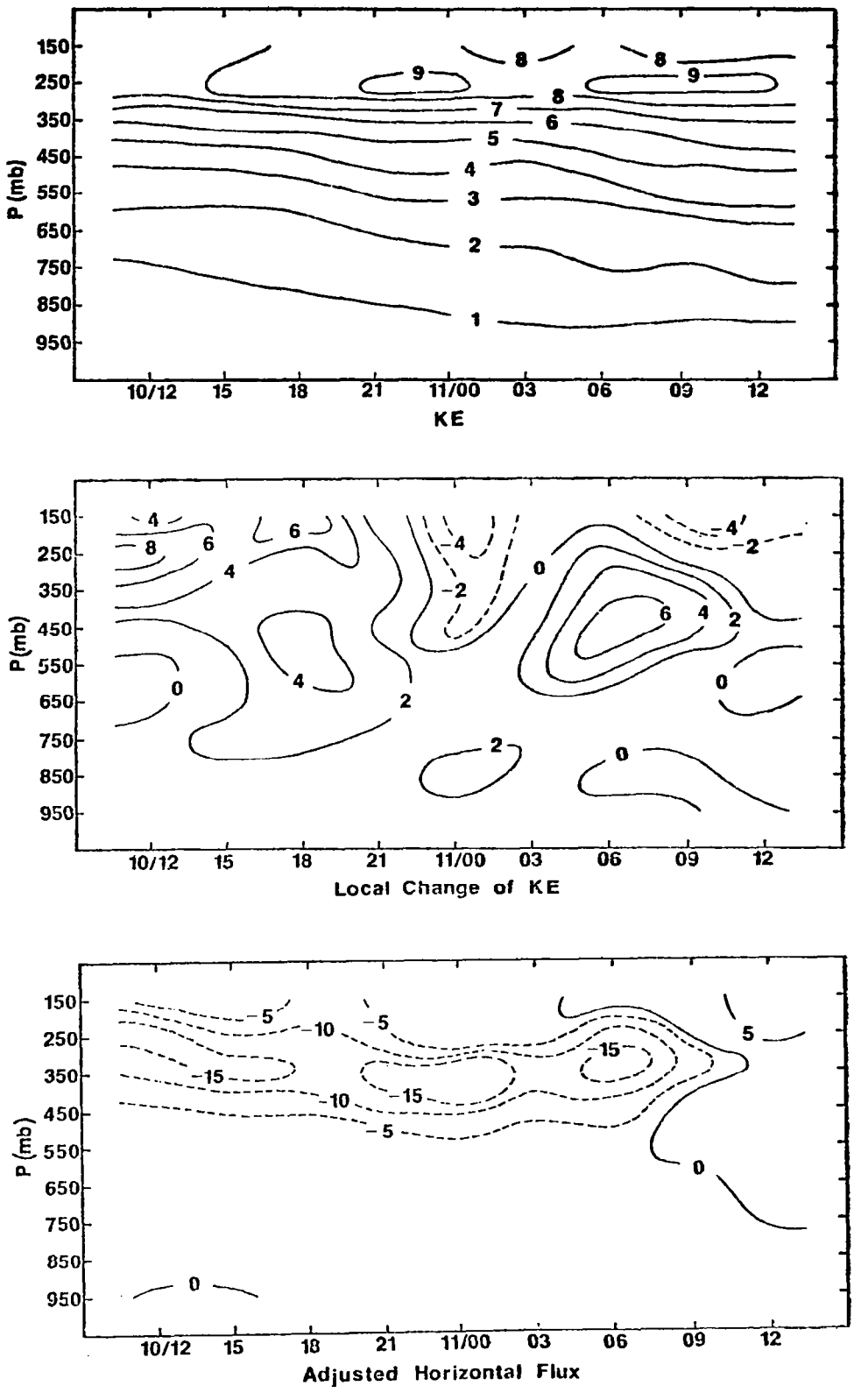

Fig. 1.17. Time-height cross sections of area-averaged energy budget terms. Units of energy content are (J m^{-2})/100 mb, others are (W m^{-2})/100 mb.

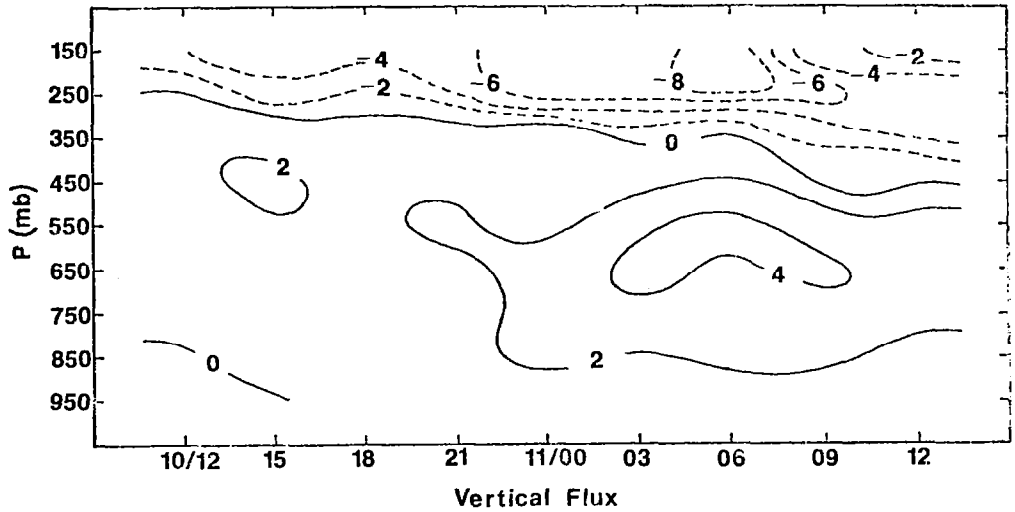

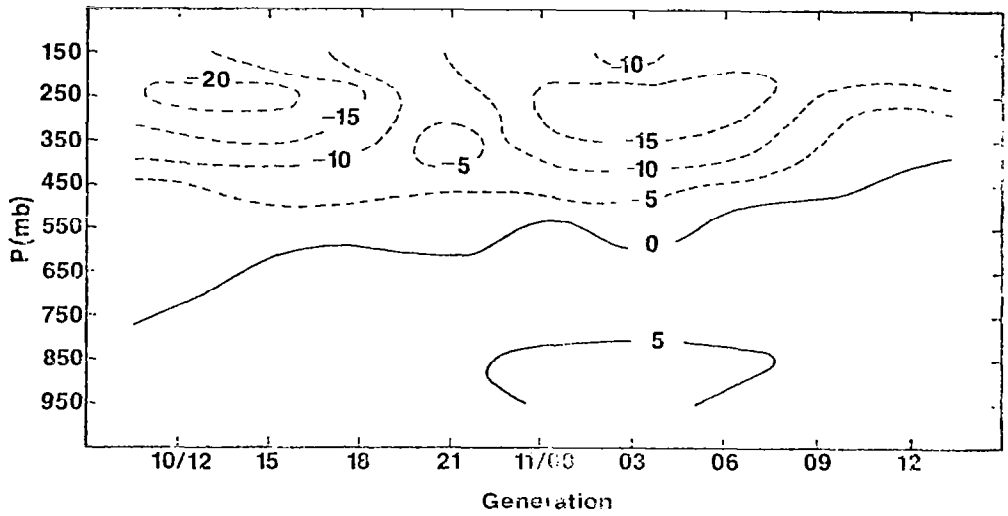

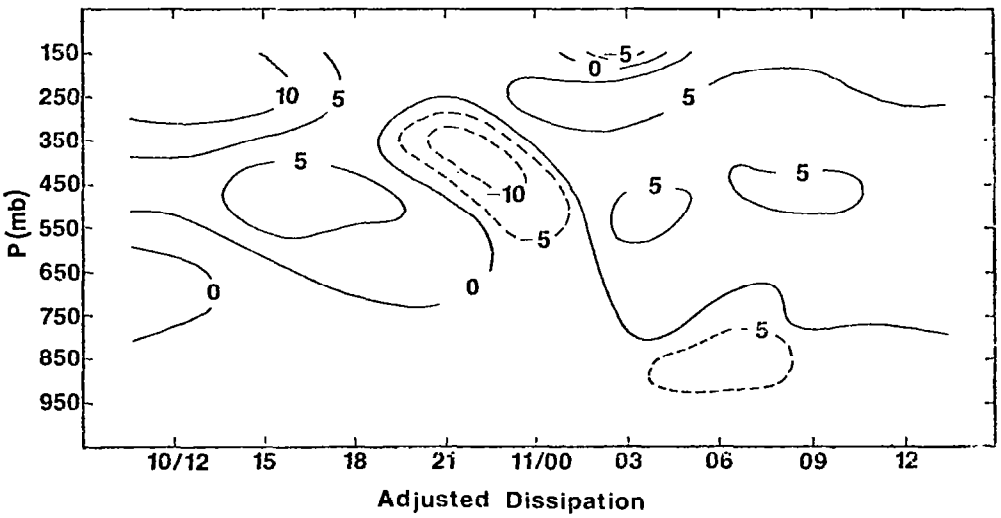

Fig. 1.17. (Concluded)

the last observation time, flux divergence then becomes a sink to the area. The results emphasize the importance of propagating jet streaks on a local energy balance. Vertical flux divergence below 300 mb, and vertical flux convergence above, occur throughout the 24 h period. This upward transport of energy is especially prominent during the latter half of the experiment when area-averaged vertical motion is strongest (Fig. 1.15). At some levels, vertical transport is larger than horizontal transport; thus, as noted by Robertson and Smith (1980), synoptic-scale kinetic energy transport cannot always be considered a quasi-horizontal process. It can be an important factor in strengthening or maintaining strong upper-level winds.

Although cross-contour flow produces an important energy sink throughout the period, the column total is closer to zero at 2100 and 0000 GMT than at other times (Fig. 1.16). The time-height cross section (Fig. 1.17) shows that upper-level destruction reaches distinct minima at these times while low-level cross-contour generation remains more constant. The zero line of generation rises from 750 mb at the initial time to near 350 mb at the last time as the major system advances into the computational region. Constant pressure maps clearly show the upper-level supergradient flow producing the negative values in advance of the major trough and jet streak. These conditions also have been noted in the Palm Sunday and Jumbo outbreaks (Robertson and Smith, 1980). Since major tornado outbreaks often are associated with advancing upper-level streaks, large-scale negative generation may be a common occurrence in such outbreaks. The generation variability observed during AVE-SESAME 1 may be due to the minor waves discussed earlier. Also, the large areas of intense storms that occurred may have caused environmental modifications that produced the variability (e.g., Fuelberg, 1979; Fuelberg and Scoggins, 1978; Maddox et al., 1980; Fritsch and Maddox, 1980). The impact of storms on their environments is seen better by considering smaller areas; such work is now underway for this case.

Dissipation is a minor source of synoptic-scale energy for the region when all nine observations are combined (Table 1.1), but the time series (Figs. 1.16-1.17) show that grid- subgrid-scale energy transfers act as a sink of this energy ($D < 0$) between 2000 GMT and

0200 GMT as a layer of negative values develops in the upper troposphere. Interpretation of the dissipation term is difficult because it is computed as a residual and because it includes the combined effects of all types of unresolvable or partially resolvable phenomena. In a recent study, Vincent and Schlatter (1979) related deep convection to positive dissipation in the middle and upper troposphere, but such a relation is not apparent in the present time series of area averages. Likewise, a relation between flux convergence of energy and positive dissipation (Robertson and Smith, 1980) is not apparent in the area-averaged time series. The time-height cross sections do reveal that the minimum upper-level generation sink near 2100 GMT corresponds to the time of negative upper-level dissipation. This inverse relationship between generation and dissipation also was described by Fuelberg (1979a). Variations in the dissipation term probably are related to the short waves that propagate through the area. Each of these hypotheses will be tested further in the upcoming year.

The various time series of area-averaged energetics (Figs. 1.16-1.17) reveal that there is considerable fluctuation in the energy balance. Time averaging smooths out this variability, but provides a single budget that conveniently describes conditions for the entire 24 h period (Table 1.1). To investigate the usefulness of the 3 h data in portraying the area-time-averaged energetics, an energy budget was computed on the basis of the three 12 h data sets (0000 and 1200 GMT) alone. Results for the surface to 100 mb layer are given at the bottom of Table 1.1. It is somewhat surprising to find the close agreement between the nine time average and the three time average. Even during this rapidly changing severe storm period, the additional data provided during AVE-SESAME 1 do not yield a greatly different view of overall conditions than do standard 12 h data. Similar results were found during the wintertime AVE 3 case (Fuelberg and Scoggins, 1980).

An inspection of the time series (Fig. 1.16) and time-height cross sections (Fig. 1.17) indicates that the AVE-SESAME 1 data provide better temporal resolution of features than would be possible with 12 h data. Horizontal maps of energy parameters to be shown in the next section will reveal large spatial variations in the upper and lower levels that have periods shorter than 24 h and therefore would not be detected with the

ordinary 12 h data. Thus the special 3 h soundings are a valuable asset in this diagnostic study. The above comparisons are based only on NWS data, but in the upcoming year the advantages of using the combination of NWS and special site data will be evaluated.

c. Horizontal fields of energy budget terms

Spatial maps of kinetic energy budget terms provide a means for directly relating energy fields to map features without area averaging. Selected maps integrated between the surface to 700 mb (lower troposphere) and 400-100 mb (upper troposphere and lower stratosphere) will be described. Because of inherent computational uncertainties, the discussion will focus only on major features. Where possible, the energy budget terms will be related to more traditional "weather map" features. Explanations for some of the energy fields are not yet available, however.

Because low-level and upper-level jet streams can vary in vertical extent, it is useful to locate these features on the basis of integrated kinetic energy content. Figure 1.18 gives fields of energy content for the 400-100 mb layer during AVE-SESAME 1. At the initial observation, 1200 GMT 10 April, maximum kinetic energy content in the upper layer is found over the southwestern portion of the computational region while smallest values are located over the northwestern portion nearer the center of the upper-level wave. These regional features correspond closely to the 300 mb chart seen earlier (Fig. 1.3) that shows strongest winds on the back side of the trough. One should note that the isopleths of energy content show only gentle curvature at this time. Between 1200 and 1800 GMT, a general increase of energy content occurs over the region (Fig. 1.16), but the isopleths of energy content (not shown) still do not exhibit any unusual perturbations. At 2100 GMT a kinetic energy maximum appears over Oklahoma (Fig. 1.18). While the 3 h data indicate that this maximum was not advected into the region, it is possible that the feature is subsynoptic in nature and has escaped earlier detection. The kinetic energy isopleths continue to reveal a perturbed pattern at 0000 GMT 11 April which is not as evident on the nationwide 300 mb map (Fig. 1.9). A maximum area is located over extreme northwestern Missouri while a distinct minimum has formed over

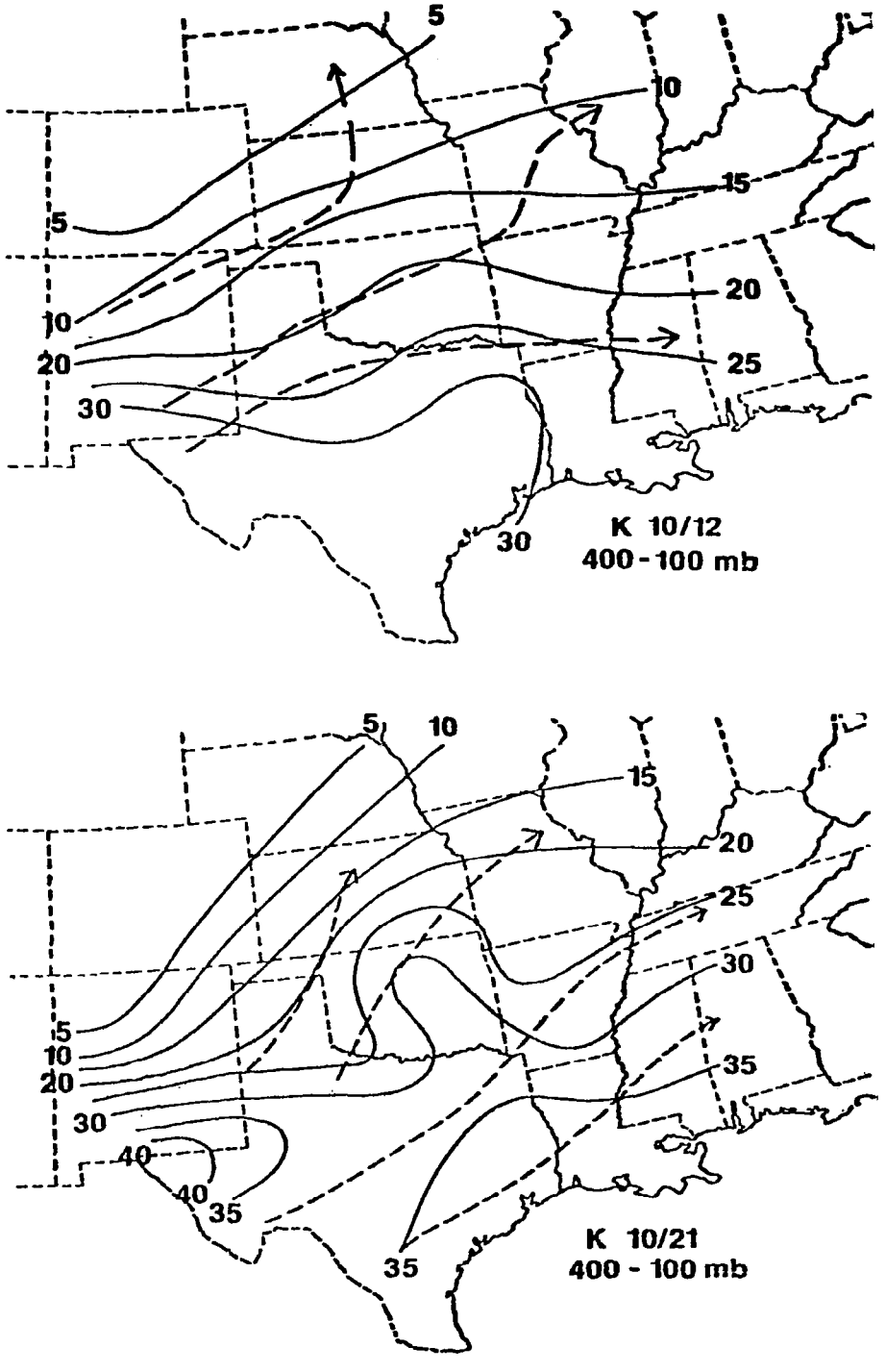

Fig. 1.18. Integrated kinetic energy content of the 400-100 mb layer (10^5 J m^{-2}) for 1200 and 2100 GMT 10 April and 0000 GMT and 0900 GMT 11 April. Dashed lines are streamlines at 300 mb.

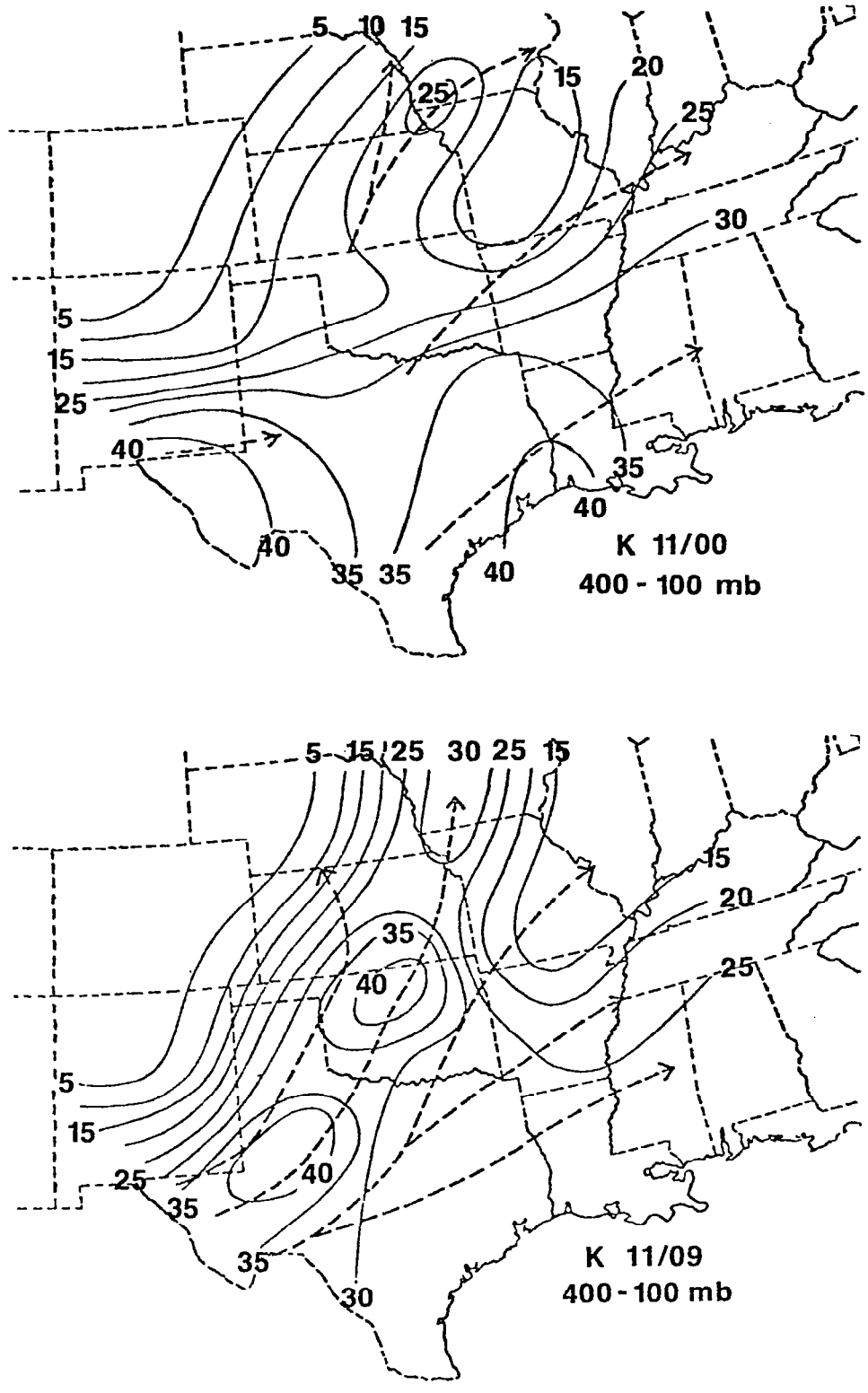

Fig. 1.18. (Concluded)

central Missouri. Several maximum and minimum centers form and dissipate between 0300-0600 GMT (not shown), but their overall continuity is poor. At 0900 GMT (Fig. 1.18), upper-level wind maxima are located over Oklahoma and western Texas while the minimum persists over central Missouri.

We only can speculate about causes for the energy maxima and minima that are observed. It is clear from the kinetic energy patterns and the constant pressure maps of Section 4 that upper-level jet intrusion is occurring from the southwest. The jet maximum, when viewed in terms of energy, does not appear to have a simple discrete center that translates into the AVE-SESAME 1 region. Instead, it apparently contains subsynoptic-scale regions of high speed air that are imbedded within the overall jet maximum (streak). As jet intrusion occurs, the subsynoptic-scale features are detected at only certain times and certain stations, giving rise to observed poor continuity. Such features probably would not be detected at all with ordinary 12 h data. Using synoptic-scale data, we can not determine whether the small-scale jet features were formed locally or were translated into the region from the southwest. Research for the coming year, hopefully, will answer this question.

The relationship of the subsynoptic-scale jet features to the convection is unclear. Evidence from previous studies suggests that synoptic-scale wind (kinetic energy) maxima can be formed due to the presence of large areas of intense convection (e.g., Fuelberg and Scoggins, 1978; Fritsch and Maddox, 1980). Such feedback mechanisms would be easiest to detect when pre-existing forcing is weak, which is certainly not the case during AVE-SESAME 1. While the feedback process may indeed be a factor in producing some of the wind perturbations, it seems more likely in this case that some (most?) of the perturbations were either a pre-existing part of the larger jet streak structure or were locally produced by processes not directly related to the convection. In that event, the wind maxima probably served to trigger the various storm areas. As an example, the Oklahoma energy (wind) maximum probably helped trigger the first round of severe storms in the Red River Valley. Because the wind maximum is observed so quickly after initial storm development (about 1800 GMT), it seems unlikely that there was sufficient time for it to be produced by a feedback mechanism.

Using synoptic-scale data, Sechrist and Whittaker (1979) and McNulty (1978) observed divergence at 300 mb in the left-front and right-rear quadrants of advancing jet streaks and convergence in the remaining two quadrants. When viewed broadly, results of the present study support their findings. The best relationship is seen at 0000 GMT when the major jet maximum in Mexico (Fig. 1.18) is associated with strong 300 mb divergence over Missouri and the Texas panhandle (left-front quadrant) and weaker convergence from Arkansas into the Big Bend (right-front quadrant) (Fig. 1.5). At 0900 GMT, 300 mb divergence over northern Missouri and Oklahoma and convergence over Kansas and southern Arkansas (Fig. 1.10) may be related to the upper-level energy maxima located over northern Oklahoma and western Texas (Fig. 1.18). The highly variable and complex jet structure of AVE-SESAME 1 and the probable interactions from storm areas, however, make it very difficult to find simple relationships.

Energy content of the surface to 700 mb layer (Fig. 1.19) is not as highly perturbed as that of the upper layer. Maximum low-level kinetic energy content is located over Kansas at the initial observation time (1200 GMT 10 April). A LLJ forms in northcentral Texas near 1800 GMT (not shown), strengthens as it moves into Oklahoma between 2100 and 0000 GMT, and then moves southeastward into Arkansas by 0900 GMT (Fig. 1.19). The LLJ develops quite rapidly; a 50% increase in energy content occurs between 2100 and 0000 GMT alone. A second LLJ (energy maximum) begins to form over the Big Bend region at 0900 GMT (Fig. 1.19) and intensifies during the final 3 h of the period. As mentioned previously, the LLJ appears to be dynamically linked to the propagating upper-level jet streak in a manner similar to that suggested by Uccellini and Johnson (1979). The LLJ does not have the complex subsynoptic-scale structure observed in the 400-100 mb layer; addition of the special site data may alter this finding however.

Spatial fields of energy budget terms for 0000 GMT 11 April will now be examined (Fig. 1.20). In the surface to 700 mb layer, major energy generation and transport (Fig. 1.20) are located near the center of the LLJ in central Oklahoma (Fig. 1.19). Strong horizontal flux convergence occurs over Kansas in advance (north) of the LLJ center, while flux divergence is found over Texas, behind the center. As expected,

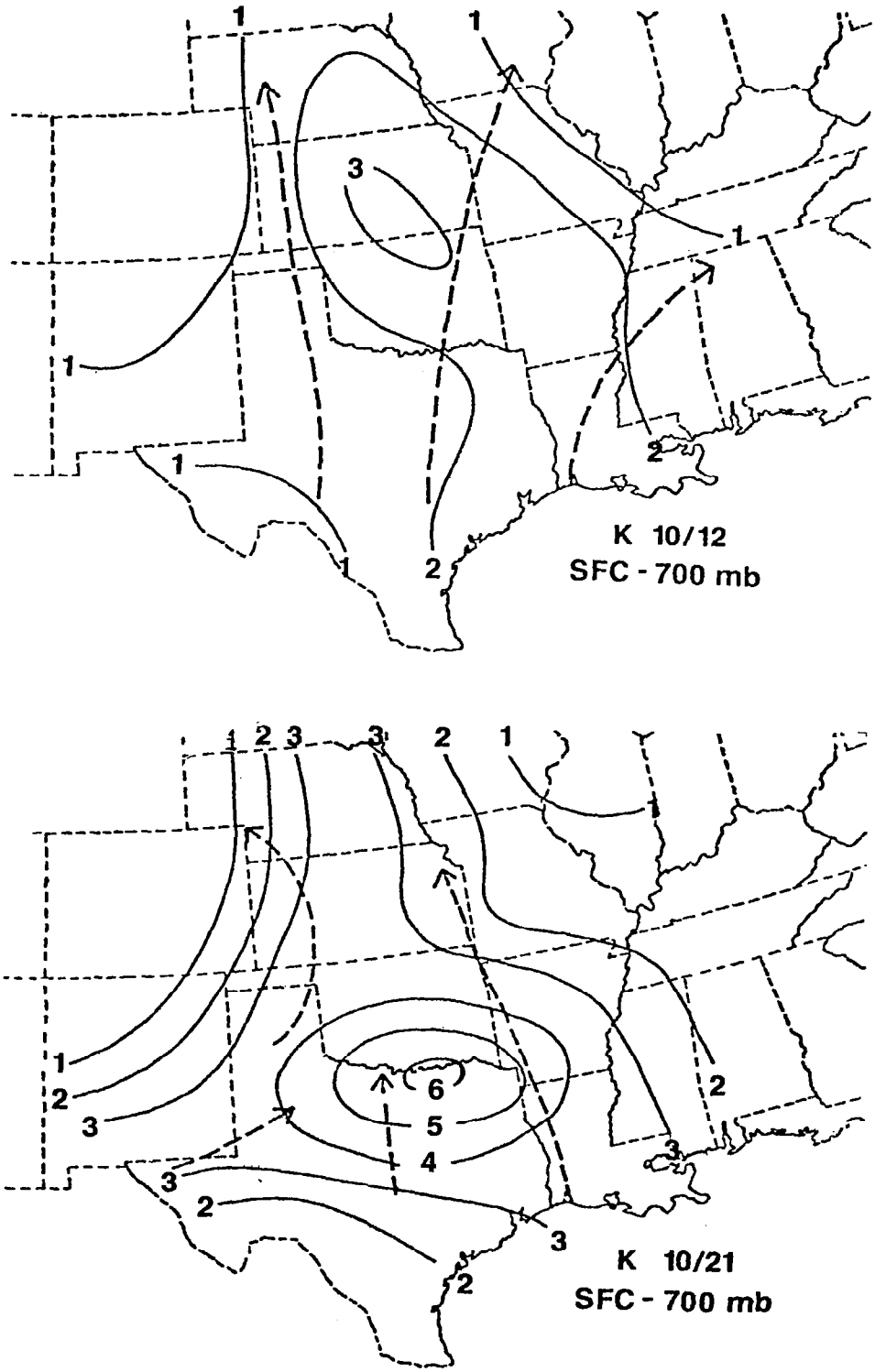

Fig. 1.19. Integrated kinetic energy content of the surface to 700 mb layer (10^5 J m^{-2}) for 1200 and 2100 GMT 10 April and 0000 and 0900 GMT 11 April. Dashed lines are streamlines at 850 mb.

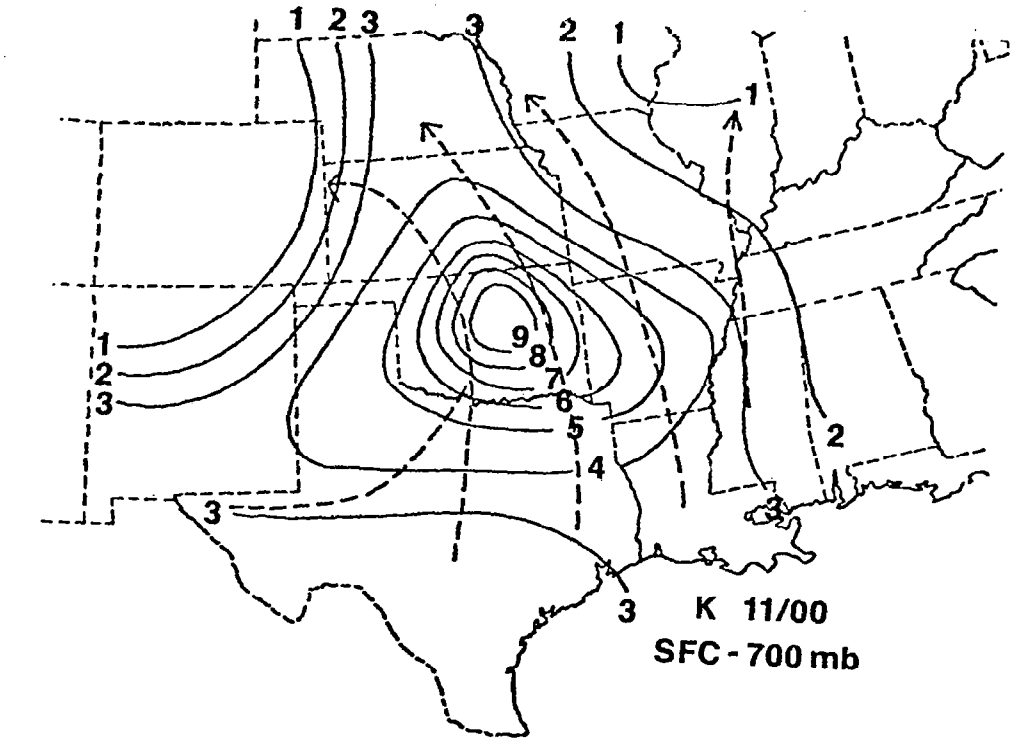

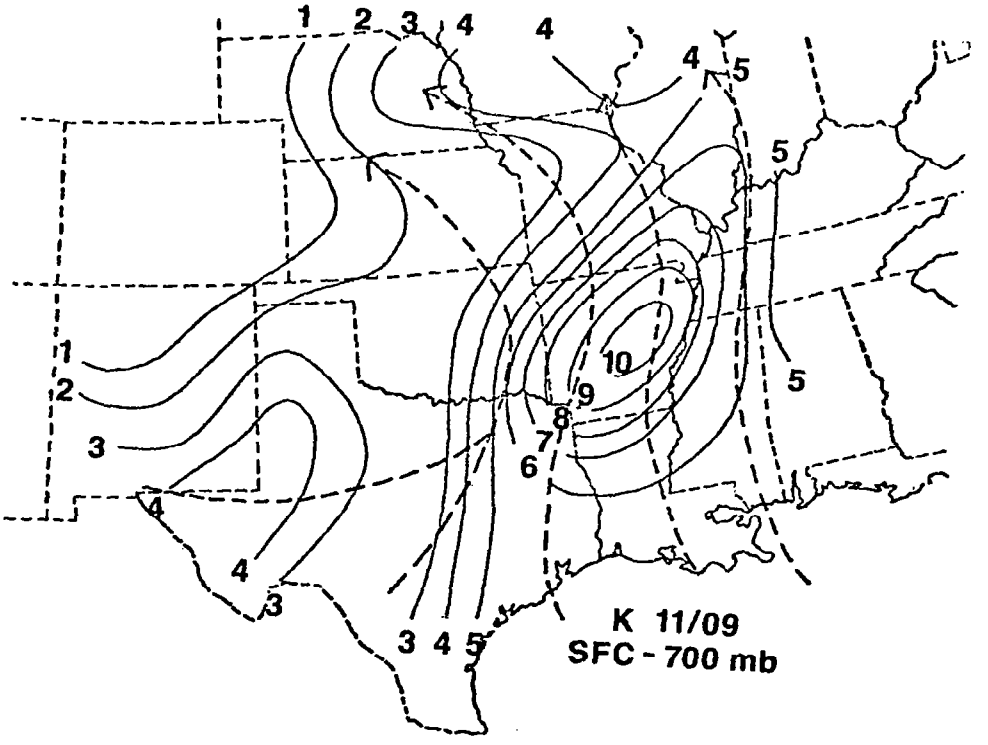

Fig. 1.19. (Concluded)

computations reveal that advection of kinetic energy (term $\vec{V}\cdot\vec{\nabla}k$) is much greater than term $k\vec{\nabla}\cdot\vec{V}$ in the vicinity of the LLJ. Since the jet region contains upward vertical motion and high energy content, strong vertical flux divergence occurs. Upward vertical transport is a major energy sink for the region and has the same magnitude as the other energy budget terms. Cross-contour flow is a source of kinetic energy over most of the region and is a maximum near the LLJ. Continuity (not shown) indicates that generation is the initial energy source for LLJ formation. The large value of generation at 0000 GMT suggests that the jet continues to be an accelerating feature within the overall flow. The jet also is a center of major grid- to subgrid-scale energy transfer (negative dissipation) which, physically, may occur in the form of low-level turbulence. Although most of the area contains negative dissipation, positive values are seen in a few locations. These centers may be related to convection, damping of upstream turbulence, or error (Ward and Smith, 1976).

The energy balance of the 400-100 mb layer at 0000 GMT is quite complex (Fig. 1.20). Horizontal flux convergence of kinetic energy occurs over much of Texas, Arkansas, and Louisiana in advance of the major upper-level kinetic energy maximum still located over Mexico (see Fig. 1.18). The rather complex pattern over the northern half of the region is related to smaller scale energy content centers located near Missouri. In contrast to the lower layer, vertical transport between 400-100 mb is generally smaller than the other terms of the budget. Vertical inflow occurs from Missouri, through Kansas, into New Mexico, while vertical export of energy occurs over Texas, Arkansas, and southeastern Oklahoma. Supergradient flow in advance of the major jet streak in Mexico produces destruction of kinetic energy by cross-contour flow over much of Texas. On the other hand, generation is a source of energy in a region stretching from Missouri into Oklahoma. The most pronounced region of positive dissipation, which indicates subgrid-scale energy sources, occurs over central Texas, in advance of the jet streak and in a region of negative generation. Negative dissipation is centered over the border of Oklahoma and Arkansas. In contrast to findings of Robertson and Smith (1980), there is no consistent relation between horizontal flux convergence and dissipation.

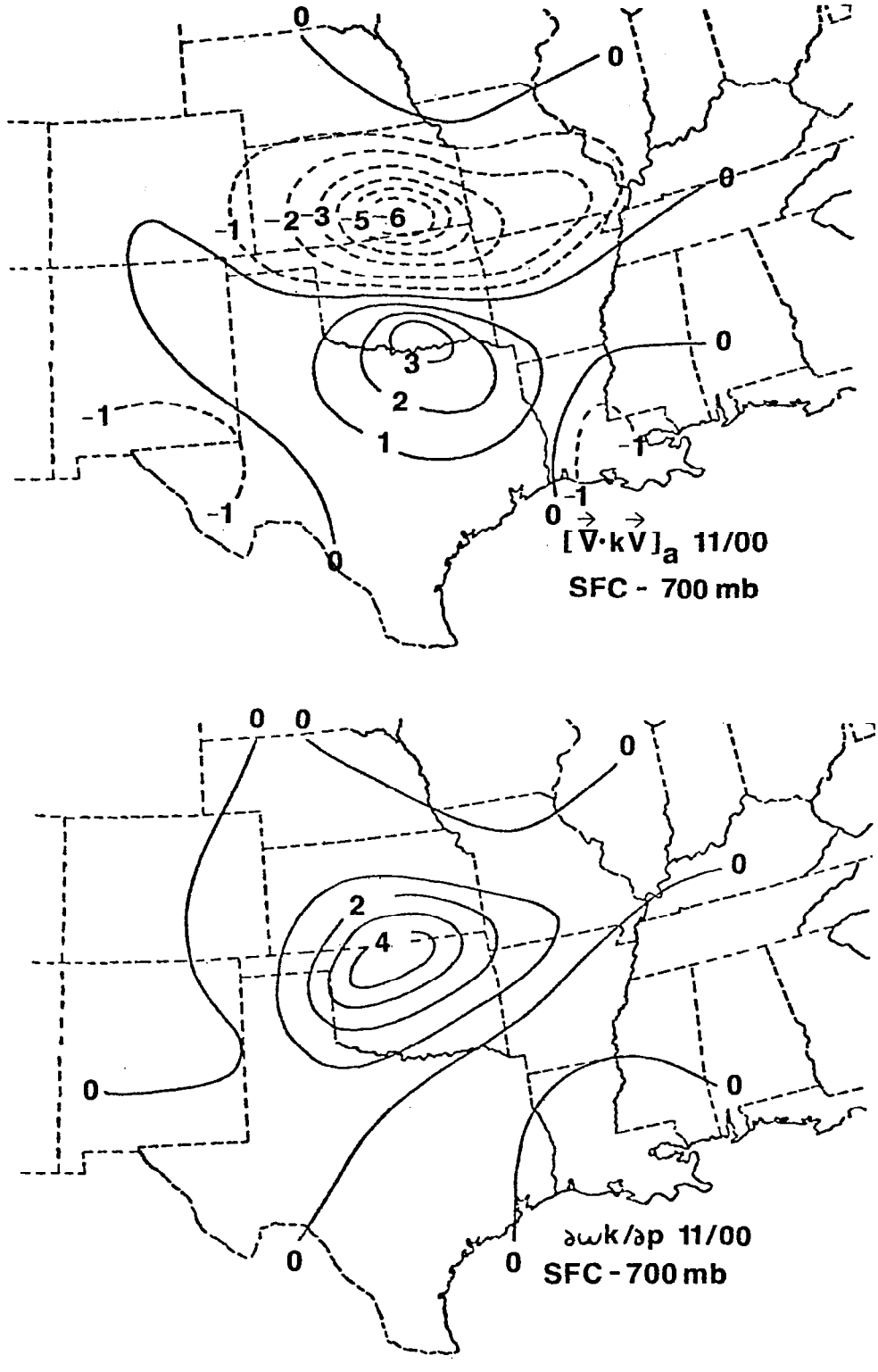

Fig. 1.20. Spatial fields of kinetic energy budget terms at 0000 GMT 11 April. Values are in 10^1 W m^{-2}.

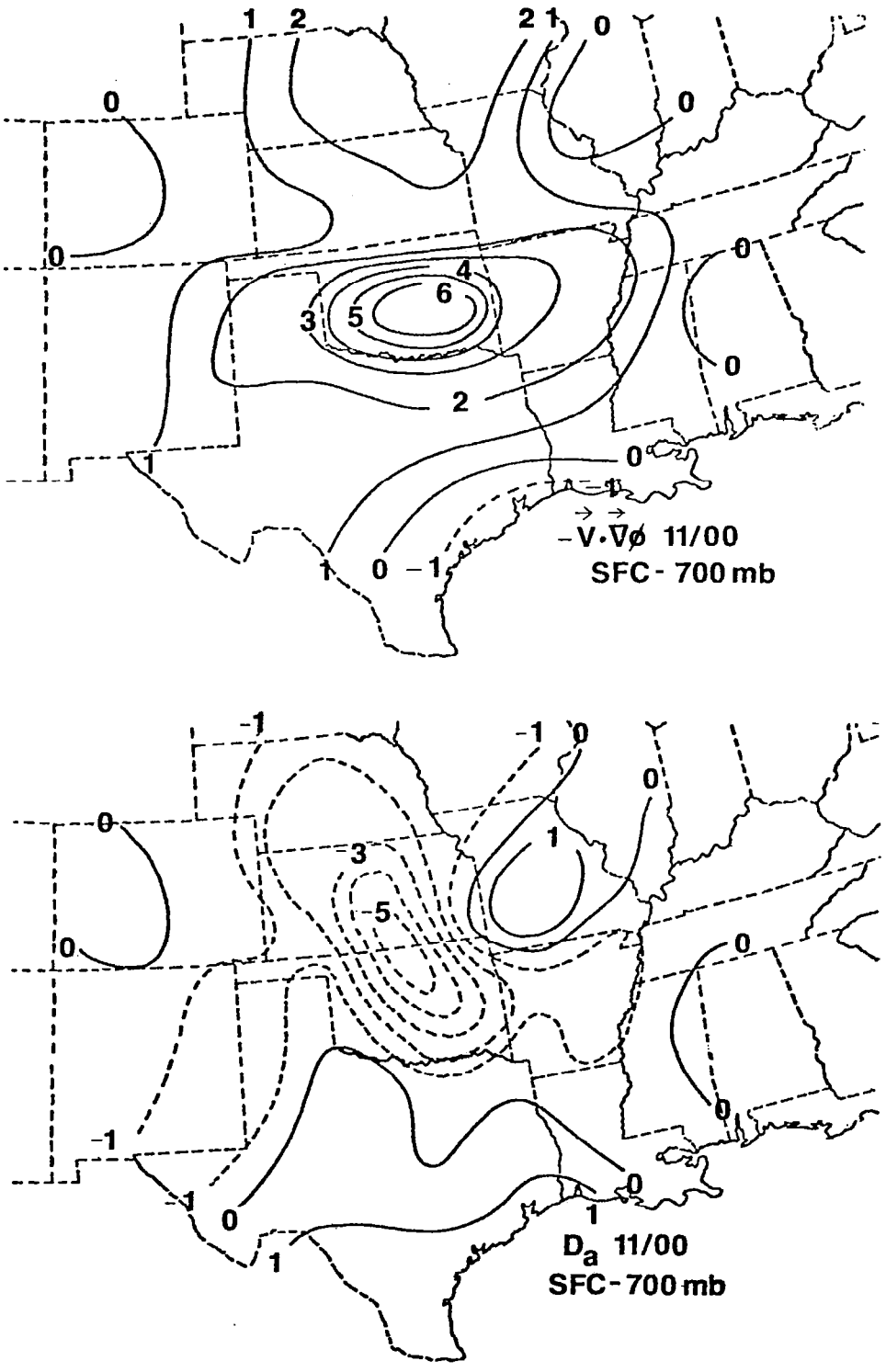

Fig. 1.20. (Continued)

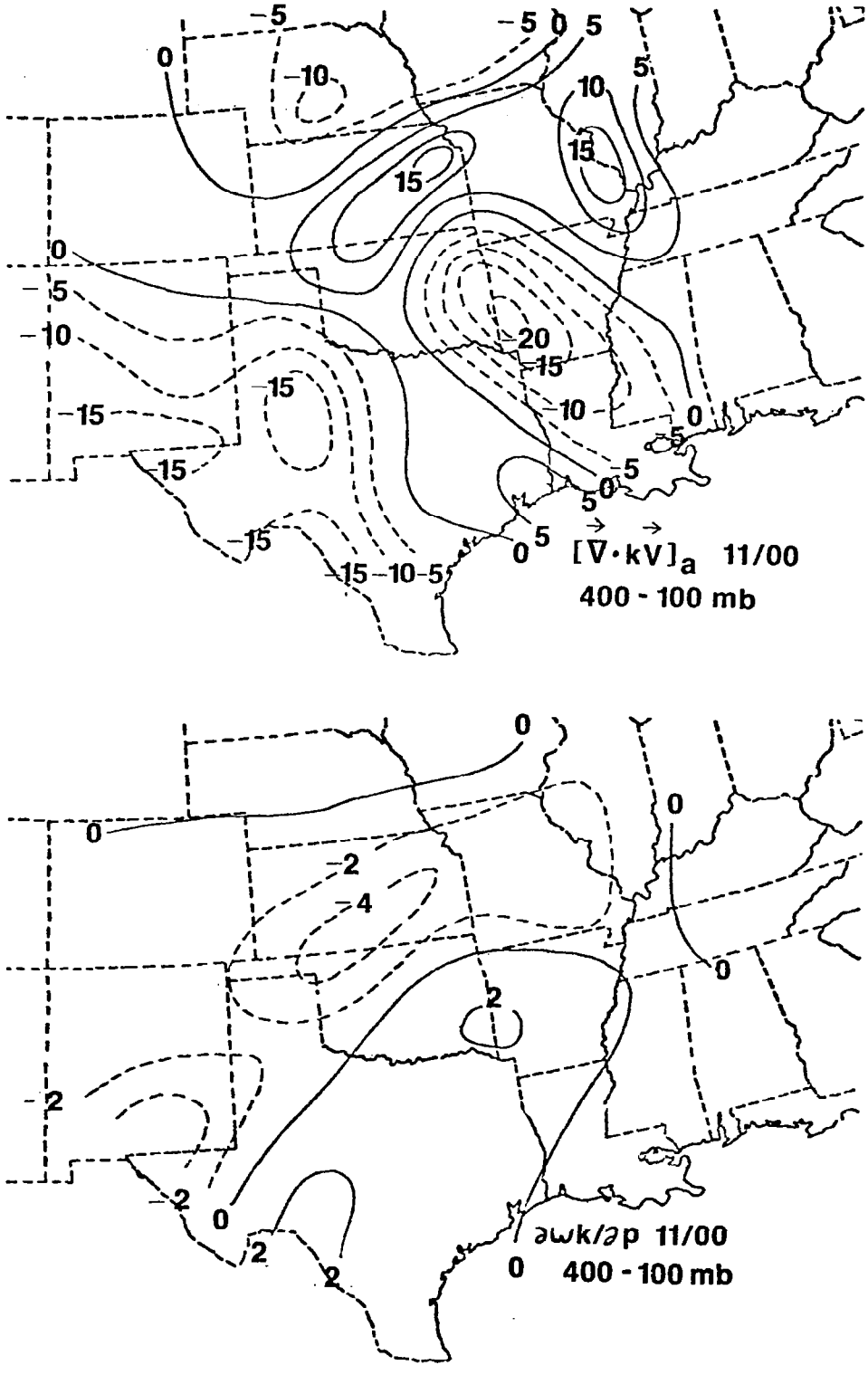

Fig. 1.20. (Continued)

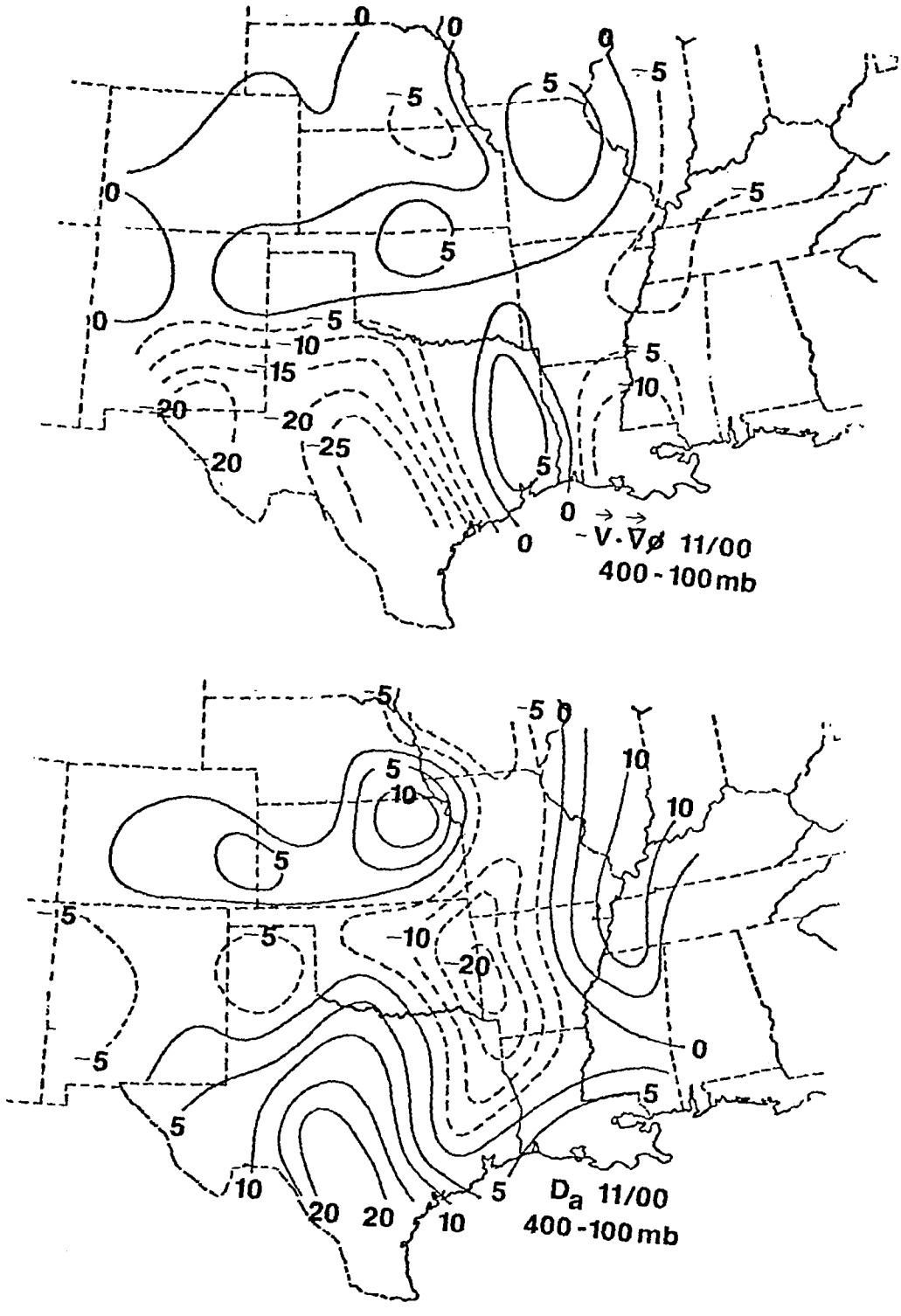

Fig. 1.20. (Concluded)

In the lower layer, energy processes are closely tied to LLJ location which, in turn, occurs near the region of maximum convection (see Fig. 1.7). However, since the LLJ develops before significant severe storm development, it is difficult to attribute features of the kinetic energy patterns to the convection as was done by Fuelberg and Scoggins (1978) and Fuelberg (1979a). In a similar way, continuity suggests that upper-level energy patterns primarily are associated with jet features that are not related directly to storm life cycles.

Figure 1.21 shows fields of the kinetic energy budget terms at 0900 GMT 11 April. This time was selected for discussion because it contains a well developed LLJ over Arkansas and a developing LLJ over the Big Bend (Fig. 1.19), as well as upper-level wind maxima over Oklahoma and western Texas (Fig. 1.18).

Looking first at the surface to 700 mb layer, the dominant features of term $\vec{V}\cdot k\vec{V}$ again are associated with the LLJ's. The well defined flux divergence-convergence couplet over the Mississippi River Valley is associated with the jet maximum over Arkansas, while flux convergence over Texas is related to the developing jet over western Texas. Vertical flux divergence, associated with upward vertical motion, corresponds closely to the precipitation areas (Fig. 1.11). An interesting pattern in the cross-contour flow term exists near Arkansas. As the air accelerates northward toward the Arkansas wind maximum of 35 m s^{-1} at 850 mb subgradient flow produces a source of kinetic energy. As the air streams out of the jet maximum heading into Missouri, supergradient flow produces a sink of energy. A second major positive area, located over northern Missouri, also indicates an accelerating flow regime. The field of dissipation indicates a transfer of kinetic energy to subgrid scales of motion near the LLJ, and over most of the region that experiences a positive generation source.

In the 400-100 mb layer (Fig. 1.21), each center of the horizontal transport term is related to kinetic energy maxima (Fig. 1.18) with flux convergence ahead of, and flux divergence, behind the jet centers. Vertical inflow of energy from below is a source to much of the region. Cross-contour flow is an energy source to the Texas panhandle and most of Oklahoma while destruction of energy occurs over Kansas. These two centers appear to be due to nongradient effects expected near the wind

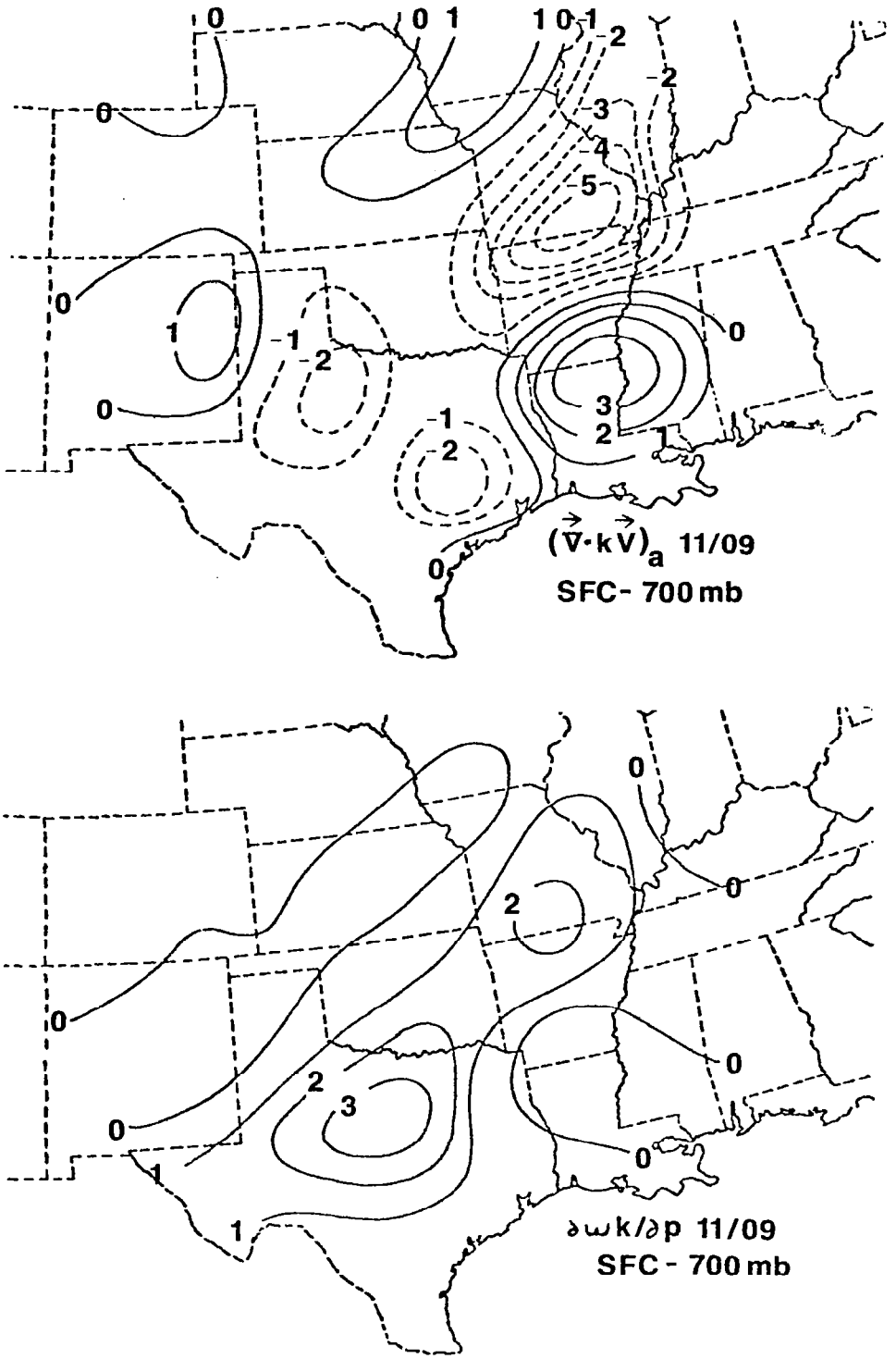

Fig. 1.21. Spatial fields of kinetic energy budget terms at 0900 GMT 11 April. Values are in 10^1 W m^{-2}.

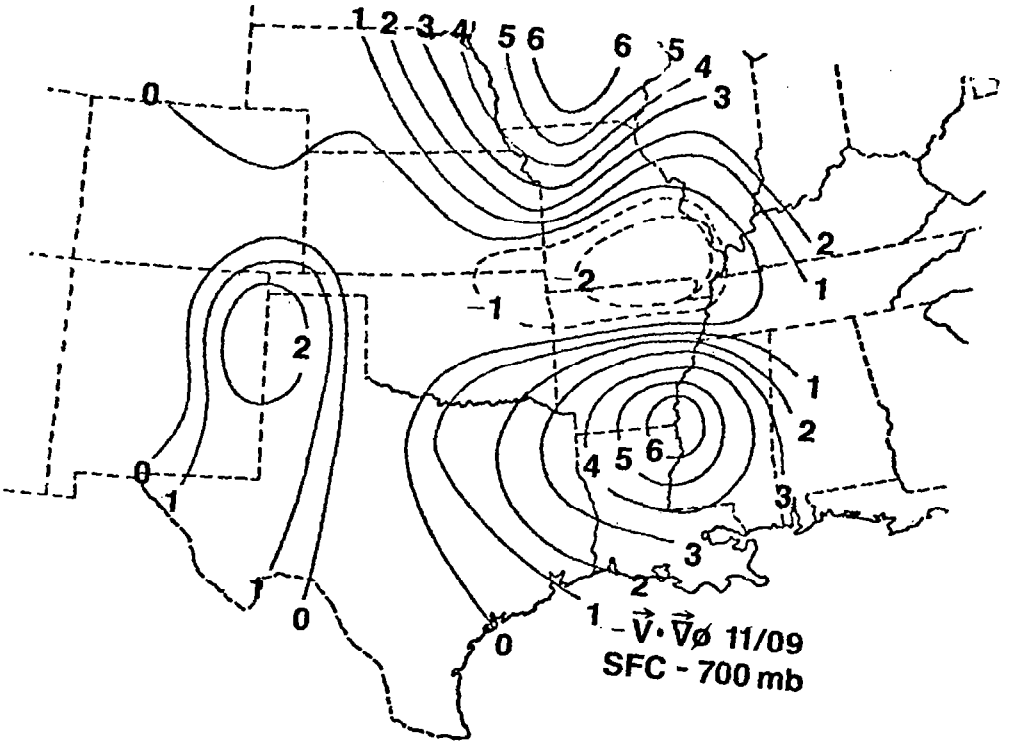

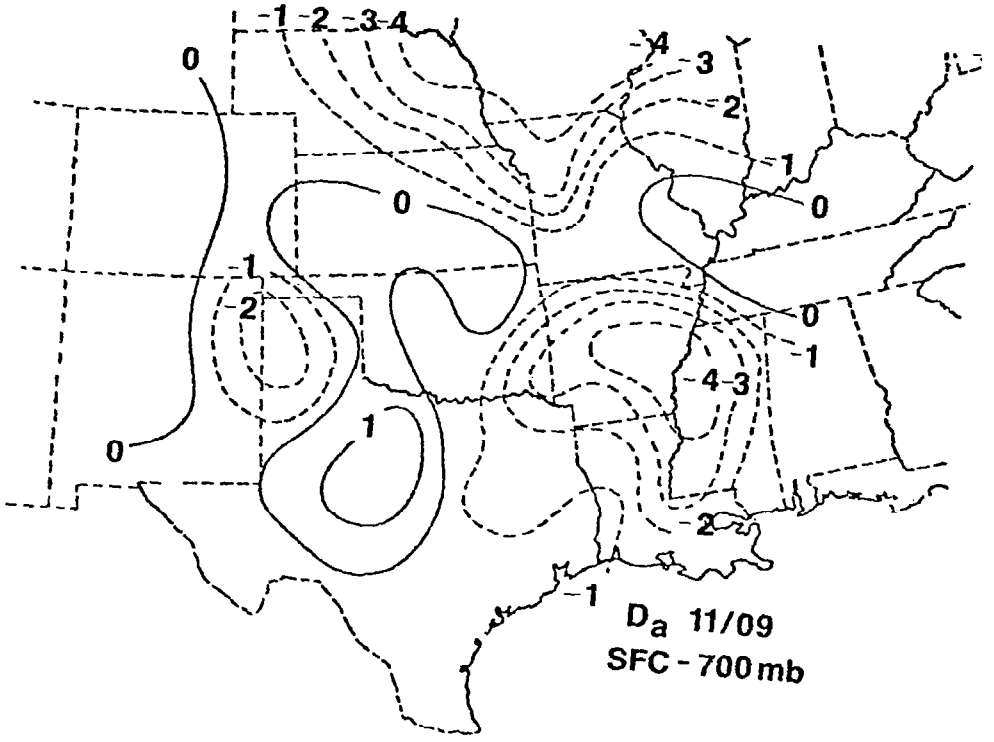

Fig. 1.21. (Continued)

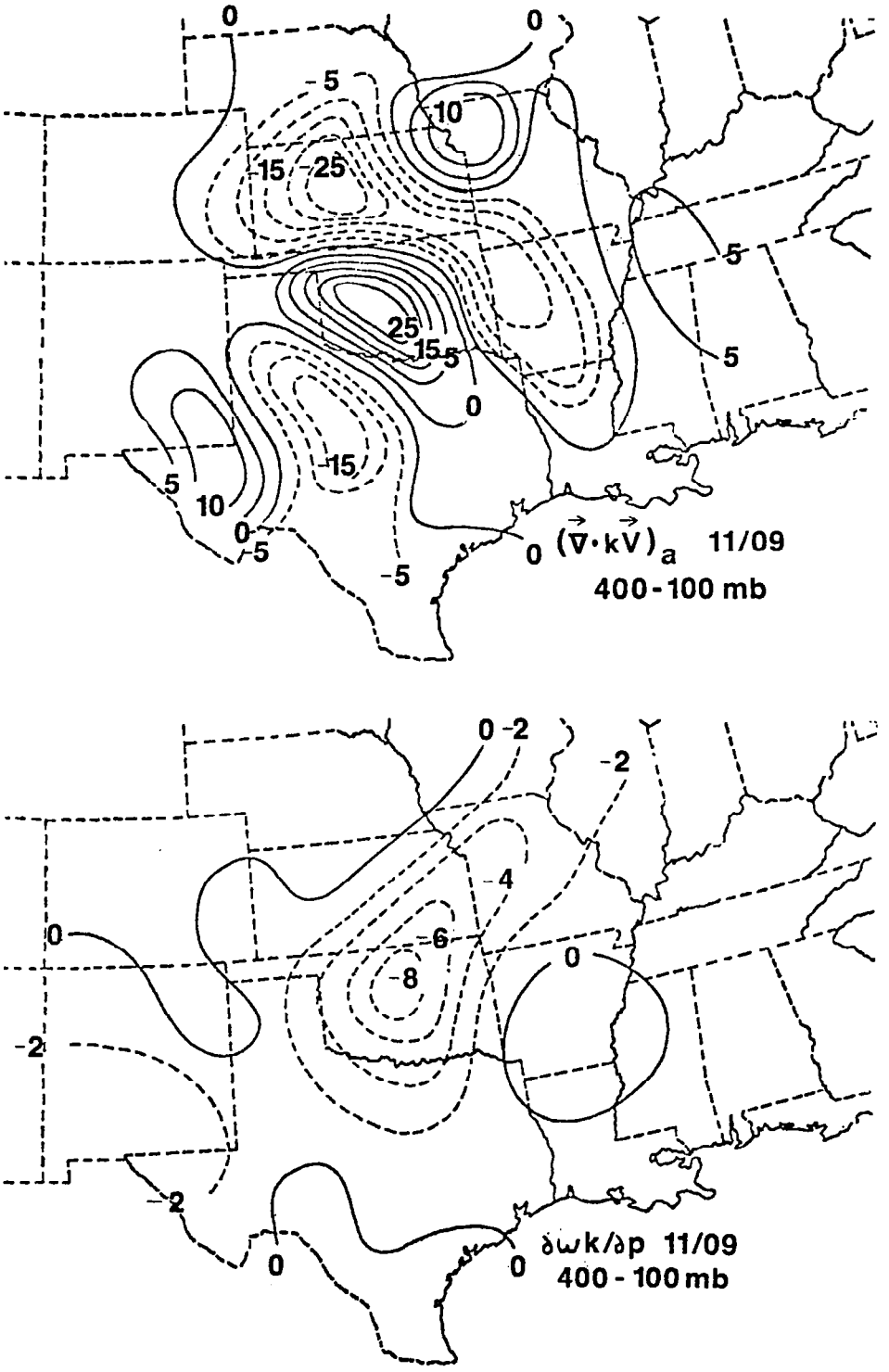

Fig. 1.21. (Continued)

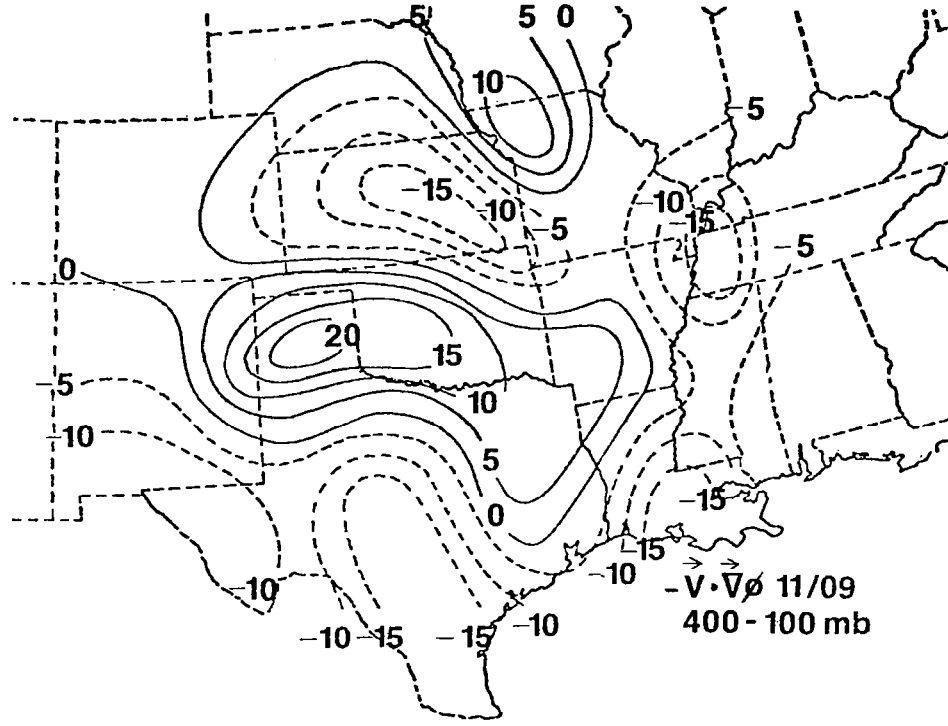

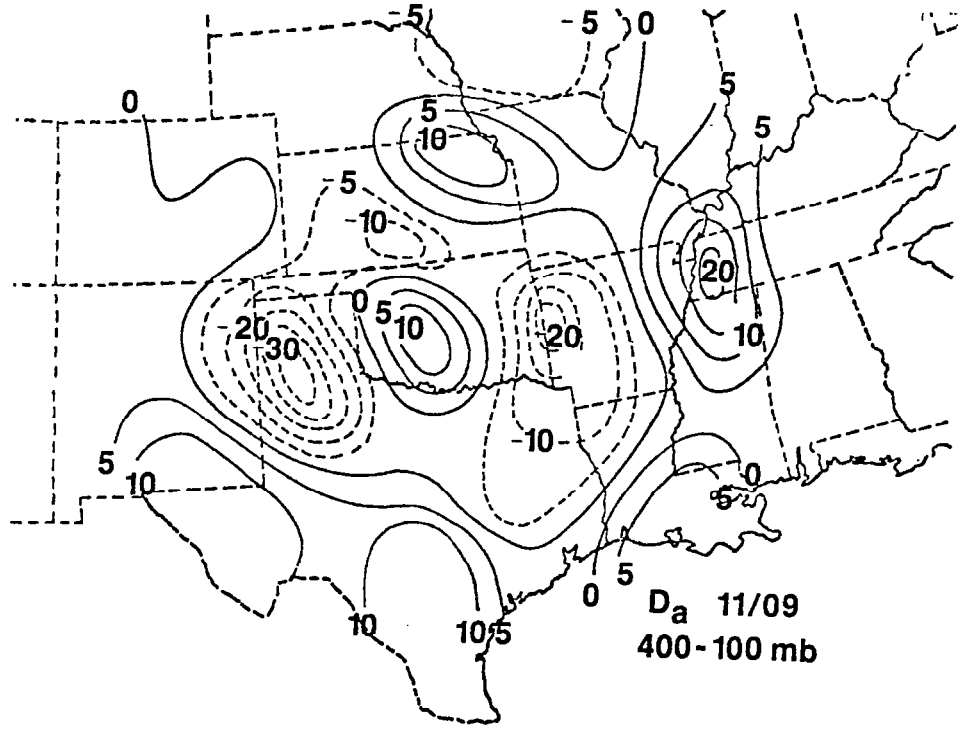

Fig. 1.21. (Concluded)

maximum over northern Oklahoma. Cross-contour destruction is widespread over southern Texas and the Mississippi River Valley. Major grid- subgrid-scale interaction associated with the jet perturbations and the convection is indicated by the dissipation term. At this time, areas of positive dissipation seem to correspond to areas of horizontal flux divergence, which is opposite that observed by Robertson and Smith (1980).

The relation of the energy patterns at 0900 GMT to the observed convection again is not clear. Large areas of intense storms have existed within the area for at least 9 h, and there is undoubtedly a feedback process to the synoptic scale. At this point, however, it has not been possible to conclusively isolate the feedback from processes associated with the jet intrusion, which appears to have been a major trigger for the storms in the beginning.

d. Energetics of convection areas

The purpose of this section is to describe the energetics of areas of convection and relate these characteristics with those of the entire AVE-SESAME 1 area and the area not experiencing precipitation. Manually Digitized Radar (MDR) data (National Weather Service, 1979) were used to objectively determine the intensity and position of radar-observed precipitation during the AVE-SESAME 1 period. The MDR data were obtained from the radar summary charts that are routinely transmitted over the facsimile circuit. MDR values were assigned to each grid point at each rawinsonde observation time by taking the maximum value within ½ grid distance (∿80 km). An average energy budget then was computed for all points with no precipitation (MDR 0) and another for all points having strong to intense convection (MDR 3-6). A similar procedure was used to obtain averages of certain kinematic parameters. This is not a traditional spatial average since grid points comprising a particular category are not necessarily adjacent. The procedure is similar to that used by Fuelberg (1979b) and Wilson (1976).

Figure 1.22 contains vertical profiles of kinematic quantities averaged for convection and non-precipitation categories. Compared

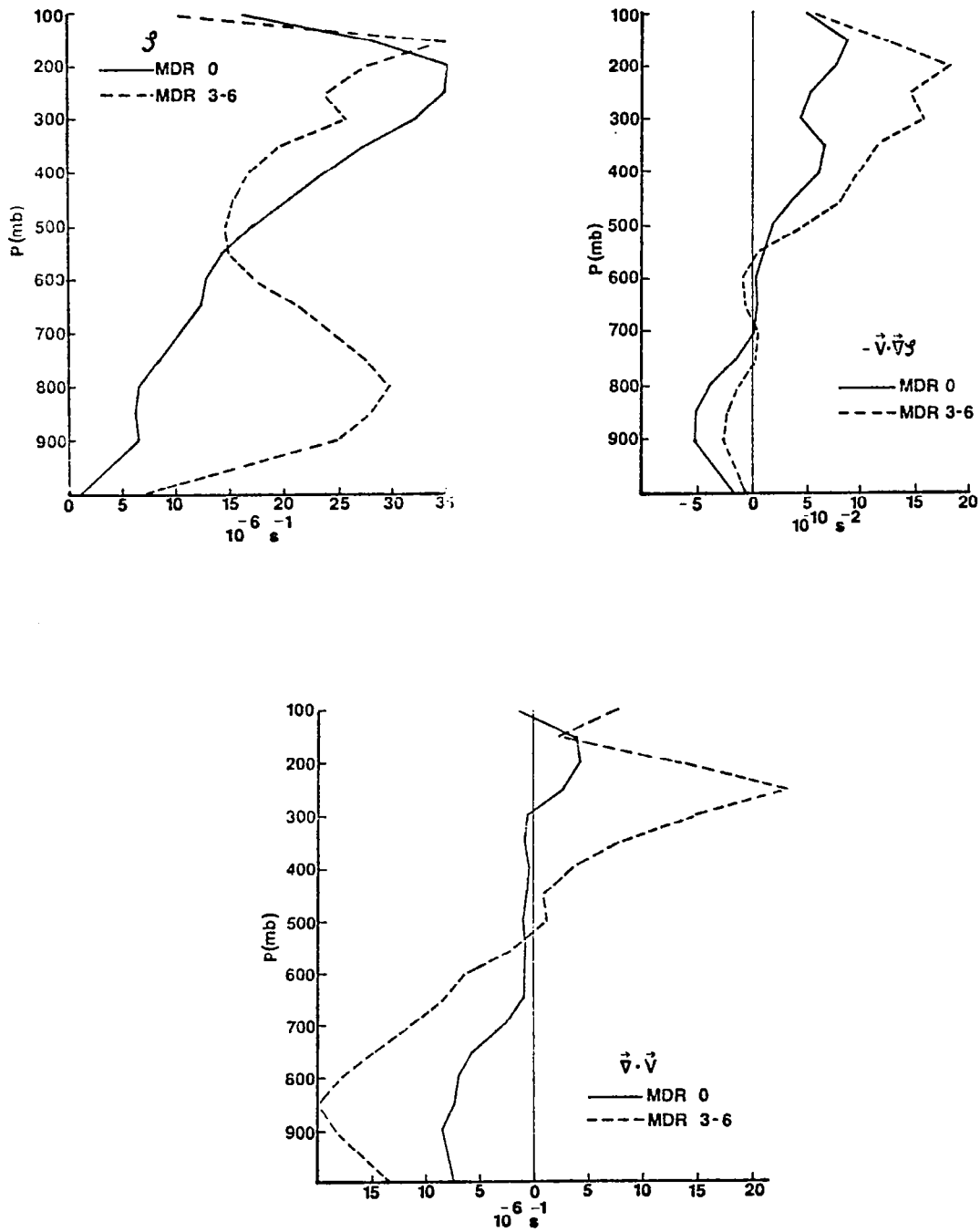

Fig. 1.22. Vertical cross sections of kinematic quantities for grid points near moderate or intense convection (MDR 3-6) and non precipitation (MDR 0).

to the non-precipitation environment, the synoptic-scale storm environment is characterized by enhanced low-level convergence, enhanced upper-level divergence, enhanced low-level positive vorticity, diminished upper-level positive vorticity, and enhanced upper-level positive vorticity advection. These contrasts suggest that storms occur in areas of greater synoptic-scale forcing, and possibly that the storms are modifying their surroundings, but as previously stated, it has not been possible to isolate these feedback processes.

The tabulated energy budget for the convection grid points, given in Table 1.3, will be compared to that of the entire area (Table 1.1). Storms occur in areas of higher kinetic energy content and larger local increases of energy content than the area as a whole, which is indicative of their tendency to form near and downwind of jet streaks. While destruction of kinetic energy by cross-contour flow and positive dissipation occur in the AVE-SESAME 1 region as a whole, just the opposite is found in the vicinities of the storms. Although vertical totals of horizontal flux divergence are similar for both categories, the vertical distributions are considerably different. Compared to the entire area, the storms occur in regions of enhanced low-level flux convergence but decreased upper-level flux convergence. Since the storms tend to form in regions of low-level velocity convergence topped by divergence, the effect enters the flux computation through term $k\vec{\nabla}\cdot\vec{V}$. Different energy contents also are a factor in these contrasts. The storm environment is a preferred region for upward vertical transport of kinetic energy and release of potential energy by vertical overturning. In spite of the large release of energy in the storm environment, the convective efficiency (COE) is still only about 1%. Figure 1.23 contrasts the energetics of the storm (MDR 3-6) and non-precipitation environments (MDR 0). The findings are quite similar to those of the convection points versus the entire area (just described) because most of the AVE-SESAME 1 region does not experience intense convection at any particular observation time.

A comparison of the MDR 0 and MDR 3-6 vertical profiles of $\vec{\nabla}\cdot k\vec{\nabla}$ (unadjusted) and dissipation (Fig. 1.23) tends to support the observation by Robertson and Smith (1980) that upper-level horizontal flux convergence is accompanied by positive dissipation; however the underlying mechanism is not understood. The profiles also indicate

Table 1.3. Kinetic energy budget for those AVE-SESAME 1 grid points having convection of MDR 3-6 at an observation. All units are W m^{-2} except for K which is 10^5 J m^{-2}.

Pressure Layer (mb)	K	$\partial K/\partial t$	$\vec{\nabla}\cdot k\vec{\nabla}$	$\{\vec{\nabla}\cdot k\vec{\nabla}\}_a$	$\partial \omega k/\partial p$	$-\vec{\nabla}\cdot\vec{\nabla}\phi$	D	D_a	$-\omega\alpha$
200-100	6.96	-0.05	-0.52	-0.44	-9.06	-2.08	-7.54	-7.46	158.1
300-200	8.93	4.46	3.09	5.18	-13.22	5.11	-10.78	-8.69	470.4
400-300	6.66	5.58	-5.10	-3.11	-3.19	7.21	-9.22	-7.93	679.3
500-400	5.28	6.73	-5.70	-4.73	0.61	6.42	-4.78	-3.81	674.5
600-500	4.28	4.59	-4.32	-4.06	6.66	7.41	-0.49	-0.22	606.8
700-600	2.82	1.57	-5.56	-5.39	8.24	4.30	-0.05	0.12	486.8
800-700	1.92	-0.29	-5.21	-4.86	5.22	0.50	-0.79	-0.44	322.1
900-800	1.37	0.28	-4.70	-4.34	3.74	2.22	-2.89	-2.54	136.7
Sfc-900	0.44	0.27	-1.04	-1.00	0.99	3.64	-3.41	-3.37	15.8
Vertical Total	38.66	23.15	-29.06	-22.76	0.00	34.73	-40.65	-34.34	3550.3

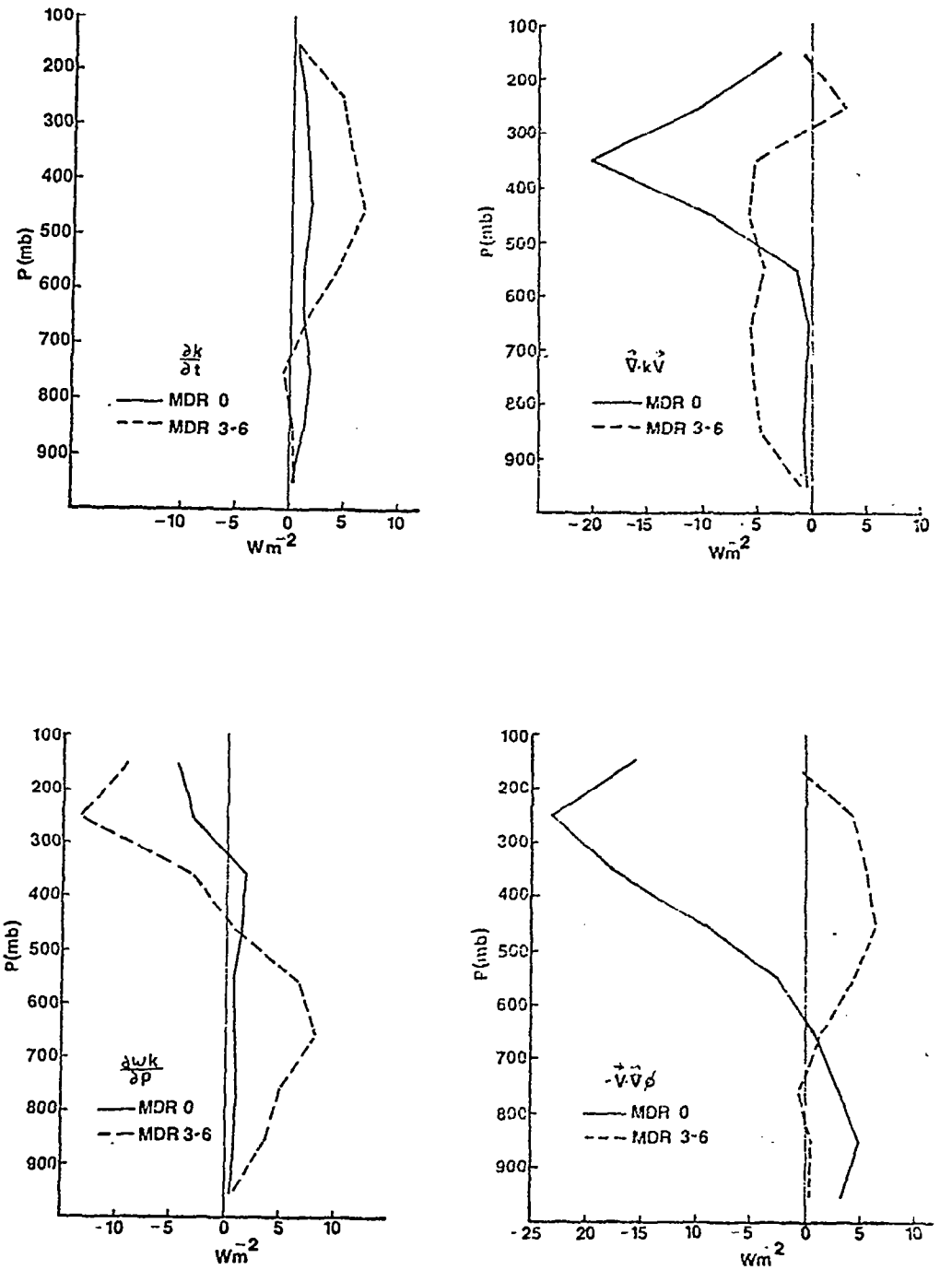

Fig. 1.23. Vertical cross sections of energy budget terms for grid points near moderate or intense convection (MDR 3-6) and non precipitation (MDR 0).

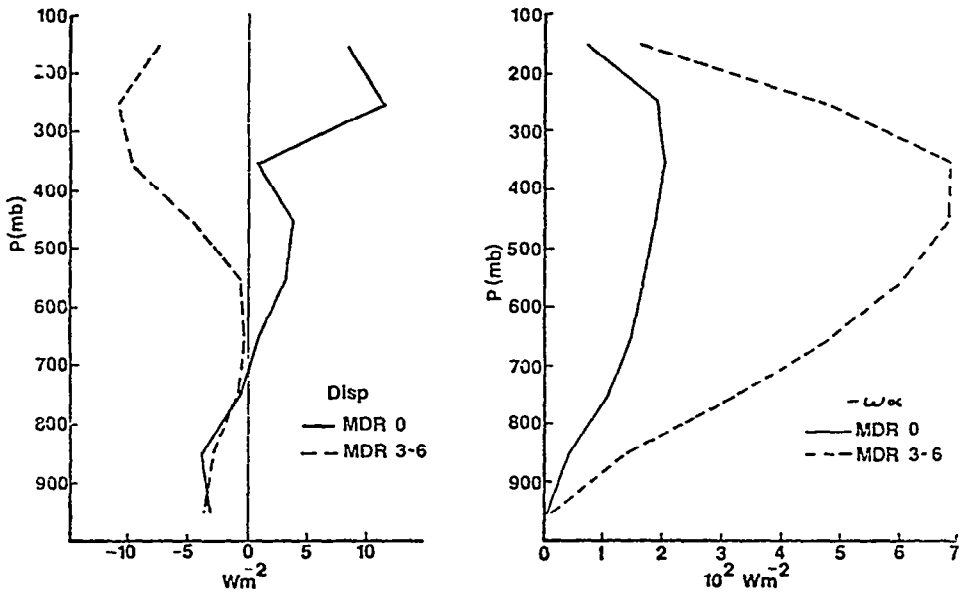

Fig. 1.2 (Concluded)

the relationship between upper-level horizontal flux convergence and cross-contour flow which is a result of nongradient conditions. These simple relationships were not always observed on the spatial maps, however. In comparing differences between the MDR 0 and MDR 3-6 budgets with differences observed in previous AVE experiments (Fuelberg, 1979a and b), simple relationships have not yet been found. If large storms would produce a consistent detectable effect on their surrounding synoptic-scale environments that was not hidden by larger scale processes, such relations would be expected.

e. Current research involving AVE-SESAME 1

The results reported here are only a part of the total effort to unravel the mysteries surrounding the Red River Valley tornado outbreak. The following studies currently are underway and will be described in future reports:

1) Using the synoptic-scale data, the kinematic and energetic properties of fixed, limited volumes that lie perpendicular to the upper-level flow are being compiled to better identify short wave phenomena.

2) Similarly, properties of limited volumes that move with the storm areas also are being studied.

3) An error analysis of the kinematic and energy budget parameters will be conducted to assess the confidence that one can place in them.

4) A new energy budget analysis will be performed on the AVE-SESAME 1 case using the combination of NWS and special site rawinsonde data. The effort should be quite fruitful since it appears that small scale systems are quite active during the period. These upcoming results will be compared with those obtained using NWS data alone to assess the effects of enhanced spatial data resolution.

6. INTRODUCTION TO AVE 6

In contrast to the AVE-SESAME 1 case, the AVE 6 period does not contain a major storm outbreak or pronounced jet intrusion. The case was selected for study because a minor wave passed through the computational region and because winds were much lighter than observed in previous cases. The discussion will focus on describing energy variability associated with the short wave passage and contrasting the energetics of storm and non-storm areas. Data used in the study were described in Section 3 of this report. Computational procedures were similar to those of AVE-SESAME 1 (Section 3) except that adjusted horizontal flux divergence and adjusted dissipation were not computed.

7. SYNOPTIC CONDITIONS OF AVE 6

Synoptic maps for the beginning (0000 GMT 27 May 1977) and end (1200 GMT 28 May) of the AVE 6 period are given in Fig. 1.24. Surface conditions at the initial time included a cool high pressure area centered over the Great Lakes and a disorganized pattern of weak fronts and cyclones over the western half of the country. Upper-level charts reveal a strong warm core ridge over the upper Mississippi River Valley and a weak low over the southeastern states. A closed low was centered off the Pacific Northwest Coast with an imbedded short wave stretching from Washington into New Mexico.

By the end of the period (Fig. 1.24), a surface low was located in southcentral Canada with a Pacific cold front extending from it into the Great Plains. At the upper levels, the ridge over the Great Lakes had weakened as the short wave rotated through the major trough located along the West Coast. The movement of this short wave through the AVE 6 computational area (see Fig. 1.2) appears quite dramatically in time-height cross sections of area-averaged relative vorticity and vorticity advection (Fig. 1.25). The AVE 6 area experiences strongest positive vorticity advection due to this wave near 1200 GMT 27 May while largest positive vorticity occurs near 0000 GMT 28 May.

Although widespread thunderstorm activity occurred during AVE 6, little of it was especially intense or organized into long-lived areas (Fig. 1.26). At the first observation time, 2335 GMT 26 May, convection was associated with the advancing short wave and stretched from the upper Midwest into west Texas. Radar tops reached 15.2 km (50,000 ft) in western Texas and Nebraska. Several weather watch boxes had been outlined by the Severe Storm Forecast Center. Another area of convection was located along the southeastern portion of the region. By the second rawinsonde observation time, 1135 GMT 27 May, the thunderstorm activity had decreased in intensity and was confined to the central portion of the computational region. The midwestern storm area underwent several periods of growth and decay through the remainder of the period. The storm area along the central Gulf Coast re-developed with afternoon heating and dissipated after nightfall.

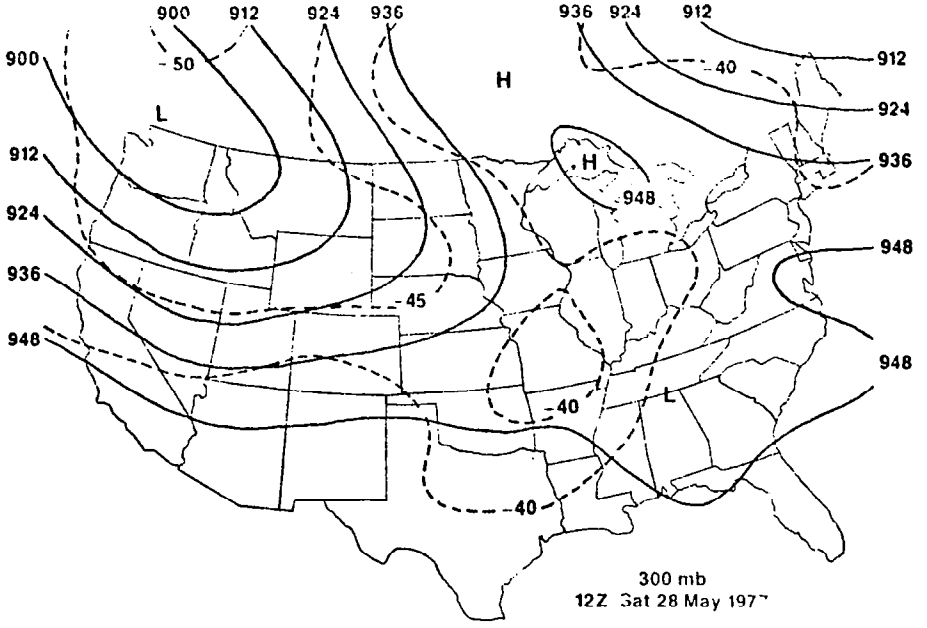

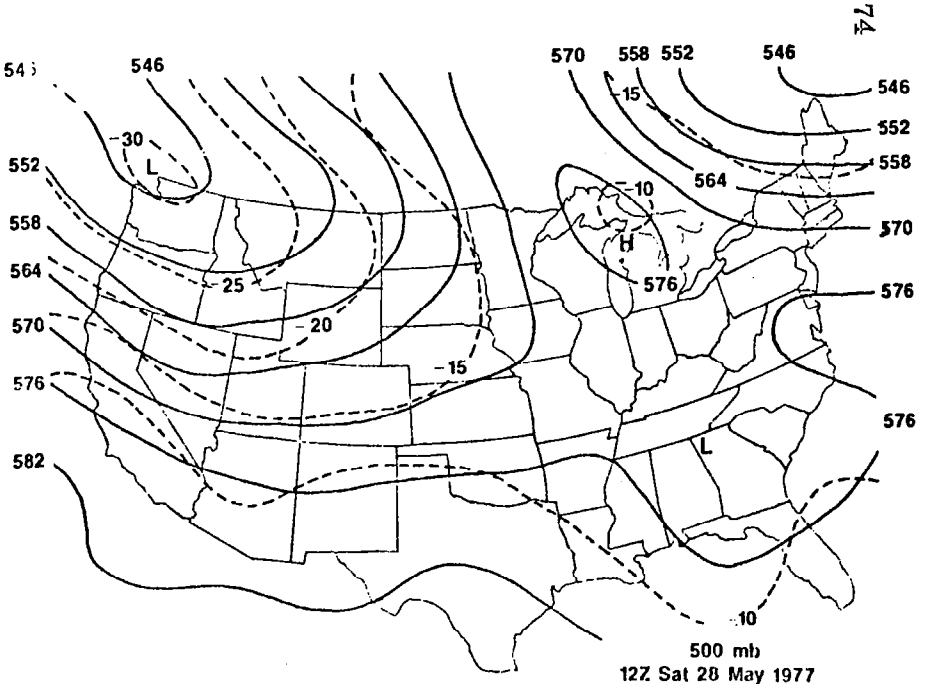

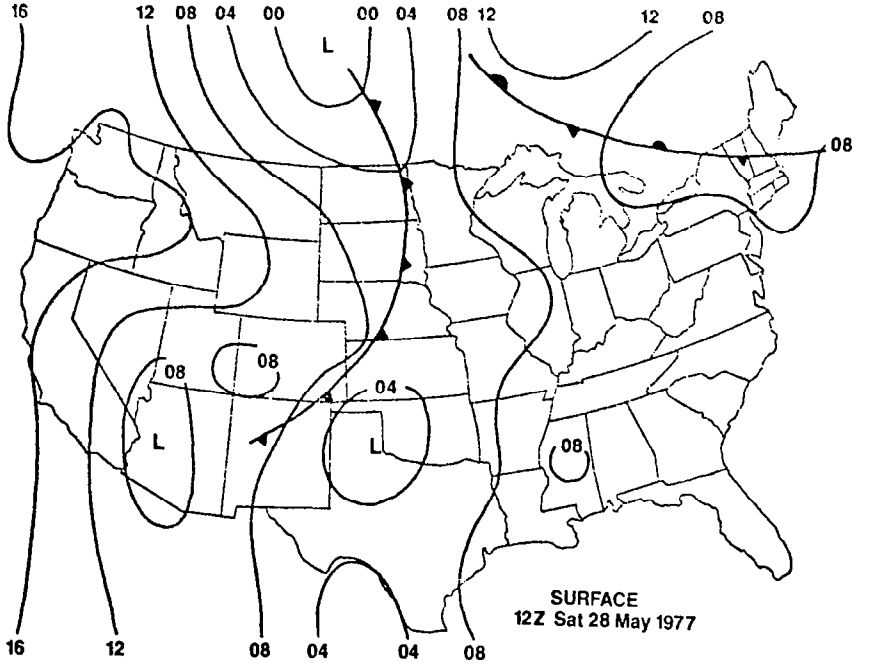

Fig. 1.24. Synoptic conditions during the AVE 6 period. Dashed lines at 500 and 300 mb are isotherms.

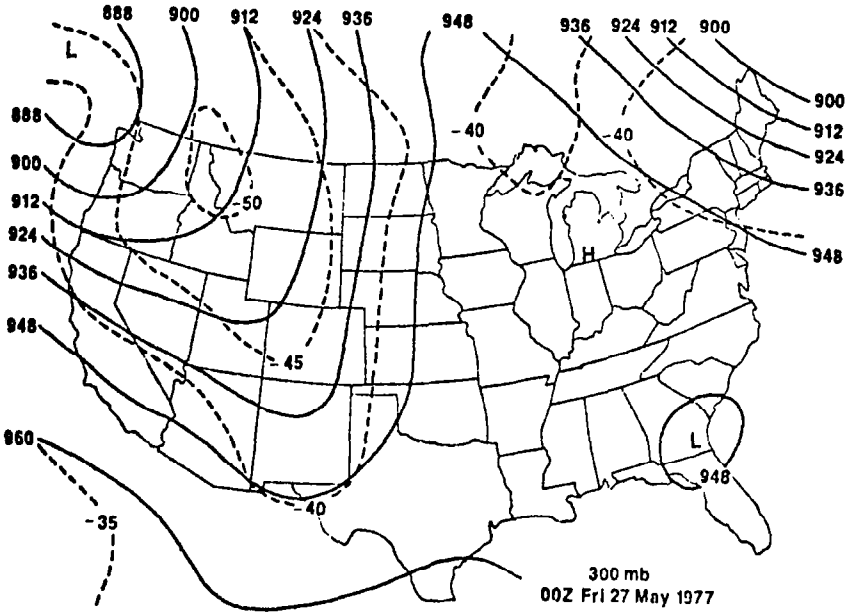

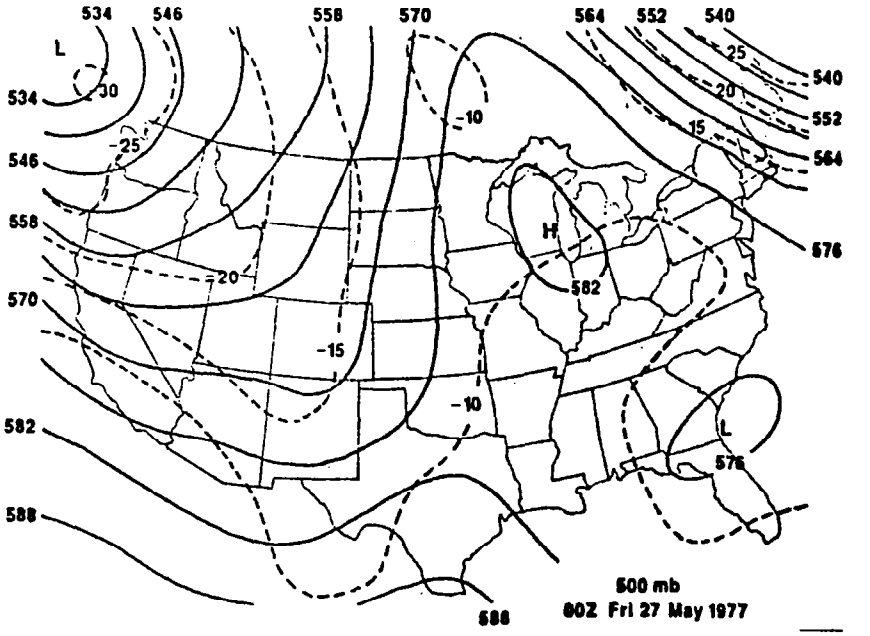

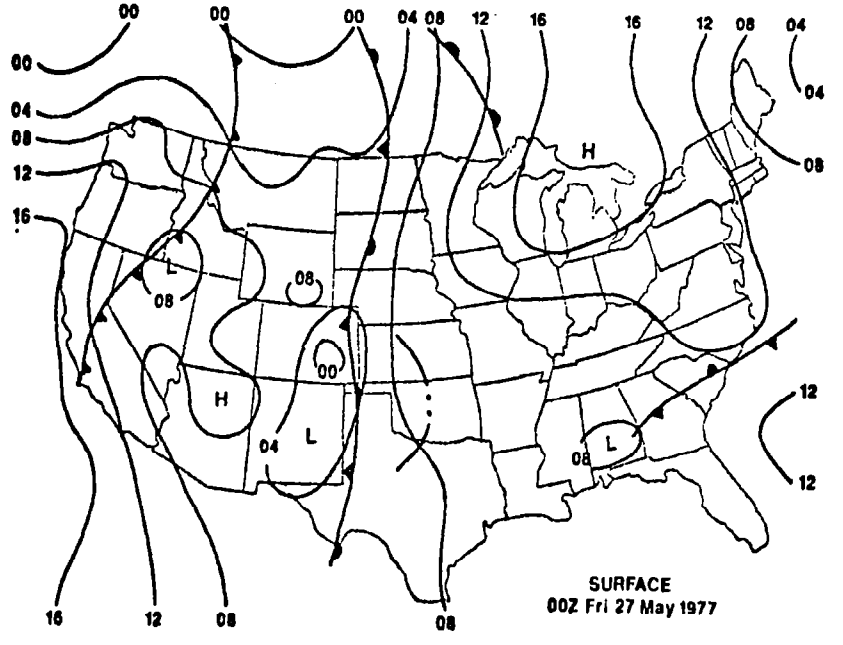

Fig. 1.24. (Concluded)

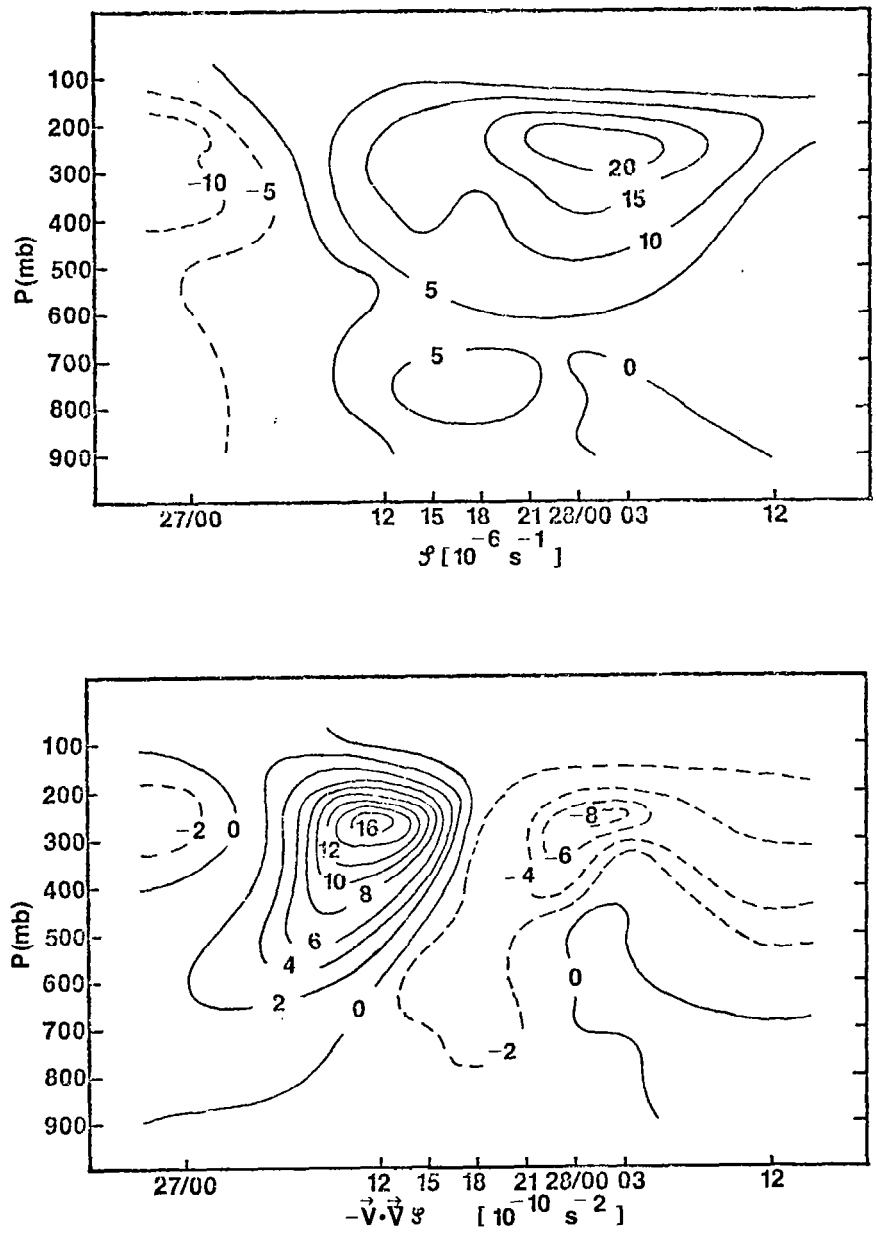

Fig. 1.25. Time-height cross sections of area-averaged relative vorticity (ζ) and vorticity advection ($-\vec{V}\cdot\vec{\nabla}\zeta$) over the AVE 6 period.

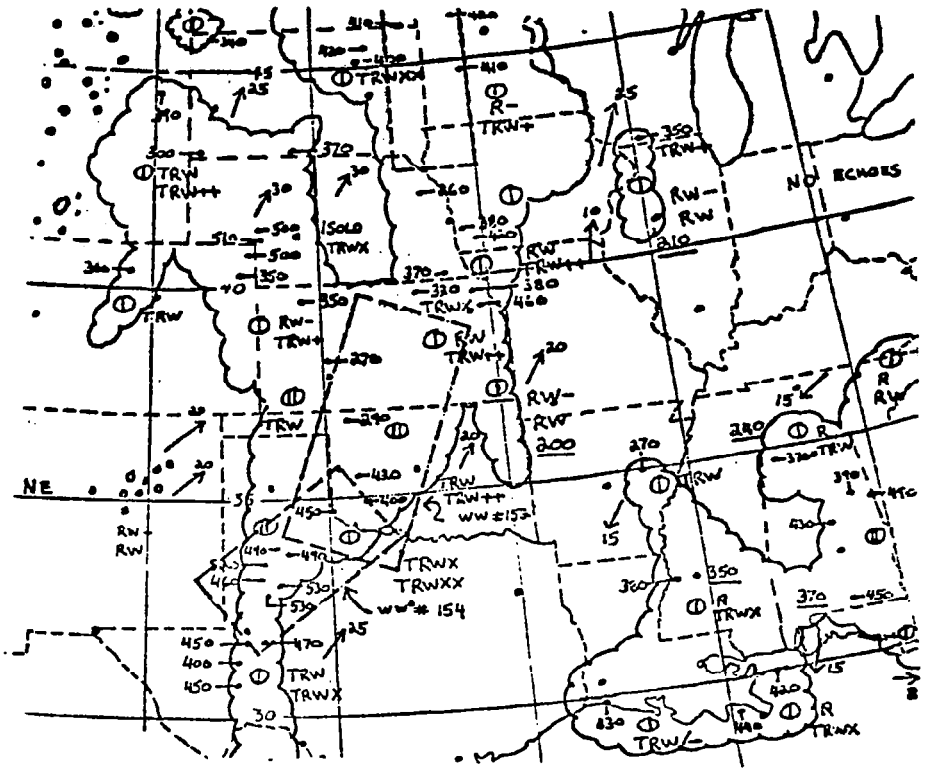

2335 GMT 26 May

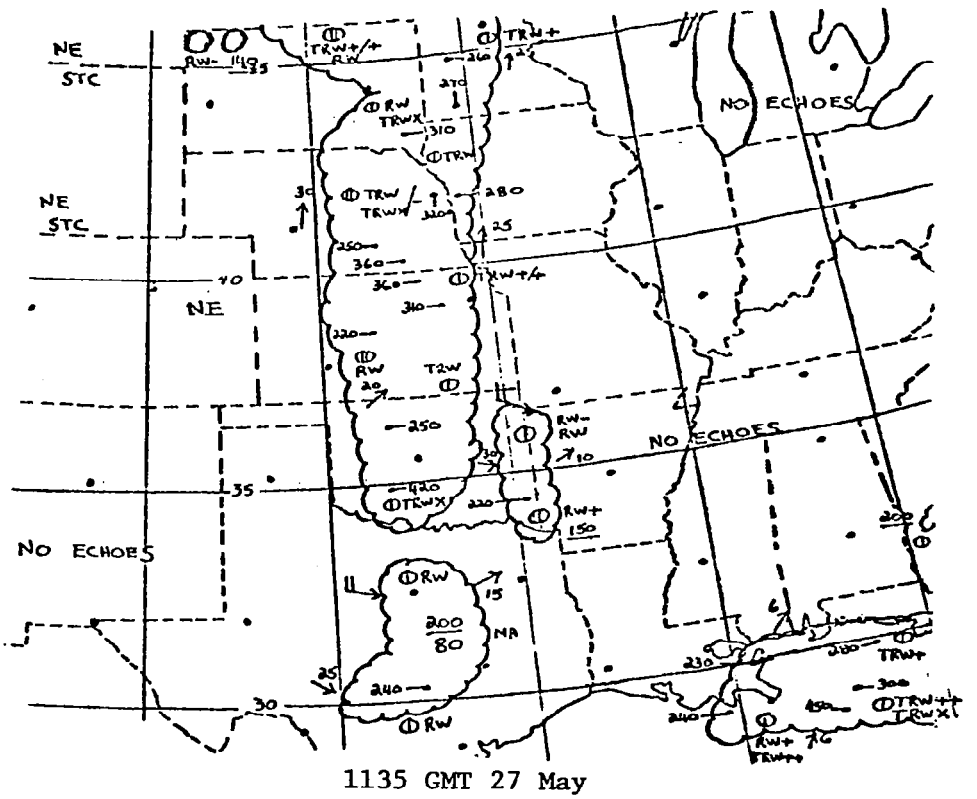

1135 GMT 27 May

Fig. 1.26. Radar summaries for the AVE 6 period.

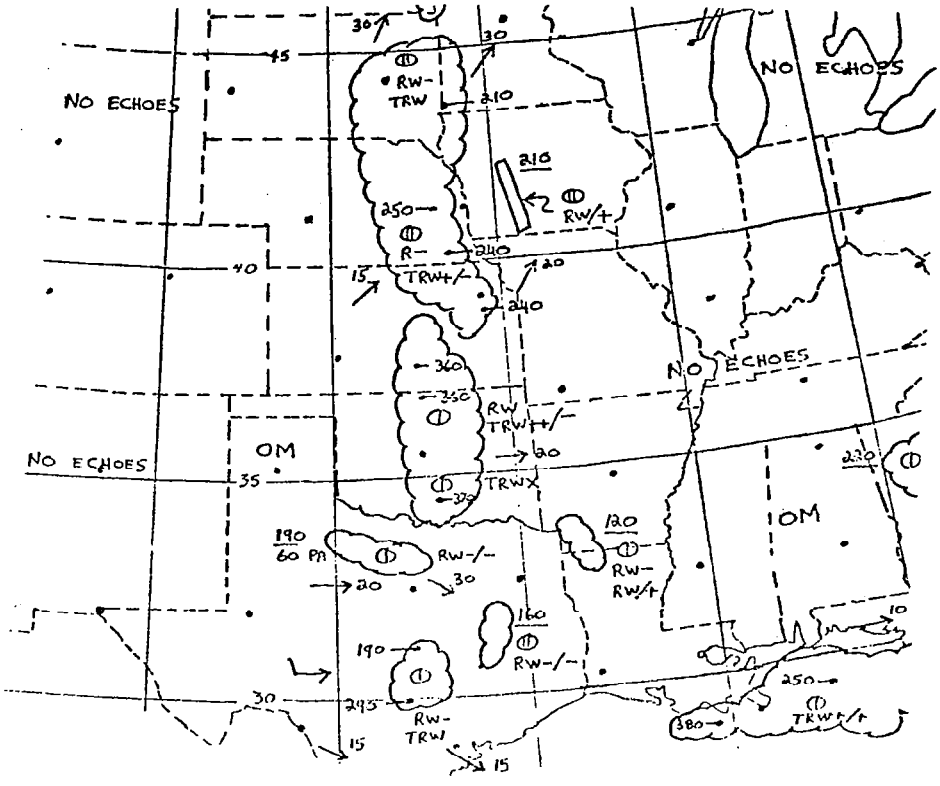

1435 GMT 27 May

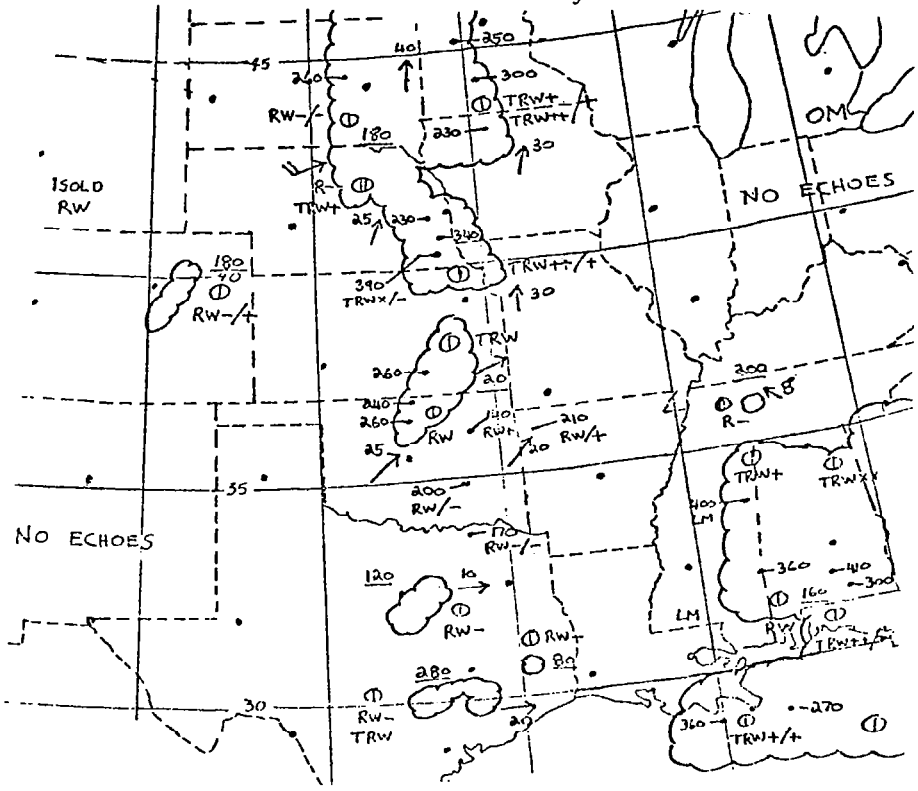

1735 GMT 27 May

Fig. 1.26. (Continued)

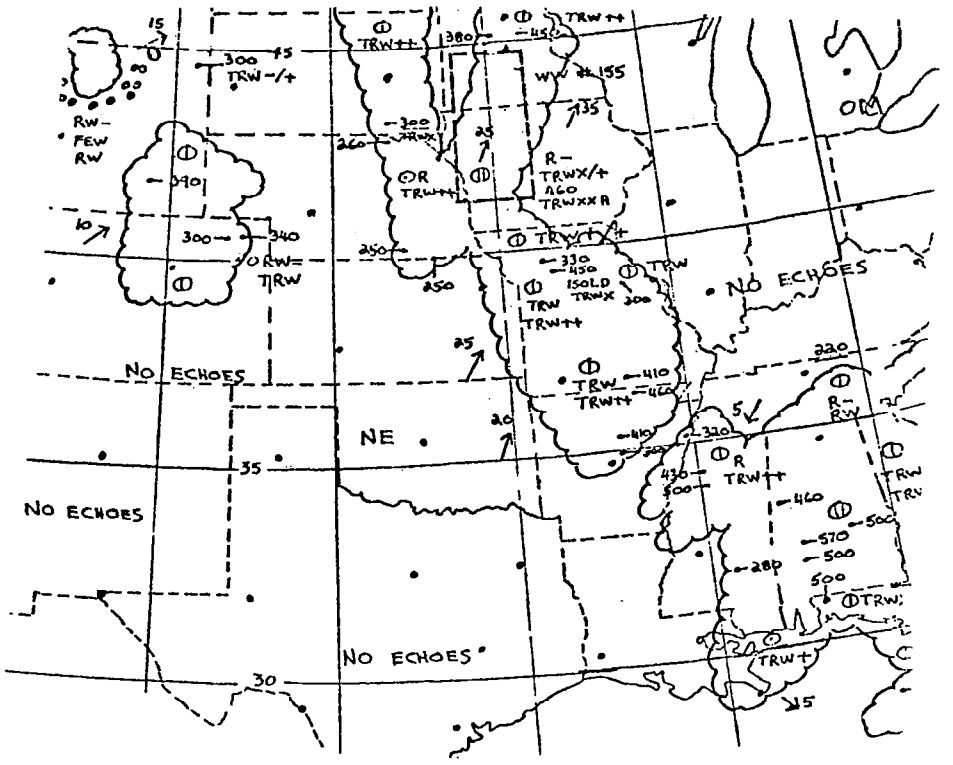

2035 GMT 27 May

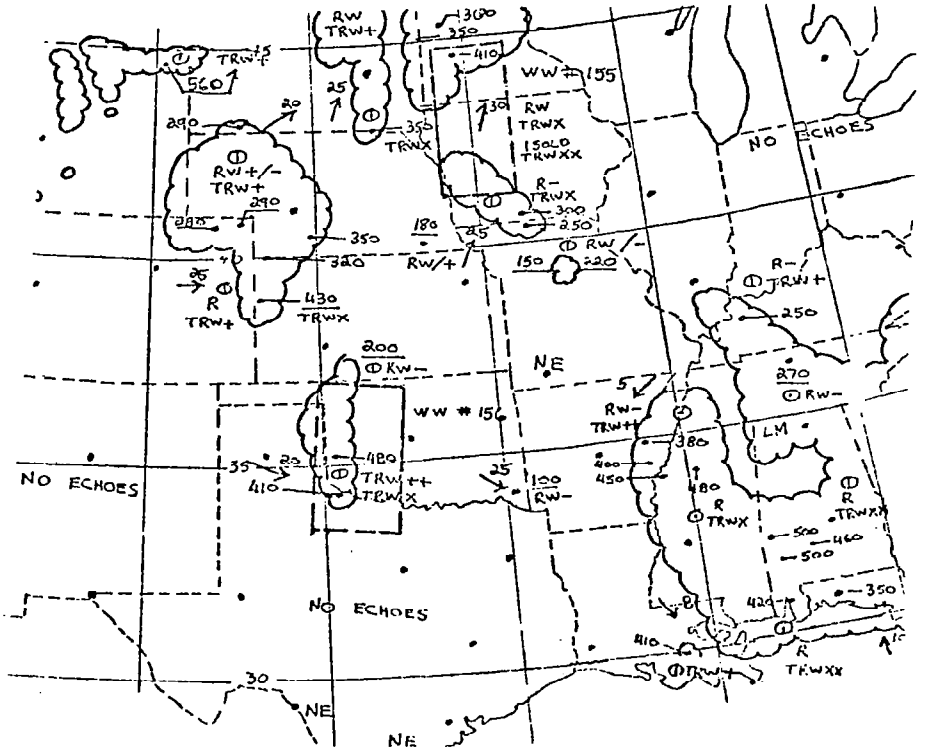

2335 GMT 27 May

Fig. 1.26. (Continued)

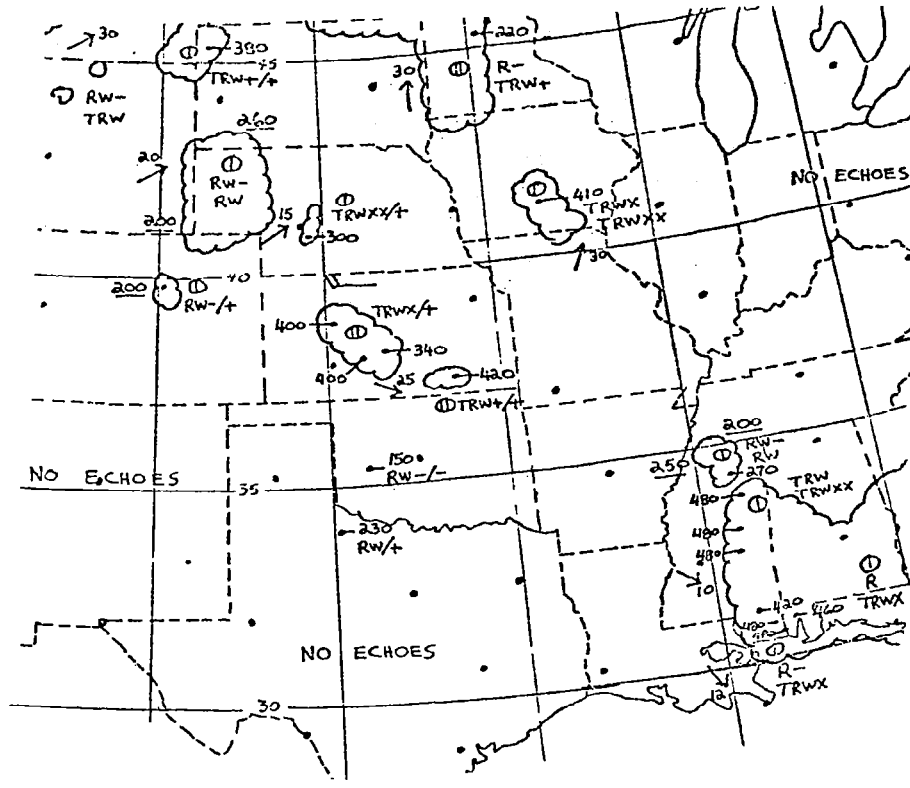

0235 GMT 28 May

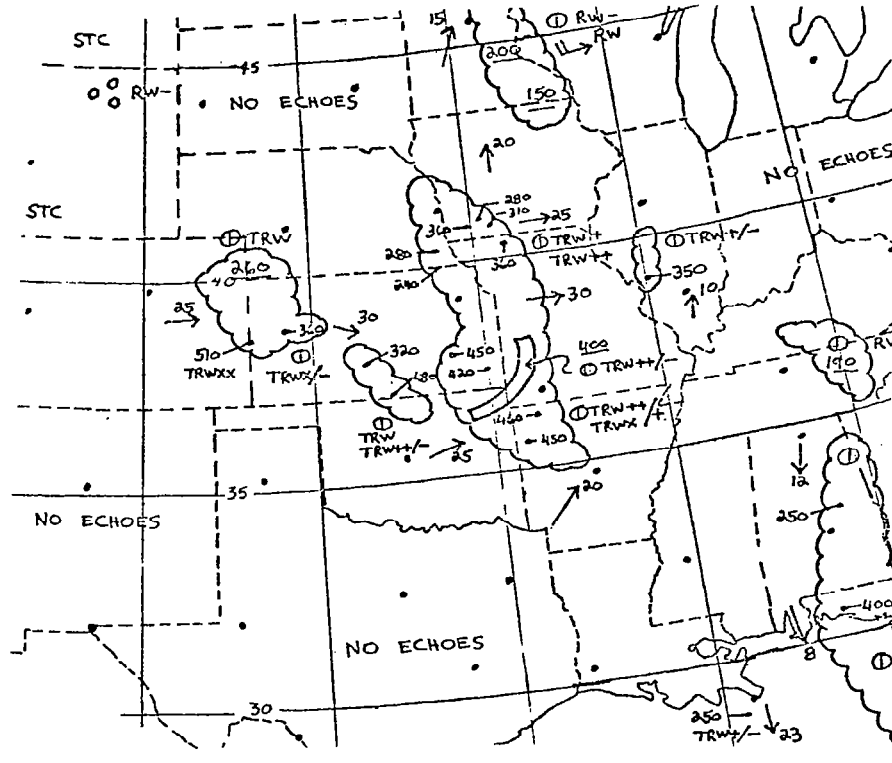

1135 GMT 28 May

Fig. 1.26. (Concluded)

8. KINETIC ENERGY BALANCE DURING AVE 6

The area-averaged kinetic energy budget for the combined eight observation times of AVE 6 is given in Table 1.4. The most striking features are small kinetic energy content and weak generation and transport of energy. The total kinetic energy content of 6.2×10^5 J m^{-2} is much smaller than other cases studied (Table 1.2), and local changes in energy content are negligible. Horizontal flux convergence provides the largest, but still small, source of local energy. Horizontal maps do not reveal major jet streaks in the area that would produce large values of $\vec{V}\cdot k\vec{V}$. Generation by cross-contour flow is the second greatest source to the the total vertical column. Some weak energy destruction occurs above 500 mb. An especially interesting feature is the lack of strong upper-level cross-contour flow; the largest, but still small, values are found in the lower troposphere. Transfer of kinetic energy from grid- to subgrid-scales of motion ($D < 0$) is the dominant energy sink. Finally, vertical transfer of energy is small within the individual sublayers of the total column.

It is useful to relate the time variability of the energy parameters to passage of the short wave through the area. Figure 1.27 is a time series of area-averaged energy parameters integrated from the surface to 100 mb, while Fig. 1.28 is a time-height cross section of the same energy terms. Energy content is greatest near 0000 GMT; largest changes in energy content occur between 400-200 mb. Horizontal flux convergence decreases during the first three observation times, but increases after 1500 GMT. Although the constant pressure maps and cross sections of vorticity show that the trough axis passes through the center of the region during the period, the region of strongest winds remains to the west of the area, producing continuing flux convergence that is a maximum in the upper troposphere. Vertical transport is the weakest process during the period. Except for the period between 1800-0000 GMT, upward transport occurs.

The generation term exhibits a marked change during the experiment. Cross-contour flow is a source of local kinetic energy on the downwind side of the trough, but after the trough line passes the center of the region, destruction kinetic energy is indicated in the area average.

Table 1.4. Area-averaged kinetic energy budget for the combined eight observation times of the AVE 6 period. All units are W m^{-2} except for K which is 10^5 J m^{-2}.

Pressure Layer (mb)	K	$\partial K/\partial t$	$\vec{\nabla}\cdot k\vec{\nabla}$	$\partial \omega k/\partial p$	$-\vec{\nabla}\cdot\vec{\nabla}\phi$	D
200-100	0.8	0.4	-1.1	-0.4	-0.1	-1.0
300-200	1.5	0.6	-1.5	-0.4	0.2	-1.5
400-300	1.2	0.2	-1.2	0.1	-0.2	-0.7
500-400	0.9	0.0	-0.8	0.2	-0.5	-0.1
600-500	0.7	0.0	-0.2	0.1	0.4	-0.5
700-600	0.5	0.0	0.0	0.2	0.5	-0.3
800-700	0.3	-0.1	0.3	0.1	0.6	-0.3
900-800	0.2	-0.2	0.1	0.1	0.8	-0.8
Sfc-900	0.1	-0.1	0.1	0.0	0.5	-0.5
Vertical Total	6.2	0.8	-4.3	0.0	2.2	-5.7

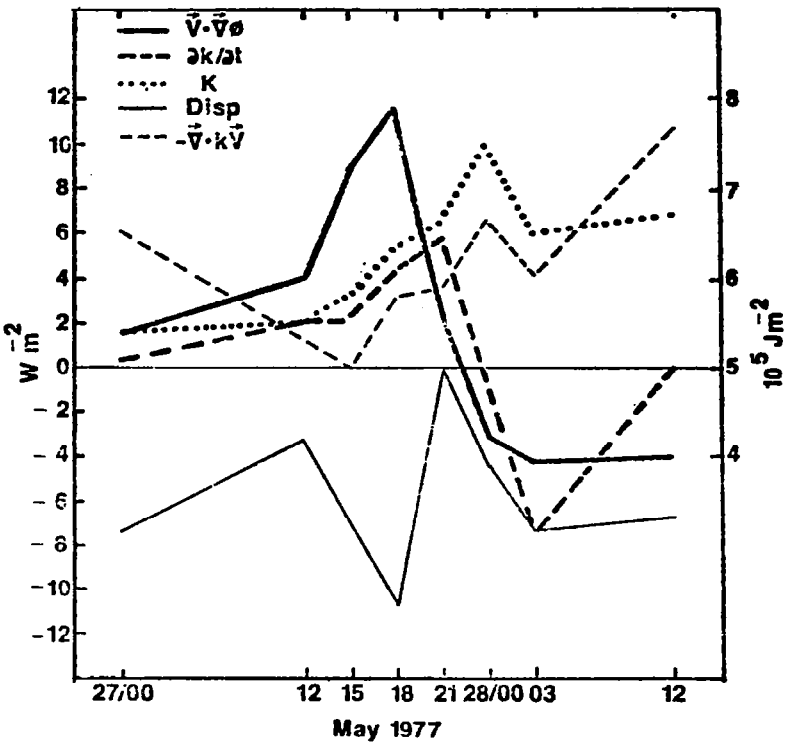

Fig. 1.27. Time series of energy budget terms for AVE 6 integrated between the surface and 100 mb.

The time-height cross section reveals that cross-contour flow is an important process at all levels of the column. In contrast to AVE-SESAME 1 and several other cases of severe storm outbreaks having strong jet intrusion (Table 1.2), supergradient flow and negative generation are not found ahead of the AVE 6 trough. Negative dissipation occurs at all eight observation times, but large fluctuations occur during the first half of the period. Magnitudes of the grid- subgrid-scale energy transfers are similar at all levels, i.e., large transfers are not confined to the upper portions of the atmospheric column.

Although major changes occur in the averages of vorticity and vorticity advection with the passage of the upper-level trough, such well defined variations are not observed in many of the energy parameters. The results suggest that the mere presence or absence of a trough or ridge is not crucial in determining kinetic energy balance. The presence or absence of a strong jet streak appears to be a more important factor.

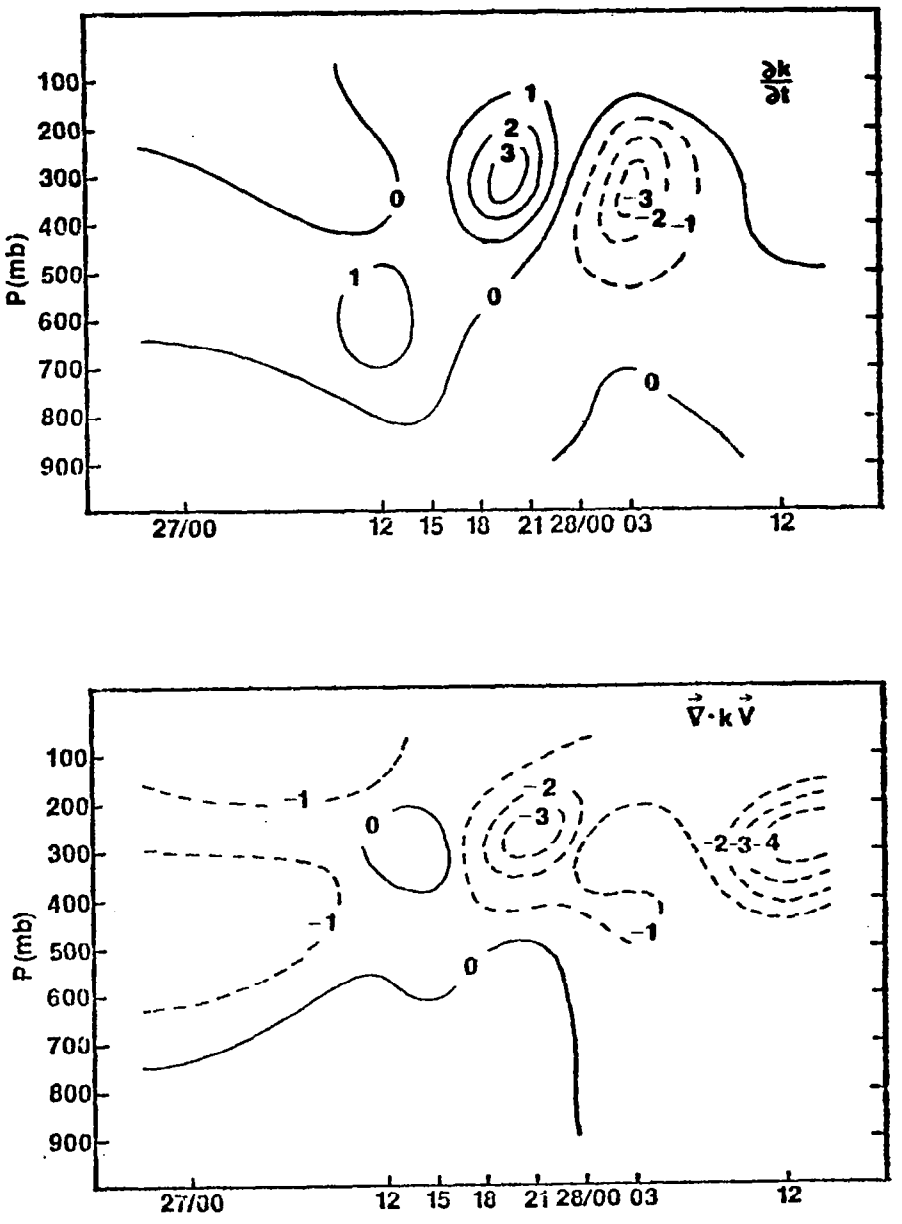

Fig. 1.28. Time-height cross sections of area-averaged energy budget terms for AVE 6. All values are (W m^{-2})/100 mb.

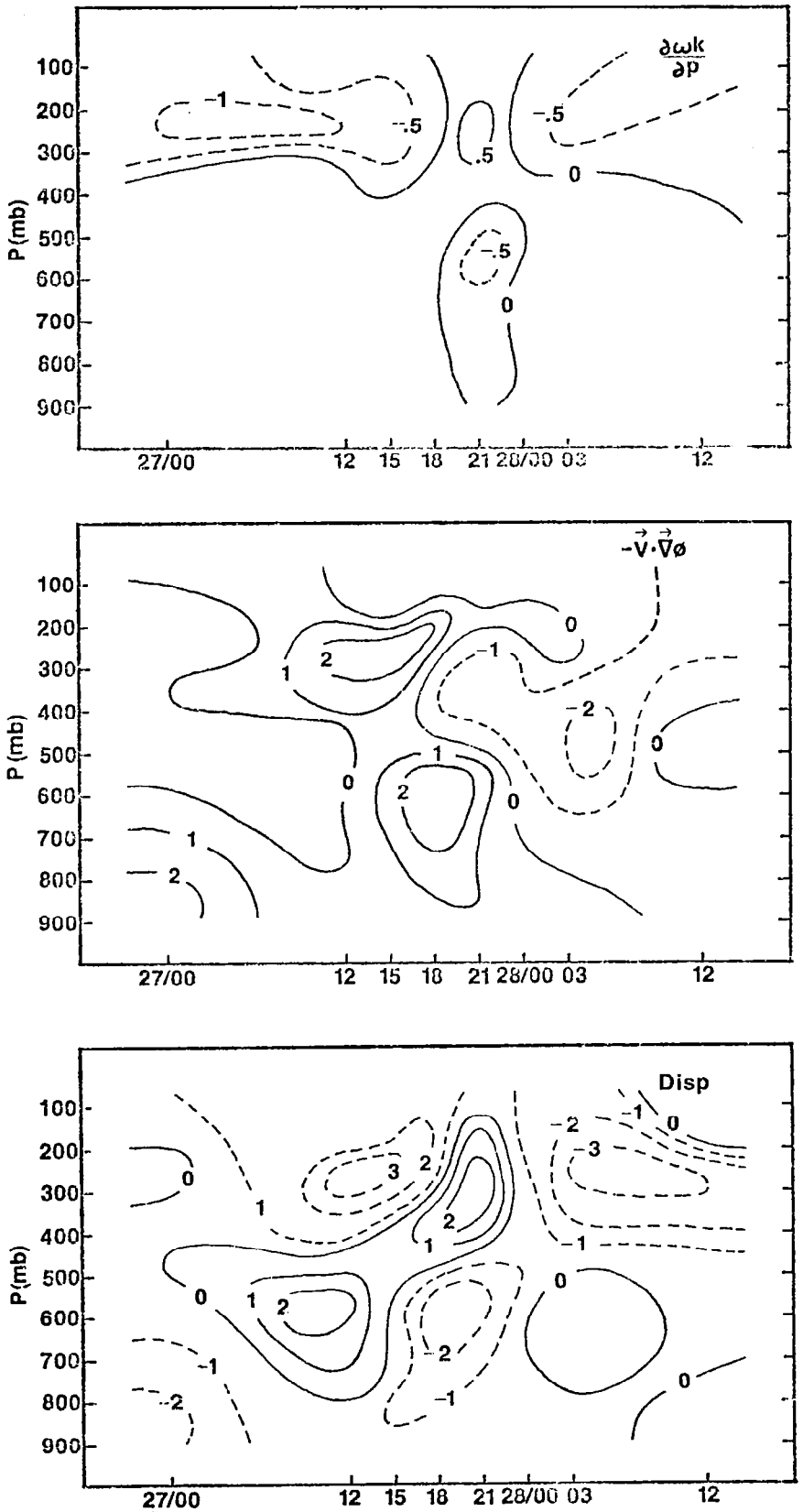

Fig. 1.28. (Concluded)

Table 1.5 gives the energy budget of those grid points having moderate to intense convection (MDR 3-6). When compared to the budget for the entire region (Table 1.4), the storm environment is seen to have larger energy content, stronger positive generation, and stronger negative dissipation. These findings are similar to those of AVE-SESAME 1 which were described earlier. Similarly, more upper-level horizontal and vertical transport are found in the storm environment.

Table 1.5. Kinetic energy budget for those AVE 6 grid points having convection of MDR 3-6 at an observation time. All units are W m^{-2} except for K which is 10^5 J m^{-2}.

Pressure Layer (mb)	K	$\partial K/\partial t$	$\vec{\nabla}\cdot k\vec{V}$	$\partial \omega k/\partial p$	$-\vec{V}\cdot\vec{\nabla}\phi$	D
200-100	0.9	0.0	-0.3	-1.0	1.5	-2.8
300-200	1.9	-0.4	3.5	-1.6	5.1	-3.6
400-300	1.4	-0.9	1.7	0.2	3.6	-2.6
500-400	1.0	-0.7	0.3	0.7	1.4	-1.1
600-500	0.8	-0.2	-0.2	0.6	1.4	-1.2
700-600	0.6	-0.2	-0.1	0.6	1.6	-1.3
800-700	0.4	-0.4	0.4	0.2	1.4	-1.2
900-800	0.3	-0.4	0.1	0.2	1.2	-1.3
Sfc-900	0.1	-0.1	0.0	0.1	0.5	-0.5
Vertical Total	7.4	-3.3	5.4	0.0	17.7	-15.6

9. SUMMARY AND CONCLUSIONS

Kinetic energy budgets have been presented for the AVE-SESAME 1 case, which coincided with the Red River Valley tornado outbreak, and the AVE 6 period which included short wave passage through the region. NWS rawinsonde data were used to describe synoptic-scale conditions during the periods. The energy balance was described in terms of time and area-averaged statistics, horizontal fields of energy parameters for both the lower troposphere and upper atmosphere, and time-height cross sections. In addition, the energetics of the entire region was compared with areas having no precipitation and areas having heavy thunderstorm activity.

Significant findings about AVE-SESAME 1 include:

1) The onset of storm activity is related to short wave passages through the area that are detectable in fields of horizontal divergence and vertical motion.

2) The region experiences significant jet intrusion from the southwest causing horizontal flux convergence to be the major energy source for the region. Positive dissipation is the second greatest source. Supergradient flow in advance of the jet streak produces cross-contour destruction of kinetic energy that is the greatest sink for the area. Significant upward energy transport occurs.

3) Spatial maps of kinetic energy content show the development of a major low-level jet within the region and the advance of an upper-level jet streak into the region. When viewed in terms of energy, the upper-level jet streak appears to contain subsynoptic-scale features embedded within the overall wind maximum. These features are only partially resolvable with the synoptic-scale NWS data.

4) Time-height cross sections reveal an increase of energy content during the period. All energy processes are found to be a maximum near the level of the jet stream. The 3 h data reveal important variations in area-averaged energetics as the jet streak moves into the region, but the area-time averaged budget based on all nine 3 h observations does not differ greatly from that based on the three

standard 12 h observations alone.

5) Spatial maps of energy generation and transport parameters show that the low-level jet has a major influence on lower tropospheric energetics. All energy processes are a maximum near this jet. Cross-contour generation is the major energy source for the jet region. In the upper troposphere, spatial maps reveal horizontal flux convergence and cross-contour destruction of energy ahead of a major jet streak. The smaller-scale features of the upper-level jet have a major influence on local energy generation and transport.

6) By computing and average energy budget for those grid points having convection in the MDR 3-6 category, the storm area is observed to have a different energy budget from that of the area as a whole and from non-precipitation areas. Energy processes are more intense in the storm area where generation rather than destruction, and negative dissipation instead of positive are observed.

7) Although the large areas of storms occurring during the period undoubtedly have a major impact on their synoptic-scale environments, it was not possible to assess the magnitude of this feedback because energy processes related to the jets are so dominant.

8) A new method for computing horizontal flux divergence is proposed. By adjusting values of the velocity divergence component of the flux term in a manner similar to that used for vertical motion, more consistent values, that show better time continuity, are obtained.

Significant findings about AVE 6 include:

1) Kinetic energy content and all energy generation and transport processes are very weak during this period of light winds.

2) The passage of an upper-level trough is clearly evident on constant pressure maps and in fields of vorticity. Its passage also is observed in the time series of the area-averaged generation term. Cross-contour flow provides an energy source when the trough line lies to the west of the center of the area but becomes a sink after passage.

Flux convergence occurs throughout the period because strongest winds are located behind the trough line.

3) The contrasts between storm area energetics and those of the entire region are similar to those found furing AVE-SESAME 1.

10. REFERENCES

Alberty, R.L., D.W. Burgess, C.E. Hane, and J.F. Weaver, 1979: SESAME 1979 Operations Summary. Environmental Research Lab, Boulder, Col., 253 pp.

Aubert, E.J., 1957: On the release of latent heat as a factor in large-scale atmospheric motions. J. Meteor., 14, 527-542.

Barnes, S.L., 1964: A technique for maximizing detail in numerical weather map analysis. J. Appl. Meteor., 3, 396-409.

_____, 1979: SESAME 1979 field processed rawinsonde data from supplementary sites: April 10-June 8. Environmental Research Lab, Boulder, Col., 252 pp.

Chen, T., and L.F, Bosart, 1977: Quasi-Lagrangian kinetic energy budgets of composite cyclone-anticyclone couplets. J. Atmos. Sci., 34, 455-464.

Chien, H., and P.J. Smith, 1973: On the estimate of kinematic parameters in the atmosphere from radiosonde wind data. Mon. Wea. Rev., 101, 252-261.

Danard, M.B., 1964: On the influence of released latent heat on cyclone development. J. Appl. Meteor., 3, 27-37.

_____, 1966: On the contribution of released latent heat to changes in available potential energy. J. Appl. Meteor., 5, 81-84.

Dupuis, L.R., and K. Hill, 1977: Data for NASA's AVE VI experiment: 25-mb sounding data and synoptic charts. NASA TM-78147, Marshall Space Flight Center, Al., 207 pp.

Fankhauser, J.C., 1969: Convective processes resolved by a mesoscale rawinsonde network. J. Appl. Meteor., 8, 778-798.

_____, 1971: Thunderstorm-environment interactions determined from aircraft and radar observations. Mon. Wea. Rev., 99, 171-197.

Fritsch, J. M., and R.A. Maddox, 1980: Analysis of upper tropospheric wind perturbations associated with midlatitude mesoscale convective complexes. Preprints Eighth Conf. on Weather Forecasting and Analysis, Denver, 339-349.

Fuelberg, H.E., 1974: Reduction and error analysis of the AVE II pilot experiment data. NASA CR-120496, George C. Marshall Space Flight Center, Al., 131 pp.

_____, 1979a: Kinetic energy budgets in areas of convection. NASA CR-3166, Marshall Space Flight Center, Al., 103 pp.

Fuelberg, H.E., 1979b: Kinetic energy budgets of storm areas. Preprints Eleventh Conf. on Severe Local Storms, Kansas City, Amer. Meteor. Soc., 7-14.

_____, and J.R. Scoggins, 1977: Relationship between the kinetic energy budget and intensity of convection. Preprints Tenth Conf. on Severe Local Storms, Omaha, Amer. Meteor. Soc., 265-270.

_____, and _____, 1978: Kinetic energy budgets during the life cycle of intense convective activity. Mon. Wea. Rev., 106, 637-653.

_____, and _____, 1980: Kinetic energy budget during strong jet stream activity over the eastern United States. Mon. Wea. Rev., 108, 69-77.

Gerhard, M.L., H.E. Fuelberg, S.F. Williams, and R.E. Turner, 1979: AVE-SESAME 1: 25-mb sounding data. NASA TM-78256, Marshall Space Flight Center, Al., 364 pp.

Hill, K., G.S. Wilson, and R.E. Turner, 1979: NASA's participation in the AVE-SESAME '79 program. Bull. Amer. Meteor. Soc., 60, 1323-1329.

Kornegay, F.C., and D.G. Vincent, 1976: Kinetic energy budget analysis during interaction of tropical storm Candy (1968) with an extratropical frontal system. Mon. Wea. Rev., 104, 849-859.

Kung, E.C., 1966: Kinetic energy generation and dissipation in the large-scale atmospheric circulation. Mon. Wea. Rev., 94, 67-82.

_____, and P.J. Smith, 1974: Problems of large-scale kinetic energy balance--A diagnostic analysis in GARP. Bull. Amer. Meteor. Soc., 55, 768-777.

_____, and T.L. Tsui, 1975: Subsynoptic-scale kinetic energy balance in the storm area. J. Atmos. Sci., 32, 729-740.

Maddox, R.A., 1980: A satellite based study of midlatitude, mesoscale convective complexes. Preprints Eighth Conf. on Weather Forecasting and Analysis, Denver, Amer. Meteor. Soc., 329-338.

_____, D.J. Perkey, and J.M. Fritsch, 1980: The evolution of upper-tropospheric features during the development of a midlatitude, mesoscale convective complex. Preprints Eighth Conf. on Weather Forecasting and Analysis, Denver, Amer. Meteor. Soc., 233-239.

McInnis, D.H., and E.C. Kung, 1972: A study of subsynoptic scale energy transformations. Mon. Wea. Rev., 100, 126-132.

McNulty, R.P., 1978: On upper tropospheric kinematics and severe weather occurrence. Mon. Wea. Rev., 106, 662-672.

Moller, A.R., 1980: Mesoscale surface analysis of the 10 April 1979 tornadoes in Texas and Oklahoma. Preprints Eighth Conf. on Weather Forecasting and Analysis, Denver, Amer. Meteor. Soc., 36-43.

National Weather Service, 1979: Digital radar code users guide. Silver Spring, Md., 26 pp.

Ninomiya, K., 1971a: Dynamical analysis of outflow from tornado-producing thunderstorms as revealed by ATS III pictures. J. Appl. Meteor., 10, 1103-1121.

_____, 1971b: Mesoscale modification of synoptic situations from thunderstorm as revealed by ATS III and aerological data. J. Appl. Meteor., 10, 1103-1121.

NOAA, 1980: Red River Valley tornadoes of April 10, 1979. National Disaster Survey Report 80-1, Rockville, Md., 60 pp.

O'Brien, J.J., 1970: Alternate solution to the classical vertical velocity problem. J. Appl. Meteor., 9, 197-203.

Robertson, F.R., and P.J. Smith, 1980: The kinetic energy budgets of two severe storm producing extratropical cyclones. Mon. Wea. Rev., 108, 127-143.

Sechrist, F.S., and T.M. Whittaker, 1979: Evidence of jet streak vertical circulations. Mon. Wea. Rev., 107, 1014-1021.

Smith, P.J., 1969: On the contribution of a limited region to the global energy budget. Tellus, 21, 202-207.

_____, 1970: A note on energy conversions in open atmospheric systems. J. Atmos. Sci., 27, 518-521.

_____, 1980: The energetics of extratropical cyclones. Rev. Geophys. Space Phys., 18, in press.

_____, and S.P. Adhikary, 1974: The dissipation of kinetic energy in large-scale atmospheric circulations. Rev. Geophys. Space Phys., 12, 281-284.

Tsui, T.L., and E.C. Kung, 1977: Subsynoptic-scale energy transformations in various severe storm situations. J. Atmos. Sci., 34, 98-110.

Vincent, D.G., and L.N. Chang, 1975: Kinetic energy budgets of moving systems: Case studies for an extra-tropical cyclone and hurricane Celia, 1970. Tellus, 27, 215-233.

_____, and T.W. Schlatter, 1979: Evidence of deep convection as a source of synoptic-scale kinetic energy. Tellus, 31, 493-504.

Uccellini, L.W., 1979: The role of upper tropospheric jet streaks and lee side cyclogenesis in the development of low level jets in the Great Plains. Preprints Eleventh Conf. on Severe Local Storms, Kansas City, Amer. Meteor. Soc., 96-103.

Uccellini, L.W., and D.R. Johnson, 1979: The coupling of upper and lower tropospheric jet streaks and implications for the development of severe convective storms. Mon. Wea. Rev., 107, 682-703.

Ward, J.H., and P.J. Smith, 1976: A kinetic energy budget over North America during a period of short synoptic wave development. Mon. Wea. Rev., 104, 836-848.

Williams, K.T., 1970: A statistical analysis of satellite-observed trade wind cloud clusters in the western north Pacific. Atmos. Science Paper No. 161, Colorado State University, Fort Collins, 80 pp.

Wilson, G.S., 1976: Large-scale vertical motion calculations in the AVE IV experiment. Geophys. Res. Lett., 3, 735-740.

CHAPTER II

AN ERROR ANALYSIS OF BASIC KINEMATIC QUANTITIES

by

Emil M. Berecek *

and

Henry E. Fuelberg
Department of Earth and Atmospheric Sciences
Saint Louis University
Saint Louis, Missouri 63103

ABSTRACT

The sensitivity of relative vorticity, advection of vorticity and temperature, horizontal divergence, and kinematic vertical motion to random errors in rawinsonde wind data is described. The study was performed during NASA's third Atmospheric Variability Experiment when a strong jet stream dominated the region. Values for each kinematic parameter were computed by standard finite-differencing techniques using the original data. Normally distributed random errors then were introduced into each original sounding so that ten differently altered data sets were produced. The kinematic parameters were recomputed using the altered data and results were compared to those from the original data at 850, 700, 500, and 200 mb. Subjective pattern comparisons and statistical methods were used. The statistical analyses were performed over the entire computational area and over two subareas chosen for their synoptic positions.

---

* Present affiliation: Captain, U.S. Air Force, Environmental Technical Applications Center, Scott AFB, IL 62225.

Results indicate that relative vorticity and temperature advection were the least sensitive parameters to the induced errors, while advection of vorticity was the most sensitive term. Maximum errors between the original and perturbed values of vorticity advection at the 200 mb level were as much as twice the total range of values of the original field. The perturbed patterns for this parameter showed major departures from the original field in the upper levels. Divergence was found to be the second most sensitive parameter. Although vertical motion was somewhat less sensitive to wind errors, the deviations were significant in the upper levels. The statistical comparison indicates that most of the kinematic parameters were more sensitive to data errors downstream of the upper level trough where the strongest winds were observed.

When the sensitivities of the parameters in this study were compared with those from a study using error propagation equations, the latter were found to be larger, suggesting the effectiveness of objective analysis and smoothing techniques in reducing the effects of input errors on derived parameters.

Although this study considered the effects of random errors in raw-insonde data, it has implications for satellite-derived data as well. The effects of errors in satellite-derived temperature, humidity, winds, and heights on derived parameters should be investigated to assess their usefulness in meteorological analysis.

Chapter II

AN ERROR ANALYSIS OF BASIC KINEMATIC QUANTITIES

1. INTRODUCTION

In meteorological studies researchers often have the option of using real or modeled data. Modeled data are generally easier to employ, while actual data usually give more realistic results since fewer "idealisms" are involved. Inherent disadvantages of observed data, in addition to the ever present problem of insufficient coverage, are systematic and random errors which influence derived computational results (Kurihara, 1961).

Computational procedures, such as smoothing for example, serve to lessen the effects of input data errors without materially affecting the validity of the finalized product. Since these schemes do not entirely remove the effects of input data errors, it is important to ascertain their influence on the final results of a research study.

Two methods are commonly used for assessing the effects of input errors on various computations involving real data.

1) Error propagation techniques use assumed errors of the input data to compute the induced errors in the terms being evaluated. This procedure has been used by Dupuis and Scoggins (1979) and Endlich and Clark (1963) to describe error magnitudes in terms such as divergence and vorticity. Similarly, Chen and Bosart (1977) used this technique to assess errors in terms of the kinetic energy budget equation.

2) Random error techniques involve the deliberate introduction of random errors into the original input data and the recomputation of values based upon this new data set for comparison with those based upon the original "uncontaminated" data. This procedure has been used frequently in kinetic energy studies such as those by Vincent and Chang (1975), Ward and Smith (1976), and Fuelberg and Scoggins (1980).

The random error method is used in this study because it allows the effects of objective data analysis and smoothing schemes to be included in the error assessment. The first method generally does not consider the effects of such procedures even though they should reduce the impact of data errors on the final results.

This paper describes the computational procedures used to obtain spatial fields of relative vorticity, advection of vorticity and temperature, horizontal divergence, and vertical motion. It investigates the effectiveness of these procedures to reduce the effects of deliberately introduced random errors, and, as a result, the study assesses the confidence which one can place on values of the derived parameters.

a. Data

Input data for this study are from the third Atmospheric Variability Experiment (AVE III) conducted on 6-7 February 1975, and sponsored by the National Aeronautics and Space Administration. Locations of the forty-one rawinsonde stations that participated in AVE III are shown in Fig. 2.1. The 2100 GMT data for 6 February were selected for this study because it was the time of strongest winds and therefore the time when the largest errors in wind data might be expected.

Data reduction procedures used to process the AVE III data were designed to obtain the highest possible accuracy and are described by Fuelberg (1974). The AVE III data at 25 mb intervals were provided by Fuelberg and Turner (1975).

b. Synoptic situation

Synoptic conditions at 2100 GMT 6 February are shown in Fig. 2.2. A weak frontal zone across central Florida separated tropical air from polar air. A secondary arctic front extended from Maine southwestward along the Appalachians to the southeast tip of Louisiana. Surface waves associated with this front were located over Maine and western Virginia. A broad trough centered along the Mississippi River Valley dominated upper air flow over the eastern United States. The jet stream with wind speeds as great as 80 m s^{-1} extended from Texas northeastward to the Virginia coast.

c. Analytical procedures

The data were converted from randomly spaced sounding locations to an equally spaced 18 x 18 grid system with a grid spacing of 159 km by using the objective analysis scheme described by Barnes (1964). Barnes' procedure is commonly referred to as successive corrections to a first guess field. A scan radius of three grid distances was used while four iterations were allowed in order to obtain as much detail as possible from the data without introducing noise into the fields. A mild filter described by Shuman (1957) with a smoothing index of 0.2 was applied to the gridded data fields to reduce the effects of input data errors.

Gridded analyses of the input data were produced at the surface and at 50 mb intervals from 900 mb to 100 mb for a total of 18 levels. Input wind data were averaged over 50 mb layers to further reduce the

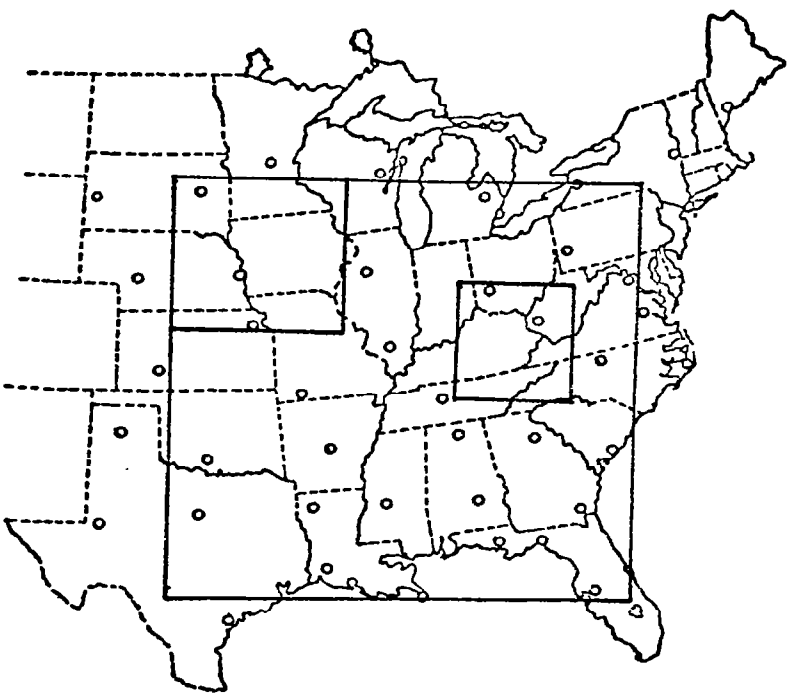

Fig. 2.1. Rawinsonde stations participating in the AVE III Experiment. The three areas in which statistical analyses were performed are indicated by boxes.

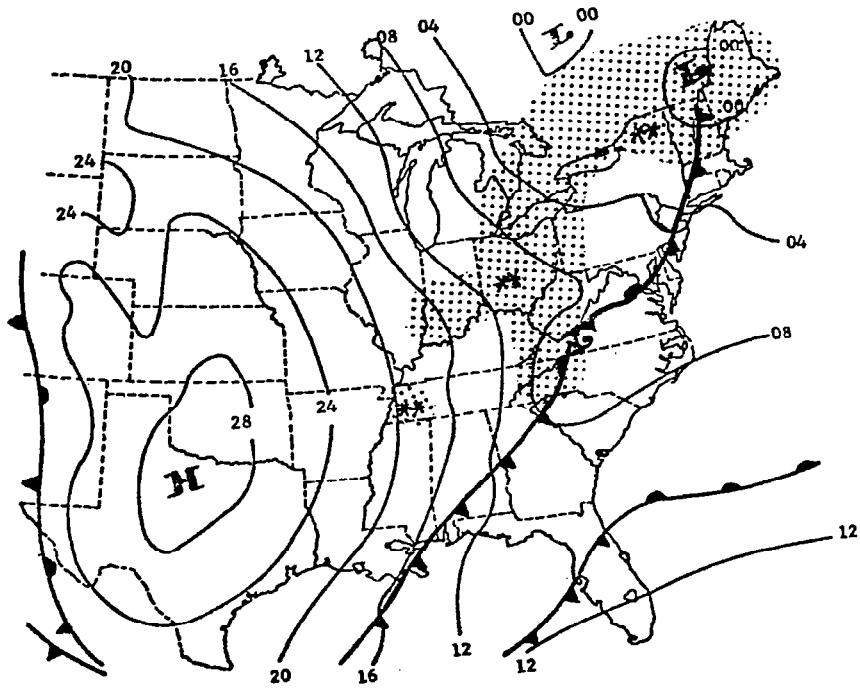

Fig. 2.2. Synoptic conditions at 2100 GMT 6 February 1975 (Fuelberg and Turner, 1975).

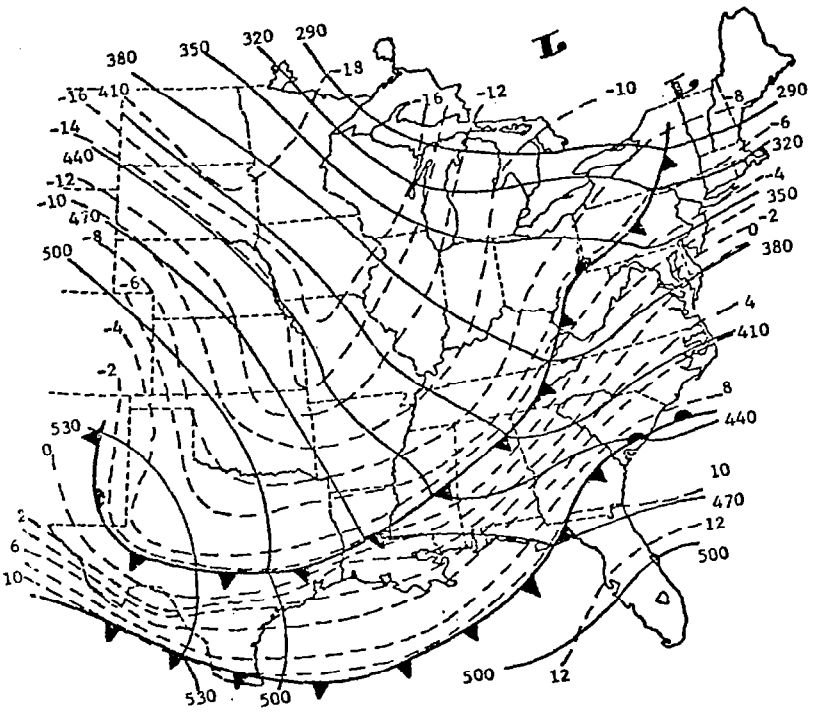

850 mb

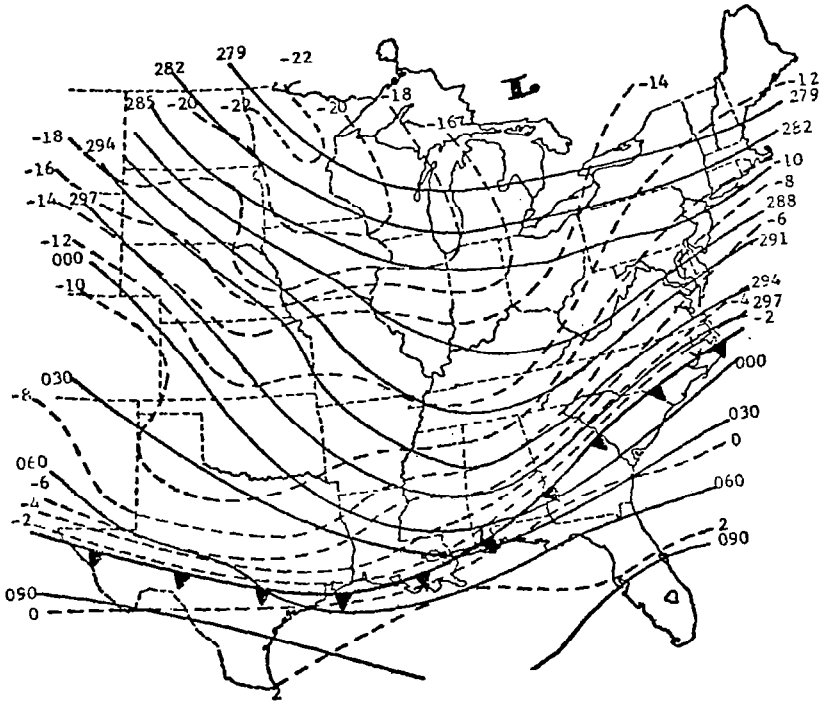

700 mb

Fig. 2.2. (Continued)

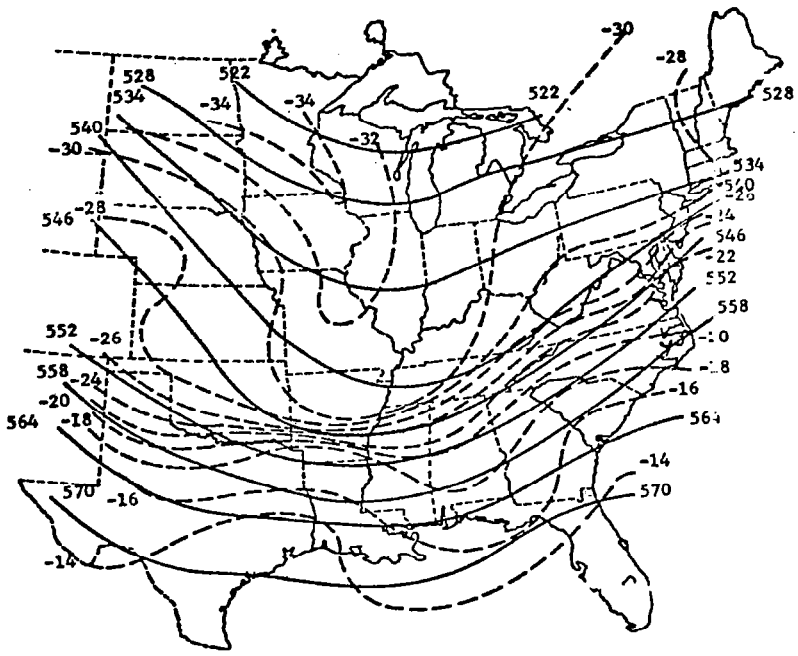

500 mb

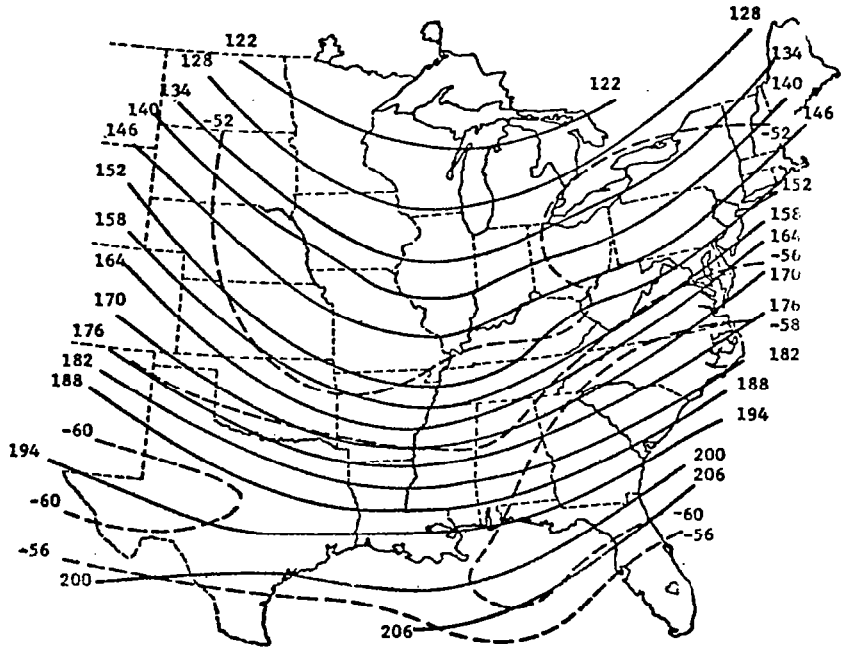

200 mb

Fig. 2.2. (Concluded)

effects of random errors.

Centered finite differences were used for computing all space derivatives needed for vorticity, divergence, and the advective terms. Vertical motion (ω) estimates were obtained by the kinematic method with surface values assumed to be zero. The vertical motion profiles were then adjusted using the technique described by O'Brien (1970) in order to reduce the cumulative bias errors associated with the kinematic method. Values of ω were adjusted so the vertical profiles approached zero at 100 mb, which is similar to the procedure used by Chien and Smith (1973) and Vincent et al. (1976). Fields of the various kinematic quantities were not smoothed after computation; only the input data were smoothed.

Calculations based upon the original rawinsonde data prior to the deliberate introduction of random errors constituted the standard for the purposes of this study.

d. Error simulation

Computer-generated random perturbations with normal distributions about zero and standard deviations varying as a function of pressure (Table 2.1) then were introduced into the sounding data. These values are similar to those proposed by Kurihara (1961) and used by Dupuis and Scoggins (1978) and Robertson and Smith (1980). Ten runs, each based upon a different set of random perturbations at the individual 25 mb levels were made. These perturbed soundings were subjected to the same horizontal and vertical smoothing and objective analysis techniques as the original data. The aforementioned kinematic parameters then were recomputed using these perturbed fields and compared to the original values.

Systematic data errors and truncation errors due to computational procedures were not considered in this study.

e. Comparison techniques

Computed fields derived from the original data were compared to those from each of the ten sets of altered data using two methods: a qualitative pattern comparison and a statistical analysis.

1) Qualitative pattern comparison. Spatial fields for each parameter, at the levels of 850, 700, 500, and 200 mb were hand analyzed and subjectively compared. A disadvantage to this technique is that unless the differences in the patterns are sufficiently sharp it is difficult to assess the overall goodness of the comparison

Table 2.1. Standard deviations of normally distributed perturbations.

Pressure Level (mb)	Wind Direction (deg)	Wind Speed $m\ s^{-1}$	Height (m)
100	15.0	5.6	45.5
200	12.7	5.1	37.5
300	10.6	4.5	28.0
500	6.2	3.4	15.0
700	4.0	2.2	10.7
900	2.0	1.1	6.0

between the deliberately contaminated field and the original field.

2) Statistical analysis. In an attempt to quantify the comparison process, the kinematic field obtained from the unaltered data was statistically compared to each of the ten fields derived from perturbed data. The region so studied is the large box depicted in Fig. 2.1 having an area of 4.9×10^6 km^2. Six statistical quantities were calculated for each pair of original and perturbed fields. In the shorthand terminology that follows, the word "error" refers to the difference between grid point values obtained from the original and perturbed data sets.

- The average magnitude of the particular parameter over the entire field (Field Average),
- The standard deviation of the error values (Standard Deviation),
- The average of the absolute error values (Mean Absolute Difference),
- The maximum error over the entire area (Maximum Deviation),
- A linear correlation coefficient between grid points of the two fields (see Panofsky and Brier, 1964), and
- The range of values over the entire area or a particular subarea (Typical Range).

3. RESULTS

a. Relative vorticity

Results of the statistical comparison for relative vorticity are given in Table 2.2 for the levels of 850, 700, 500, and 200 mb. The table indicates that field averages of vorticity increase with height for each of the eleven data sets and that average values for the original and the ten perturbed fields are quite similar at each level. Values of standard deviation, mean absolute difference, and maximum deviation likewise increase with height with the values at 200 mb being two to three times greater than those at 500 mb. This is expected since assumed wind errors increase with height (Table 2.1). At all levels, magnitudes of the mean absolute difference and the standard deviation of the errors are considerably smaller than the field average of the original values. Although the maximum deviation approaches the field average above 700 mb, it is still much smaller than the total range of values. Values of the correlation coefficient are quite high at all levels ranging from 0.97 or higher below 500 mb to not less than 0.81 at 200 mb.

Since vorticity at the 500 mb level is widely used in synoptic studies, the pattern discussion to follow will be restricted to that level. Figure 2.3a shows that the original unaltered data field for 500 mb produced a broad area of positive relative vorticity across the southeastern United States associated with the upper air trough. Relatively weak areas of negative vorticity occur over Ohio, west Texas and southern Florida. Each of the perturbed fields exhibits this same general pattern. Figure 2.3b shows the vorticity field for Run 8 which exhibited the lowest correlation with the original. It can be seen that even the most altered pattern demonstrates very good agreement with the original field. Even at the 200 mb level (not shown), where the random wind errors are the largest, no major differences are found in the resultant vorticity fields.

In summary, vorticity calculations based upon the original and perturbed data for this study are quite consistent. Qualitatively, no major differences in the patterns are discernable, and the statistical analyses reveal that overall, the grid point values are not significantly affected by the introduction of reasonable random errors.

Table 2.2. Statistical data of relative vorticity (10^{-6} s^{-1}) for the original and ten perturbed fields.

Run	Field Avg	Std Dev	Mean Abs Dif	Max Dev	Cor Coef
Level: 850 mb Avg of Original Field: 7.8 Range of Values: -38.5 to 35.1					
1	7.7	2.5	2.0	6.6	.98
2	8.3	2.2	1.8	6.2	.99
3	8.0	2.6	2.0	7.4	.98
4	8.2	2.5	2.0	6.5	.98
5	8.1	2.7	2.1	9.2	.98
6	8.1	2.4	2.0	6.5	.99
7	8.0	2.7	2.1	8.1	.98
8	7.9	3.0	2.4	8.2	.98
9	7.6	2.4	1.7	6.9	.99
10	7.5	2.2	1.8	6.7	.99
Level: 700 mb Avg of Original Field: 16.8 Range of Values: -28.4 to 81.6					
1	17.2	4.3	3.4	13.7	.98
2	17.5	4.5	3.6	12.3	.98
3	17.7	4.3	3.5	13.1	.98
4	17.2	4.2	3.5	11.8	.98
5	17.3	3.7	3.0	9.4	.99
6	17.3	4.4	3.6	12.5	.98
7	17.6	4.3	3.3	17.6	.98
8	16.7	3.6	2.7	10.5	.99
9	16.8	4.0	3.2	12.0	.98
10	16.5	4.4	3.4	11.5	.98
Level: 500 mb Avg of Original Field: 24.2 Range of Values: -49.7 to 154.8					
1	25.5	6.7	5.1	21.3	.99
2	24.0	6.8	5.4	19.6	.99
3	23.4	8.1	6.8	19.3	.98
4	23.8	7.4	5.8	21.0	.99
5	24.3	8.8	6.7	28.8	.98
6	22.9	8.4	6.6	29.7	.98
7	24.5	9.4	8.0	21.7	.98
8	24.6	9.2	7.4	26.6	.97
9	23.5	8.3	6.7	24.0	.98
10	23.4	8.7	7.1	19.5	.98
Level: 200 mb Avg of Original Field: 36.4 Range of Values: -33.5 to 119.2					
1	37.2	14.2	11.5	27.9	.91
2	36.5	17.7	13.6	46.7	.85
3	37.2	17.3	13.3	58.3	.86
4	38.2	19.3	14.4	64.6	.81
5	38.1	14.2	10.6	40.9	.92
6	34.9	15.5	12.1	43.3	.90
7	32.3	13.2	10.9	45.6	.93
8	35.2	15.2	11.8	46.3	.92
9	36.1	16.0	12.5	53.4	.90
10	38.4	13.4	10.4	38.4	.92

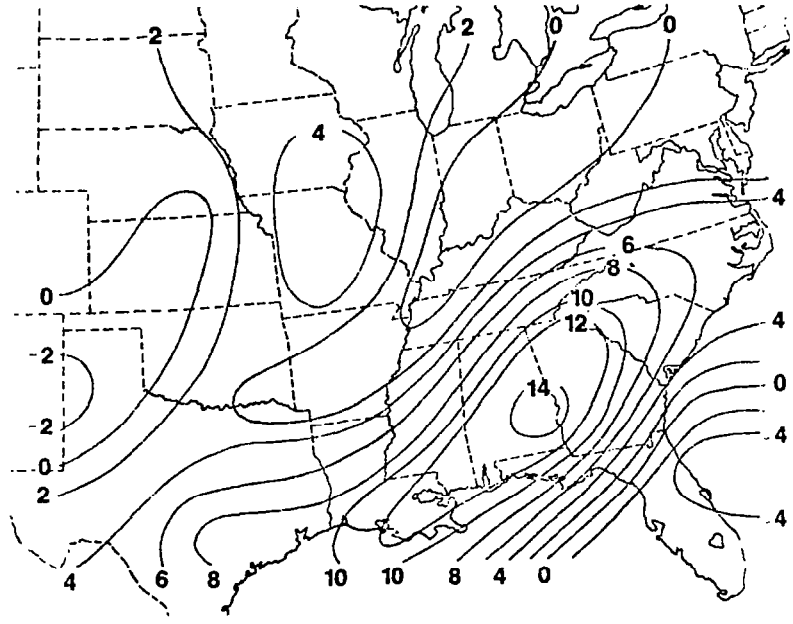

(a) Unaltered

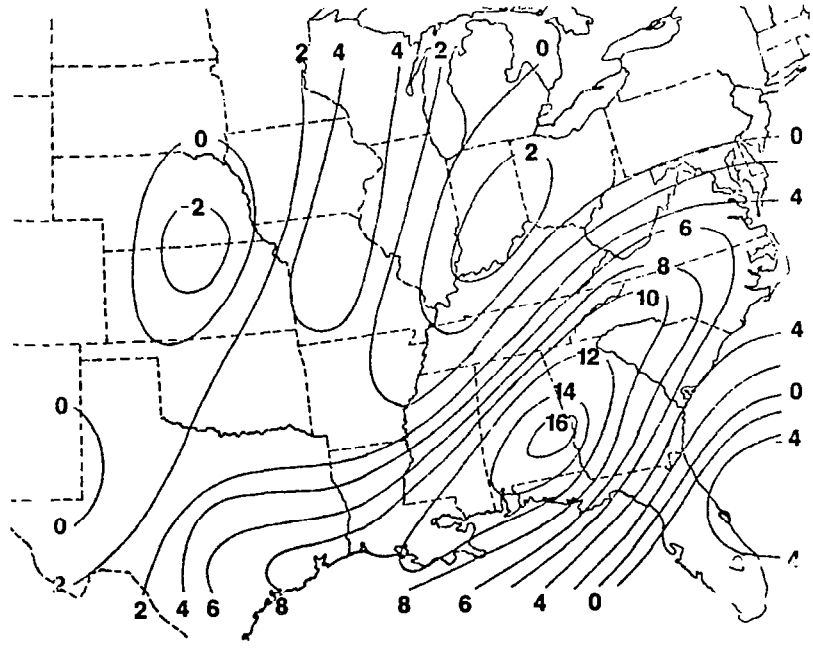

(b) Most Perturbed

Fig. 2.3. Spatial fields of relative vorticity (10^{-5} s^{-1}) at 500 mb. Part A was derived from the unaltered data while part B represents the most perturbed field.

b. Vorticity advection

Table 2.3 shows that the field averages of vorticity advection are quite variable above 700 mb with sign changes occurring between the original and some of the perturbed fields. The field averages are near zero at all levels since the vorticity maximum in Fig. 2.3 is nearly centered over the area of study. Hence, one-half the area exhibits PVA, while the other half exhibits NVA of near equal magnitudes. Standard deviations, mean absolute differences, and maximum deviations all increase with height, with the values at 200 mb being two to three times larger than those at 500 mb. Understandably, magnitudes of the mean absolute differences and maximum deviations are much larger than the field averages for this variable since the latter are near zero, but maximum deviations of some of the perturbed fields at 200 mb are greater than the typical range of values of the original field. Typically, however, values of maximum deviation at 200 mb are about three-fourths of the total range. This fraction is far greater than that of any of the other parameters studied. At 500 mb and below, maximum deviations are less than one-half the values of the typical range. Correlation coefficients at 700 mb and below are high (>0.95). At 500 mb they range from 0.87 to 0.93, while at 200 mb they are much lower, ranging between 0.16 to 0.82. The fact that values of vorticity advection are more sensitive to the input data perturbations than are values of vorticity alone is not surprising since the wind values are used an additional time and since the gradient of the perturbed vorticity is needed for the advection term. The advection computation thereby enhances the amplitudes of the random error perturbations disguised as short wave phenomena. Thus, patterns of the perturbed fields of vorticity advection are similar to the original fields at 850 mb and 700 mb (not shown) where the amplitudes are small. Since the random errors were allowed to increase with height, the qualitative agreement becomes progressively worse with height.

Although advection of vorticity at 500 mb is commonly used in synoptic applications, it is more informative for this discussion to view the maps at 200 mb since the poorest agreements are found at this level (Table 2.3). In the original 200 mb field (Fig.2.4a), a center of PVA is located along the Appalachians, with areas of NVA occurring over Florida and the Arkansas-Louisiana border. Figure 2.4b, which is the most altered field (Run 4, a correlation coefficient of

Table 2.3. Statistical data of vorticity advection (10^{-10} s^{-2}) for the original and ten perturbed fields.

Run	Field Avg	Std Dev	Mean Abs Dif	Max Dev	Cor Coef
Level: 850 mb Avg of Original Field: -.52 Range of Values: -13.9 to 9.4					
1	-.6	1.2	1.0	8.5	.98
2	-.5	1.1	.9	3.7	.98
3	-.4	1.1	.8	3.3	.98
4	-.6	1.1	.9	2.7	.98
5	-.4	1.5	1.2	4.6	.96
6	-.5	1.2	.9	3.4	.98
7	-.6	1.2	1.0	3.9	.97
8	-.3	1.5	1.1	4.4	.97
9	-.4	1.0	.8	3.1	.98
10	-.5	1.0	.8	2.8	.98
Level: 700 mb Avg of Original Field: -.02 Range of Values: -30.8 to 35.4					
1	.4	3.1	2.4	8.7	.97
2	.1	3.6	2.7	12.0	.96
3	.1	2.4	1.9	6.6	.98
4	-.6	3.1	2.3	12.6	.97
5	.1	3.4	2.5	11.2	.96
6	.0	3.1	2.6	8.9	.97
7	.4	3.3	2.4	11.1	.97
8	.4	2.7	2.1	9.6	.97
9	-.0	3.5	2.5	11.8	.97
10	.2	3.5	2.7	10.8	.96
Level: 500 mb Avg of Original Field: -.25 Range of Values: -63.8 to 59.3					
1	.3	10.3	6.8	44.6	.93
2	.7	10.1	7.2	29.2	.93
3	-2.0	10.5	8.8	23.2	.92
4	.2	10.5	7.4	35.6	.92
5	-1.5	13.7	9.7	49.9	.87
6	1.2	13.1	8.8	58.9	.89
7	-.6	13.5	9.8	38.7	.89
8	.6	13.1	9.6	50.4	.91
9	-.0	11.1	8.0	38.5	.92
10	.0	10.5	7.6	36.7	.92
Level: 200 mb Avg of Original Field: -.74 Range of Values: -78.3 to 45.2					
1	-1.0	26.6	19.3	104.0	.73
2	-.9	32.0	24.2	91.1	.51
3	.9	25.9	17.5	96.7	.74
4	1.0	43.3	28.5	205.0	.16
5	-2.7	30.2	21.4	132.0	.68
6	-.3	28.5	19.9	101.0	.62
7	1.0	26.9	19.8	90.3	.67
8	-1.0	24.9	18.4	85.4	.80
9	3.0	37.2	25.2	123.0	.38
10	-.1	25.3	19.1	70.8	.82

(a) Unaltered

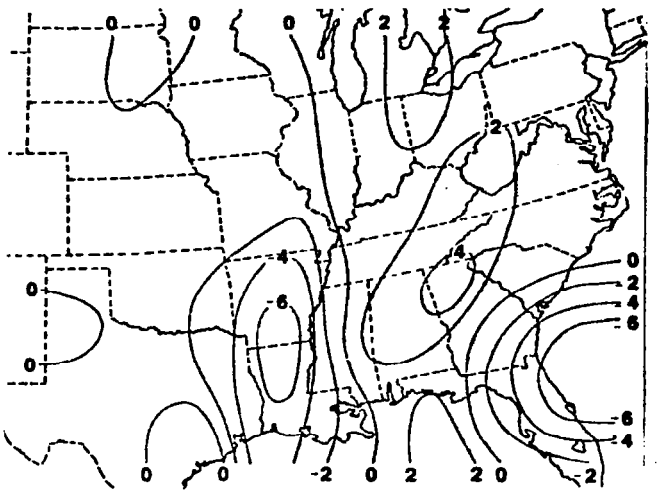

(b) Most Perturbed

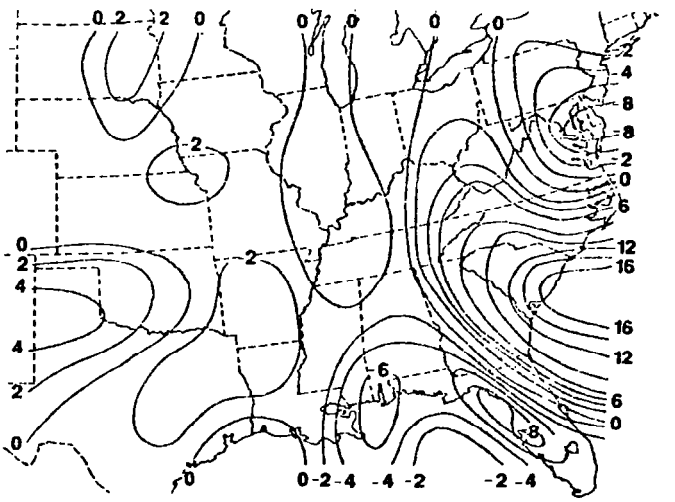

(c) Typically Perturbed

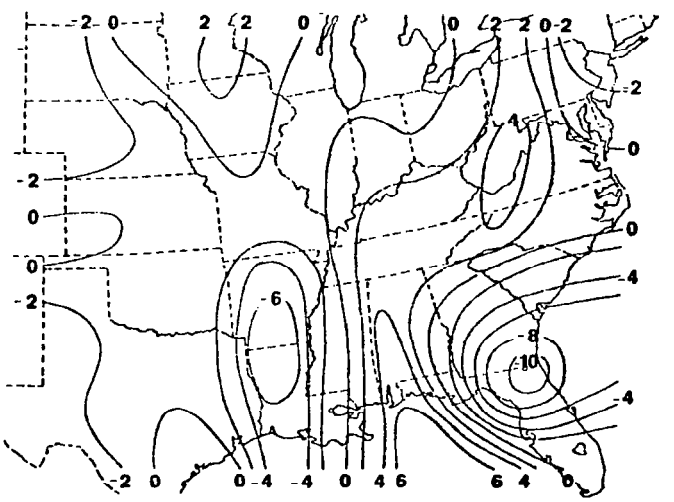

Fig. 2.4. Spatial fields of vorticity advection (10^{-9} s^{-2}) at 200 mb. Part A was derived from the unaltered data, part B represents the most perturbed field, while part C represents a more typical perturbed pattern.

0.16), is a complete distortion of the original pattern. The most pronounced differences are found along the Eastern Seaboard where a large positive maximum forms off South Carolina and where a strong NVA center forms over the Delaware Peninsula. Shifts of vorticity advection patterns such as this would adversely affect forecasting procedures. Figure 2.4c shows the field for Run 3 (a correlation coefficient of 0.74) which displayed a better comparison with the original pattern. Although significant deviations of central values occur, the perturbed pattern is still in general agreement with the original field. Qualitatively, the fields with correlation coefficients above 0.70 seem to represent a reasonable pattern agreement.

c. Temperature advection

Since the RMS error of rawinsonde-derived temperature data is estimated to be 0.2^{o} C (Lenhard, 1973), the maximum random error in the horizontal temperature gradient that could result is very small. Hence, random errors were not added to the original temperature data. Temperature advection "errors" for each of the ten runs of this study arise solely due to introduced random errors in the winds.

Table 2.4 shows that the field averages of temperature advection are very similar with no changes in sign at any level between those based on the original and perturbed data. The standard deviations and the mean absolute differences increase with height but are very small when compared to the typical range of values calculated from the original data. Maximum deviations are much smaller than the typical range of values at all levels, which further indicates the insensitivity of this parameter to random errors in wind data. Correlation coefficients are near 0.99 in most cases, with the lowest values being 0.96 at 200 mb.

The patterns at all levels show excellent consistency between the original and perturbed fields. Qualitatively, all matched well, even at the 200 mb level where the wind errors are greatest. Figure 2.5a is the original field at 500 mb, while Fig. 2.5b shows the field for Run 6. Not only does the general pattern match closely, but there is little change in central values as well.

Temperature advection is the least sensitive parameter to random errors which we have examined. If random errors had been applied to the temperature field, a somewhat poorer agreement might be expected, but such results would probably not depart significantly from those obtained in this study.

Table 2.4. Statistical data of temperature advection (10^{-5} deg s^{-1}) for the original and ten perturbed fields.

Run	Field Avg	Std Dev	Mean Abs Dif	Max Dev	Cor Coe
Level: 850 mb Avg of Original Field: 11.5 Range of Values: -8.1 to 47.9					
1	11.7	.8	.6	2.7	.99
2	11.4	.6	.5	1.5	.99
3	11.2	.8	.6	2.6	.99
4	11.6	.8	.6	2.3	.99
5	11.3	.9	.6	2.6	.99
6	11.6	.8	.6	2.4	.99
7	11.6	.8	.6	2.8	.99
8	11.4	.9	.6	3.4	.99
9	11.6	.6	.5	2.3	.99
10	11.4	.9	.6	4.0	.99
Level: 700 mb Avg of Original Field: 13.6 Range of Values: -16.5 to 57.2					
1	13.8	1.1	.8	3.1	.99
2	13.5	1.3	1.0	4.2	.99
3	13.8	1.0	.7	3.3	.99
4	13.6	1.1	.8	3.8	.99
5	13.5	1.0	.7	3.8	.99
6	13.7	1.1	.8	2.8	.99
7	13.8	1.4	1.0	4.2	.99
8	13.7	1.1	.7	3.7	.99
9	13.3	1.1	.9	3.4	.99
10	13.7	1.1	.8	3.8	.99
Level: 500 mb Avg of Original Field: 21.7 Range of Values: -17.4 to 187.1					
1	22.1	1.8	1.2	7.4	.99
2	22.3	2.5	1.5	12.4	.99
3	20.5	3.6	2.2	17.5	.99
4	21.7	2.4	1.4	12.4	.99
5	21.6	3.2	1.8	13.4	.99
6	22.2	3.2	1.6	18.7	.99
7	22.0	2.4	1.4	8.9	.99
8	21.4	2.6	1.5	14.0	.99
9	22.5	3.4	1.8	19.0	.99
10	22.0	2.4	1.6	7.9	.99
Level: 200 mb Avg of Original Field: -4.9 Range of Values: -97.7 to 56.5					
1	-6.7	6.8	3.6	34.4	.97
2	-7.5	7.1	3.9	34.0	.97
3	-5.7	5.6	3.3	27.0	.98
4	-6.9	6.9	4.0	28.5	.97
5	-5.9	5.3	3.0	23.4	.98
6	-3.1	5.4	3.3	27.9	.98
7	-7.4	7.4	3.6	39.8	.96
8	-5.4	5.2	3.2	18.7	.98
9	-6.1	4.8	3.3	16.1	.99
10	-5.2	3.4	2.1	15.8	.99

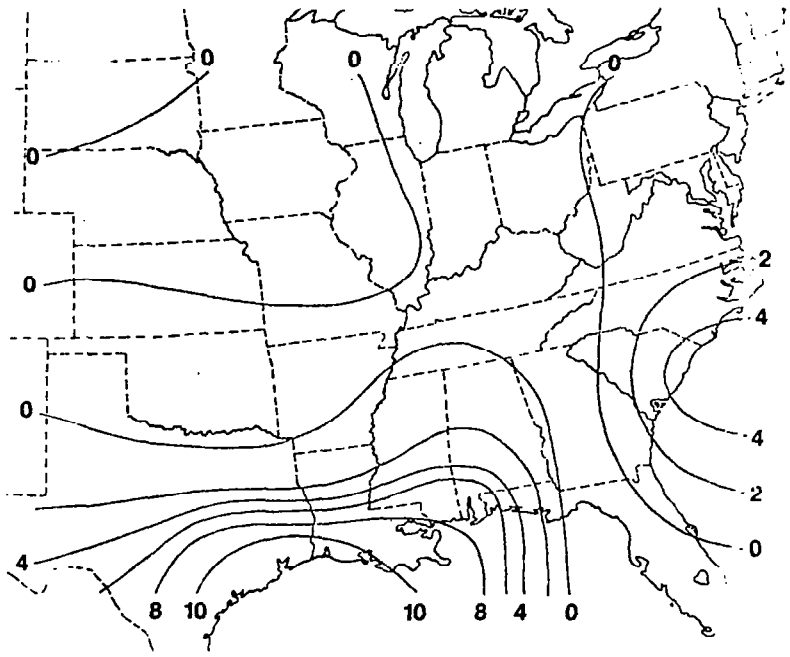

(a) Unaltered

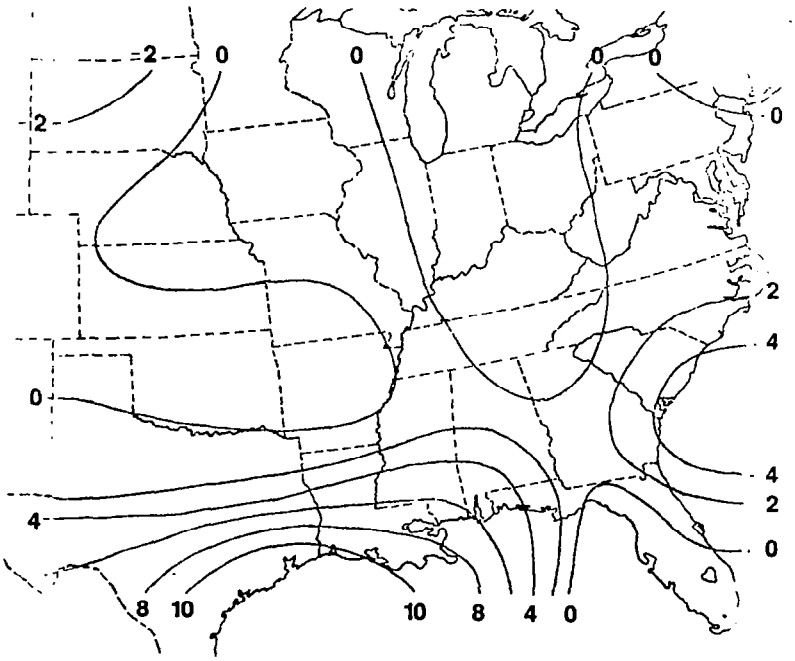

(b) Most Perturbed

Fig. 2.5. Spatial fields of temperature advection (10^{-5} deg s^{-1}) at 500 mb. Part A was derived from the unaltered data while part B represents the most perturbed field.

d. Horizontal divergence

Table 2.5 reveals that the standard deviations, mean absolute differences, and maximum deviations of horizontal divergence increase with elevation in a manner similar to that of the previously described parameters (Tables 2.2-2.4). Field averages based on original data are very small at all levels, due partially to the centered location of the upper air trough whereby near equal amounts of divergence and convergence are distributed over the area as a whole. Field averages based on the ten perturbed data sets exhibit wide fluctuations, and sign changes between the original and perturbed fields occur at 500 mb and above. The typical range of original divergence values at 200 mb is about twice as large as the maximum deviations. For the more insensitive parameters such as temperature advection, the range of values was more than five times that of the maximum deviation. Correlation coefficients at 850 and 700 mb are fairly high, ranging between 0.93 and 0.99. These coefficients progressively decrease with height ranging between 0.87 to 0.92 at 500 mb and 0.47 to 0.85 at 200 mb.

Comparisons of Tables 2.2 and 2.5 show that the values of standard deviation, mean absolute difference, and maximum deviation are quite similar for divergence and vorticity at all levels, while the field averages and the typical range of values differ considerably. The statistics for perturbed divergence indicate a poorer agreement with the original values than do those of vorticity. Similarly, the correlation coefficients are higher at all levels for vorticity than for the corresponding divergence fields. These findings confirm the often-mentioned statement that divergence is more sensitive to data errors than is vorticity.

The original divergence fields at 700 and 500 mb (not shown) indicate areas of convergence along the Gulf Coast from eastern Texas to the Florida panhandle and along the East Coast from South Carolina to New Jersey. Each of the ten perturbed fields for these levels displays the same general distribution. At 200 mb the original field (Fig. 2.6a) is characterized by a diffuse, almost disorganized pattern. Figure 2.6b shows that the field for Run 7 (the worst correlation) has distinct centers of convergence over Oklahoma and the Carolinas and centers of divergence over Texas and Maryland. These spurious centers are not evident in the original field.

Table 2.5. Statistical data of horizontal divergence (10^{-6} s^{-1}) for the original and ten perturbed fields.

Run	Field Avg	Std Dev	Mean Abs Dif	Max Dev	Cor Coef
Level: 850 mb Avg of Original Field: 3.5			Range of Values: -22.9 to 27.5		
1	3.7	2.1	1.6	7.0	.99
2	2.8	2.3	1.9	7.3	.98
3	4.1	2.5	2.0	7.3	.97
4	3.4	2.5	2.0	6.0	.97
5	3.4	3.2	2.6	8.9	.96
6	3.4	3.2	2.6	8.1	.96
7	3.7	2.8	2.1	9.3	.97
8	4.0	2.4	2.0	5.7	.98
9	3.1	2.1	1.6	7.3	.98
10	3.1	2.3	1.9	6.5	.98
Level: 700 mb Avg of Original Field: -3.5			Range of Values: -31.7 to 26.4		
1	-2.9	3.5	3.0	9.1	.95
2	-4.0	3.5	2.9	9.5	.96
3	-3.8	4.3	3.4	12.8	.93
4	-3.8	3.7	2.9	12.4	.95
5	-3.7	3.1	2.5	7.9	.96
6	-3.9	4.2	3.3	12.8	.96
7	-4.3	4.1	3.3	10.1	.94
8	-3.5	4.6	3.6	13.8	.95
9	-3.4	3.7	2.9	10.4	.95
10	-2.9	4.1	3.1	12.1	.93
Level: 500 mb Avg of Original Field: -1.3			Range of Values: -53.8 to 54.7		
1	-1.7	7.5	6.1	16.8	.92
2	-1.6	8.1	6.5	24.4	.90
3	-.5	8.1	7.0	16.3	.89
4	-.9	8.4	6.3	25.8	.91
5	-.4	8.7	6.8	25.9	.91
6	.6	9.0	7.3	25.7	.87
7	-.5	9.2	7.1	32.3	.81
8	-1.3	7.4	6.1	19.8	.91
9	-1.4	9.6	7.4	31.9	.87
10	.0	8.2	6.9	17.9	.91
Level: 200 mb Avg of Original Field: .3			Range of Values: -35.5 to 77.6		
1	2.8	18.1	14.6	40.2	.58
2	.5	16.8	13.9	44.8	.85
3	-.2	19.5	15.1	53.9	.64
4	-2.0	22.3	18.1	57.4	.50
5	4.0	13.3	10.9	35.5	.82
6	-.4	17.3	14.8	37.8	.82
7	-2.5	20.1	16.2	51.3	.47
8	.7	12.4	9.9	35.1	.84
9	3.0	14.7	12.8	41.8	.83
10	-.8	15.3	12.7	42.8	.75

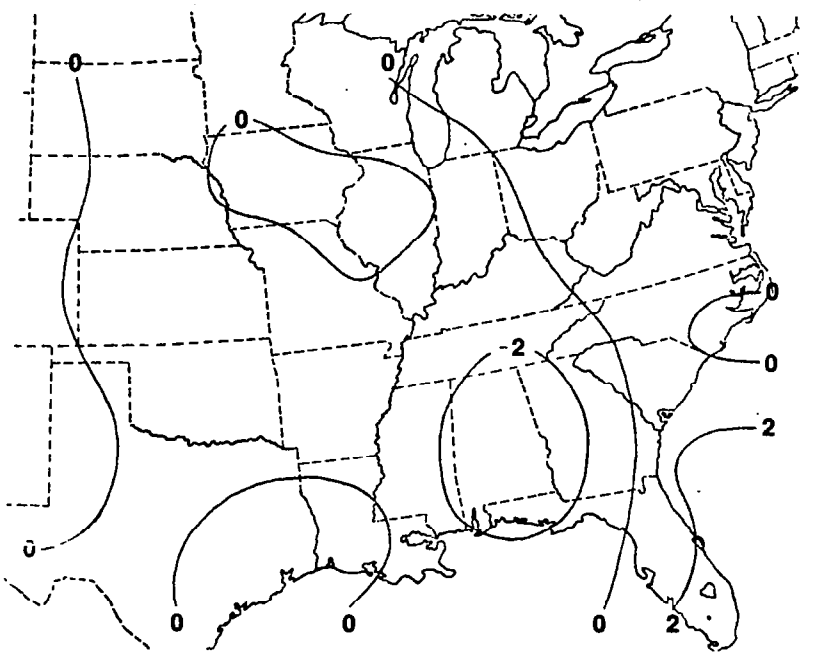

(a) Unaltered

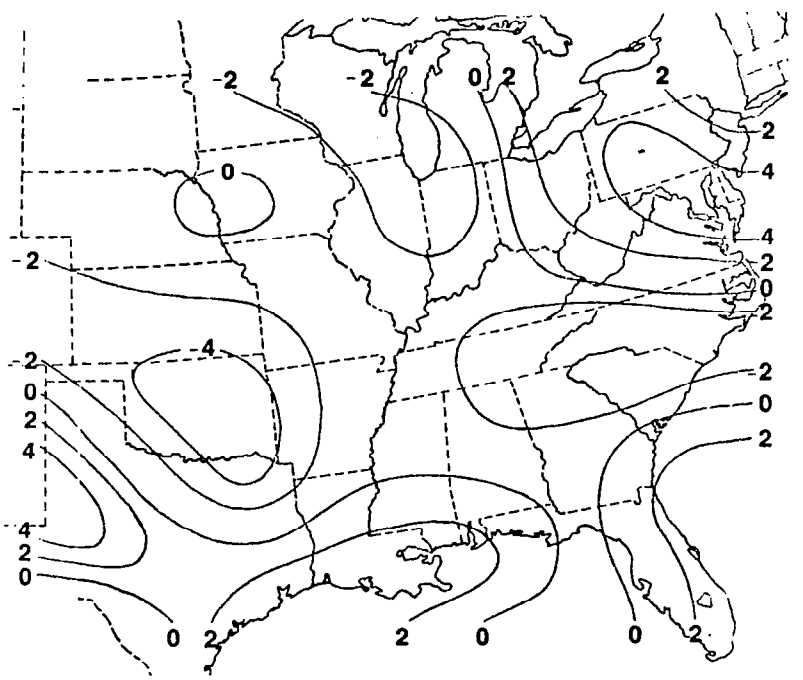

(b) Most Perturbed

Fig. 2.6. Spatial fields of horizontal divergence (10^{-5} s^{-1}) at 200 mb. Part A was derived from the unaltered data while part B represents the most perturbed field.

In summary, divergence values are fairly insensitive to data errors in the lower troposphere as indicated by the similarity of the patterns and the statistical analyses. At 500 mb and above, however, divergence is more sensitive and major differences in the patterns are discernible.

e. Unadjusted vertical motions

Table 2.6 shows that the differences between original and perturbed values of unadjusted vertical motion increase with height due to the larger wind errors at the upper levels and the fact that errors in divergence accumulate with height in the kinematic method of computation. Since the original and perturbed values of ω are unadjusted, they do not necessarily reach maximum values in the middle troposphere as often idealized. In this study the maximum values of ω occur at the highest level studied (200 mb). Field averages of vertical velocity are more consistent at all levels than were averages of divergence (Table 2.5). Only two runs, one at 500 mb and another at 200 mb, exhibit a different sign from that of the original average. The range of values for the original data is greatest at 200 mb and is three to five times larger than the maximum deviations at this level. Correlation coefficients between the original and perturbed fields are high, being greater than 0.95 in all cases up to 500 mb. At 200 mb the coefficients range from 0.88 to 0.95. These coefficients are higher than those for corresponding values of the divergence fields (Table 2.5) but not as high as those for vorticity and temperature advection (Tables 2.2 and 2.4).

The statistical parameters indicate that values of vertical velocity are not as variable as values of divergence despite the fact that kinematic vertical velocity is calculated by an integration of divergence through a column of the atmosphere. The fluctuations of divergence, being random, may tend to cancel themselves upon vertical integration.

From the synoptician's point of view, vertical motions in the lower and middle troposphere are very important since upward vertical motion coupled with adequate moisture at these levels gives rise to clouds and precipitation. Figure 2.7a shows the original vertical motion field at 700 mb. Two significant areas of upward vertical motion are indicated. One is located over west Texas while the other occurs in a band stretching from Florida, northward across the Carolinas, into Virginia, ahead of the upper level trough. Figure 2.7b is the perturbed field from Run 4. Although it is the field with the worst statistical comparison to the

Table 2.6. Statistical data of unadjusted vertical velocity (ω) ($\mu b\ s^{-1}$) for the original and ten perturbed fields.

Run	Field Avg	Std Dev	Mean Abs Dif	Max Dev	Cor Coef
Level: 850 mb Avg of Original Field: .6			Range of Values: -3.6 to 3.4		
1	.6	.2	.1	.2	.99
2	.6	.2	.1	.5	.99
3	.6	.2	.2	.5	.99
4	.5	.2	.2	.6	.99
5	.6	.2	.2	.6	.98
6	.6	.2	.2	.5	.98
7	.6	.2	.2	.5	.99
8	.6	.2	.2	.6	.99
9	.5	.2	.1	.4	.99
10	.6	.2	.1	.6	.99
Level: 700 mb Avg of Original Field: .5			Range of Values: -6.7 to 5.9		
1	.5	.3	.3	.8	.99
2	.5	.4	.3	1.1	.99
3	.5	.5	.4	1.2	.98
4	.4	.5	.4	1.1	.98
5	.5	.4	.3	1.4	.99
6	.5	.5	.4	1.3	.98
7	.5	.5	.4	1.1	.99
8	.5	.3	.3	.8	.99
9	.5	.5	.4	1.4	.98
10	.5	.4	.3	1.0	.99
Level: 500 mb Avg of Original Field: -.1			Range of Values: -7.5 to 10.0		
1	-.1	.7	.6	1.8	.98
2	-.1	.8	.6	2.8	.97
3	-.1	1.0	.8	3.3	.96
4	-.2	.7	.5	1.9	.98
5	-.3	.8	.7	1.9	.97
6	-.1	1.1	.8	3.4	.96
7	-.1	.9	.7	2.5	.97
8	-.1	.7	.6	2.4	.98
9	-.1	.9	.7	2.2	.97
10	+.1	.7	.6	2.5	.98
Level: 200 mb Avg of Original Field: .3			Range of Values: -14.0 to 16.6		
1	.8	2.9	2.1	10.3	.88
2	.4	2.4	1.9	7.0	.93
3	.5	2.5	2.0	7.0	.92
4	-.1	2.0	1.6	5.5	.94
5	.1	2.0	1.5	7.3	.95
6	.5	2.8	2.3	6.7	.89
7	.2	1.8	1.5	4.8	.95
8	.6	2.1	1.6	7.0	.95
9	.5	1.9	1.6	4.5	.95
10	.6	2.0	1.7	5.6	.94

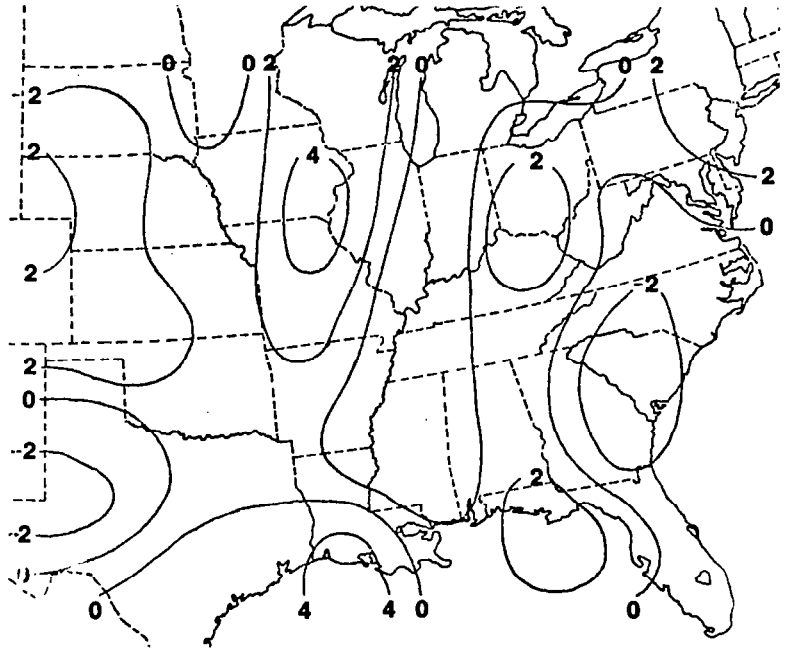

(a) Unaltered

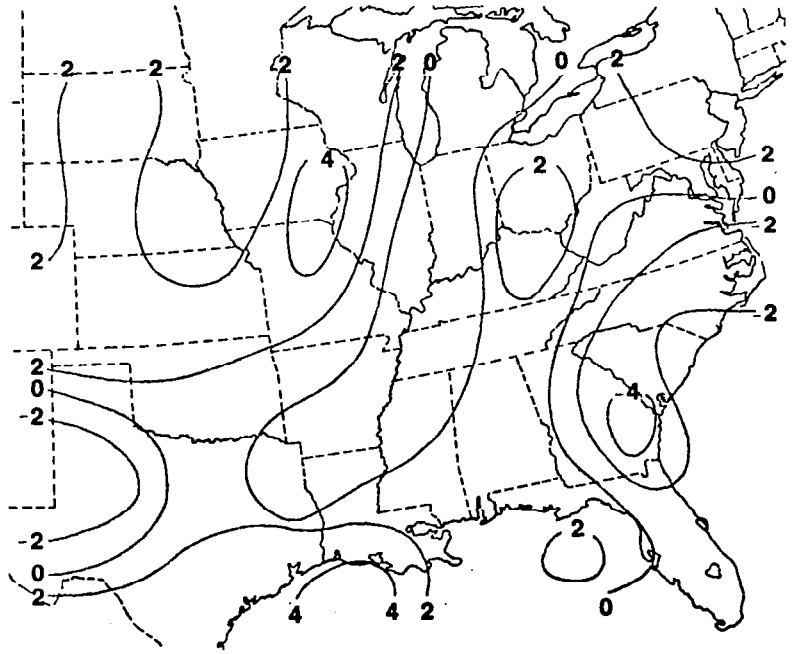

(b) Most Perturbed

Fig. 2.7. Spatial fields of unadjusted vertical motion (ω) ($\mu b\ s^{-1}$) at 700 mb. Part A was derived from the unaltered data while part B represents the most perturbed field.

original, it still shows good agreement with it. Each of the perturbed fields at 700 mb exhibits this same general pattern. Figures 2.8a and b show that even at 200 mb the field that statistically differs the most from the original (Run 1) agrees rather well with the unperturbed field. The positive and negative areas are located in the same general areas, but some differences of central values are evident. In general, the pattern comparisons for unadjusted vertical motions at 200 mb, show much better agreement than did values of divergence (Fig. 2.6).

f. Adjusted vertical motions

Statistical information concerning the adjusted vertical motions is given in Table 2.7. The range of values for the original fields is greatest at 500 mb because of the O'Brien adjustment scheme. The field averages are more consistent between the original and perturbed fields than were averages of the unadjusted values (Table 2.6), with a change of sign occurring only once, at 200 mb. The standard deviations, mean absolute differences, and maximum deviations increase with height from 850 to 500 mb, and magnitudes are approximately the same as those of the unadjusted vertical motions (Table 2.6). At higher levels, the statistical values for adjusted motion are nearly the same at 200 mb as at 500 mb but are approximately half the sizes of those for the unadjusted motions. This indicates the usefulness of the O'Brien scheme in producing reasonable profiles of vertical motion in spite of errors that may exist in the wind data. Correlation coefficients are quite high at 500 mb and below with the lowest being 0.95. At 200 mb the coefficients range from 0.79 to 0.91. The finding of lower correlations at the higher altitudes might be somewhat surprising since the adjustment scheme forces each of the profiles to zero at 100 mb. However, one should recall that even though adjusted values at 200 mb are smaller than those in the middle troposphere, the standard deviations at 200 mb are similar to those at 500 mb. Correlation coefficients are higher for both forms of vertical motion (Table 2.6-2.7) than for divergence (Table 2.5) at all levels.

In the lower and middle troposphere the original fields of adjusted vertical motions are not significantly different from the corresponding unadjusted fields. This is expected because wind errors are small in the lower layers and because the O'Brien scheme produces only a small adjustment below about 500 mb. Figure 2.9a shows the original field of adjusted vertical motion at 700 mb. When compared with the original field of the unadjusted motion (Fig. 2.7a) it is seen that the patterns are quite

Table 2.7. Statistical data of adjusted ω ($\mu b\ s^{-1}$) for the original and ten perturbed fields.

Run	Field Avg	Std Dev	Mean Abs Dif	Max Dev	Cor Coef
Level: 850 mb Avg of Original Field: .6				Range of Values: -4.2 to 3.1	
1	.5	.2	.2	1.1	.99
2	.6	.2	.2	.7	.99
3	.6	.2	.2	.6	.99
4	.6	.2	.2	.5	.99
5	.5	.2	.2	.7	.99
6	.6	.2	.2	.6	.99
7	.6	.2	.2	.5	.99
8	.6	.2	.2	.6	.99
9	.5	.1	.1	.4	.99
10	.6	.2	.2	.7	.99
Level: 700 mb Avg of Original Field: .5				Range of Values: -8.7 to 6.0	
1	.4	.5	.4	1.6	.98
2	.4	.5	.4	1.8	.98
3	.5	.5	.4	1.5	.98
4	.5	.5	.4	1.1	.98
5	.4	.5	.4	1.5	.99
6	.4	.5	.4	1.3	.99
7	.4	.5	.4	1.3	.99
8	.5	.3	.3	.9	.99
9	.4	.4	.3	1.4	.99
10	.5	.4	.4	1.2	.99
Level: 500 mb Avg of Original Field: -.2				Range of Values: -10.1 to 6.8	
1	-.4	1.0	.8	3.3	.96
2	-.3	1.1	.9	3.9	.96
3	-.2	1.1	.9	2.8	.95
4	-.1	1.1	.8	3.4	.95
5	-.4	1.1	.9	3.3	.96
6	-.2	1.1	.8	2.7	.95
7	-.1	.8	.6	2.5	.97
8	-.3	.9	.7	2.7	.97
9	-.3	.8	.6	2.4	.98
10	-.1	.8	.6	3.1	.97
Level: 200 mb Avg of Original Field: .1				Range of Values: -7.5 to 6.1	
1	.1	.9	.7	2.3	.91
2	.0	1.0	.8	3.2	.87
3	.2	1.2	.9	3.8	.89
4	.2	1.2	.9	2.9	.80
5	-.2	.8	.6	3.0	.92
6	.0	1.2	.9	3.7	.79
7	.2	1.1	1.0	2.8	.90
8	.1	1.1	.9	3.2	.88
9	.0	1.2	.9	3.7	.90
10	.3	.9	.8	2.3	.88

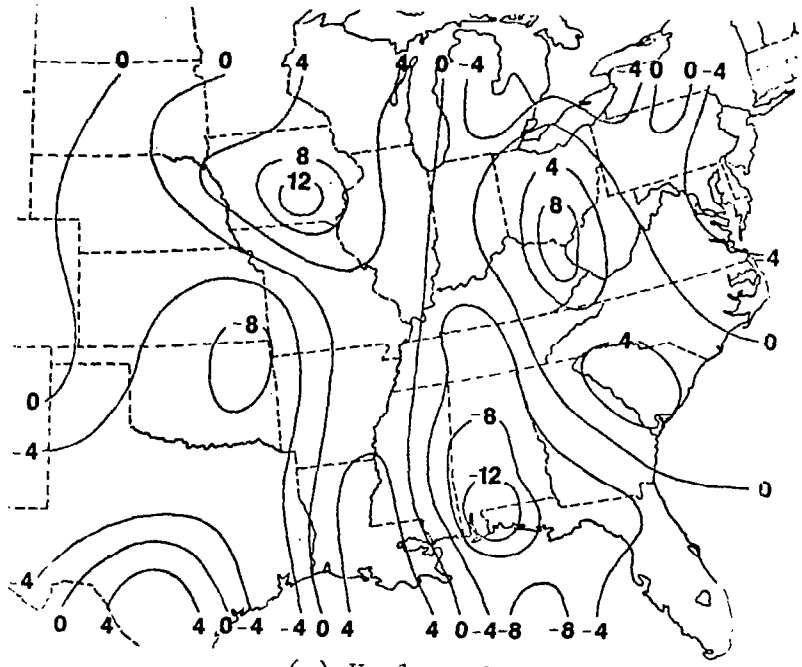

(a) Unaltered

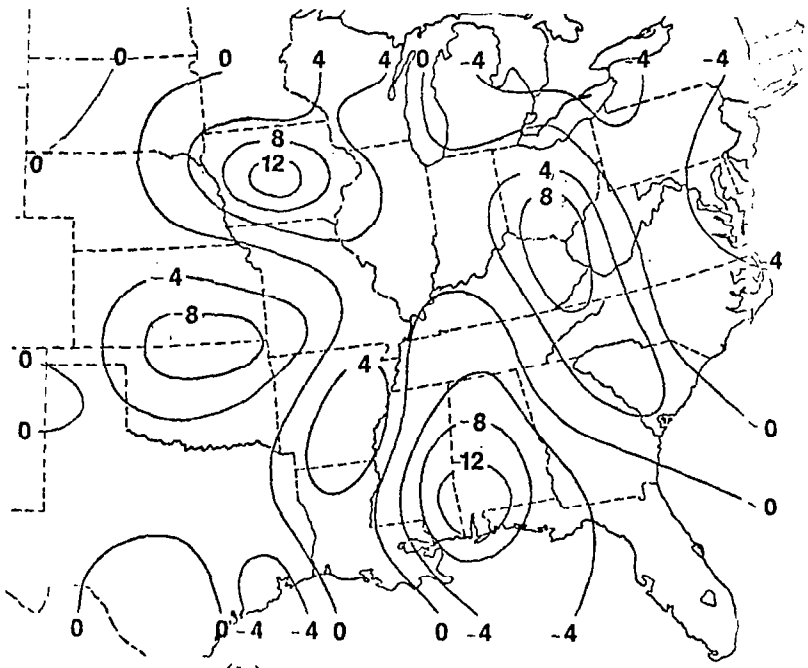

(b) Most Perturbed

Fig. 2.8. Spatial fields of unadjusted ω ($\mu b\ s^{-1}$) at 200 mb. Part A was derived from the unaltered data while part B represents the most perturbed field.

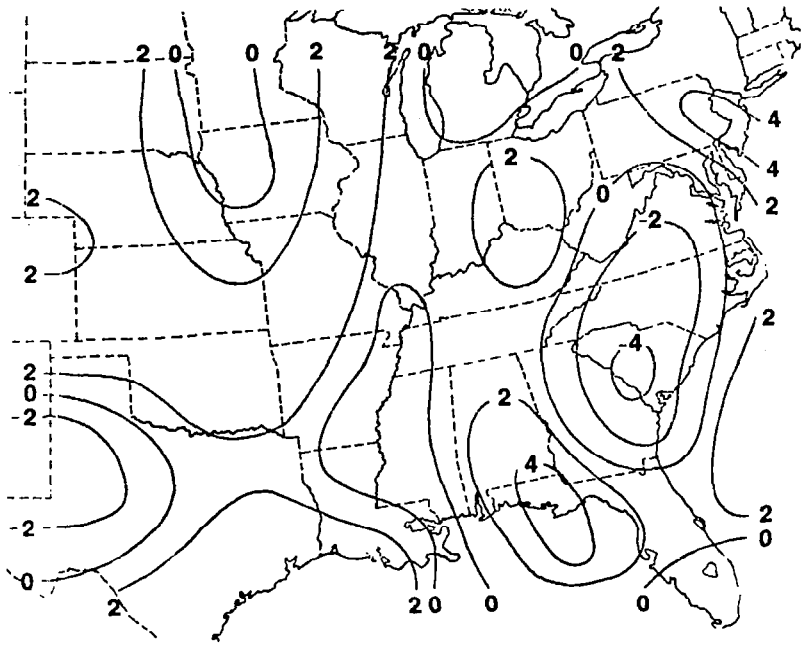

(a) Unaltered

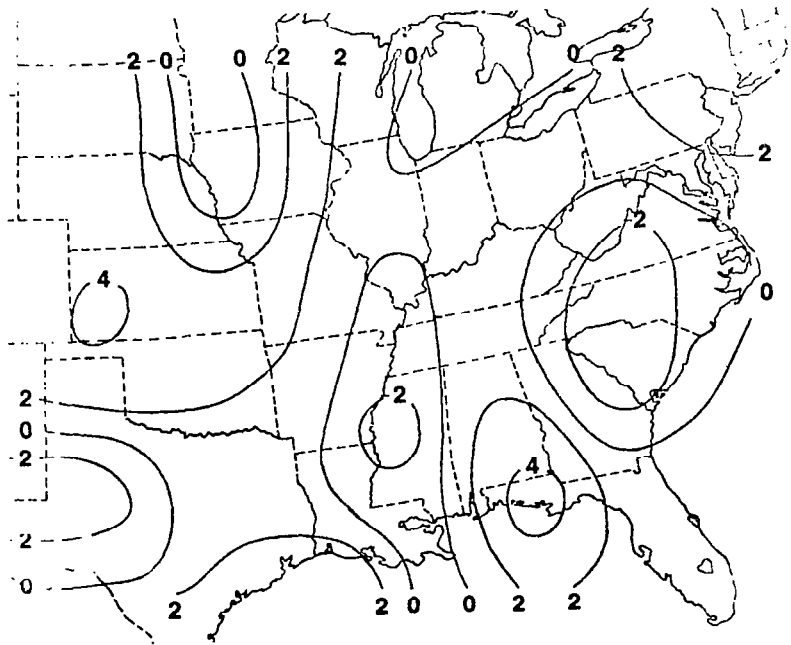

(b) Most Perturbed

Fig. 2.9. Spatial fields of adjusted ω (μb s^{-1}) at 700 mb. Part A was derived from the unaltered data while part B represents the most perturbed field.

similar; the main difference being that the positive and negative centers of the adjusted field are strengthened slightly. At 200 mb, unadjusted vertical motions (Fig. 2.8a) are much stronger than those of the adjusted field (Fig. 2.10a) due to the nature of the O'Brien technique.

In comparing the original and the perturbed fields of adjusted vertical motions, the perturbed fields again show very close agreement at and below 500 mb. At these levels, the integration of divergence extends over layers in which the random wind errors are small. A slightly poorer agreement is seen at 200 mb. Figures 2.9a and 2.10a represent the original fields for the adjusted vertical motions at 700 mb and 200 mb, respectively. Figure 2.9b is the 700 mb field from Run 9, and Fig.2.10b is the 200 mb field from Run 6; both are the perturbed fields that statistically differ the most from the original. The strong similarity of the original and perturbed fields at both levels should be noted.

g. Comparison with a previous study

Table 2.8 compares the range of the standard deviations found during this study with those values predicted by error equations given by Dupuis and Scoggins (1979). The assumed errors of the rawinsonde wind data were similar for both studies (Table 2.1). The error simulation technique of the present study allows for the effects of horizontal and vertical smoothing and the effects of the objective analysis while the study of Dupuis and Scoggins does not. With the exception of vorticity advection, the central points of the range of standard deviations of the present study are smaller than those obtained by Dupuis and Scoggins. A different synoptic situation might yield a different range of errors in the present study, but the procedure used by Dupuis and Scoggins is not dependent on the synoptic situation. The current results suggest that the smoothing techniques and objective analysis that were used have reduced the effects of the deliberately introduced data errors.

h. Statistical analysis of limited areas

To ascertain the effects of random data errors on areas smaller than already discussed, the statistical analysis was performed on two subareas of the total region. These areas were selected on the basis of their positions in relation to synoptic features and are depicted as the smaller boxes in Fig. 2.1. Subarea 1 is located in the eastern United States and has an area of 2.27×10^5 km^2, is located over the central Great Plains, upstream of the upper air trough and enclosing a strong

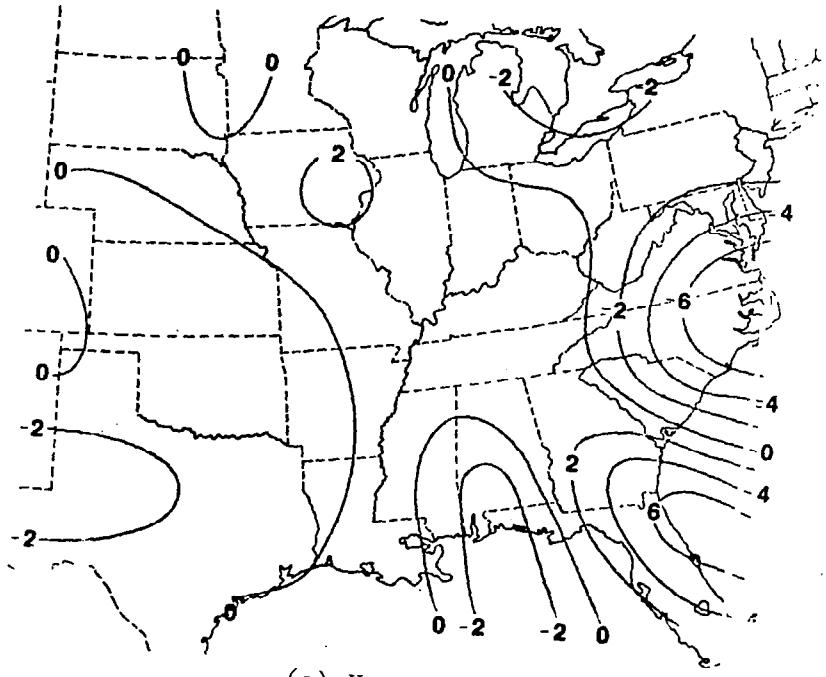

(a) Unaltered

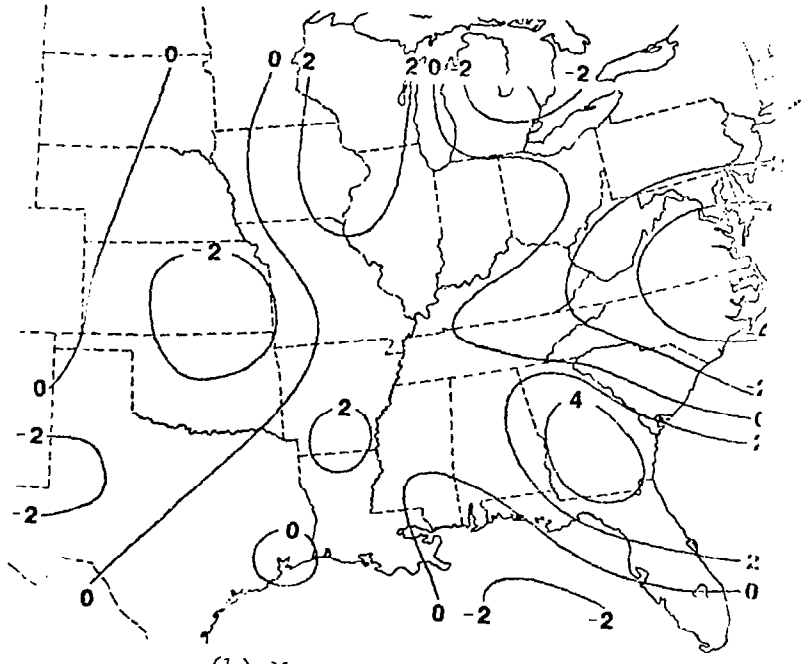

(b) Most Perturbed

Fig. 2.10. Spatial fields of adjusted ω ($\mu b\ s^{-1}$) at 200 mb. Part A was derived from the unaltered data while part B represents the most perturbed field.

Table 2.8. Comparison of standard deviations from the present study with those obtained using error equations (Dupuis and Scoggins, 1979).

Parameter	Level (mb)	Dupuis and Scoggins	Range in Current Study	
Relative Vorticity ($10^{-5}s^{-1}$)				
	850	.5	.2 to .3	
	700	1.0	.4 to .5	
	500	1.5	.7 to .9	
	300	2.2	1.3 to 2.2	
Vorticity Advection ($10^{-10}s^{-2}$)				
	850	4.0	1.0 to 1.5	
	700	9.0	2.7 to 3.6	
	500	16.0	10.1 to 13.7	
	300	22.0	21.0 to 55.0	
Temperature Advection (10^{-5}deg s^{-1})				
	850	1.9	.6 to .9	
	500	4.5	1.8 to 3.6	
Horizontal Divergence ($10^{-5}s^{-1}$)				
	850	.5	.2 to .3	
	700	1.0	.3 to .5	
	500	1.5	.8 to 1.0	
	300	2.2	1.3 to 2.2	
Vertical Motion (μb s^{-1})			Unadjusted	Adjusted
	850	.4	.2	.1 to .2
	700	1.5	.3 to .5	.3 to .6
	500	4.0	.7 to 1.1	.8 to 1.2
	300	7.0	1.3 to 2.0	.8 to 1.2

surface high.

Table 2.9 gives the ranges of several statistical indicators over the ten perturbed fields of the various kinematic parameters. The reader should note that in most cases the mean values for both subareas fluctuate over a greater range than do the mean values for the total area (Tables 2.2-2.7). This is not unexpected because averages based on a few points should exhibit wider variations than averages derived from a larger number of points. The mean absolute differences, standard deviations, and correlation coefficients also display a greater range of values over the subareas than for the total area.

The range of area means and mean absolute differences for vorticity and the two advection terms are generally much greater for the area downstream of the upper air trough (Subarea 1) than for the upstream region (Subarea 2). This is especially true at 500 mb and above. Vorticity advection, once again, is the most sensitive parameter with downstream values of mean absolute differences as much as four times greater than the upstream values. Even a normally insensitive parameter like temperature advection exhibits sizeable variabilities as the size of the area over which the values are averaged decreases. Mean values for Subarea 1 at 200 mb ranged from -4.2 to $+11.6 \times 10^{-5}$ deg s^{-1} with a correlation coefficient as low as 0.60. This degree of fluctuation is not evident in Subarea 2 or in the total area values (Table 2.4). The observed difference in the two subareas may be due to stronger winds occurring in the downstream region.

The ranges of the mean absolute differences and standard deviations for the divergence and vertical motion terms are approximately the same for both subareas. Correlation coefficients are slightly lower for the area upstream of the trough (Subarea 2) which is probably due to the fact that the original fields were not as well defined over the Great Plains as over the East Coast. Once again, the two vertical motion terms are not as sensitive to input data errors as is horizontal divergence at individual levels.

Table 2.9. Statistical data for two subareas of the total region (see Fig. 2.1). The ranges were computed from the ten sets of perturbed data. Subarea 1 is located east of the upper-level trough while subarea 2 is located west of the trough.

	SUBAREA 1				SUBAREA 2			
Level	Area Mean	Mean Abs Dif	Stnd Dev	Corr Coef	Area Mean	Mean Abs Dif	Stnd Dev	Corr Coef
				Relative Vorticity (10^{-6} s^{-1})				
850	14.6 to 18.5	1.8 to 3.7	1.8 to 3.6	.97 to .99	-3.1 to -.3	.7 to 2.5	.9 to 2.7	.92 to .99
700	32.4 to 37.9	1.4 to 4.7	1.6 to 5.3	.98 to .99	14.9 to 21.3	2.2 to 5.4	2.5 to 6.8	.70 to .98
500	70.5 to 79.7	2.7 to 9.4	3.4 to 11.8	.96 to .99	20.3 to 29.0	2.6 to 7.6	3.1 to 8.1	.93 to .98
200	46.0 to 81.4	5.5 to 20.5	7.0 to 25.3	.35 to .96	35.4 to 50.9	5.8 to 12.6	7.9 to 12.0	.49 to .86
				Vorticity Advection (10^{-10} s^{-2})				
850	1.7 to 2.7	.6 to 1.0	.8 to 1.3	.96 to .99	-1.3 to -.6	.4 to 1.2	.5 to 1.5	.97 to .99
700	2.7 to 4.5	1.0 to 2.9	1.2 to 3.5	.98 to .99	-1.3 to -2.5	1.3 to 3.5	1.7 to 4.3	.84 to .97
500	7.1 to 15.0	4.5 to 14.2	5.0 to 19.6	.85 to .99	-1.8 to -5.5	1.6 to 7.0	1.8 to 8.5	.92 to .99
200	-4.6 to 38.3	15.1 to 49.5	11.6 to 61.9	-.33 to .93	-5.3 to -16.7	6.1 to 12.8	7.9 to 16.4	.38 to .90
				Temperature Advection (10^{-6} Deg s^{-1})				
850	30.1 to 38.0	2.4 to 6.4	3.4 to 7.5	.96 to .99	39.1 to 43.6	1.8 to 4.0	1.8 to 5.2	.98 to .99
700	21.3 to 35.5	4.1 to 8.0	4.6 to 9.5	.98 to .99	94.4 to 108.0	5.8 to 13.7	7.0 to 16.6	.98 to .99
500	23.6 to 76.7	12.1 to 34.5	17.6 to 53.3	.93 to .99	28.7 to 50.0	3.6 to 12.5	4.0 to 13.8	.97 to .99
200	-41.8 to 116.0	22.7 to 124.0	31.7 to 135.0	.60 to .94	-12.5 to -3.1	4.1 to 9.0	5.2 to 13.3	.95 to .99

Table 2.9. (Concluded)

Level	SUBAREA 1 Area Mean	Mean Abs Dif	Stnd Dev	Corr Coef	SUBAREA 2 Area Mean	Mean Abs Dif	Stnd Dev	Corr Coef
				Horizontal Divergence (10^{-6} s^{-1})				
850	-2.7 to 0.7	.6 to 2.6	.7 to 3.1	.91 to .99	8.5 to 10.5	1.3 to 3.3	1.5 to 3.7	.88 to .97
700	0.1 to 2.6	1.7 to 4.0	1.9 to 4.2	.90 to .98	-0.6 to 3.5	1.6 to 5.3	1.9 to 5.7	.81 to .98
500	-1.2 to 9.3	4.5 to 11.1	5.4 to 12.5	.69 to .98	-5.8 to 2.0	4.1 to 8.5	2.9 to 10.0	.75 to .98
200	-17.4 to 8.4	8.0 to 17.7	9.5 to 14.9	.63 to .97	-17.2 to 5.0	8.7 to 16.8	10.4 to 18.1	-.61 to .81
				Unadjusted Vertical Velocities (μb s^{-1})				
850	-0.6 to 0.4	0.1 to 0.2	0.1 to 0.2	.98 to .99	0.8 to 1.0	0.1 to 0.2	0.1 to 0.2	.92 to .98
700	-0.7 to -0.1	0.2 to 0.6	0.2 to 0.5	.93 to .99	1.5 to 2.3	0.1 to 0.5	0.2 to 0.6	.93 to .99
500	-0.5 to 0.1	0.4 to 1.0	0.5 to 1.2	.94 to .98	0.8 to 1.8	0.4 to 1.0	0.5 to 1.4	.92 to .98
200	0.2 to 2.0	0.9 to 2.7	0.1 to 3.2	.86 to .98	0.2 to 2.0	0.9 to 2.5	1.0 to 3.0	.90 to .98
				Adjusted Vertical Velocities (μb s^{-1})				
850	-0.6 to -0.5	0.1 to 0.2	0.1 to 0.2	.98 to .99	0.7 to 1.0	0.1 to 0.2	0.1 to 0.2	.91 to .98
700	-0.9 to -0.2	0.2 to 0.6	0.2 to 0.7	.94 to .99	1.5 to 2.1	0.2 to 0.6	0.3 to 0.7	.87 to .98
500	-1.1 to -0.2	0.5 to 1.2	0.5 to 1.4	.92 to .99	0.4 to 1.3	0.4 to 1.0	0.4 to 1.3	.80 to .98
200	-1.0 to 0.7	0.7 to 1.7	0.5 to 1.9	.89 to .99	-0.2 to 1.0	0.5 to 1.1	0.5 to 1.2	.57 to .93

4. CONCLUSIONS

In this study, random errors have been deliberately introduced into a set of rawinsonde data in order to study their effects on derived kinematic parameters. Fields of vorticity, vorticity advection, temperature advection, horizontal divergence, and vertical motions based on unaltered data were hand analyzed and compared to fields obtained from the perturbed data. A statistical comparison between computations based upon original and altered fields also was performed.

The following conclusions are made:

1) Fields of 500 mb vorticity and 700 mb vertical velocity, which are frequently used in synoptic-scale forecasting schemes, showed minimal effects of the deliberately introduced errors.

2) Vorticity advection was found to be the most sensitive term to input data errors. Large fluctuations in fields of this parameter were evident both statistically and qualitatively. Maximum deviations at 200 mb approached values twice as large as the total range of original values. Patterns based on the perturbed data occasionally were greatly different from those based on the original data.

3) Values of temperature advection and vorticity were quite insensitive to the deliberately introduced wind errors.

4) Values of divergence were greatly affected by the induced data errors, especially in the upper atmosphere. Values of unadjusted and adjusted vertical motion obtained by the kinematic method were less sensitive to the wind errors than divergence. Pattern comparisons between original and altered fields of vertical motion and divergence indicated that the assumed random errors would not destroy major features of the original fields.

5) Deviations between the original and perturbed fields of all parameters increased with altitude in response to increases in the allowable random error.

6) The use of objective analysis together with horizontal and vertical smoothing techniques removed much of the deliberately introduced random error from the data. Without such schemes, the effects of such errors would undoubtedly have been much greater.

7) Vorticity and the two advection terms seemed more sensitive to data errors downstream of the upper air trough where the strongest winds were located. The sensitivity of divergence and vertical motion was similar in both upwind and downwind regions. Error-induced deviations for subareas of the total region were much larger than for the entire region as a whole.

The results of this study are based on a single synoptic situation. Additional studies of this type, during severe storm outbreaks for example, would be useful. While this study considered rawinsonde data, its results have implications for other types of data as well. For example, the effects of errors in satellite-derived temperature, heights, humidity, and winds on computed parameters should be investigated. A study such as this would be especially useful in the proposed evaluation of the upcoming VAS geostationary sounder.

5. REFERENCES

Barnes, S.L., 1964: A technique for maximizing detail in numerical weather map analysis. J. Appl. Meteor., 3, 396-409.

Chen, T.J., and L.F. Bosart, 1977: Quasi-Lagrangian kinetic energy budgets of composite cyclone-anticyclone couplets. J. Atmos. Sci., 34, 452-464.

Chien, H., and P.J. Smith, 1973: On the estimation of kinematic parameters in the atmosphere from radiosonde wind data. Mon. Wea. Rev., 101, 252-261.

Dupuis, S.R., and J.R. Scoggins, 1979: Differences between measured and linearly interpolated synoptic variables over a 12 h period during AVE IV. NASA CR-3150, George C. Marshll Space Flight Center, Alabama, 126 pp.

Endlich, R.M., and J.R. Clark, 1963: Objective computations of some meteorological quantities. J. Appl. Meteor., 2, 66-81.

Fuelberg, H.E., 1974: Reduction and error analysis of the AVE II pilot experiment data. NASA CR-120496, Geroge C. Marshall Flight Center, Alabama, 131 pp.

_____, and R.E. Turner, 1975: Data for NASA's AVE III experiment: 25 mb sounding data and synoptic charts. NASA TM X-64938, George C. Marshall Space Flight Center, 462 pp.

_____, and J.R. Scoggins, 1980: Kinetic energy budget during strong jet stream activity over the eastern United States. Mon. Wea. Rev. 108, 69-77.

Kurihara, Y., 1961: Accuracy of winds aloft data and estimation of error in numerical analysis of atmospheric motions. J. Meteor. Soc. Japan, 39, 331-345.

Lenard, R.W., 1973: A revised assessment of radiosonde accuracy. Bull. Amer. Meteor. Soc., 54, 691-693.

O'Brien, J.J., 1970: An alternate solution to the classical vertical velocity problem. J. Appl. Meteor., 9, 197-203.

Panofsky, H.A., and G.W. Brier, 1968: Some applications of statistics to meteorology. The Pennsylvania State University, University Park, Pennsylvania, 224 pp.

Robertson, F.R., and P.J. Smith, 1980: The kinetic energy budgets of two severe storm producing extra tropical cyclones. Mon. Wea. Rev., 108, 127-143.

Shuman, F.G., 1957: Numerical methods in weather prediction: II. Smoothing and filtering. Mon. Wea. Rev., 85, 357-361.

Smith, P.J., 1971: An analysis of kinematic vertical motions. Mon. Wea. Rev., 99, 715-724.

Vincent, D.G., and L.N. Chang, 1975: Kinetic energy budgets of moving systems: Case studies for an extratropical cyclone and hurricane Celia, 1970. Tellus, 27, 215-233.

_____, E.K. Bossingham, and H.J. Edmon, Jr., 1976: Comparison of large scale vertical motions computed by the kinematic method and quasi-geostropic ω-equation. Sixth Conf. on Weather Forecasting and Analysis, Amer. Meteor. Soc., Albany, 357-364.

Ward, J.H., and P.J. Smith, 1976: A kinetic energy budget over North America during a period of short synoptic wave development. Mon. Wea. Rev., 104, 836-848.

CHAPTER III

AN ERROR ANALYSIS OF THE KINETIC ENERGY BALANCE DURING THE AVE 3 PERIOD

by

Henry E. Fuelberg

Department of Earth and Atmospheric Sciences
Saint Louis University
Saint Louis, Missouri 63103

ABSTRACT

The sensitivity of the kinetic energy budget to random errors in rawinsonde data is assessed during the AVE 3 experiment. The approach is to compare the budget obtained from unaltered data with budgets obtained after random perturbations have been introduced into the data set. Results indicate that area-averaged budget values during AVE 3 generally are quite reliable. One must consider the effects of rawinsonde data errors in assigning significance to features of an energy balance.

CHAPTER III

AN ERROR ANALYSIS OF THE KINETIC ENERGY BALANCE DURING THE AVE 3 PERIOD

1. INTRODUCTION

Chapter II of this report described the effects of random errors in rawinsonde data on various kinematic parameters such as divergence and vertical motion. Since input data errors also affect values of a derived kinetic energy budget, it is important to consider the uncertainty of such computations. This is especially necessary when assessing the significance of fluctuations in time series analyses.

The kinetic energy budget equation (1.1 of Chapter I) describes the various sources and sinks of energy in a fixed limited volume. The AVE 3 period (6-7 February 1975) was selected for the initial error analysis because it contained a major jet stream. One observation time was chosen, 2100 GMT 6 February. Information about synoptic conditions, the AVE 3 data, and basic computational procedures are given in Chapter II of this report and in Fuelberg and Scoggins (1980). The approach used is similar to that described in Chapter II for the kinematic parameters. The first step was to compute the energy budget values at 2100 GMT using the original data. These values constituted the standard for purposes of the study although they certainly were not error free. The energy budgets then were recomputed after random perturbations were added to the original 25 mb values of wind and height data. Budget values obtained using the perturbed data were compared to those derived from the original data to test the sensitivity of the various terms. As in Chapter II, the effects of systematic data errors and computational inadequacies such as truncation error are not considered in this approach.

Computer-generated random perturbations were normally distributed about zero with standard deviations varying as a function of pressure (Table 2.1 of Chapter II). These values are similar to those proposed by Kurihara (1961) and used by Robertson and Smith (1980). Ten runs, each with a different set of perturbations at the individual 25 mb levels were made.

2. RESULTS

The original area-averaged kinetic energy budget at 2100 GMT 6 February along with mean absolute differences between the original and ten perturbed budgets, and the range of the perturbed budgets are given in Table 3.1. Since details of the original budget have already been described by Fuelberg and Scoggins (1980), the current discussion will focus only on the error analysis. Results indicate that kinetic energy content is the least sensitive parameter to input data errors. Cross-contour generation and horizontal and vertical flux divergence are considerably more sensitive, but mean absolute differences usually are less than 15% of the original values. Mean absolute differences of the local derivative and dissipation terms sometimes are as large as the original values themselves, especially in the 400-100 mb layer. Part of the problem is that original values of these terms were rather small. Ward and Smith (1976) noted that the dissipation term is unreliable if it occurs as a small difference between larger terms (the situation here), but is more reliable if it has a value similar to those of the contributing terms.

The conclusion is that values of area-averaged kinetic energy budgets during AVE 3 generally are quite reliable; however, one must bear in mind error-produced uncertainties when attaching significance to observed energy variabilities. Even though previous studies (e.g., Robertson and Smith, 1980; Ward and Smith, 1976; Vincent and Chang, 1975) also have ascribed overall confidence to energy budget calculations, an error analysis currently is underway for the AVE-SESAME 1 case and will be described in a future report.

Table 3.1. Area-averaged kinetic energy budget for 2100 GMT 6 February 1975. Values in parentheses are mean absolute differences between the original and ten perturbed budgets. Numbers in brackets are the ranges of differences between the original and ten perturbed runs. All units are W m^{-2} except for K which is 10^5 J m^{-2}.

Pressure Layer (mb)	K	$\partial K/\partial t$	$\vec{\nabla}\cdot k\vec{V}$	$\partial \omega k/\partial p$	$-\vec{V}\cdot\vec{\nabla}\phi$	D
400-100	29.3 (0.8) {1.1}	-0.9 (6.6) {10.1}	59.8 (4.7) {14.0}	-8.4 (1.0) {4.8}	61.0 (6.4) {22.4}	-10.5 (10.4) {30.6}
700-400	14.0 (0.2) {0.4}	0.6 (1.1) {3.1}	8.4 (1.0) {4.7}	8.1 (0.9) {4.6}	16.2 (2.4) {9.5}	0.9 (3.4) {13.6}
Sfc-700	2.9 (0.0) {0.2}	-1.9 (0.2) {0.9}	0.3 (0.1) {0.7}	0.6 (0.1) {0.3}	6.0 (0.3) {1.0}	-7.0 (0.4) {2.0}
Vertical Total	46.2 (1.0) {1.2}	-2.2 (7.6) {10.9}	68.5 (5.1) {17.1}	0.3 (0.0) {0.0}	83.2 (8.2) {23.5}	-16.6 (12.7) {37.3}

3. REFERENCES

Fuelberg, H.E., and J.R. Scoggins, 1980: Kinetic energy budget during strong jet stream activity over the eastern United States. Mon. Wea. Rev., 108, 69-77.

Kurihara, Y., 1961: Accuracy of winds aloft data and estimation of errors in numerical analysis of atmospheric motions. J. Meteor. Soc. Japan, 39, 331-345.

Robertson, F.R., and P.J. Smith, 1980: The kinetic energy balance of two severe storm producing extratropical cyclones. Mon. Wea. Rev., 108, 127-143.

Vincent, D.G., and L.N. Chang, 1975: Kinetic energy budgets of moving systems: Case studies for an extratropical cyclone and hurricane Celia, 1970. Tellus, 27, 215-233.

Ward, J.H., and P.J. Smith, 1976: A kinetic energy budget over North America during a period of short synoptic wave development. Mon. Wea. Rev., 104, 836-848.

CHAPTER IV

A DIAGNOSTIC STUDY OF VARIATIONS IN THE KINEMATIC METHOD OF COMPUTING VERTICAL MOTIONS

by

David M. Ebel *

and

Henry E. Fuelberg
Department of Earth and Atmospheric Sciences
Saint Louis University
Saint Louis, Missouri 63103

ABSTRACT

Fields of kinematic vertical motion at 500 mb are obtained using upward integration from the surface to 500 mb and downward integration from 100 mb to 500 mb. Downward-integrated values should reveal upper-level divergence patterns. A comparison of results from the two methods indicates that the downward-derived patterns at 500 mb showed surprisingly good continuity and related better to some storm areas than did patterns derived from upward integration. Upward-derived profiles then were adjusted using the O'Brien scheme while downward-derived values were adjusted using a scheme that is dependent on wind speed. The downward "wind adjusted" profiles were found to be essentially identical to the upward O'Brien adjusted profiles.

---

* Present affiliation: Colorado State University, Fort Collins 80521

Chapter IV

A DIAGNOSTIC STUDY OF VARIATIONS IN THE KINEMATIC METHOD OF COMPUTING VERTICAL MOTIONS

1. INTRODUCTION

Vertical motion is a very important meteorological parameter because rising air is ultimately responsible for the condensation of water vapor and resultant clouds and precipitation. Rising air also is required for the formation of severe thunderstorms and their associated tornadoes which take a heavy toll in lives and property each year. To understand the presence of clouds, precipitation and thunderstorms it is necessary to diagnose and understand the vertical motion that is associated with the given phenomena.

There are several ways to compute vertical motion on the synoptic scale, among them the kinematic, adiabatic, vorticity, and omega equation methods. Each of these techniques entails a number of assumptions and has advantages and disadvantages in a given situation. The meteorologist is limited to using those methods whose assumptions are not violated by the weather conditions and the type of data available.

The adiabatic, kinematic, and omega equation methods are the most commonly used techniques for computing vertical motion. However, there has been much question as to which method is the best on the synoptic scale. Wilson (1976) compared the adiabatic and kinematic methods during the severe storm outbreaks occurring during the fourth Atmospheric Variability Experiment (AVE IV) conducted by the National Aeronautics and Space Administration (NASA) and concluded that the kinematic technique produced the best overall vertical velocities. Vincent et al. (1976) compared the kinematic method with the quasi-geostrophic omega equation method in the vicinity of mid-latitude cyclones. Their conclusion was that values from the kinematic method were superior to those from the quasi-geostrophic form of the omega equation. Smith and Lin (1978) made a comparison study between the kinematic method, the quasi-geostrophic omega equation, and the general balance model omega equation in the vicinity of an intense extratropical

cyclone. They, too, concluded that the kinematic method was superior to the two forms of the omega equation and found that the quasi-geostrophic omega equation was better than the general balance equation. The fact that the kinematic method of computing large-scale vertical motion has consistently proven superior to the other techniques, coupled with its ease of computation and lack of restrictive assumptions, has made the kinematic method the most popular technique for computing vertical motion.

In the kinematic method, vertical velocity is computed by integrating the continuity equation between two isobaric surfaces. By making the hydrostatic assumption, vertical motion can be computed solely on the basis of horizontal divergence which, in turn, is computed from horizontal wind data. Because wind measurements are not totally accurate and computational procedures have limitations, errors in the horizontal divergence fields occur. These errors accumulate with height upon vertical integration through the atmosphere, often resulting in large magnitudes of vertical velocity near the top of the atmosphere where the values clearly should be small.

Correction schemes which force values at the top of the atmosphere to a prescribed value, usually zero, have been devised to produce a more realistic vertical motion profile. Such schemes are based on the assumption that as the sonde rises and drifts downstream, the wind measurements decrease in accuracy. A correction technique developed by O'Brien is designed to be a linear function of pressure. Smith (1971) found O'Brien's correction scheme superior to an earlier procedure developed by Lateef (1967). All of the previously mentioned case studies, Smith and Lin (1978), Wilson (1976), and Vincent et al. (1976) have used the O'Brien correction scheme. The kinematic method, coupled with the O'Brien correction scheme, is the most popular technique for computing vertical motion in diagnostic studies.

In situations of strong upper-level divergence, for example, it might be desirable to integrate downward through the atmosphere instead of upward In such a case, a correction scheme still must be used to adjust the vertical motion values if they are to approach zero at the Earth's surface. The O'Brien correction scheme can not be used for this purpose because it assumes that wind and divergence errors are greatest at the end of the integration process, at the top of the atmosphere. In the proposed inverted method of integration, the greatest correction would occur closest

to the ground where wind and divergence values should, in fact, contain the fewest errors. Thus, a different correction scheme must be used for downward integration purposes.

O'Brien (1970) offers an alternative correction scheme that is not pressure related. This scheme assumes that errors in the horizontal divergence fields at a given level can be directly related to the magnitude of the wind at that level, i.e., large wind speeds cause large errors in the wind components and thus large errors in the horizontal divergence fields. The wind-related scheme also is based on the assumption that wind speeds generally increase with height and that rawinsonde wind measurements become less accurate with height. Thus, O'Brien's wind-related correction technique could theoretically be used to correct vertical motion values computed from the kinematic method with downward integration.

This paper will evaluate unadjusted vertical velocities computed by the kinematic method using both upward and downward integration and will test the hypothesis that the wind-related correction scheme, when applied to both upward and downward integration, will produce the same values of adjusted vertical velocity as those computed by upward integration with the standard correction scheme. The purpose is to investigate possible variations in the application of the kinematic method that would be useful to the field of meteorology.

2. COMPUTATIONAL PROCEDURES AND DATA

The kinematic method involves integration of the continuity equation between two isobaric surfaces. The continuity equation in pressure coordinates can be written as

$$\frac{\partial u}{\partial x} + \frac{\partial v}{\partial y} + \frac{\partial \omega}{\partial p} = 0, \tag{4.1}$$

where u and v represent the horizontal velocity components and ω is vertical velocity. By integrating (4.1) between two isobaric surfaces, p and $p + \Delta p$ and employing the trapezoidal rule, it can be rewritten as

$$\omega_{p+\Delta p} = \omega_p - \left(\overline{\frac{\partial u}{\partial x} + \frac{\partial v}{\partial y}}\right)_p^{p+\Delta p} \tag{4.2}$$

where $\left(\overline{\frac{\partial u}{\partial x} + \frac{\partial v}{\partial y}}\right)_p^{p+\Delta p}$, is the average of the divergence values at the top and bottom of the layers of integration.

Vertical motions at the surface of the earth and the top of the atmosphere, assumed to be 100 mb due to data limitations, often are assumed to be zero. These assumptions are good since terrain-induced vertical motions and surface pressure tendencies generally are small and the vertical motion at 100 mb also is generally small.

The traditional O'Brien (1970) correction scheme, which assumes that wind errors are a linear function of pressure, is given by the equation

$$\omega_k' = \omega_k - (\omega_K - \omega_T)\ \frac{k(k+1)}{K(K+1)} \tag{4.3}$$

where K is the integer value of the top level of the atmosphere, k is the integer value at the level being adjusted, ω_K is the computed unadjusted vertical motion at 100 mb, ω_T is the assumed correct value at 100 mb (usually 0), and the prime denotes the adjusted vertical motion value.

The wind-related correction scheme proposed by O'Brien can be written as

$$\omega_k' = \omega_k - \frac{Q_k}{Q_K}(\omega_K - \omega_T), \tag{4.4}$$

where Q_K is the sum of the scalar wind speeds in a column extending from the surface of the earth to the top of the atmosphere, and Q_k is the sum of the scalar wind speeds from the original level to a given level k.

The data used in this study came from the second Atmospheric Variability and Severe Storm Experiment (AVSSE II) conducted on 6-7 May 1975, and sponsored by NASA. Soundings were taken at 3 and 6 h time intervals by standard rawinsonde stations in the central United States. Figure 4.1 shows the area encompassed by

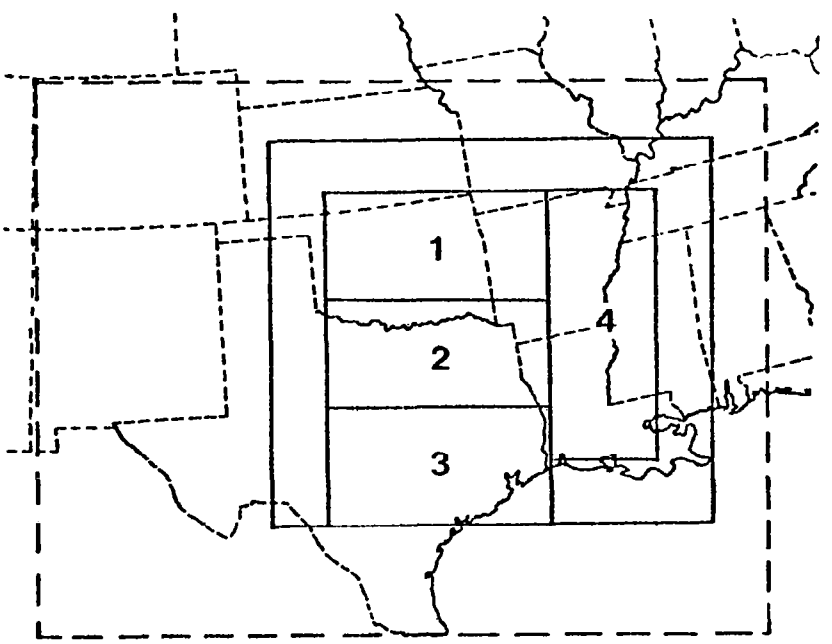

Fig. 4.1. Area encompassed by the AVSSE II Experiment (dashed line) and the total computational area (solid line). The four smaller boxes were used in computing limited area averages of vertical motion.

AVSSE II. The seven sounding times were 6 May at 1200, 1500, 1800 and 2100 GMT and 7 May at 0000,0300, and 1200 GMT. Data reduction procedures used to process the rawinsonde data are described by Fuelberg (1974), while the AVSSE II data at 25 mb intervals are given by Fucik and Turner (1975).

The data were interpolated from the randomly spaced stations onto an equally spaced grid system with a spacing of 158 km using an objective analysis scheme (Barnes, 1964). These gridded analyses of the required input data were produced at 18 levels in the atmosphere

starting with the surface and then in 50 mb intervals from 900 to 100 mb for each of the seven observation times.

In this study, divergence was computed at each grid point for all 18 levels by using centered finite differences. These values were then used in (4.2) to compute vertical motion. Two integration schemes were used: upward integration starting at the surface and working up to 100 mb, and downward integration beginning at 100 mb and working down to the Earth's surface. The O'Brien correction scheme, given by (4.3), was used to adjust values produced by upward integration. The wind-related correction scheme (4.4) was applied to unadjusted values produced from both upward and downward integration. For the upward case, a running vertical sum of wind speed, Q_k, was computed for each level beginning at the surface. For the downward case, the running sum was computed by beginning at 100 mb. In all two types of unadjusted vertical motion and three types of adjusted values were calculated in the study.

3. WEATHER CONDITIONS

Surface features at the beginning of AVSSE II (1200 GMT 6 May 1975) are shown in Fig. 4.2. A low pressure area was located over South Dakota with a cold front extending southward into Texas. A warm front stretched from South Dakota eastward into Pennsylvania. Remnants of an old frontal system were located along the lower Mississippi River Valley and across Florida.

A closed low pressure center dominated the flow at 500 mb at the start of AVSSE II (Fig. 4.2). A weak ridge was located along the Mississippi River Valley. Strongest winds occurred from New Mexico into Nebraska along the eastern side of the low. The AVSSE II experiment area encompassed the southeastern portions of the low and much of the associated downstream ridge.

In the radar summary for 1200 GMT 6 May, convection is indicated along the lower Mississippi River Valley where maximum radar tops reached 14.6 km (48,000 ft., Fig. 4.3a). As the day progressed, this area of convection expanded into Arkansas, Missouri and Illinois (Fig. 4.3b). The most intense storm activity of the period, however, formed along the slowly advancing cold front. Storms began forming from Oklahoma to Nebraska at around 1700 GMT while an area of storms in Texas began to form from an area of rain-showers at around 1800 GMT (Fig. 4.3c). The northern section of storms merged with the area of convection located in the middle Mississippi River Valley and underwent several periods of decay and reintensification during the remainder of the AVSSE II period. Radar tops of 15.2 km (50,000 ft) were quite common in this storm area. The showers in central Texas that began to form near 1400 GMT developed rapidly near 1800 GMT, reached peak coverage and areal intensity (18.6 km, 61,000 ft) near 2100 GMT (Fig 4.3d), and had completely dissipated by 0100 GMT 7 May (Figs. 4.3e and 4.3f). Radar summaries for the end of period (Figs. 4.3g and 4.3h) indicate that convection is confined to the lower Mississippi River Valley.

Synoptic conditions at the end of the AVSSE II period are shown in Fig. 4.4. The surface low pressure center remained nearly stationary and showed gradual weakening during the period. Frontal systems showed little change. The closed low remained nearly stationary over Wyoming at 500 mb; 24 h height changes over the area were generally less than 30 m.

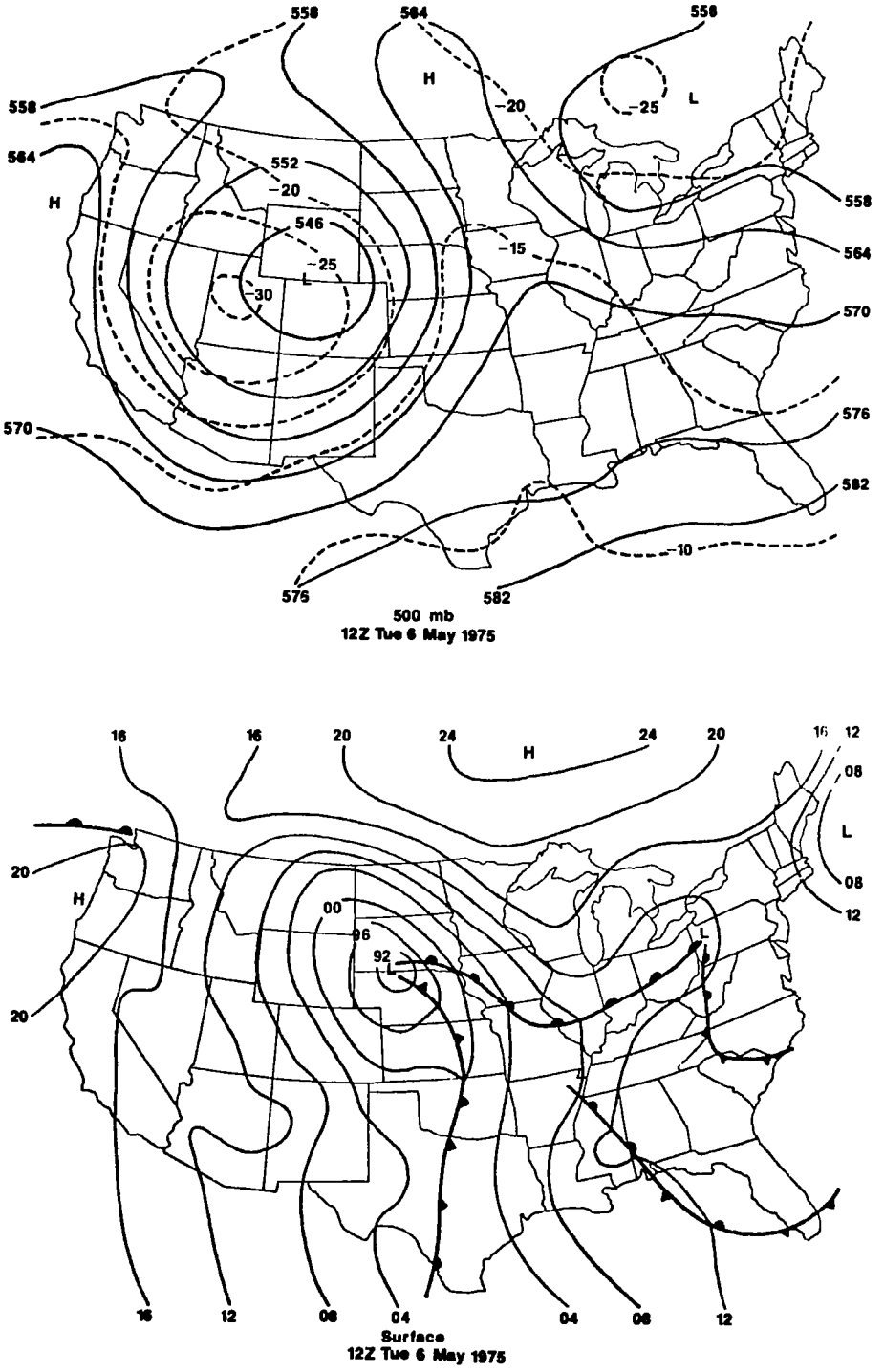

Fig. 4.2. Synoptic conditions at the beginning of the AVSSE II period, 1200 GMT 6 May 1975.

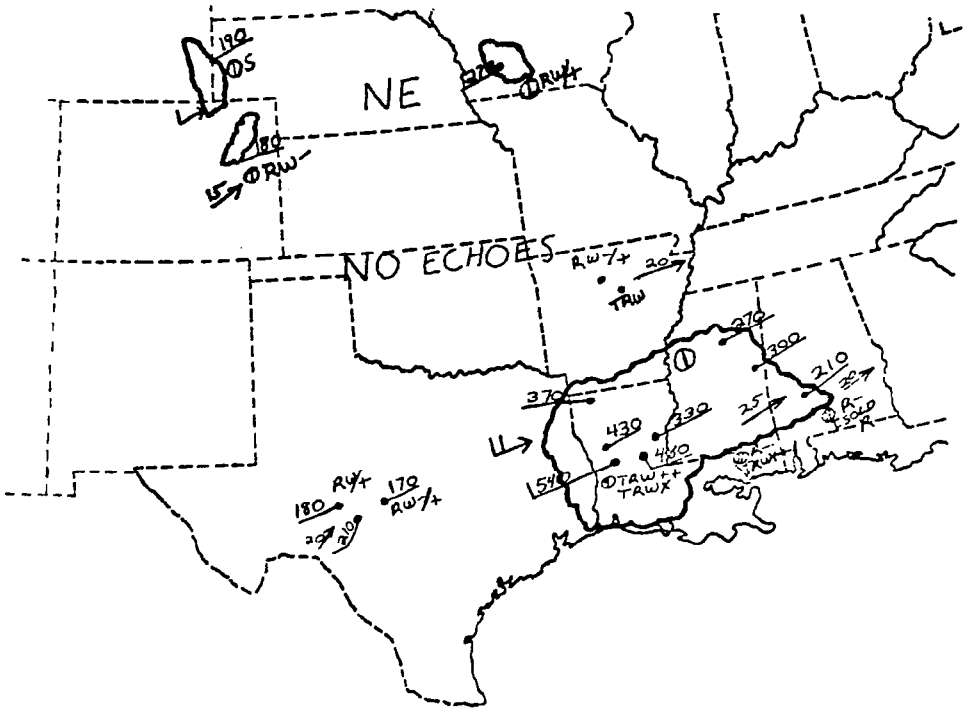

(a) 1135 GMT 6 May 1975

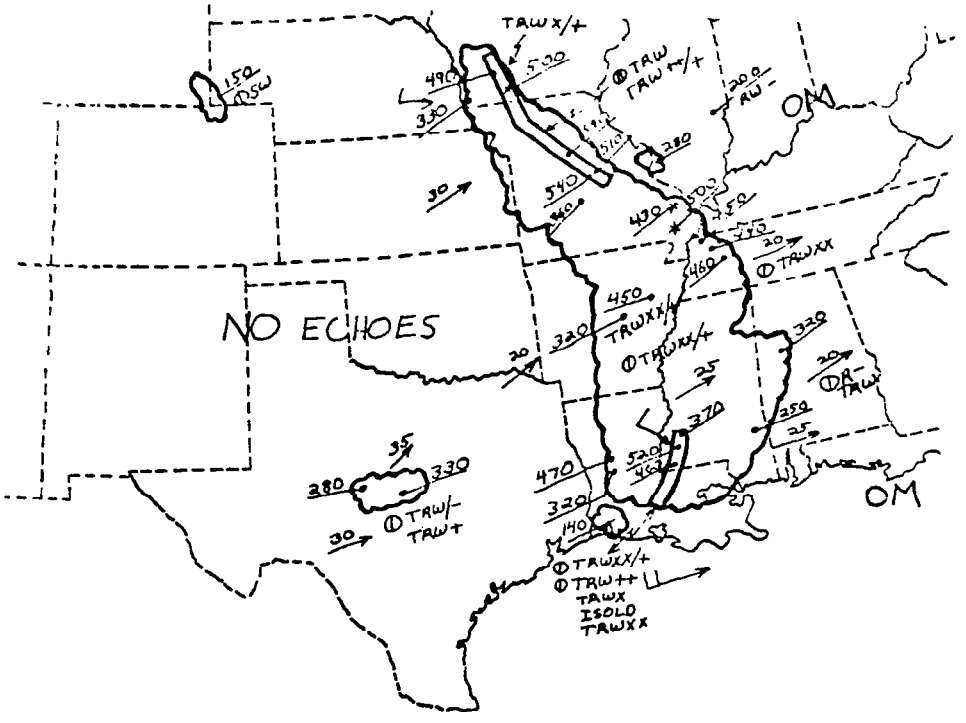

(b) 1435 GMT 6 May 1975

Fig. 4.3. Radar summary charts for the AVSSE II period.

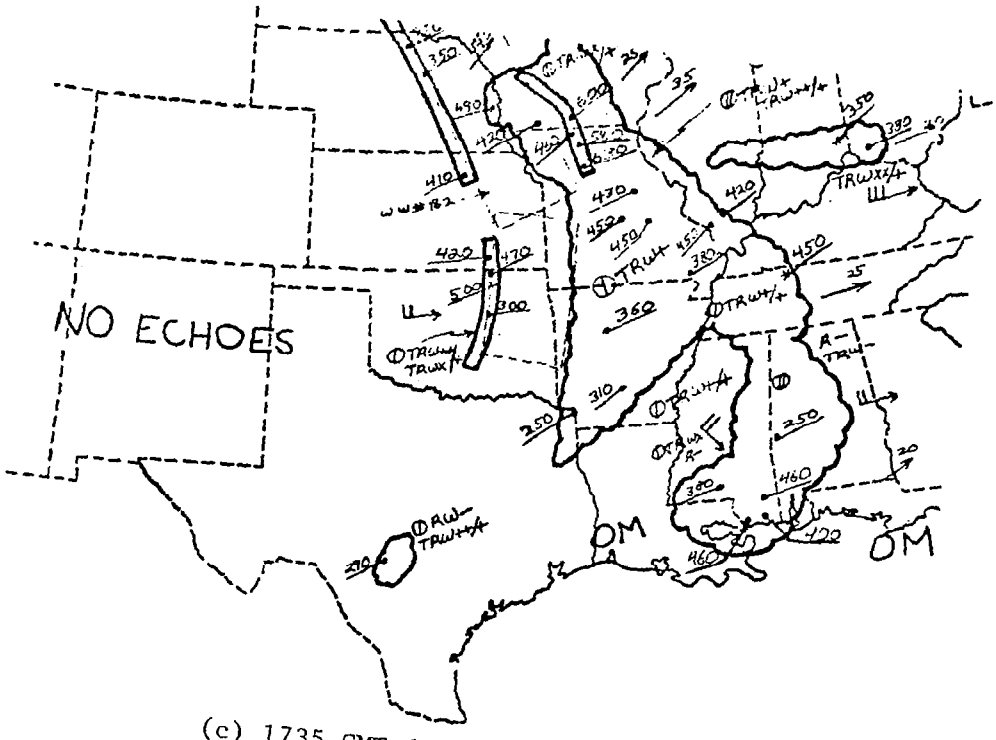

(c) 1735 GMT 6 May 1975

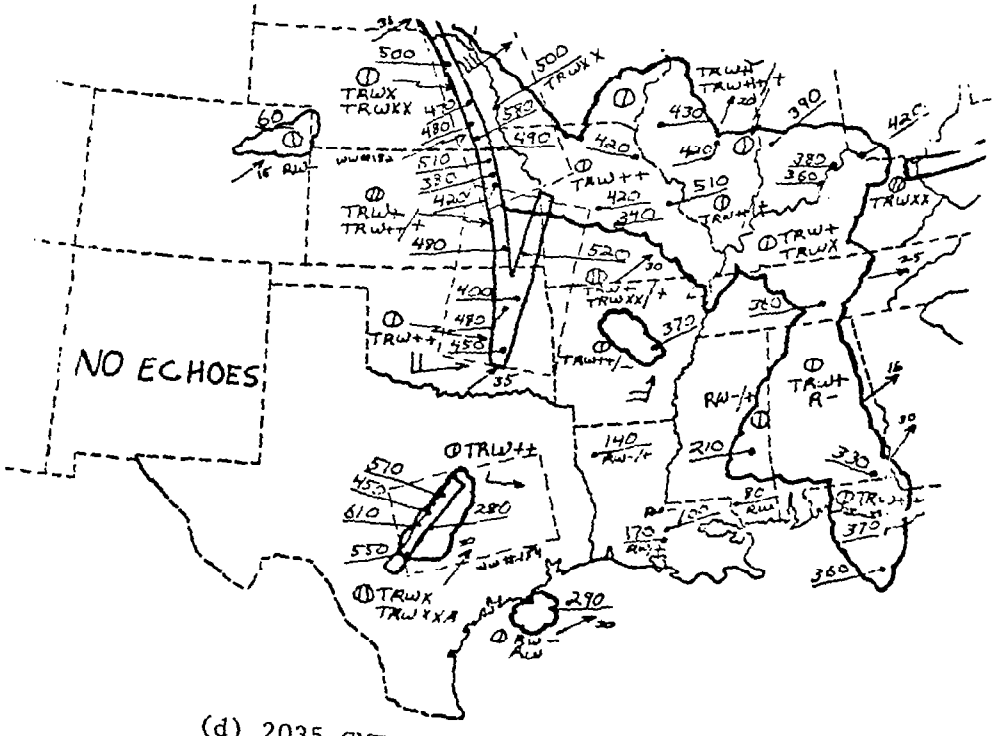

(d) 2035 GMT 6 May 1975

Fig. 4.3. (Continued)

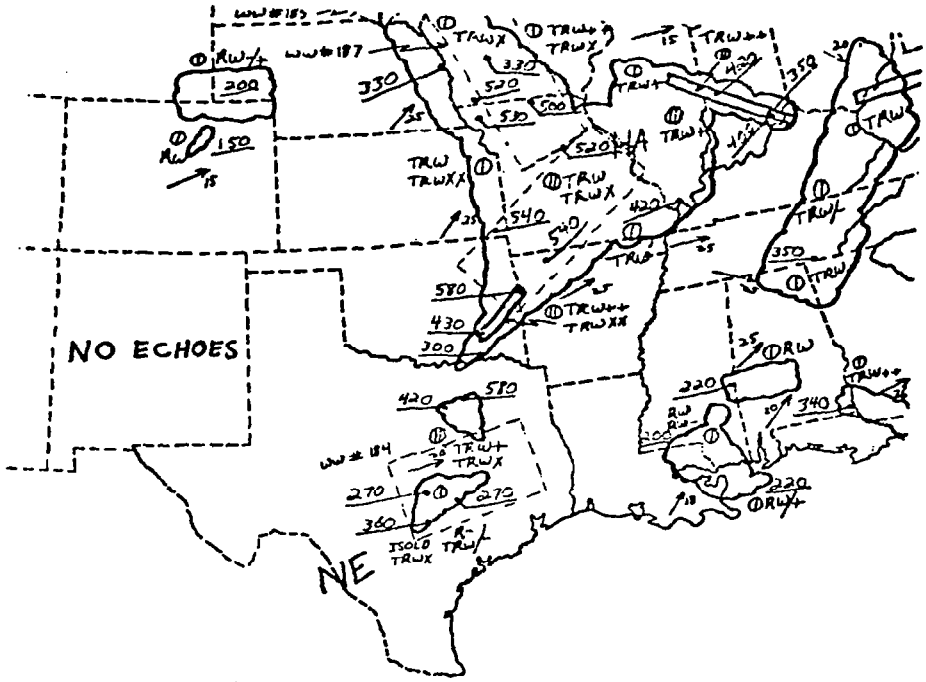

(e) 2335 GMT 6 May 1975

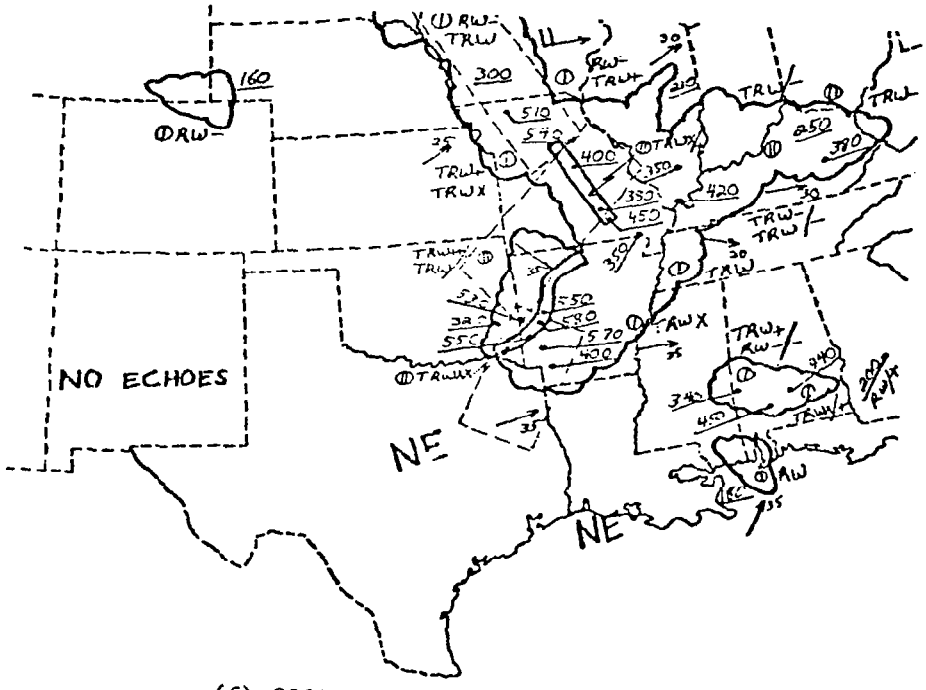

(f) 0235 GMT 7 May 1975

Fig. 4.3. (Continued)

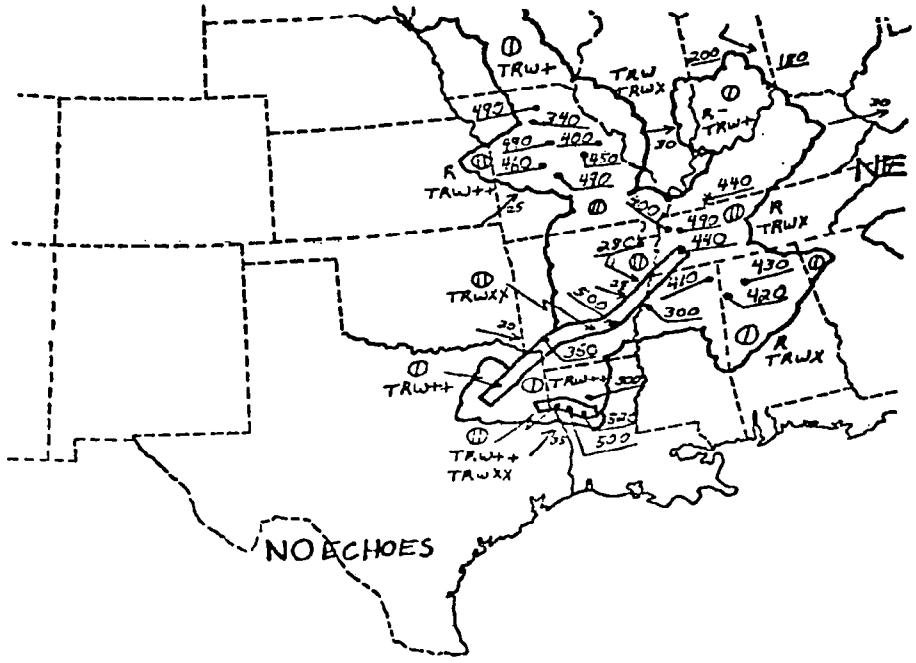

(g) 0735 GMT 7 May 1975

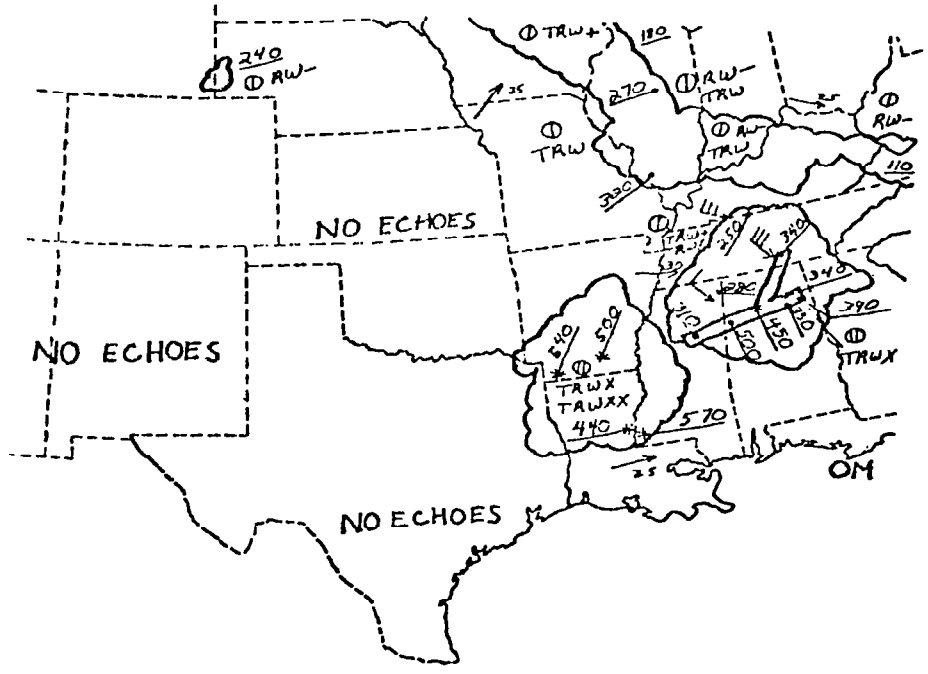

(h) 1135 GMT 7 May 1975

Fig. 4.3. (Concluded)

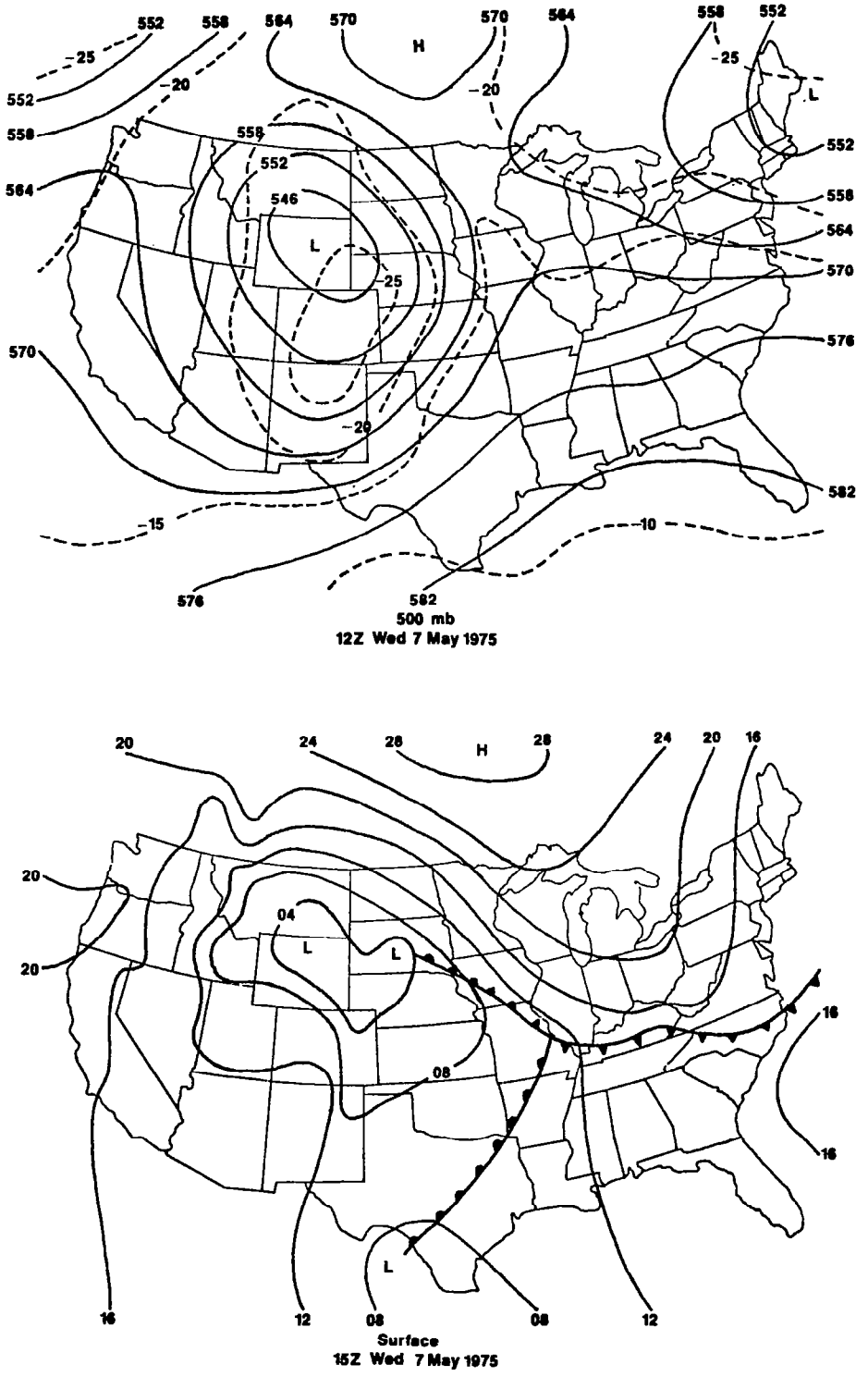

Fig. 4.4. Synoptic conditions near the end of the AVSSE II period.

4. RESULTS

a. Spatial fields of unadjusted vertical motion

As mentioned earlier, unrealistic values of vertical motion often occur at the top of the atmosphere when the kinematic method with upward integration is used without adjustment schemes. In this study, magnitudes of vertical velocity ranged from -13 to 19 μ b s^{-1} at 100 mb which are comparable to values computed by O'Brien (1970) and Chien and Smith (1973). Values this large are greater than normally would be expected at 100 mb on the synoptic scale. These unrealistic values have several sources: inaccurate measurement of the horizontal wind (Wilson, 1976, and O'Brien, 1970), and truncation and other types of computational inadequacies (Smith, 1971), such as use of the trapezoidal rule.

A description of spatial fields of unadjusted vertical velocities at 500 mb will now be given (Fig. 4.5). Values were obtained by integrating upward through the atmosphere starting at the surface (designated by $\omega_{\uparrow}$), and by integrating downward through the atmosphere starting at 100 mb (designated by $\omega_{\downarrow}$). These spatial fields reveal many interesting similarities and differences. At 1200 GMT 6 May (Fig. 4.5a), the $\omega_{\uparrow}$ field shows a prominent area of upward vertical motion (negative values of ω designate rising air) in central Kansas and northern Oklahoma. This area moves southward and increases in size by 1500 GMT (Fig. 4.5b). The $\omega_{\downarrow}$ fields for 1200 GMT and 1500 GMT (Figs 4.5c and 4.5d) do not exhibit this feature; in fact, sinking air (positive values of ω) is indicated over much of this same area. Another difference in the two methods is an area of strong upward vertical motion that is centered over southeast Missouri at 1500 GMT in the $\omega_{\downarrow}$ field but is not so prominent in the $\omega_{\uparrow}$ field. Both the $\omega_{\uparrow}$ and $\omega_{\downarrow}$ fields at 1200 GMT show strong upward motions centered over southeast Louisiana. At 1800 GMT, downward integration (Fig. 4.5g) produces an area of strong rising air over southcentral Missouri that is not evident in the $\omega_{\uparrow}$ field at this time (Fig. 4.5e). Otherwise, the two fields show general agreement.

Fields of both $\omega_{\uparrow}$ and $\omega_{\downarrow}$ exhibit centers of strong rising air in central Texas at 2100 GMT (Figs. 4.5f and 4.5h). Rising motions also are indicated over the middle Mississippi River Valley although the exact locations differ somewhat between the two methods. Dissimilar fields are evident over much of Kansas and Oklahoma. At 0000 GMT (Figs. 4.5i and 4.5k), there is still disagreement between the $\omega_{\uparrow}$ and $\omega_{\downarrow}$ fields in the Kansas region. Both fields have a center of strong rising

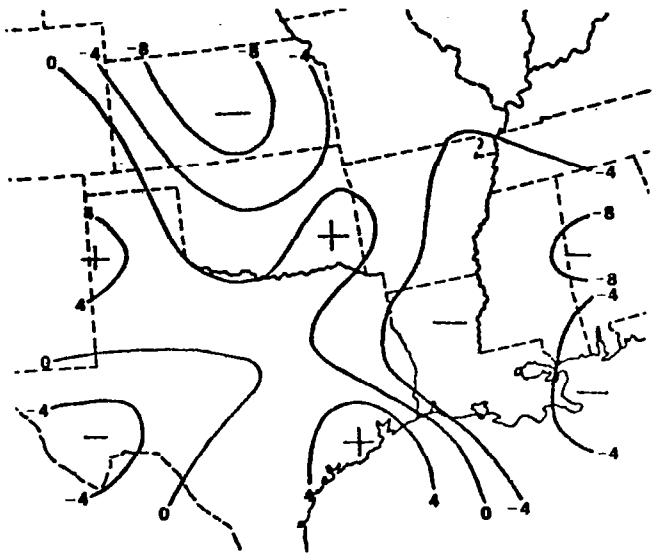

(a) $\omega_{\uparrow}$, 1200 GMT
6 May 1975

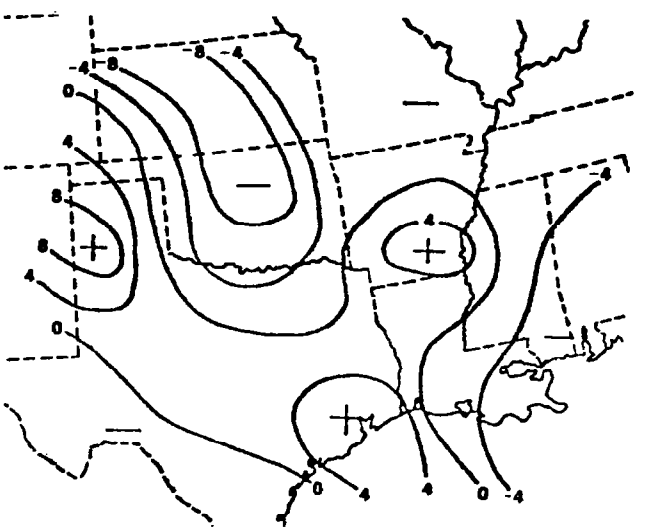

(b) $\omega_{\uparrow}$, 1500 GMT
6 May 1975

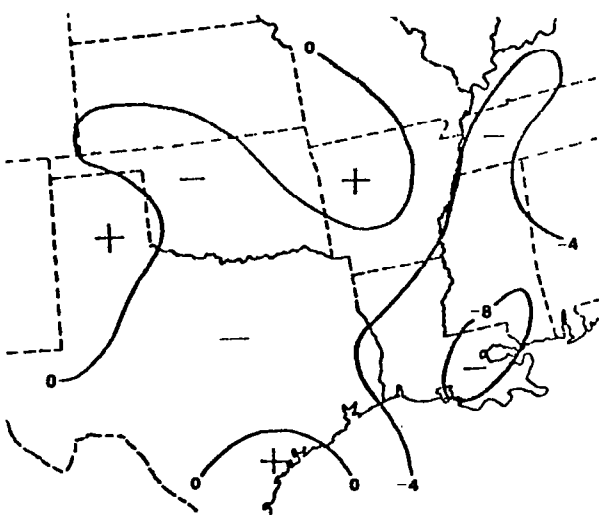

(c) $\omega_{\downarrow}$, 1200 GMT
6 May 1975

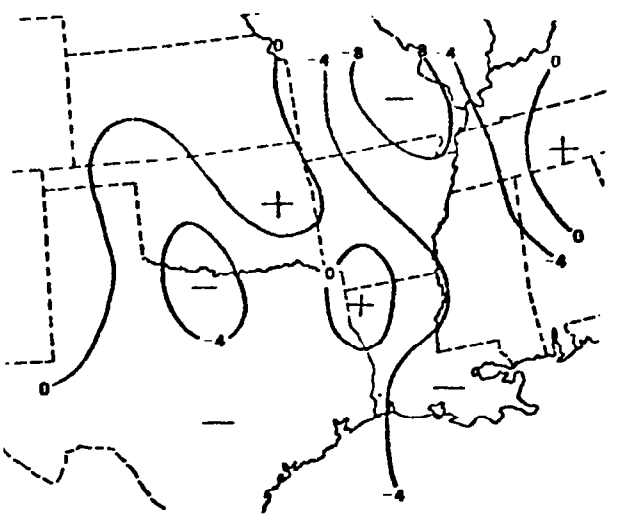

(d) $\omega_{\downarrow}$, 1500 GMT
6 May 1975

Fig. 4.5. Fields of unadjusted vertical motion ($\mu b\ s^{-1}$) at 500 mb obtained from upward ($\omega_{\uparrow}$) and downward ($\omega_{\downarrow}$) integration.

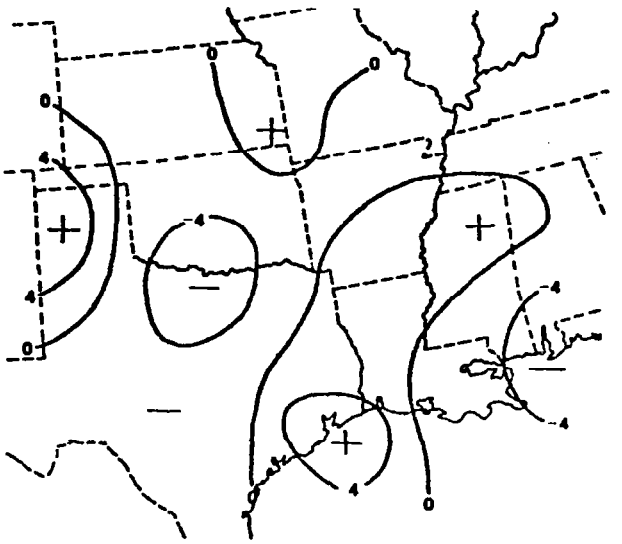

(e) $\omega_{\uparrow}$, 1800 GMT
6 May 1975

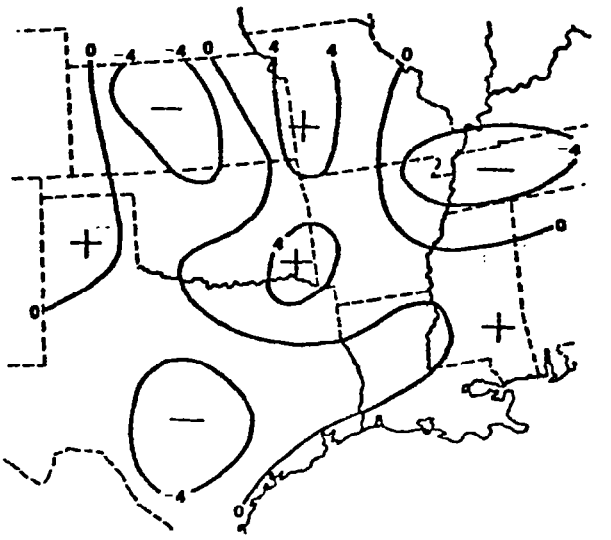

(f) $\omega_{\uparrow}$, 2100 GMT
6 May 1975

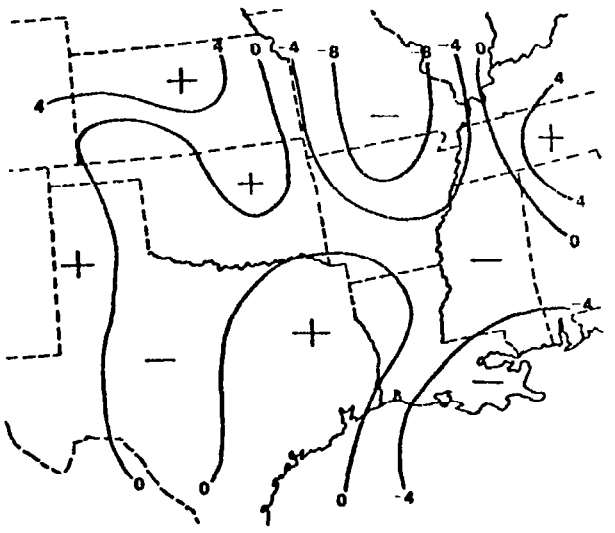

(g) $\omega_{\downarrow}$, 1800 GMT
6 May 1975

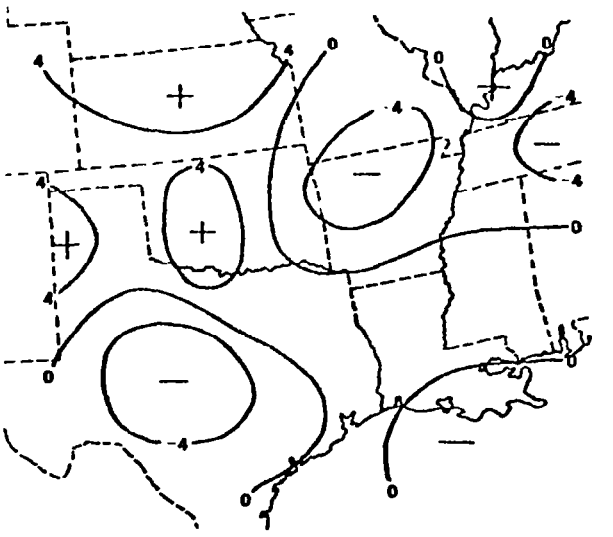

(h) $\omega_{\downarrow}$, 2100 GMT
6 May 1975

Fig. 4.5. (Continued)

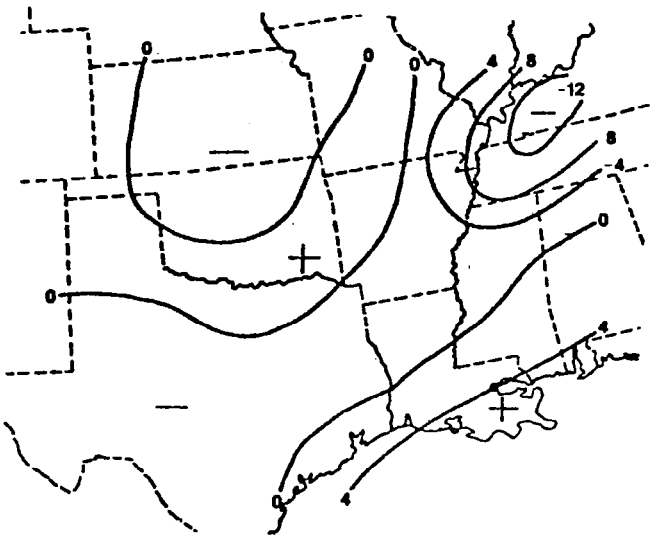

(i) $\omega_{\uparrow}$, 0000 GMT
7 May 1975

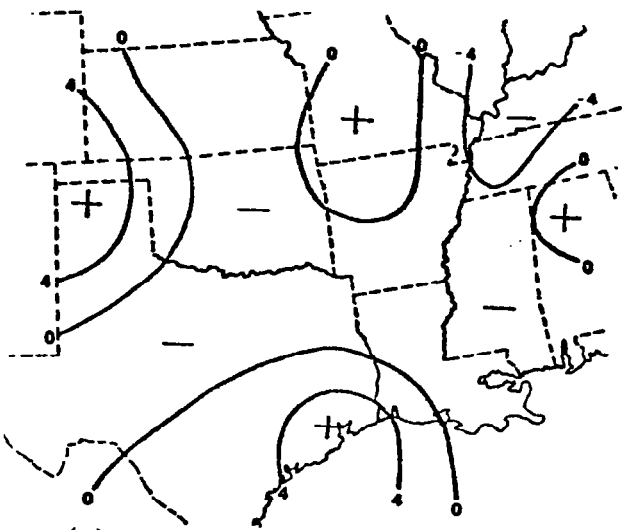

(j) $\omega_{\uparrow}$, 0300 GMT
7 May 1975

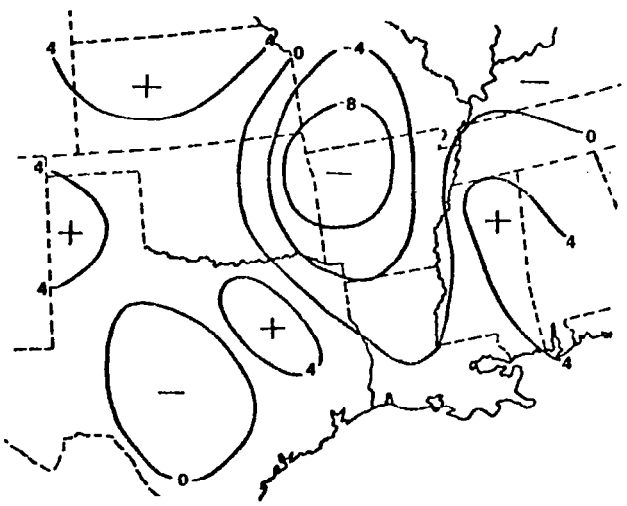

(k) $\omega_{\downarrow}$, 0000 GMT
7 May 1975

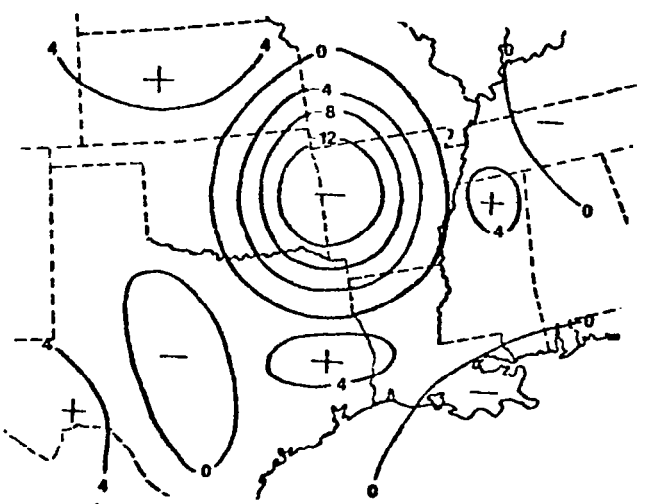

(l) $\omega_{\downarrow}$, 0300 GMT
7 May 1975

Fig. 4.5. (Continued)

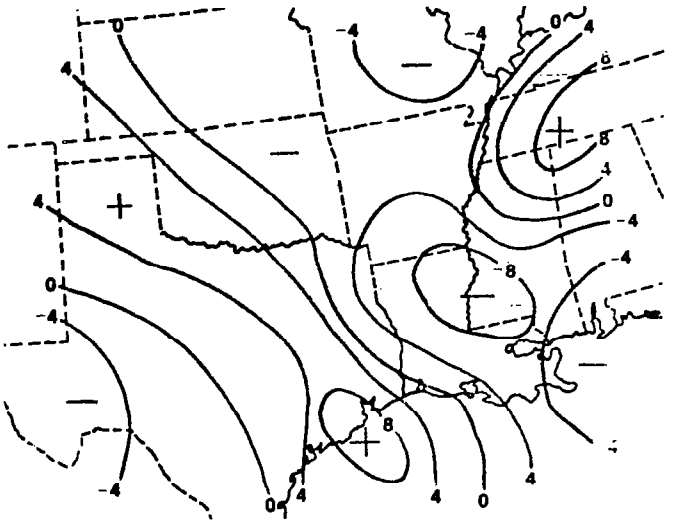

(m) $\omega_{\uparrow}$, 1200 GMT 7 May 1975

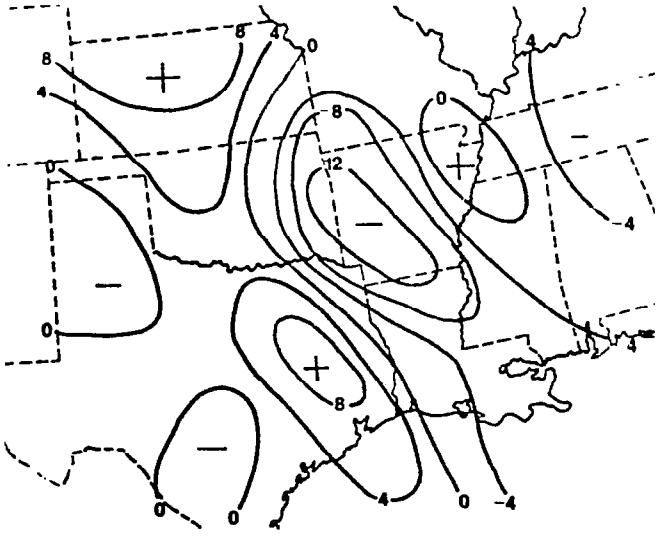

(n) $\omega_{\downarrow}$, 1200 GMT 7 May 1975

Fig. 4.5. (Concluded)

air in the northeast quadrant of the experiment area; however, the field resulting from upward integration is centered over western Kentucky while the one resulting from downward integration is centered over northwest Arkansas. Another major difference is the area of sinking air that extends to northern Mississippi in the $\omega_{\downarrow}$ field but is confined to southern Louisiana in the $\omega_{\uparrow}$ field. By 0300 GMT (Figs. 4.5j and 4.5l), the center of strong rising air in western Kentucky in the $\omega_{\uparrow}$ field has decreased greatly in intensity (from -12 to -4 $\mu b\ s^{-1}$) while the center of rising air in northwest Arkansas in the $\omega_{\uparrow}$ field has increased in magnitude (from -8 to -12 $\mu\ b\ s^{-1}$). At the last time period, 1200 GMT 7 May (Figs. 4.5m and 4.5n), both $\omega_{\uparrow}$ and $\omega_{\downarrow}$ are very similar with strong centers of rising air in southern Arkansas accompanied by areas of sinking air to the northeast and southwest.

The previous discussion has shown that major differences often exist between the unadjusted fields of $\omega_{\uparrow}$ and $\omega_{\downarrow}$ at 500 mb. Such differences result from the differing levels of the atmosphere through which integration is performed to obtain the values at 500 mb. In the $\omega_{\uparrow}$ integration scheme, the horizontal divergence fields from the surface to 500 mb are used to compute values at 500 mb while the converse is true for the $\omega_{\downarrow}$ integration scheme. This means that horizontal divergence fields from entirely different levels of the atmosphere contribute to the vertical motions at 500 mb computed by the two techniques. In light of this, differences in the unadjusted spatial fields at 500 mb for $\omega_{\uparrow}$ and $\omega_{\downarrow}$ are not surprising. One should see, for example, that rising air resulting from divergence between 100-500 mb would not necessarily be accompanied by convergence of the same magnitude between the surface and 500 mb. Such a case would produce differing values of vertical motion at 500 mb from the two integration methods. An example of this in the present case study can be found at 0300 GMT. Low-level divergence in the northeast corner of Arkansas (Fig. 4.5j) has produced sinking air in this region at 500 mb when upward integration is performed. However, strong upper-level divergence has resulted in very strong upward vertical motion in the same region at 500 mb (Fig. 4.5l) when downward integration is used.

Obtaining different values of ω at the same level immediately raises the question about which is more representative of the real atmosphere. As implied by Smith (1971), it is impossible to know the true values of ω in the free atmosphere. Agreement of the vertical motion

fields with areas of cloudiness and precipitation as well as their continuity provide valuable insight into assessing the quality of the computed values. Both $\omega_{\uparrow}$ and $\omega_{\downarrow}$ values contain errors at 500 mb because of the reasons previously cited. In fact, values of $\omega_{\downarrow}$ at 500 mb may contain more error than those of $\omega_{\uparrow}$ because the downward integration uses the more unreliable wind data. Even still, downward integration to 500 mb should reveal vertical motion features from certain upper-level conditions more clearly than would upward integration. The use of $\omega_{\downarrow}$ would appear desirable in some synoptic situations. This aspect will now be investigated further by considering the continuity and relation of the $\omega_{\uparrow}$ and $\omega_{\downarrow}$ fields to weather conditions.

It is interesting to note the continuity of prominent features in the unadjusted spatial fields. Considering upward integration first, one finds that fields show good continuity over the 24 h experiment period. The large area of rising air (negative values of ω) over Kansas and Oklahoma at 1200 GMT and 1500 GMT (Figs.4.5a and 4.5b) suddenly weakens at 1800 GMT (Fig. 4.5e). Another prominent area of rising air ($-4\ \mu b\ s^{-1}$) in the $\omega_{\uparrow}$ field appears in the Missouri Bootheel at 2100 GMT (Fig. 4.5f), intensifies to $-12\ \mu b\ s^{-1}$ by 0000 GMT in the same area (Fig 4.5i), and then decreases in intensity over the next 3 h to $-4\ \mu b\ s^{-1}$. An area of sinking air over southeast Texas and Oklahoma at 1200 GMT (Fig. 4.5a) is very persistant feature that slowly shifts eastward into Louisiana by 0000 GMT (Fig. 4.5i) and then back again to southeast Texas by 1200 GMT 7 May (Fig. 4.5m). The intensity of this feature ($4\ \mu b\ s^{-1}$) remains nearly constant throughout the entire experiment period.

Features of the $\omega_{\downarrow}$ fields show excellent continuity in their movements and intensities. The best example is an area of upward vertical motion centered over western Tennessee at 1200 GMT (Fig. 4.5c). The area moves slowly southwestward during the next 24 h while increasing in intensity to $-12\ \mu b\ s^{-1}$ (Figs. 4.5d, g, h, k, and l).

b. Spatial fields of adjusted vertical motion

One needs to modify unadjusted values of vertical motion in order to obtain reasonable vertical profiles since unrealistic values often occur near the end of the integration process. In this study, the wind-related correction technique proposed by O'Brien (1970) was applied to values obtained using upward and downward integration. The more commonly used O'Brien pressure related scheme also was applied to vertical motions obtained from upward integration.

Fields of adjusted vertical motion at 500 mb for 2100 GMT 6 May 1975 are shown in Fig. 4.6. Values of $\omega_{\uparrow}$ adjusted by O'Brien's pressure related technique are denoted by $\omega_{\uparrow}$(O'Brien) while values of $\omega_{\uparrow}$ and $\omega_{\downarrow}$ adjusted by the wind-related scheme are denoted by $\omega_{\uparrow}$ (WIND) and $\omega_{\downarrow}$ (WIND), respectively. A comparison of the three fields of adjusted vertical motions in Fig. 4.6 reveals that they are essentially identical with only a few minor differences. The adjusted fields of $\omega_{\uparrow}$(O'BRIEN), $\omega_{\uparrow}$ (WIND), and $\omega_{\downarrow}$ (Wind) for 0000 GMT 7 May 1975 (Fig. 4.7) also are essentially identical with only a few minor differences. The same statement can be made for the adjusted fields for 0300 GMT 7 May 1975 (Fig. 4.8) and for all other times of this case study, which have not been shown.

It is remarkable that all three of the adjusted fields at a given time period are so similar. However, some degree of similarity is to be expected due to the basic design of the adjustment schemes. When values of $\omega_{\uparrow}$ are modified by O'Brien's pressure-related technique, most of the correction occurs above 500 mb where the more unrealistic vertical motions are found. The same holds true, in general, for values of $\omega_{\uparrow}$ and $\omega_{\downarrow}$ which are adjusted using O'Brien's wind-related scheme. Since the strongest winds occur above 500 mb, the greatest correction occurs in this same region. In the present study, the profile of horizontal winds aloft was such that the pressure- and wind-related schemes produced almost identical results. It should be noted, however, that situations could exist where the vertical distribution of horizontal winds would yield a wind-adjusted profile that was considerably different from the standard O'Brien technique. For example, this might occur when a poorly defined wind maximum occurs above a station.

Because the unadjusted $\omega_{\uparrow}$ vertical motion fields from the surface up to the 500 mb level are changed very little after application of either adjustment scheme, the fields of adjusted vertical motion should closely resemble those of unadjusted $\omega_{\uparrow}$ at and below 500 mb. A comparison of these fields at 500 mb (Figs 4.5-4.8) reveals that this is true.

It is important to note that adjusting values of $\omega_{\downarrow}$ eliminates prominent features evident in those fields. Since most diagnostic

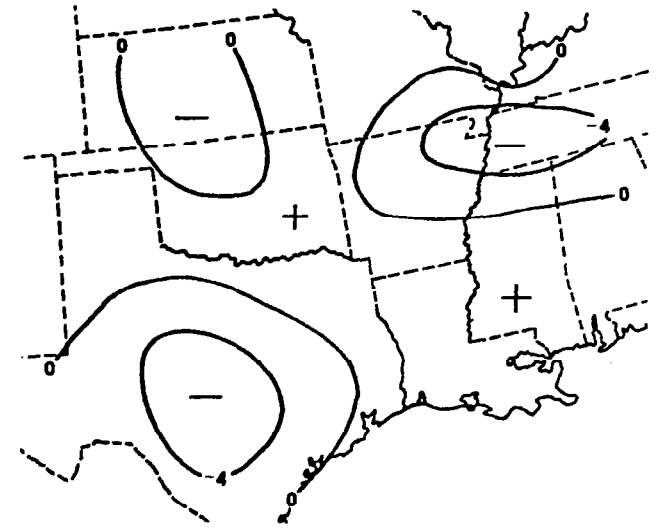

(a) $\omega_{\uparrow}$ (O'BRIEN)

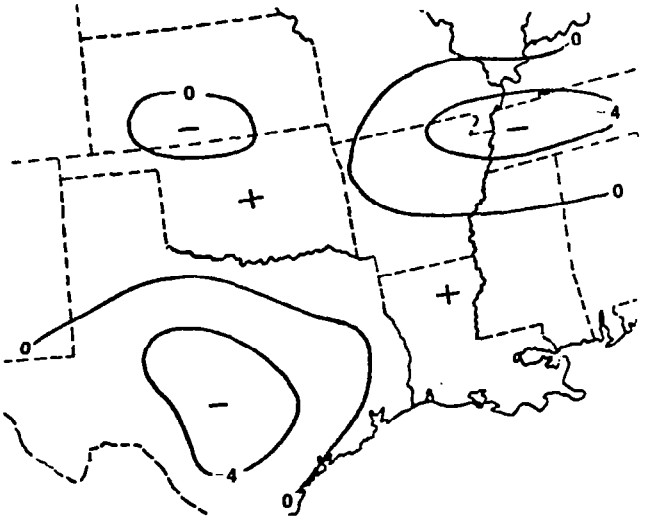

(b) $\omega_{\uparrow}$ (WIND)

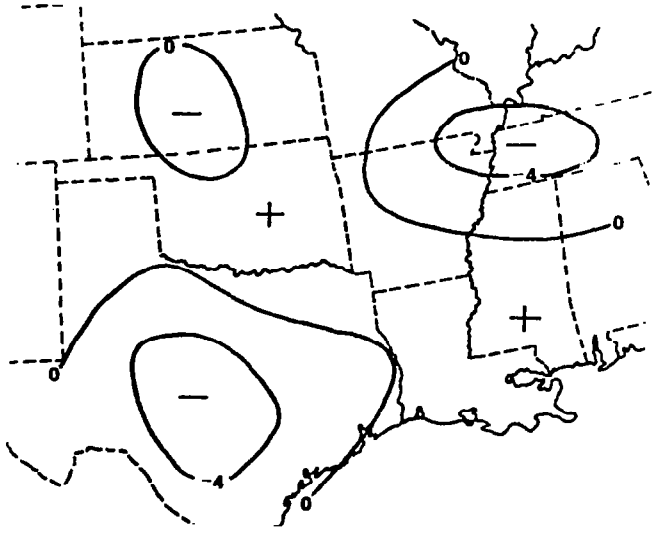

(c) $\omega_{\downarrow}$ (WIND)

Fig. 4.6. Fields of adjusted vertical motion ($\mu b\ s^{-1}$) at 500 mb at 2100 GMT 6 May 1975.

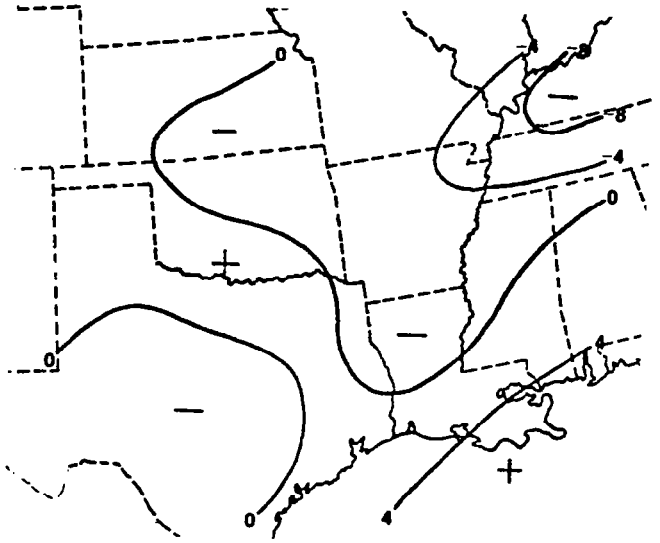

(a) $\omega_{\uparrow}$ (O'BRIEN)

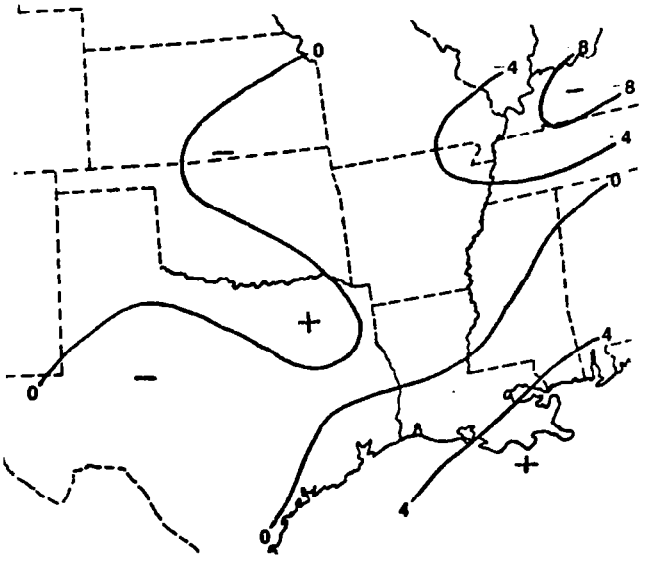

(b) $\omega_{\uparrow}$ (WIND)

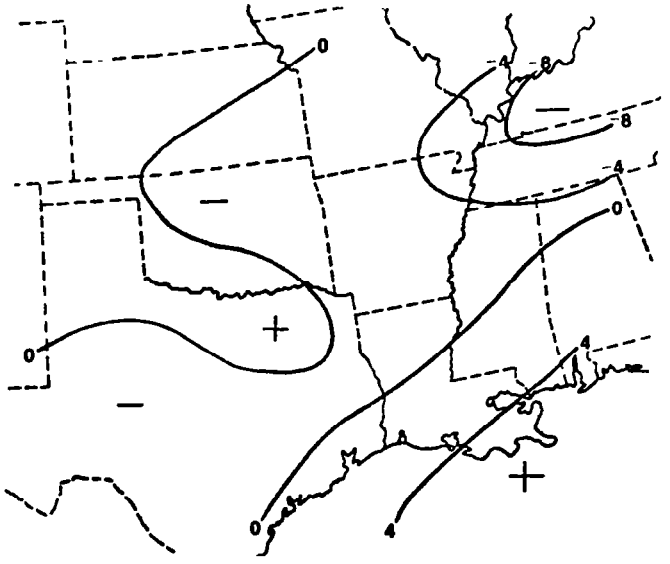

(c) $\omega_{\downarrow}$ (WIND)

Fig. 4.7. Fields of adjusted vertical motion ($\mu b\ s^{-1}$) at 500 mb at 0000 GMT 7 May 1975.

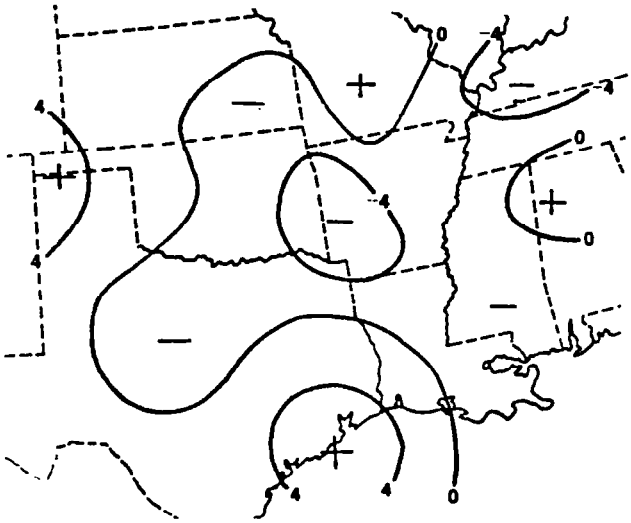

(a) $\omega_{\uparrow}$ O'BRIEN

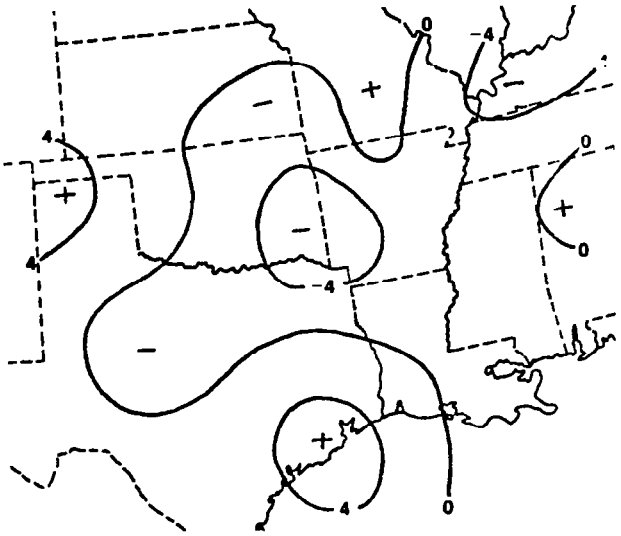

(b) $\omega_{\uparrow}$ (WIND)

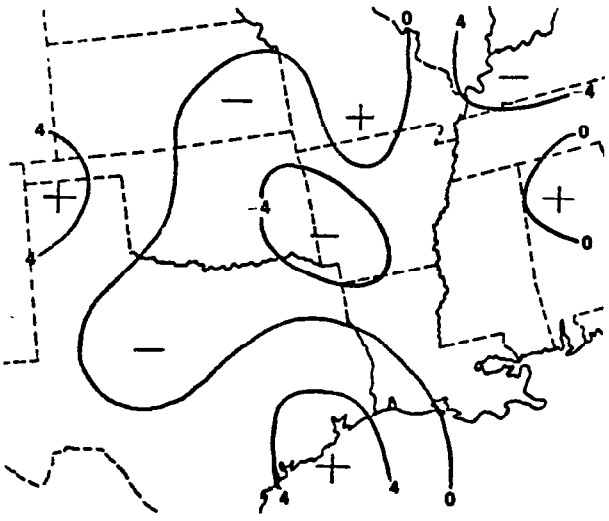

(c) $\omega_{\downarrow}$ (WIND)

Fig. 4.8. Fields of adjusted vertical motion ($\mu b\ s^{-1}$) at 500 mb at 0300 GMT 7 May 1975.

studies use only the adjusted $\omega_{\uparrow}$ fields, which in this study were found to be practically identical to $\omega_{\downarrow}$ adjusted, important features evident in the unadjusted $\omega_{\downarrow}$ fields are never considered. Although unadjusted values of $\omega_{\downarrow}$ do contain errors, earlier sections of this report have shown that such fields do have continuity and might be useful to the meteorologist.

Visually comparing fields of adjusted values (Figs. 4.6-4.8) and unadjusted values (Figs. 4.5f, h, i, j, k, and l) with the radar summaries yields interesting results. It should be noted, however, that visually comparing precipitation fields to vertical motions for the same times has limitations since Smith and Lin (1978) noted that the development of precipitation may lag the formation of a rising mass of air. In addition, adequate water vapor content is needed for the formation of precipitation, while instability also is required for thunderstorms. These two factors were not considered in this comparison.

At 2100 GMT (Fig. 4.3d), a squall line extended through the eastern portions of Nebraska, Kansas, and Oklahoma, an area of thunderstorms was located in central Texas, and storms were occurring in the middle Mississippi River Valley. The unadjusted $\omega_{\uparrow}$ field at 2100 GMT (Fig. 4.5f), shows rising motion in these areas. The unadjusted $\omega_{\downarrow}$ field (Fig. 4.5h) has a center of upward vertical velocity that corresponds well with the Texas area of convection, and rising air is indicated over much of Missouri and Arkansas where storms are located. Upward motion is not indicated, however, in Oklahoma and Kansas near the squall line. In fact, sinking air is indicated over Kansas and Nebraska where thunderstorm tops reach up to 58,000 ft. The adjusted fields of $\omega_{\uparrow}$ and $\omega_{\downarrow}$ for 2100 GMT (Fig. 4.6) match both convective areas well except in the region of southern Oklahoma.

At 0000 GMT 7 May (Fig. 4.3e), the Texas convection area is dissipating, but a general area of thunderstorms is occurring over Missouri with a squall line developing near the border of Oklahoma and Arkansas. The unadjusted $\omega_{\downarrow}$ field at 0000 GMT (Fig. 4.5k) relates very closely to the convection mentioned. A large area of upward vertical velocity centered in northwest Arkansas has increased in magnitude from -4 to -8 $\mu b\ s^{-1}$ between 2100 GMT and 0000 GMT and

closely matches the large area of convection occurring in Missouri and Arkansas, particularly the developing squall line along the western border of Arkansas. The area of upward motion in the unadjusted $\omega_{\uparrow}$ field (Fig. 4.5i) in Texas matches the convection in that area since both have decreased in area size and intensity, but the area of upward motion centered over western Kentucky is located to the east of most of the convection. The adjusted fields of $\omega_{\uparrow}$ and $\omega_{\downarrow}$ at 0000 GMT (Fig. 4.7) are similar to those of $\omega_{\uparrow}$ unadjusted and generally do not correspond as well to the convection as do fields of unadjusted $\omega_{\downarrow}$.

At 0300 GMT, a strong squall line continues to develop rapidly in northwest Arkansas while another line has developed in central Missouri (Fig. 4.3f). The unadjusted $\omega_{\uparrow}$ field at 0300 GMT (Fig. 4.5j) does not match these features very well since sinking air is evident in the areas where the squall lines are developing. The unadjusted $\omega_{\downarrow}$ field at 0300 GMT (Fig. 4.5l), however, is greatly different from the unadjusted $\omega_{\uparrow}$ field just mentioned. The $\omega_{\downarrow}$ field shows an extensive and strong (-12 μb s^{-1}) area of upward motion centered in western Arkansas near the locations of the storms. The adjusted $\omega_{\uparrow}$ and $\omega_{\downarrow}$ vertical motion fields at 0300 GMT (Fig. 4.8) correspond to the Arkansas convection, but do not match the convection in Missouri.

The formation of the squall line over Kansas and Oklahoma near 1800 GMT is not related to strong upper-level divergence since this area of storms is not well explained by the fields of unadjusted $\omega_{\downarrow}$ which reflect high-level divergence. On the other hand, storm development over Oklahoma and Arkansas near 0000 GMT is related to upper-level divergence. Fields of unadjusted $\omega_{\downarrow}$ correspond better to this storm feature than do fields of unadjusted $\omega_{\uparrow}$ or any of the three adjusted fields.

c. Vertical motion profiles

After evaluating values of unadjusted and adjusted vertical motion at only one level, 500 mb, values at all levels now will be investigated to further describe the qualities of the adjustment schemes.

Figure 4.9 gives profiles of unadjusted vertical motion and values adjusted by the wind and pressure related techniques that have been averaged over the entire computational area (see Fig. 4.1). In the unadjusted profiles, it is seen that the areal-averaged vertical

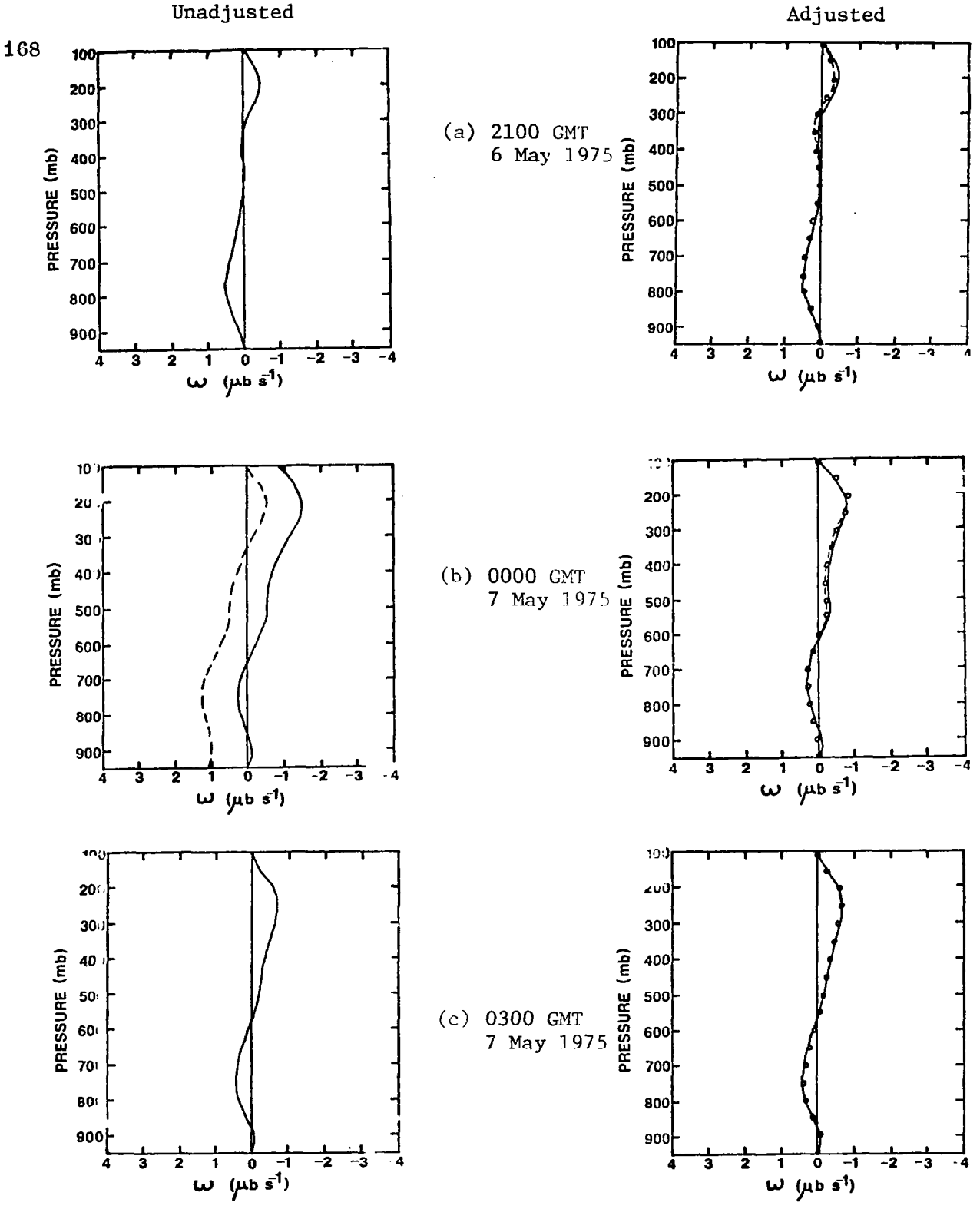

Fig. 4.9. Profiles of vertical motion for the entire computational area for three consecutive times. Unadjusted values are on the left side where ——— is ω from upward integration and ---- is ω from downward integration. Adjusted values are on the right side where ——— is $\omega_{\uparrow}$ (O'BRIEN), ---- is $\omega_{\uparrow}$ (WIND), and 0000 is $\omega_{\downarrow}$ (WIND).

velocity does not always approach zero at the end of the integration process (Fig. 4.9b). In this case, the profiles of $\omega_{\uparrow}$ and $\omega_{\downarrow}$ do not coincide. When vertical motion is zero at the end of the integration, the unadjusted profiles are identical (Figs. 4.9a and c). After adjustment, it is evident that all of the vertical motions correspond closely at any given level.

Tht total computational area was subdivided into four sub-areas (Fig. 4.1) in which average vertical motion profiles were computed (Fig. 4.10). Unlike the total-area profiles, neither upward nor downward integration produced zero vertical velocity at the end of the integration process in the smaller areas; therefore the profiles do not coincide. This result is consistent with Smith (1971), who noted that as values of vertical velocity are averaged over smaller areas and shorter time periods, that cumulative bias errors become more apparent. After application of the adjustment schemes, the new values correspond quite closely. It is clear that vertical motions obtained from downward integration are often quite different from those of upward integration, but that adjustment schemes cause both methods to give similar results.

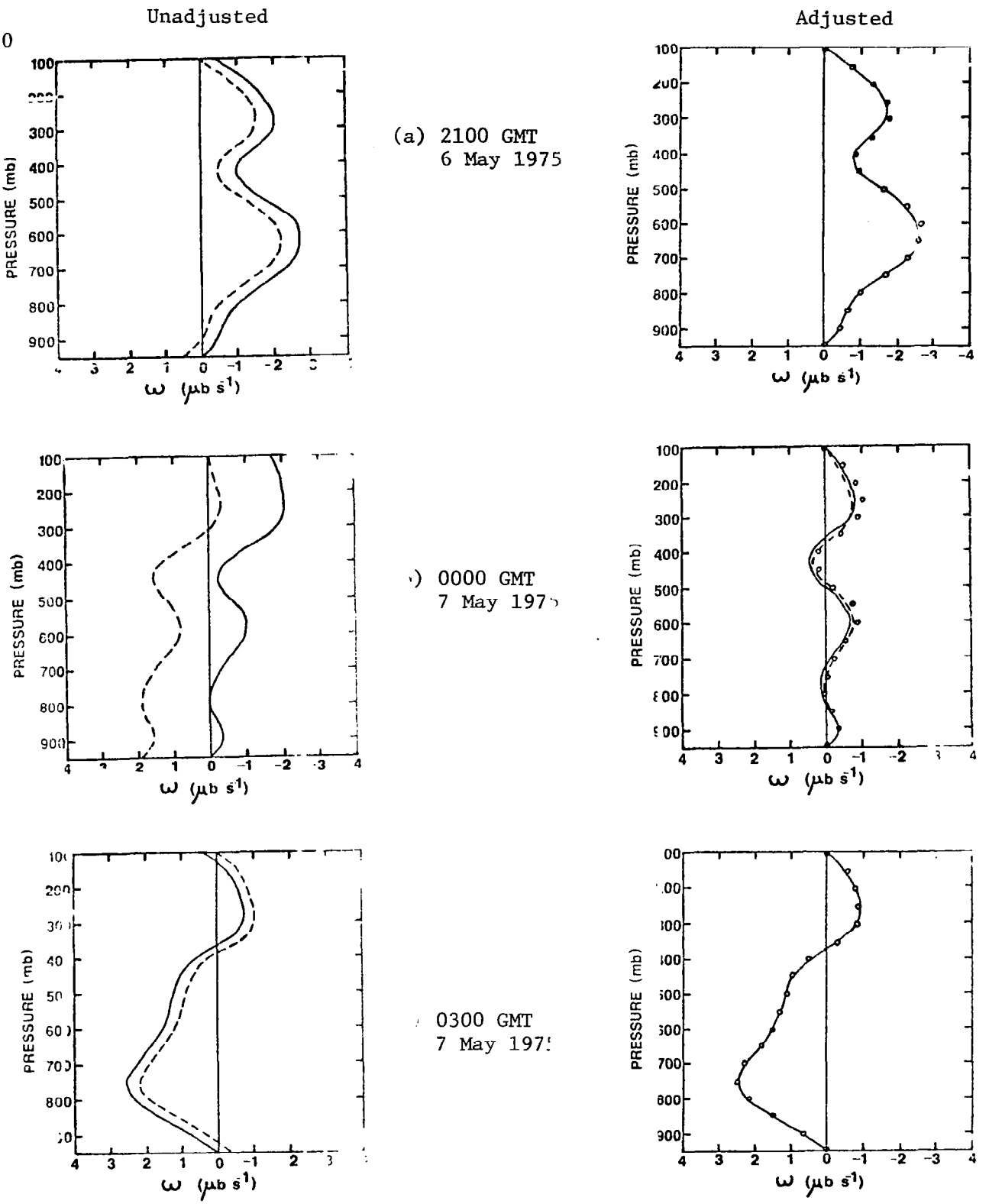

Fig. 4.10. Profiles of vertical motion of Box 3 in the computational area for 3 consecutive times. Unadjusted values are on the left side where ——— is ω from upward integration and ---- is ω from downward integration. Adjusted values are on the right side where ——— is $\omega_{\uparrow}$ (O'BRIEN), ---- is $\omega_{\uparrow}$ (WIND), and 0000 is $\omega_{\downarrow}$(WIND).

5. SUMMARY AND CONCLUSIONS

Fields of kinematic vertical motion derived from both upward integration from the surface, and downward integration from 100 mb have been evaluated for continuity, agreement with precipitation areas, and consistency with previous studies. Unadjusted values together with profiles modified using the O'Brien pressure scheme and a wind-related scheme have been studied during NASA's AVSSE II Experiment when rawinsonde data at 3 h intervals were available.

Values of unadjusted $\omega_{\downarrow}$ generally are quite different from those of unadjusted $\omega_{\uparrow}$. Neither tend to approach zero at the end of the integration process where unrealistic values occur. Values of unadjusted $\omega_{\downarrow}$ in the middle troposphere probably are less reliable than those of unadjusted $\omega_{\uparrow}$ because downward integration uses the poorer quality wind data at the beginning of the computation process. However, because fields of unadjusted $\omega_{\downarrow}$ have reasonable continuity and relate well to certain precipitation areas, they may be more useful than previously realized.

The wind-related adjustment scheme can be used to adjust both $\omega_{\uparrow}$ and $\omega_{\downarrow}$. In this study, the wind adjusted profiles were nearly identical to $\omega_{\uparrow}$ adjusted by the traditional O'Brien scheme. Vertical wind distributions where the maximum winds are not in the upper levels, however, could produce wind-adjusted profiles that are not identical to those from the O'Brien scheme. Reasonable profiles result from adjustment by both the pressure and wind-related adjustment schemes. The ability to adjust vertical motions working down from the top of the atmosphere would allow greater freedom in studying vertical motions and open up possibilities for investigating the vertical motions in upper levels of the atmosphere independent of the lower levels.

In some uses, a complete vertical profile of ω is not needed. In forecasting situations, for example, values at a single level, often 500 mb, are used. This study suggests that use of unadjusted and adjusted $\omega_{\uparrow}$ values at 500 mb will indicate low-level forcing, while values of unadjusted $\omega_{\downarrow}$ will indicate the integrated effects of upper-level forcing. It is important to note that adjusting values of $\omega_{\downarrow}$ eliminates prominant features that seem important for explaining

observed weather conditions.

The feasibility of using unadjusted $\omega_{\downarrow}$ should be investigated further. The present results suggest that it, together with $\omega_{\uparrow}$, might be a valuable aid to the forecaster.

6. REFERENCES

Barnes, S.L., 1964: A technique for maximizing detail in numerical weather map analysis. J. Appl. Meteor., 14, 396-409.

Chien, H., and P.J. Smith, 1973: On the estimation of kinematic parameters in the atmosphere from radiosonde wind data. Mon. Wea. Rev., 101, 252-261.

Fucik, N.F., and R.E. Turner, 1975: Data for NASA's AVSSE II experiment: 25 mb sounding data and synoptic charts. NASA TMX-64957. George C. Marshall Space Flight Center, Al., 174 pp.

Fuelberg, H.E., 1974: Reduction and error analysis of the AVE II pilot experiment data. NASA CR-120496. George C. Marshall Space Flight Center, Al., 131 pp.

Lateef, M.A., 1967: Vertical motion, divergence, and vorticity in the troposphere over the Caribbean Aug. 3-5, 1963. Mon. Wea. Rev., 95, 778-790.

O'Brien, J.J., 1970: Alternate solutions to the classical vertical velocity problem. J. Appl. Meteor., 9, 197-203.

Smith, P.J., 1971: An analysis of kinematic vertical motions. Mon. Wea. Rev., 99, 715-724.

_____, and C.P. Lin, 1978: A comparison of synoptic scale vertical motions computed by the kinematic method and two forms of the omega equation. Mon. Wea. Rev., 106, 1687-1694.

Vincent, D.G., K.E. Bossingham, and H.J. Edmon, Jr., 1976: Comparison of large scale vertical motions computed by the kinematic method and quasi-geostrophic ω-equation. Preprints of Sixth Conf. on Weather Forecasting and Analysis, Albany, Amer. Meteor. Soc., 357-364.

Wilson, G.S., 1976: Large scale vertical motion calculation in the AVE IV experiment. Geophys. Res. Lett., 3, 735-738.

1. REPORT NO.	2. GOVERNMENT ACCESSION NO.	3. RECIPIENT'S CATALOG NO.
NASA CR-3336		

4. TITLE AND SUBTITLE	5. REPORT DATE
Kinetic Energy Budgets in Areas of Intense Convection	November 1980
	6. PERFORMING ORGANIZATION CODE

7. AUTHOR(S)	8. PERFORMING ORGANIZATION REPORT #
Henry E. Fuelberg, Emil M. Berecek, David M. Ebel, and Gary J. Jedlovec	

9. PERFORMING ORGANIZATION NAME AND ADDRESS	10. WORK UNIT NO.
Department of Earth and Atmospheric Sciences Saint Louis University Saint Louis, Missouri 63103	M-305
	11. CONTRACT OR GRANT NO. NAS8-33370
	13. TYPE OF REPORT & PERIOD COVERED Contractor Report
12. SPONSORING AGENCY NAME AND ADDRESS National Aeronautics and Space Administration Washington, D.C. 20546	14. SPONSORING AGENCY CODE

15. SUPPLEMENTARY NOTES

NASA Marshall Technical Monitor: Kelly Hill
Final Report

16. ABSTRACT

Three studies are included in this report. The first section contains a kinetic energy budget analysis of the AVE-SESAME 1 period which coincided with the deadly Red River Valley tornado outbreak. Horizontal flux convergence was found to be the major kinetic energy source to the region, while cross-contour destruction was the major sink. Kinetic energy transformations were dominated by processes related to strong jet intrusion into the severe storm area. A kinetic energy budget of the AVE 6 period also is contained in this section.

The second phase of the report describes effects of inherent rawinsonde data errors on widely used basic kinematic parameters, including velocity divergence, vorticity advection, and kinematic vertical motion. In addition, an error analysis is performed on terms of the kinetic energy budget equation.

Finally, results obtained from downward integration of the continuity equation to obtain kinematic values of vertical motion are described. This alternate procedure shows promising results in severe storm situations.

17. KEY WORDS	18. DISTRIBUTION STATEMENT
Convection Rawinsonde Data Wind Perturbations	Unclassified - Unlimited STAR Category 47

19. SECURITY CLASSIF. (of this report)	20. SECURITY CLASSIF. (of this page)	21. NO. OF PAGES	22. PRICE
Unclassified	Unclassified	184	A09

For sale by National Technical Information Service, Springfield, Virginia 22161

NASA-Langley, 1980